

# Thermomechanical Simulation of Direct Chill Casting

**Dissertation**

zur Erlangung des akademischen Grades

Doktoringenieur

**(Dr.-Ing.)**

vorgelegt von

**M.Tech. Ashok Kumar Nallathambi**

geb. am 19.02.1980

in Dindigul, Tamil Nadu, India

genehmigt durch die

Fakultät für Verfahrens- und Systemtechnik  
der Otto-von-Guericke-Universität Magdeburg

Gutachter:

Prof. Dr.-Ing. E. Specht,  
Institute of Fluid Dynamics and Thermodynamics,  
Universität Magdeburg.

Prof. Dr.-Ing. A. Bertram,  
Institute of Mechanics, Universität Magdeburg.

Eingereicht am: 03.05.2010

Promotionskolloquium am: 10.06.2010

# Preface

This dissertation is submitted to Otto von Guericke University, Magdeburg for the degree of Doctor of Philosophy. The research described herein was conducted under the supervision of Prof. Eckehard Specht and Prof. Albrecht Bertram between March 2007 and May 2010. To the best of my knowledge, this work is original, except where suitable references are made to previous works. Neither this, nor any substantially similar dissertation has been submitted for any degree, diploma or qualification at any other university or institution.

Ashok Kumar Nallathambi  
Magdeburg, 03.05.2010

*Our wisdom comes from our experience, and our experience comes from our foolishness*

Sacha Guitry (1885-1957)

# Acknowledgments

I would like to express my sincere gratitude to my supervisors **Prof. Dr.-Ing. E. Specht** and **Prof. Dr.-Ing. A. Bertram** for providing me the opportunity to work with them and pursue a doctoral degree. Prof. Specht continuously encouraged me to finish this work successfully. His strong motivation and trust enriched my confidence level to solve the solidification problem. His friendly way of handling the research students has broken the communication barriers. He is the man who links the industry with universities. He made me to visit more than 15 manufacturing plants in and around the Germany. His commitment with the industries, motivated us to investigate the inverse heat conduction problem. Further, he encouraged me to handle the computational heat and mass transfer course for the international master students.

Prof. Bertram provided his valuable guidance for the mechanical part of the work. His *nonlinear continuum mechanics* course improved my basic understanding of solid mechanics. Even though, every time I go with some demand, he never denied anything. He sincerely corrected and gave the valuable suggestions for all of our journal papers. During the GKMM meeting, he always encouraged me to actively participate in the discussion.

The start-up phase is the most critical phase in DC casting. This also applicable to every new beginner who start his PhD study. My senior **Dr.-Ing. Yalcin Kaymak** helped me to overcome all the research hurdles during the starting phase. He also exposed me to learn the modeling of quenching distortion. His systematic approach for the MATLAB programming is the basis for my work. He is the one who established the FE mesh generation and post processing code in MATLAB. This saved considerable amount of programming time. He also encouraged me to write research papers from his thesis. Even though he left the university, he helped me whenever I face any computational difficulties.

I feel immense pleasure in saluting the **Otto von Guericke University, Magdeburg** for giving me a great opportunity to pursue the research study in Germany. I would like to acknowledge the financial support provided by the **Graduiertenkolleg-828 (GKMM)** through the **German Research Foundation (DFG)**. I would like to

thank my GKMM colleagues **Jan Kalisch**, Sebastian Borsch, Rainer Glüge, Thorsten Hoffmann, Dr.-Ing. Stephanie Fest Santini, Ulf Cunäus, Fabian Weigler, Dr.-Ing. Dana Zöllner, Dr.Sashikumaar Ganesan, Dr.Abdolreza Kharaghani, Prof. Jitendra Kumar, Dr. Vikranth Kumar Surasani, and Dr. Yashodhan Gokhale. We all actively involved in the 6 meetings of GKMM for the past 3 years.

During the development of line-search algorithm, the technical discussions with professor **G. Warnecke** was very useful. He voluntarily invited me to give a speech in mathematics department. The communication with the research experts **J.M. Drezet** and **Victor.D.Fachinotti** are sincerely acknowledged. It is my duty to acknowledge my indian professors **Prof. M.S. Sivakumar**, **Prof. C. Lakshmana Rao**, and **Dr. A. Arockiarajan** for their timely suggestions and caring. I would like to thank my friend **Karsten Quint** for providing the opportunity to present and discuss about the phase change phenomena in steel. The experimental support provided by my colleagues **Umair Alam** and **Khalid HM Abdalrahman** are greatly appreciated. The technical discussions with an internship student **Mohit Tyagi** was really helpful to implement the viscoplastic part.

Its my duty to thank **Dr.-Ing. Hermann Woche** for his valuable technical supports. I would like to personally thank my colleague **Zhiguo Xu** for his encouragement and understanding. He introduced me a new way of life style. He frequently insisted me that the poor always think in a poor way and the rich person always think rich. I whole heartedly thank my colleagues **Nadine Lorenz**, Ping meng, Haido, Yogesh, Fabian, Magda, Tareq, Kotsev, and Dr. Shi. I would like to thank Frau Lotz, Frau Rudolph, and Frau Zacke for helping me to handle the financial issues. I express my sincere thanks to **Christin Hasemann** for helping me to solve the official issues.

Finally, I would like to express my sincere thanks to every individual German citizens for contributing either directly or indirectly. During my stay in Germany, I learnt self discipline, punctuality and time management from the fellow citizens of Germany. Similarly, I would like to thank my home country and Indian Institute of Technology Madras. Further, I extend my thanks to indian friends Kamesh, Ramakrishna, Darshan, Thirumalesha, Sukumar, Polu, **Koteswara Rao Sunkara**, Dr. Pavan and his wife, Shanmugam and his wife, Dr. Jayabal, Subbu, Sangamitra, Sowmya, and Deepthi. I thank my friend **B.V. Krishna Murthy** for his moral support. Last but not the least, the word *thank* is not sufficient to thank my closest friend **Purna Chandra Gourisankar Sandaka**.

The continuous encouragement given by my loving parents and younger brother **N. Senthil Kumar** are greatly acknowledged. Especially, I thank my mother who is the reason for my existence and establishment.

# Abstract

Direct chill (DC) casting is a semi-continuous casting technique which is used to produce rolling ingots and extrusion billets. Generally, non-ferrous metals such as aluminum and magnesium alloys are cast through the DC casting. During the DC casting, the liquid metal is poured into a bottomless static mold which is initially enclosed by the bottom block. After certain time, the bottom block is withdrawn with a specified speed along with the casting. As the lower part of the casting leaves the mold, the cooling water flows downward and directly chills the surface of the casting. During this process, three different cooling zones are identified: primary mold cooling, secondary water cooling, and bottom block cooling. The start-up, steady state or pseudo steady state, and end-up are the three different stages of DC casting. Transient nature of the start-up phase is the most critical phase in which the quality of the ingot is questioned. Apart from other quality issues, the hot crack and cold crack are the two major problems in the DC casting which originate during and after the solidification.

In this work, the thermal, metallurgical, and the mechanical fields of DC casting are modeled. The attention is focused on the mushy state of alloy where the chances are high for the hot tearing. The heat conduction and metallurgical phase-change phenomenon are modeled together in a strongly coupled manner. An isothermal staggered approach is followed to couple the thermal and mechanical parts within a time step. Finite element method is used to discretize the thermal and mechanical field equations. A finite element program is developed for mesh generation and solving the coupled field equations by using MATLAB programming language. A temperature-based fixed grid method is followed to incorporate the latent heat. The computational difficulties associated with a pure metal solidification is addressed. A line-search algorithm is introduced within the Newton-Raphson iterations. Also, an attempt is made to predict the boiling curve which is essential to describe the secondary cooling of DC casting. Experimental setup is established for the quenching of hot rectangular plate by an array of jets. An infrared thermography is used to measure the temperature profiles on the plate surface with known emissivity. A non-iterative inverse finite element is developed to compute the heat flux from the experimental temperature profiles. The influence of water flow rate is

investigated by using Nickel (Ni200), and aluminum alloy (AL2024) plates. It is found that the water velocity and wetting front movement are not linearly varying. There is a critical water flow rate below which increase in water velocity increases the speed of the wetting front and the magnitude of heat flux. Beyond the critical water flow rate, increase in water flow rate does not promote the cooling.

The strain tensor is additively decomposed into elastic, thermal, and viscoplastic strain tensors. Thermal strain is computed through the thermal expansion coefficient. The mushy state of alloy is characterized through the Norton-Hoff viscoplastic law and the solid phase is modeled through the Garafalo law. An axisymmetric round billet is simulated. The casting material is considered as AA1201 aluminum alloy. It is found that all the components of stress and viscoplastic strain are maximum at the billet center. Further, the start-up phase stresses and strains are always higher than the steady state phase. Therefore, the chances of hot crack formation are higher during the start-up phase and specifically at the billet center. The influence of casting speed, secondary cooling, and melt superheat on the sump parameter and stress-strain evolution are studied thoroughly. It is proved that through the ramping procedure, the vulnerability of start-up phase can be lowered. Ramping delays the time and increases the billet height to reach the steady state. Increase in casting speed, secondary cooling, and melt temperature promote the chances of hot tearing. The influence of secondary cooling parameters are studied in depth. Increased cooling reduces stresses in the mushy at the steady state and rises probability of hot tearing during the start-up phase whereas the reduced cooling influences in exactly opposite manner. Therefore, an attempt is made to illustrate the importance of varying the secondary cooling with respect to time. It is demonstrated that through the optimized secondary cooling, the evolution of residual stresses and inelastic strains can be lowered. The Leidenfrost temperature, maximum, and film boiling heat transfer coefficients have the negligible influence on the sump parameters.

**Keywords:** Direct chill casting, Solidification, Hot tear, Residual stresses, Viscoplastic strain, Cold crack.

# Zusammenfassung

Der Direkte Kokillenguss ist eine halbkontinuierliche Technik, die zur Produktion von Walzbarren oder Pressbarren verwendet wird. Generell werden Nichteisenmetalle wie Aluminium- und Magnesiumlegierungen mit dem Kokillengusses hergestellt. Während des Kokillengusses wird das flüssige Metall in eine bodenlosen statische Form gegossen, die zunächst von einem Unterblock geschlossen ist. Nach einiger Zeit wird der untere Block mit einer bestimmten Geschwindigkeit zurückgezogen und das Kühlwasser fließt direkt auf die Oberfläche des Gusses. Während dieses Prozesses werden drei verschiedene Kühlzonen identifiziert: Hauptgussformkühlung, Sekundäre Wasserkühlung und die Unterblock Kühlung. Anlaufen, stationärer Punkt oder pseudo- stationärer Punkt und end up sind die drei verschiedenen Stufen des Kokillengusses. Der schwankende Charakter der Anlaufphase ist die kritischste Phase, in der die Qualität des Barrens bestimmt wird. Abgesehen von anderen Qualitätseigenschaften, sind der Heiß- und Kaltriss das Hauptproblem, diese können während und nach der Erstarrung entstehen.

In dieser Arbeit werden der thermische, metallurgische und mechanische Bereich des Kokillengusses modelliert. Das Augenmerk liegt auf dem weichen Zustand der Legierung, wo die Wahrscheinlichkeit für Rissbildung hoch ist. Die Wärmeleitung und die metallurgischen Phasenveränderungen wurden in einer stark gekoppelten Weise modelliert. Ein isothermisch versetzter Ansatz verfolgt die Kopplung der thermischen und mechanischen Anteile innerhalb eines Zeitschrittes. Die Finite-Elemente-Methode wird verwendet, um die Feldgleichungen aus dem thermischen und mechanischen Teil des Kokillengusses zu diskretisieren. Ein Finites-Elemente-Programm in MATLAB ist für die Netzgenerierung und für die Lösung der gekoppelten Feldgleichungen entwickelt worden. Eine auf der Temperatur basierende feste Gitter Methode verfolgt die Inkorporation der latenten Wärme. Die rechnerischen Schwierigkeiten liegen bei einer reinen Metallerstarrung vor. Ein Line-Search-Algorithmus ist mit der Newton-Raphson-Iterationen eingeführt worden. Es wird versucht, die Siedekurve vorherzusagen, die wesentlich für die Beschreibung der Kühlung des sekundären Kokillengusses ist. Ein Versuchsaufbau für das Abschrecken einer heißen rechteckigen Platte durch eine Reihe von Jets wurde entwickelt. Die Infrarot-Thermographie wurde verwendet, um die Temperaturprofile auf der

Rückseite der Platte, dessen Emissionsgrad bekannt ist, zu messen. Ein nichtiteratives inverses Finite Element wurde entwickelt, um den Wärmefluss aus den experimentellen Temperaturprofile zu berechnen. Der Einfluss des Wasserdurchflusses wird durch die Verwendung von Nickel(Ni200)- und Aluminiumlegierungen(AL2024) Platten untersucht. Es wurde festgestellt, dass die Wassergeschwindigkeit und die Bewegung der Benetzung nicht linear variieren. Es existiert eine kritische Wassermenge unterhalb derer bei Erhöhung der Wassergeschwindigkeit sich die Geschwindigkeit der Benetzung und die Größe des Wärmestromes erhöht. Jenseits der kritischen Wassermenge, fördert eine Erhöhung der Wassermenge die Kühlung nicht.

Der Verzerrungstensor ist additiv in elastische, thermische und viskoplastische Verzerrungstensoren zerlegt. Die thermische Belastung wird durch den thermischen Ausdehnungskoeffizienten berechnet. Der weiche Zustand der Legierung wird durch das Norton-Hoff-Viskoplastizitätsgesetz charakterisiert wobei die feste Phase durch das Garafalo Gesetz modelliert wird. Ein asymmetrischer Walzbarren wurde simuliert. Der Gusswerkstoff wird als Aluminiumlegierung AA1201 berücksichtigt. Das Maximum der Spannungs- und viskoelastischen Verzerrungskomponenten konnte im Zentrum des Walzblockes verifiziert werden. Des Weiteren sind die Spannungen und Verzerrungen in der Anlaufphase immer höher als in der stationären Phase. Deswegen ist das Auftreten von Heißrissbildung im Zentrum des Walzbarren während der Anlaufphase wahrscheinlich. Weiterhin wird der Einfluss von Gießgeschwindigkeit, Sekundärkühlung und Schmelzüberhitzung auf die Sumpfp Parameter sowie auf die Spannungs-/Verzerrungsentwicklung untersucht. Es werde gezeigt, dass durch das Rampingverfahren die Anfälligkeit der Anlaufphase gemindert wird. Das Hochlaufverfahren verzögert die Zeit und erhöht die Länge des Walzblockes, um stationären Zustand zu erreichen. Ein Erhöhen von Gießgeschwindigkeit, Sekundärkühlung und Schmelztemperatur erhöht die Wahrscheinlichkeit der Rissbildung. Der Einfluss von Sekundärkühlungsparametern wird detailliert untersucht. Vermehrtes Kühlen reduziert zum Einen die Spannungen im weichen Zustand in der stationären Phase. Zum Anderen erhöht es die Wahrscheinlichkeit der Rissbildung während der Anlaufphase. Wohingegen eine Verringerung der Kühlung exakt Gegenläufiges bewirkt. Daher wird die Bedeutung der Variation des Sekundärkühlens in Abhängigkeit von der Zeit dargestellt. Es kann gezeigt werden, dass eine optimale Sekundärkühlung die Entwicklung der Restspannung und der unelastischen Verzerrung reduziert. Die Leidenfrosttemperatur, der maximale Wärmeübergangskoeffizient sowie der Wärmeübergangskoeffizient durch Filmverdampfung haben einen vernachlässigbaren Einfluss auf die Sumpfp Parameter.

**Schlagwörter:** Direkter Kokillenguss, Erstarrung, Wärmeriss, Eigenspannungen, Viskoplastische Belastung, Kaltrisse



# Contents

<b>Preface</b>	<b>i</b>
<b>Acknowledgments</b>	<b>ii</b>
<b>Abstract</b>	<b>iv</b>
<b>Zusammenfassung</b>	<b>vi</b>
<b>List of Tables</b>	<b>xi</b>
<b>List of Figures</b>	<b>xvi</b>
<b>Abbreviations</b>	<b>xvii</b>
<b>1 Introduction</b>	<b>1</b>
1.1 Overview and Motivation . . . . .	1
1.2 Aluminum and its alloys . . . . .	6
1.3 DC casting . . . . .	8
1.3.1 Cooling mechanisms . . . . .	10
1.3.2 Common DC casting problems . . . . .	11
1.4 Problem definition . . . . .	15
1.5 Mathematical modeling of DC casting . . . . .	18
1.5.1 Thermal model . . . . .	20
1.5.2 Mechanical model . . . . .	23
1.5.3 Coupling strategy . . . . .	24
1.6 Literature review . . . . .	25
1.6.1 Thermal aspects of DC casting . . . . .	25
1.6.2 Mechanical aspects of DC casting . . . . .	32
1.6.3 Hot tearing and cold cracking . . . . .	35
1.6.4 General aspects of DC casting . . . . .	39
1.7 Thesis outline . . . . .	40

1.8	Summary . . . . .	41
<b>2</b>	<b>Modeling of Solidification Problem</b>	<b>42</b>
2.1	Definition . . . . .	42
2.2	Solution Methodology . . . . .	46
2.2.1	Weak form . . . . .	47
2.2.2	Finite Element Technique . . . . .	48
2.2.3	Iterative incremental scheme . . . . .	49
2.3	Computational difficulty . . . . .	51
2.4	Line-Search Algorithm . . . . .	54
2.5	Element computations . . . . .	56
2.6	Thermal interface . . . . .	58
2.7	Numerical results . . . . .	59
2.7.1	Isothermal solidification of 1-D bench-mark problem . . . . .	60
2.7.2	Isothermal solidification of aluminum in a steel mold . . . . .	61
2.8	Summary . . . . .	65
<b>3</b>	<b>Inverse Problem</b>	<b>66</b>
3.1	Secondary cooling in DC casting . . . . .	66
3.2	Experimental arrangements . . . . .	69
3.3	Mathematical formulation . . . . .	70
3.3.1	Direct Heat Conduction Problem (DHCP) . . . . .	70
3.3.2	Inverse Heat Conduction Problem (IHCP) . . . . .	71
3.3.3	Element computations . . . . .	73
3.4	Quenching of nickel plate . . . . .	73
3.4.1	Validation . . . . .	75
3.4.2	Temperature profiles . . . . .	76
3.4.3	Estimated heat flux . . . . .	77
3.4.4	Maximum heat flux propagation . . . . .	78
3.4.5	Surface heat flux vs. temperature . . . . .	79
3.5	Quenching of aluminum plates . . . . .	81
3.6	Other considerations . . . . .	84
3.7	Summary . . . . .	85
<b>4</b>	<b>Modeling of Displacement Field</b>	<b>86</b>
4.1	Mathematical formulation . . . . .	86
4.1.1	Thermal strain . . . . .	87
4.1.2	Plastic strain . . . . .	88

4.1.3	Viscoplastic strain . . . . .	90
4.2	Solution Methodology . . . . .	93
4.2.1	Weak form . . . . .	93
4.2.2	Finite element method . . . . .	94
4.2.3	Iterative incremental scheme . . . . .	98
4.2.4	Integration of plastic constitutive relation . . . . .	99
4.2.5	Integration of viscoplastic constitutive relation . . . . .	102
4.3	Element computations . . . . .	104
4.4	Contact model . . . . .	107
4.5	Numerical examples . . . . .	109
4.5.1	Mechanical loading . . . . .	110
4.5.2	Thermal loading . . . . .	112
4.6	Summary . . . . .	114
<b>5</b>	<b>Numerical simulation of DC casting</b>	<b>117</b>
5.1	Description of DC casting Model . . . . .	117
5.2	Simulation of DC casting . . . . .	122
5.3	Influence of casting speed . . . . .	138
5.3.1	Thermal field . . . . .	138
5.3.2	Mechanical field . . . . .	142
5.3.3	Hot tearing criterion . . . . .	148
5.4	Influence of secondary cooling . . . . .	151
5.4.1	Influence of secondary cooling HTC profile . . . . .	151
5.4.2	Time dependent HTC profiles . . . . .	159
5.4.3	Influence of other parameters . . . . .	168
5.5	Influence of melt superheat . . . . .	168
5.6	Mesh convergence study . . . . .	170
5.7	Summary and conclusions . . . . .	175
	<b>Bibliography</b>	<b>178</b>
	<b>List of Publications</b>	<b>192</b>
	<b>Curriculum Vitae</b>	<b>194</b>
	<b>Contact Information</b>	<b>195</b>

# List of Tables

1.1	Industrial consumption of aluminum (CIB) . . . . .	7
2.1	Material properties for 1-D isothermal phase-change problem . . . . .	60
2.2	Parameters used in solidification of pure aluminum inside a steel mold (Celementano <i>et al.</i> 1996) . . . . .	63
3.1	Geometry and Material Details . . . . .	74
3.2	Aluminum AA2024 alloy - Material properties . . . . .	81
4.1	Displacement field: Global iterative-increment scheme . . . . .	99
4.2	Displacement field: Local integration point computation for elasto-viscoplastic problem . . . . .	104
4.3	Material properties - Mechanical loading problem . . . . .	110
4.4	Material properties [pure aluminum] - Thermal loading problem . . . . .	113
5.1	Material properties of <b>AA1201</b> . . . . .	121
5.2	Parameters of Norton-Hoff law ( <b>AA1201</b> ) . . . . .	121

# List of Figures

1.1	Schematic diagram (Barral and Quintela, 2000): (a) Direct Chill casting, and (b) Electromagnetic casting . . . . .	2
1.2	Schematic diagram of DC casting apparatus (Suyitno, 2005) . . . . .	3
1.3	Direct Chill casting of aluminum alloys (Suyitno, 2005) . . . . .	3
1.4	Wrought alloy classifications . . . . .	7
1.5	DC casting of (a) billets and (b) ingots . . . . .	9
1.6	Typical hot tears which occur during pseudo steady state phase (Suyitno, 2005) . . . . .	13
1.7	A typical (a) cold crack (Lalpoor <i>et al.</i> , 2009), and (b) exudation (Thevik <i>et al.</i> 1999) . . . . .	14
1.8	Butt curl and cross-sectional bone-shaped deformation of ingot (Barral and Quintela, 1999) . . . . .	15
1.9	DC casting model . . . . .	19
1.10	A typical boiling curve . . . . .	30
2.1	Domain of the heat conductor . . . . .	45
2.2	Phase-change function for: (a) isothermal case and (b) non-isothermal case	45
2.3	Derivative of phase-change function with respect to temperature: (a) isothermal case and (b) non-isothermal case (linear phase-change function) . . .	50
2.4	Isothermal phase-change (Knoll <i>et al.</i> , 1999) (a) Enthalpy as a function of temperature and (b) Temperature as a function of enthalpy . . . . .	52
2.5	Liquid phase fraction function for an isothermal phase change: (a) Heaviside function and (b) Dirac delta function . . . . .	53
2.6	Possible choices of interpolation and extrapolation during line-search (Crisfield, 1991) . . . . .	55
2.7	Line-search Algorithm (Crisfield, 1991) . . . . .	56
2.8	4-noded quadrilateral element: (a) parent element and (b) typical element	57
2.9	Thermal interface element . . . . .	59
2.10	1-D semi infinite slab: Domain with boundary conditions . . . . .	60

2.11	1-D semi infinite slab: (a) temperature evolution at $x = 1$ m and (b) temperature distribution at $t = 4$ s . . . . .	61
2.12	1-D semi infinite slab: (a) interface evolution and (b) number of iterations and mean line search per iteration . . . . .	62
2.13	Pure aluminum solidification in steel mold (Celentano <i>et al.</i> , 1996): FE mesh	64
2.14	Pure aluminum solidification in steel mold (Celentano <i>et al.</i> 1996): (a) temperature evolution at different locations and (b) evolution of air gap	64
3.1	Secondary cooling in DC casting . . . . .	67
3.2	Experimental arrangement for water quenching of hot plate . . . . .	69
3.3	Schematic representation of plate and finite element model . . . . .	74
3.4	Validation of inverse algorithm: HTC vs. Temperature . . . . .	75
3.5	Repeatability of the experimental setup: Temperature profiles . . . . .	76
3.6	Nickel: experimental temperature profile at center line . . . . .	77
3.7	Nickel: heat flux distribution . . . . .	78
3.8	Nickel: propagation of MaxHF . . . . .	79
3.9	Nickel: Heat flux vs. Temperature . . . . .	80
3.10	Nickel: Heat flux and HTC as a function of temperature . . . . .	80
3.11	Verification of Inverse algorithm: HTC as a function of space and time for $v = 1.5$ m/s . . . . .	81
3.12	Verification of Inverse algorithm: Comparison of temperature profiles . .	82
3.13	Quenching of aluminum: wetting front movement . . . . .	83
3.14	Quenching of aluminum: heat flux vs. temperature . . . . .	83
3.15	Quenching of aluminum: HTC vs. temperature . . . . .	84
4.1	Plasticity: plastic loading at $\mathbf{T}$ . . . . .	89
4.2	Viscoplasticity (Neto <i>et al.</i> , 2008): (a) Strain rate dependence: uniaxial tests at different strain rates and (b) Creep: plastic flow at constant stress	91
4.3	9-noded quadrilateral element: (a) parent element and (b) typical element	105
4.4	Schematic representation of interface contact element . . . . .	108
4.5	Mechanical loading: (a) axisymmetric domain with boundary conditions and (b) finite element mesh . . . . .	111
4.6	Stress-strain curve: Perzyna model . . . . .	112
4.7	Stress-strain curve: Norton-Hoff and Garafalo law . . . . .	112
4.8	Thermal loading: (a) axisymmetric domain with boundary conditions and (b) finite element mesh . . . . .	114
4.9	Thermal loading: Temperature evolution . . . . .	115
4.10	Thermal loading: Evolution of stresses at center (A) and outer(B) . . . .	115

4.11	Thermal loading: Distribution of von Mises equivalent stress at $t = 250$ s (a) Perzyna model and (b) rate-independent plasticity . . . . .	116
4.12	Thermal loading: Distribution of stresses at $t = 250$ s (a) radial ( $\sigma_{xx}$ ), (b) axial ( $\sigma_{yy}$ ), (c) shear ( $\tau_{xy}$ ), and (d) circumferential ( $\sigma_{zz}$ ) . . . . .	116
5.1	Computational domain of DC casting billet with thermal and mechanical boundary conditions . . . . .	118
5.2	Computational domain of DC casting billet at time $t$ and $t + \Delta t$ . . . . .	118
5.3	Bottom block and mold boundary HTC's . . . . .	119
5.4	Secondary water cooling region HTC (Williams <i>et al.</i> 20003) as a function of temperature . . . . .	120
5.5	Flowchart of DC casting model algorithm . . . . .	123
5.6	Casting speed 120 mm/min: Temperature evolution nearby bottom block	124
5.7	Casting speed 120 mm/min: Temperature contours at before and after water impingement . . . . .	125
5.8	Casting speed 120 mm/min: Temperature contours at different stages of DC casting: (a) during start-up phase, (b) end of start-up phase, and (c) pseudo steady state . . . . .	125
5.9	Casting speed 120 mm/min: evolution of sump depth and mushy zone . .	126
5.10	Casting speed 120 mm/min: radial distribution of sump depth and mushy zone at steady state . . . . .	127
5.11	Casting speed 120 mm/min: Characteristic time and surface temperature of billet at which water strikes first vs. distance from bottom of the billet	128
5.12	Casting speed 120 mm/min: different boiling zone length as a function of billet height . . . . .	128
5.13	Casting speed 120 mm/min: evolution of stress at center and a radial distance of 90 mm (50 mm from bottom) . . . . .	129
5.14	Casting speed 120 mm/min: circumferential stress and viscoplastic strain as a function of temperature . . . . .	131
5.15	Casting speed 120 mm/min: axial stress and viscoplastic strain as a func- tion of temperature . . . . .	132
5.16	Casting speed 120 mm/min: circumferential stress and viscoplastic strain at solidus temperature as a function of distance from bottom of the billet	134
5.17	Casting speed 120 mm/min: stress contours at pseudo steady state . . .	135
5.18	Casting speed 120 mm/min: viscoplastic strain contours at pseudo steady state . . . . .	136
5.19	Casting speed 120 mm/min: deformed shape with equivalent stress distri- bution at pseudo steady state . . . . .	137

5.20	Casting speed 120 mm/min: butt curl evolution . . . . .	137
5.21	Casting speed profiles vs. length of billet . . . . .	139
5.22	Influence of casting speed profile: steady state temperature distribution for (a) case-1 and (b) case-3 . . . . .	139
5.23	Influence of casting speed profile: evolution of sump depth and mushy zone at center . . . . .	141
5.24	Influence of casting speed: radial distribution of sump depth and mushy zone at steady state . . . . .	143
5.25	Influence of casting speed profile: steady state circumferential stress dis- tribution for (a) case-6, and (b) case-3 . . . . .	144
5.26	Influence of casting speed profile: steady state circumferential viscoplastic strain distribution for (a) case-6 and (b) case-3 . . . . .	144
5.27	Influence of casting speed and profile: evolution of circumferential stresses at 56 mm from bottom (a) center and (b) subsurface of 90 mm from center	145
5.28	Influence of casting speed profile: circumferential stress and viscoplastic strain as a function of temperature . . . . .	146
5.29	Influence of casting speed: circumferential stress and viscoplastic strain as a function of temperature . . . . .	147
5.30	Influence of casting speed profile: circumferential stress and viscoplastic strain at solidus temperature as a function of distance from bottom of the billet . . . . .	149
5.31	Influence of casting speed: axial stress and viscoplastic strain at solidus temperature as a function of distance from bottom of the billet . . . . .	150
5.32	Influence of casting speed and profile: butt curl evolution for (a) different casting profiles and (b) different constant casting speeds . . . . .	150
5.33	Influence of casting speed: (a) HTS for different casting speed profiles vs. distance from bottom and (b) radial distribution of HTS at steady state .	152
5.34	Influence of secondary cooling: different HTC profiles . . . . .	153
5.35	Influence of secondary cooling profile: steady state temperature distribu- tion for (a) case-A and (b) case-D . . . . .	154
5.36	Influence of secondary cooling profile: temperature evolution and butt curl	155
5.37	Influence of secondary cooling profile: evolution of sump depth and mushy zone at center . . . . .	156
5.38	Influence of secondary cooling profile: radial distribution of sump depth and mushy zone at steady state . . . . .	157



5.39	Influence of secondary cooling profile: Characteristic time and surface temperature of billet at which water strikes first vs. distance from bottom of the billet . . . . .	157
5.40	Influence of secondary cooling profile: different boiling zone length as a function of billet height . . . . .	158
5.41	Influence of secondary cooling profile: steady state circumferential stress distribution for (a) case-A and (b) case-D . . . . .	158
5.42	Influence of secondary cooling profile: steady state circumferential viscoplastic strain distribution for (a) case-A and (b) case-D . . . . .	159
5.43	Influence of secondary cooling profile: evolution of stress at center and a radial distance of 90 mm (50 mm from bottom) . . . . .	160
5.44	Influence of secondary cooling profile: circumferential stress and viscoplastic strain as a function of temperature . . . . .	161
5.45	Influence of secondary cooling profile: stress and viscoplastic strain at solidus temperature as a function of distance from bottom of the billet at center . . . . .	162
5.46	Time varying HTC profile: evolution of sump depth and mushy zone at center . . . . .	164
5.47	Time varying HTC profile: circumferential stress and viscoplastic strain as a function of temperature at center (50 mm from bottom) . . . . .	165
5.48	Time varying HTC profile: circumferential stress and viscoplastic strain as a function of temperature at center (300 mm from bottom) . . . . .	166
5.49	Time varying HTC profile: circumferential stress and circumferential viscoplastic strain at solidus temperature as a function of distance from bottom of the billet at center . . . . .	167
5.50	Influence of (a) maximum HTC and (b) LFP on sump parameters . . . . .	169
5.51	Influence of (a) film boiling HTC, and (b) melt superheat . . . . .	170
5.52	Melt superheat: circumferential stress as function of temperature and distance from bottom . . . . .	171
5.53	Melt superheat: circumferential viscoplastic strain as function of temperature and distance from bottom . . . . .	172
5.54	Mesh convergence: sump depth . . . . .	173
5.55	Mesh convergence: mushy zone length . . . . .	174
5.56	Computational details: thermal problem . . . . .	174
5.57	Computational time per time step . . . . .	175

# Abbreviations

## Tensor operations

$a$  : a scalar - zeroth order tensor.

$\vec{a} = a_i \vec{e}_i$  : a vector - first order tensor.

$\mathbf{A} = A_{ij} \vec{e}_i \otimes \vec{e}_j$  : a second order tensor.

$\mathbf{C} = C_{ijkl} \vec{e}_i \otimes \vec{e}_j \otimes \vec{e}_k \otimes \vec{e}_l$  : a fourth order tensor.

$\vec{a} \cdot \vec{b} = a_i b_i$  : scalar product of vectors is a scalar.

$\mathbf{A} \cdot \vec{b} = A_{ij} b_j \vec{e}_i$  : scalar product of second order tensor with a vector is a vector.

$\mathbf{A} \cdot \mathbf{B} = A_{ij} B_{jl} \vec{e}_i \otimes \vec{e}_l$  : tensor product of second order tensors is a second order tensor.

$\mathbf{A} : \mathbf{B} = A_{ij} B_{ij}$  : scalar product of second order tensors is a scalar.

$\mathbf{C} : \mathbf{A} = C_{ijkl} A_{kl} \vec{e}_i \otimes \vec{e}_j$  : scalar product of fourth order tensor with second order is a second order tensor.

$\nabla = \frac{\partial}{\partial x_i} \vec{e}_i$  : Nabla operator is a vector operator

$\nabla \cdot \mathbf{A} = \frac{\partial A_{ij}}{\partial x_j} \vec{e}_i$  : divergence of a second order tensor is a vector.

$\nabla a = \frac{\partial a}{\partial x_i} \vec{e}_i$  : gradient of a scalar is a vector.

## Matrix and vector operations

$\mathbf{A}$  : a matrix (either square or rectangular)

$\mathbf{B}$  : a vector (column vector with dimensions  $n \times 1$ )

$\mathbf{AB}$  : multiplication of matrices with same size

$\mathbf{AB}$  : matrix and vector multiplication for compatible size matrices and vector.

$\text{tr}(\mathbf{A})$  : trace of a square matrix (or tensor) is the sum of diagonal elements.

$|\mathbf{A}|$  : determinant of a square matrix.

$\mathbf{A}^T, \mathbf{B}^T$  : transpose of matrix and vector.

$\mathbf{A} \cdot \mathbf{B} = \mathbf{A}^T \mathbf{B}$  : dot product of two vectors is a scalar.

$\mathbf{A} : \mathbf{B} = \text{tr}(\mathbf{AB}^T)$  : matrix inner multiplication is a scalar.

## Matrix, tensor and scalar field variables

$h$	Heat transfer coefficient [W/m <sup>2</sup> K]
$\varepsilon^{pl}$	Hardening state variable
$\varepsilon^{vp}$	Equivalent viscoplastic strain
$\varepsilon_{\text{eff}}^{pl}$	Effective plastic strain
$\sigma_{\text{eff}}$	Effective/Equivalent von Mises stress [N/m <sup>2</sup> ]

$\theta$	Temperature [ $^{\circ}\text{C}$ ]
$\theta_{\infty}$	Ambient temperature [ $^{\circ}\text{C}$ ]
$\Theta$	Nodal temperature vector
$\mathbf{E}^t$	Thermal strain tensor
$\mathbf{E}^e$	Elastic strain tensor
$\mathbf{E}^{ie}$	Inelastic strain tensor
$\mathbf{B}$	Strain displacement (mech) and gradient operator matrix (thermal)
$\mathbb{C}$ & $\mathbf{C}$	Elasticity tensor & matrix
$\mathbb{P}_1$ & $\mathbf{P}_1$	Spherical projector tensor & matrix
$\mathbb{P}_2$ & $\mathbf{P}_2$	Deviatoric projector tensor & matrix
$\mathbf{E}$ & $\mathbf{E}$	Tensorial total strain tensor & engineering total strain vector
$\mathbf{E}_{\text{eng}}$ & $\mathbf{E}_{\text{eng}}$	Engineering strain tensor & vector
$\mathbf{T}$ & $\mathbf{T}$	Stress tensor & vector [ $\text{N}/\text{m}^2$ ]
$f_{pc}$ & $f_l$	Volumetric liquid phase fraction
$f_s$	Volumetric solid phase fraction
$k_t$	Tangential contact stiffness [ $\text{Pa}/\text{m}$ ]
$k_n$	Normal contact stiffness [ $\text{Pa}/\text{m}$ ]
$\vec{u}$ & $\hat{U}$	Displacement vectors [ $m$ ]
$\vec{u}_s$	Prescribed surface displacement vector [ $m$ ]
$\vec{b}_f$ & $\hat{B}_f$	Body force vectors [ $\text{N}/\text{m}^3$ ]
$\vec{t}_f$ & $\hat{T}_f$	Prescribed surface traction vectors [ $\text{N}/\text{m}^2$ ]
$\mathbb{I}$ & $\mathbf{I}$	Fourth order identity tensor & matrix
$\mathbf{I}$ & $\mathbf{I}$	Second order identity tensor & matrix
$\vec{n}$	Unit normal vector
$\tilde{\mathbf{N}}$ & $\tilde{\mathbf{N}}$	Flow surface normal tensor & vector
$\Theta$	Nodal temperature vector (global)
$\Theta^e$	Nodal temperature vector (element)
$\mathbf{U}$	Nodal displacement vector (global)
$\mathbf{U}^e$	Nodal displacement vector (element)
$\mathbf{J}$	Material Jacobian matrix
$\tilde{\mathbf{J}}$	Coordinate Jacobian matrix
$r_q$	Heat generation per unit volume [ $\text{J}/\text{m}^3$ ]
$\vec{q}$	Heat flux vector [ $\text{J}/\text{m}^2$ ]
$\vec{v}$	Velocity vector [ $\text{m}/\text{s}$ ]

## Material properties

$\kappa$	Bulk modulus [ $\text{N}/\text{m}^2$ ]
$\mu$	Shear modulus [ $\text{N}/\text{m}^2$ ]
$\rho$	Density [ $\text{kg}/\text{m}^3$ ]
$\nu$	Poisson's ratio
$\sigma_y$	Yield strength [ $\text{N}/\text{m}^2$ ]
$\theta_l$	Liquidus temperature [ $^{\circ}\text{C}$ ]
$\theta_s$	Solidus temperature [ $^{\circ}\text{C}$ ]

$\theta_c$	Coherency temperature [ $^{\circ}\text{C}$ ]
$\theta_m$	Isothermal phase-change temperature [ $^{\circ}\text{C}$ ]
$\theta_{ref}$	Reference temperature at zero thermal strain [ $^{\circ}\text{C}$ ]
$\alpha$	Coefficient of thermal expansion [ $1/^{\circ}\text{C}$ ]
$E_y$	Young's modulus [ $\text{N}/\text{m}^2$ ]
$C_p$	Specific heat capacity [ $\text{J}/\text{kgK}$ ]
$H$	Plastic hardening modulus [ $\text{N}/\text{m}^2$ ]
$k$	Thermal conductivity [ $\text{W}/\text{mK}$ ]
$L$	Latent heat [ $\text{J}/\text{kg}$ ]
$R$	Universal gas constant [ $\text{J}/\text{K.gmol}$ ]

## Abbreviations

<b>AA</b>	Aluminum Alloy
<b>BC</b>	Boundary Condition
<b>CT</b>	Characteristic time
<b>DC</b>	Direct Chill
<b>DCC</b>	Direct Chill Casting
<b>EBC</b>	Essential Boundary Condition
<b>FEM</b>	Finite Element Method
<b>GDE</b>	Governing Differential Equation
<b>HTC</b>	Heat Transfer Coefficient
<b>LFP</b>	Leidenfrost Point temperature
<b>MZL</b>	Mushy Zone Length
<b>NBC</b>	Natural Boundary Condition
<b>DHCP</b>	Direct Heat Conduction Problem
<b>FHTC</b>	Film boiling Heat Transfer Coefficient
<b>IHCP</b>	Inverse Heat Conduction Problem
<b>IHTC</b>	Interfacial Heat Transfer Coefficient
<b>MHTC</b>	Maximum Heat Transfer Coefficient at nucleate & transition boiling
<b>MaxHF</b>	Maximum Heat Flux
<b>MaxHTC</b>	Maximum Heat Transfer Coefficient

# Chapter 1

## Introduction

### 1.1 Overview and Motivation

Casting is a manufacturing process by which a liquid metal is allowed to solidify inside the mold with desired shape. It is the first stage of metal production process followed by various forming and heat treating processes. Shape casting is a kind of casting process in which liquid metal is poured in a mold to obtain a solid product meeting a set of geometrical requirements [1]. Apart from the shape casting, the cast material generally known as ingot (non-circular cross-section) or billet (circular cross-section) is the prerequisite block for the metal forming processes such as extrusion, rolling, etc. To meet the demand in metal forming industry, mass production of ingot/billet has to be performed continuously. Steel like metals has to be cast in a continuous manner because of its lower thermal conductivity. Metals like aluminum and magnesium can be easily cast through the semi-continuous casting techniques.

Electromagnetic casting (EMC) and Direct chill (DC) casting are the two important semi-continuous casting techniques for the production of extrusion billets and rolling ingots [2]. In both the methods, the ingot is supported by a moving bottom block which is withdrawn with a certain velocity while the fresh liquid flows into the pool from above. EMC and DC casting are schematically represented in Fig. 1.1. In DC casting, the solidifying alloy is in contact with a mold whereas in EMC, the liquid pool is supported by electromagnetic forces. These forces are produced by the interaction of currents induced in the aluminum by an inductor surrounding the metal, and the magnet. Since the alloy solidifies without contacting a physical mold, the ingot has a better surface quality than a DC ingot. In both the methods, water is used as the secondary cooling medium which extracts the major portion of heat from the surface of the ingot.

DC casting process can be classified based on the movement of bottom block: (a) horizontal DC casting and (b) vertical DC casting. In horizontal DC casting, the bot-

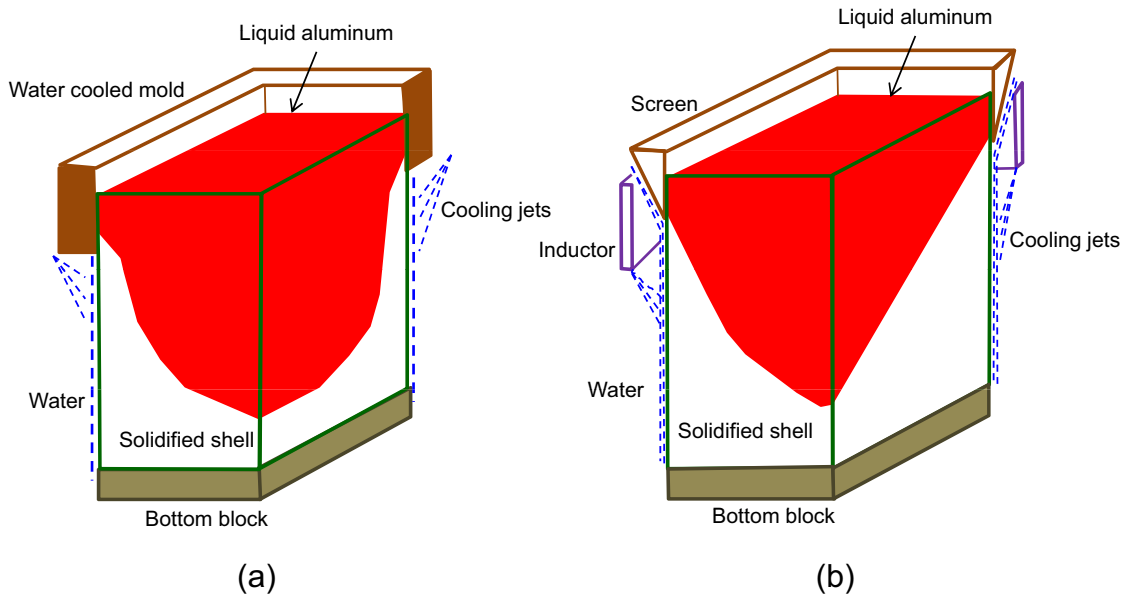


Figure 1.1: Schematic diagram (Barral and Quintela, 2000): (a) Direct Chill casting, and (b) Electromagnetic casting

tom block moves in the horizontal direction whereas the bottom block moves vertically downward in the later case. The vertical DC casting process is used to produce the ingots that have larger cross sections [3]. The vertical DC casting process is schematically shown in Fig. 1.2. Initially, the molten metal is transferred to the casting furnace. In the casting furnace the temperature is increased to  $50\text{ }^{\circ}\text{C}$  above the liquidus temperature of the alloy. The entrapped gases are removed from the melt by blowing Argon/Nitrogen gas through the melt [4]. In the last part of the launder system grain-refiner is added in the form of wire into the molten metal. Casting is performed by pouring the molten metal from furnace through the launder to a stationary mold which is initially enclosed by the bottom block [5]. The bottom block moves vertically downwards and the billet or slab will moves with it. The mold is surrounded by cooling water which is known as *primary cooling*. At the exit of the mold, the cooling water directly impinges on the billet or slab that is called as *secondary cooling*. Due to the high cooling rate in the secondary region, the solidification proceeds rather fast. The casting is terminated when the ingot reaches a desired length. Therefore, it is known as semi-continuous casting. The name *Direct Chill* is coined with this casting process because the cooling water directly chills the ingot.

The schematic view of solidification process which occurs during the DC casting of aluminum alloy is as shown in Fig. 1.3. It shows three different metallurgical zones such as solid, mushy and liquid. Alloys transform gradually from liquid to solid over a temperature interval. Unlike alloys, pure metals solidify at one particular temperature.

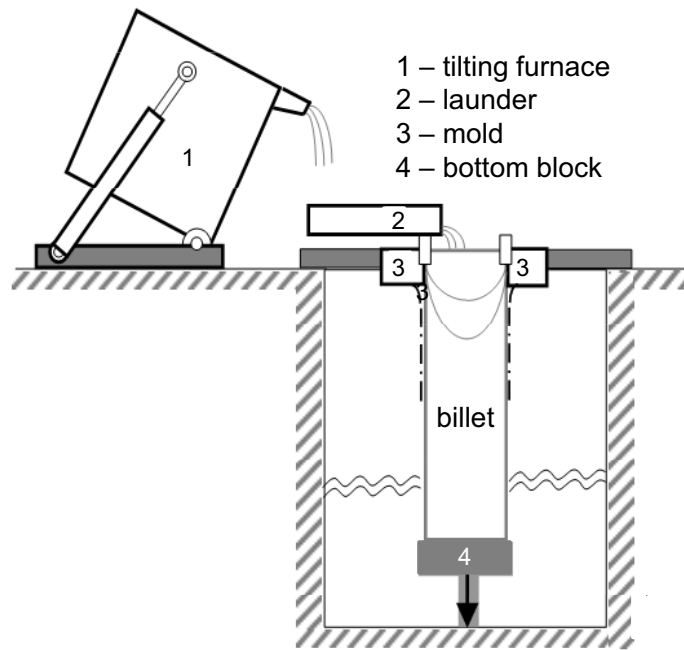


Figure 1.2: Schematic diagram of DC casting apparatus (Suyitno, 2005)

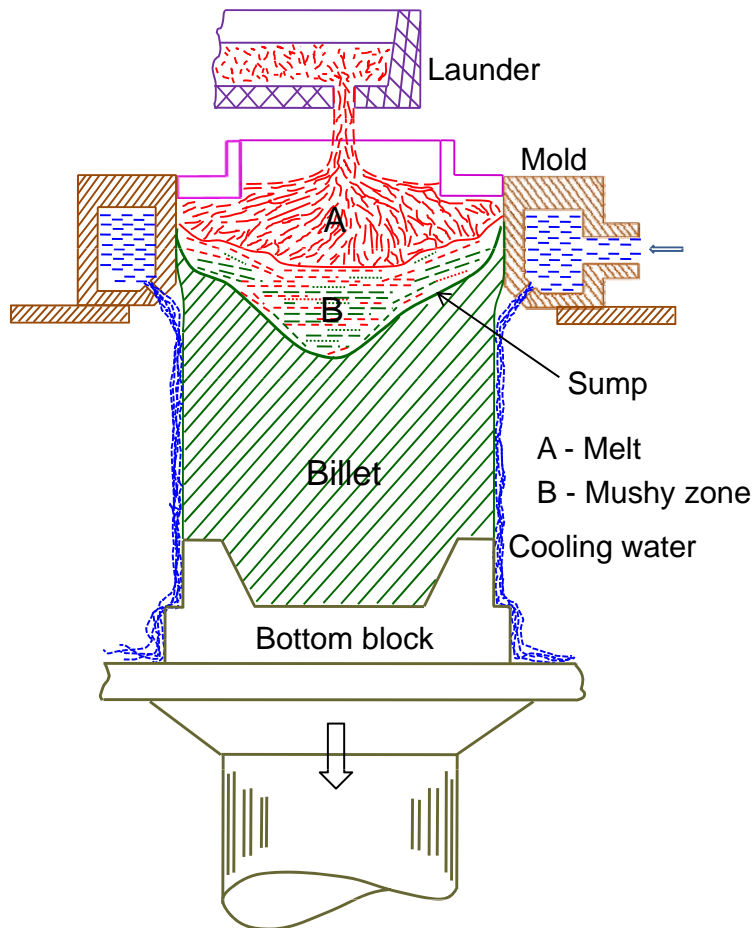


Figure 1.3: Direct Chill casting of aluminum alloys (Suyitno, 2005)

During the casting the alloy spends considerable amount of time in a semi-solid state. The material in this semi-solid state can be divided into two categories: slurries and mushes. A slurry is defined as a liquid with suspended solid particles. At some temperature solid grains start to interact with each other and the material gains certain strength. Below this temperature, the material is called a mush, i.e. a solid network with liquid in between. Fig. 1.3 shows the solidification front forms a sump which its depth increases with distance from the surface of billet or slab [5].

The complete DC casting process can be divided into three stages: (a) start-up phase, (b) pseudo steady state, and (c) end phase. In the start-up phase, the bottom block lies inside the mold and the liquid metal is poured from the top through a distribution bag into the bottomless mold. The level of liquid metal is maintained constant in the mold by means of continuous addition of liquid metal. A solidified shell is formed over the bottom block and along the mold wall. As soon as the solidified shell is strong enough to support the molten metal inside, the bottom block is lowered with certain velocity [6]. When the cooling water directly touches the surface of the billet, the solidification process gets accelerated. This complete sequence of processes are known as start-up phase. The start-up phase is the most critical phase of DC casting during which the position of solidification front, accumulation of stress and strain, and thermal and mechanical boundary conditions change along with time. Modeling the transient start-up phase is one of the challenging task because of the complexity associated with this. After the start-up phase, a pseudo steady state is reached during which the thermal and mechanical field quantities reach a constant values. In general, during this phase the velocity of bottom block is maintained constant. During this phase, if the attention is focused on a particular spatial point, the temperature will not change with respect to time. The same is not true for the material point. Due to this reason it is known as pseudo steady state. The spatial position of the solidification front is almost fixed during the pseudo steady state. This is also frequently referred as steady state. Therefore, this phase is not a strong function of time. At last, the liquid metal feeding and the movement of bottom block are stopped and the billet is kept for certain time so that there is no liquid or semi-solid material left. This phase is known as the end phase. Both the start-up and end phase are transient in nature.

Producing the high quality ingot with less consumption of energy is one of the most important industrial objectives which is also a challenging task for the engineers. As far as the DC casting is concerned, if the ingot fails to meet the quality requirements, excessive machining and remelting are the only two possible remedies. Both the operations consume considerable amount of energy and money. Further, the machining operation can only provide the better surface quality. Even though, the ingot has to undergo further processing before it made into the final product, the quality of the ingot strongly



influences in all the consequence stages. Therefore, it is mandatory to understand the physics of DC casting process for the production of high quality ingot. DC casting is a complex process because of the strong interaction and coupled nature of multi-physics associated with it.

During the DC casting, the ingot thermo-mechanically interact with the moving bottom block and the static mold. Apart from these two contact areas, the remaining portion of the ingot except the top surface, thermally interact with the cooling water which flows vertically downward. The top portion of the ingot is in liquid stage and the liquid metal is continuously supplied. The ingot surface itself is subjected to non-uniform thermal boundary conditions, therefore the thermal gradients are very high in the core. Due to this non-uniform thermal forces, the ingot deforms continuously and develops residual stresses and strains. The residual stresses are compressive in the outer region and tensile in the core. The excessive tensile thermal stresses in the core is a favorable situation for the formation of hot cracks. Once the hot crack or generally known as *hot tear* forms, due to its brittle nature, it may extend in the entire length of the ingot or it can open up in the radial/horizontal direction and there are chances of liquid metal flow out and contact with cooling water which may cause accidents in the casting plant. There are other quality issues associated with the DC casting such as macrosegregation, micro porosity, cold cracks, butt curl, butt swell, etc.

With the help of sophisticated experimental techniques, it is possible to understand some of the above-mentioned phenomena. Apart from the experimental observations, mathematical modeling of the physical process gives the clear insight into the problem. Through the modeling and simulations, it is always possible to address most of the issues associated with the DC casting process. Of course, experiments are also equally important for the purpose of validations and material characterizations. The evolution of computational techniques give the strong motivation to the engineers to model and simulate the entire DC casting process. Thermal, mechanical, metallurgical, chemical, and fluid mechanics are the major physical fields associated with the DC casting. Due to the strong coupling between these fields, it is highly complicated to address all the issues related to the DC casting.

This work is dedicated to model the thermo-mechano-metallurgical effects of vertical DC casting process. The objective of this work is to simulate the temperature evolution and residual stresses and strains development during the start-up phase of DC casting. With the help of temperature and stress-strain histories at every material point, it is possible to predict the chances of hot tearing in the early stages of solidification. The finite element method (FEM) is effectively implemented to discretize the energy and momentum equations. The thermal and metallurgical fields are modeled in a strongly coupled manner

due to the release of latent heat during the phase-change. Further, the computational difficulties of isothermal phase-change are addressed elaborately. The thermal boundary conditions are estimated through the quenching characteristics of a hot plate made up of casting material. A non-iterative finite element method is adopted to solve the inverse problem using the experimental temperature profiles. An isothermal staggered approach is followed to couple the thermo-metallurgy and mechanical fields. Elastic-plastic and elasto-viscoplastic material models are used to characterize the mechanical behavior of the mushy and solid regions. Separate constitutive relations are used in the mushy and solid regions. The influence of casting parameters such as casting speed and cooling characteristics are investigated in a detailed manner.

## 1.2 Aluminum and its alloys

In 1886, Paul Louis Toussaint Héroult (France) and Charles Martin Hall (USA) independently invented the electrolytic process known as Hall-Héroult process which is the basis for all aluminum production today [7]. In this process, the dissolved aluminum oxide (alumina) in a bath of molten cryolite is subjected to strong electrical forces which leave the molten aluminum at the bottom of the bath. This pioneering invention revolutionized the world and presented a new metal which has enormous applications starting from the house-hold usages to aircraft industries. The percentage consumption of aluminum [8] by different industries are given in Table. 1.1. The world production of aluminum increases steadily and reached 38 million tonnes per year in 2007 which is nearly 4 times when compared to the year 1970 [9].

Aluminum is the third largest available metal up to 8% by weight of the earth's solid surface after oxygen and silicon. Aluminum is a nonmagnetic and nonsparking material. The yield strength of a pure aluminium is 7-11 MPa, while its alloys have yield strengths ranging from 200 to 600 MPa at elevated temperature. Corrosion resistance of aluminum is excellent due to a thin surface layer of aluminum oxide that forms when the metal is exposed to air which effectively prevents further oxidation. It is a good thermal and electrical conductor, having 62% the conductivity of copper. It is also a strongly reactive metal that forms a high-energy chemical bond with oxygen. Extraction of aluminum from its ore, such as bauxite is difficult when compared to other metals. This is due to the higher energy requirements in the reduction of aluminium oxide ( $\text{Al}_2\text{O}_3$ ).

The typical alloying elements for the aluminum are copper, zinc, manganese, silicon, and magnesium. In general, the aluminum alloys can be categorized as cast alloys and wrought alloys. Cast alloys are directly cast into their final form by one of various methods such as sand-casting, die or pressure die casting. Wrought alloys, which are

Table 1.1: Industrial consumption of aluminum (CIB)

Industry	% usage
Transport	26
Packaging	22
Construction	22
Electrical	8
Machinery	8
Miscellaneous	14

initially cast as ingots or billets and subsequently processed through the hot and/or cold worked mechanically into the desired form [10]. i.e. rolling, extrusion, forming and forging. Cast aluminum alloys yield cost effective products due to the low melting point, although they generally have lower tensile strengths than wrought alloys. The British Standards Institution categorized the wrought alloys based on the alloying elements. There are 8 series of wrought alloys as shown in Fig. 1.4. These are designated by a 4 digit number that may be preceded or followed by letters.

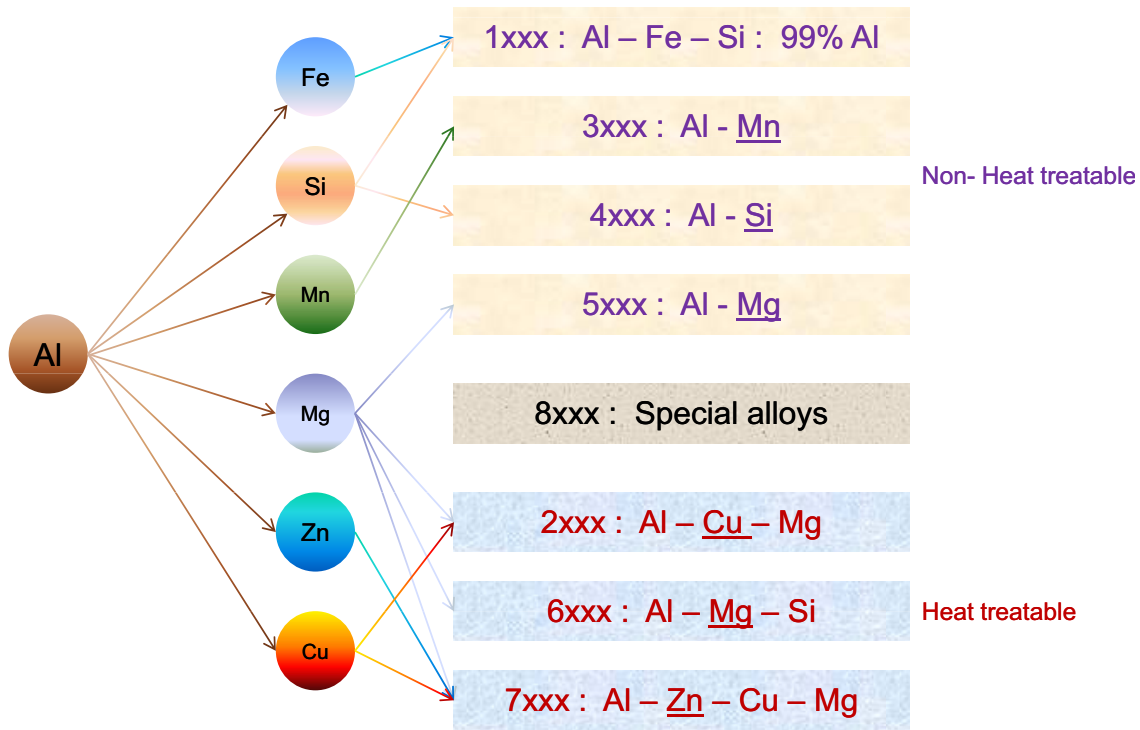


Figure 1.4: Wrought alloy classifications

Both the cast and wrought alloys can be further classified as heat treatable alloys and

non-heat treatable alloys. The strength of the non-heat treatable alloys can only be improved through the cold working. In general, four different strengthening mechanisms [10] are used to strengthen the aluminum alloys: (a) strain hardening, (b) solute hardening, (c) precipitation hardening, and (d) grain size hardening. Strain hardening is achieved by mechanical deformation of the material at ambient temperature [11]. Solute hardening allows soluble alloying elements to enter into solid solution. Precipitation hardening, also known as age hardening, is a heat treatment technique which is used to increase the yield strength of the alloys. It relies on changes in solid solubility with temperature to produce fine particles of an impurity phase, which impede the movement of the dislocations or defects in a crystal's lattice. Reducing the grain size of a polycrystalline material is an effective way of increasing its strength.

The thermo-physical properties of aluminum and its alloys constantly attracting the engineers to make use of its potential to the fullest. The density of aluminum is almost one third of the density of steel. Therefore, it is a good alternative for steel where the weight is a deciding factor. Even though, the elastic modulus of aluminum is one third that of steel, it is extensively used in the aircraft industry rather than steel. When it comes to casting / solidification, the thermal properties are more important than the mechanical properties. The melting temperature of aluminum alloys is significantly lower than that of steel. The aluminum casting plant operates at relatively lower temperature environment than that of steel. The thermal conductivity of aluminum alloys is an order of magnitude higher than that of steel. The thermal diffusivity of liquid aluminum is about 6 times higher than that of liquid steel. This means that liquid aluminum tends to lose its superheat faster than liquid steel, for a given fluid flow pattern [12]. Apart from these features, the aluminum alloys have few drawbacks over steel. The solidification shrinkage experienced by aluminum alloys is almost twice that of steel. Therefore, higher thermal stresses can be generated within the solidification range by aluminum alloys. Further, the thermal contraction coefficient of solid aluminum is higher than in steel.

### 1.3 DC casting

Steel have to be cast continuously because of its lower thermal conductivity. In the continuous casting of steel, the solidifying strand moves vertically for a certain distance and can be bent into the horizontal direction with an appropriate curvature. This kind of continuous casting is not possible for a material having higher thermal conductivity because the metal completely solidifies with a relatively smaller distance. This normally limits the length of the ingot to 8–10 m. Further, this restriction motivated to develop a new casting technique known as *semi-continuous casting*. Direct chill casting (DCC) is

one of the semi-continuous casting technique for a metal having higher thermal conductivity. The DCC technique was developed in 1930s. In addition to being reliable, DCC has proved to be a very economical production technique for casting non-ferrous metals such as aluminum, magnesium, copper and zinc [13]. However, the DCC technique is well known for the aluminum alloys. The horizontal DCC is restricted to the smaller ingot dimensions and low strength alloys. However, the vertical DCC has no such restrictions. Therefore, here onwards the word DCC means vertical DCC, unless otherwise explicitly stated.

The DCC method differs from the continuous casting method in two ways: (a) relatively shorter mold length - in continuous casting of steel, the molds are 700–1200 mm long but in DCC it is around 70–90 mm and (b) relatively lower casting speed - generally DCC speed is 10 times lower than the continuous casting. The casting speed during the DCC varies from 60 mm/min to 200 mm/min. The typical DCC billets and ingot are shown in Fig. 1.3. The extrusion billets are usually cylindrical with diameters typically within the range of 100–400 mm. The rolling ingots typically have thickness of 400–600 mm and widths in the range of 1500–2200 mm. The length of the rolling ingot may vary from 6500 to 8000 mm. For extrusion billets, casting up to 200 molds may be situated on a single casting table depending on the billet diameter [14], e.g. Fig. 1.3(a) shows 110 molds on a single casting table.



Courtesy: [www.alibaba.com](http://www.alibaba.com)

(a)



Courtesy: NOVELIS INC.

(b)

Figure 1.5: DC casting of (a) billets and (b) ingots

### 1.3.1 Cooling mechanisms

As stated before, the heat flows from the ingot through the three distinguished cooling zones: (a) primary cooling zone, (b) secondary cooling zone, and (c) bottom block zone. The heat transfer mechanisms in all the three zones differ completely and each zone has its own complexity. In the primary cooling zone, before the melt starts solidifying, almost a perfect contact between the mold and the ingot is established. The heat transfer is rather fast during this stage. Once the nearby liquid metal starts solidifying, the ingot locally loses the contact with the mold due to the solidification shrinkage. This forms an air gap in between the ingot and the mold. It is a well known fact that air is a good insulator. Due to this air gap, the convective heat transfer coefficient (HTC) between the mold and the ingot decreases drastically. Generally, the mold is cooled by the cooling water which also flows vertically and impinges on the ingot below the mold level. Further, there is a small distance in between the water impingement point and the contact point of the mold known as *air cooling zone*, which is left uncovered by either mold or cooling water. Taking everything into consideration, only 20% of ingot heat is extracted through the primary mold cooling.

The secondary cooling zone can be further divided into two regions such as the *impingement zone* and the *free flow regime*. In the impingement region, the cooling water strikes the hottest surface of the ingot. The cooling water can not wet the surface because of immediate vaporization. A thin water vapor layer is formed which covers the ingot surface and acts as an insulator. This phenomena is known as *water ejection*. Film boiling is the primary mechanism of heat transfer in this region. After the impingement zone, the temperature of the ingot drops below the Leidenfrost point where the film collapses and transition and nucleate boiling, and forced convection dominates. During the transition and nucleate boiling, the heat flux reaches a maximum value. A thin wetting front separates these two regions and tries to move against the ingot movement. More than 75–80% of ingot heat is removed through the secondary cooling.

In the bottom block zone, the liquid metal establishes a perfect contact with the bottom block before the start of solidification which is similar to the primary cooling zone. During the start-up phase, the ingot butt is chilled by both the bottom block and the mold. Gradually an air gap develops in between the bottom block and the solidified strand from which starts the outer corner. However, the center of the bottom block is connected with a solidified portion of the ingot by means of specially designed bolts known as *starter block*. Without this connecting element, the bottom block can not pull the ingot continuously. During the start-up phase, when the water start striking the ingot surface, the temperature drop on the surface is very high which makes the ingot deform plastically. This excessive deformation on the surface nearby butt is known as

*butt curl*. Due to this butt curl, a considerable amount of gap will be formed in between the ingot and bottom block. Therefore, the cooling water enters into the gap which improves the cooling in the bottom block zone for a small period. This is called *water intrusion*. Further, the rapid vaporization of water in the gap may lead to a bumping of the ingot [15]. And also the excessive butt curl reduces the rigid standing of the ingot on the starter block and causes a portion of the ingot to lose contact with the bottom block, leading to possible shell remelting. Even though the heat transfer in this zone is slightly improved during the time of water intrusion, the total contribution of bottom block zone is less than 5% during the pseudo steady state. However, in the start-up phase, a significant amount of heat is extracted through this zone.

All the above-mentioned cooling zones are strongly interconnected. The excessive cooling effect given by the secondary zone greatly influences the primary and bottom block zones. During the start-up phase, it is typical to reduce secondary cooling to avoid excessive butt curl. Several technologies are introduced to control the rate of heat transfer in the secondary zone. There are several production problems associated with a butt curl, which include: run outs of the melt, cold shuts, reduced rigid standing (instability) of the ingot on bottom block, which can lead to low recovery rates [16]. A simple strategy to reduce the secondary cooling is to allow the vapor film for a longer period on the ingot surface. This can be achieved by increasing the water flow rate. Further, the water flow rate and the heat removal rate are not exactly linear. However, there are practical difficulties associated with this. The secondary zone influences the primary zone considerably during the start-up and pseudo steady phases through the air gap between the mold and the ingot.

### 1.3.2 Common DC casting problems

Due to high demand, a wide variety of aluminum alloys are being cast continuously by means of DC casting process. In search for better properties such as corrosion resistance and higher strength, new alloys are being developed which may impose constraints on the production process. The knowledge of process parameters and its controlling technique have to be developed for the production of defect free billets [17]. A large number of casting problems arise during the DC casting process. It is almost impossible to eliminate all the quality issues related with the DC casting. It is mandatory to overcome all the casting hurdles for improving the casting efficiency. However, here the attention is only focused on the major issues which have the dominant influences on the quality of cast ingot. The major DC casting problems and their origins are discussed as follows:

1. **Hot tearing:** A crack which originates during the solidification is called as hot

crack or hot tear or hot shortness. The word hot itself indicates that the crack propagates in the high temperature regions or above the solidus temperature. The mushy region with higher solid fraction is the most vulnerable portion of the ingot where the hot tears supposed to be originated. In the worst situation, hot tear may run the entire ingot in the axial direction or it can extend in the lateral direction which can divide the ingot into two parts or two pieces and the liquid metal may come out. A typical hot tear which originates during the pseudo steady state is shown in Fig. 1. Both the horizontal and vertical expansion of hot tears lead to stop the casting process and consequently the ingot has to be remelted. Hot tear brings down the production efficiency and the ingot quality. Therefore, its an industrial objective to produce the ingots without hot tears.

The mechanisms of hot tear formation in the DC casting are still not well understood in the research community. However, it is generally accepted that the hot tear occurs within the mushy zone where the solidification shrinkage is not compensated by interdendritic melt flow due to insufficient liquid feeding in the presence of thermal stresses. The thermally induced deformation due to non-uniform cooling contraction is one of the major reason for the hot tearing [18]. Hot tears are easily identifiable as they take the form of ragged, intergranular cracks that often occur at a hot spot or thin section within the casting [19]. Generally, pure metals and alloys of eutectic composition are not prone to hot tearing or less susceptible to hot tearing due to narrow solidification range. Hot tearing susceptibility increases when the phase-change temperature interval increases. Apart from this, the structure development during the phase-change also significantly influences the hot tearing susceptibility. Hot tearing is not yet uniquely related to alloy composition but is affected by a range of interrelated factors including: composition, superheat, hot-spot size, structure of the grain and its size, solid–liquid interface morphology, casting geometry, and mold type [19].

Initially, the solid grains nucleate in the liquid pool when the temperature drops below the liquidus point. These grains may be of columnar or dendritic structures based on the alloy composition. When the solid fraction increases, the chemical diffusion occurs and the grains start interacting each other physically. The temperature at which the grains start gaining mechanical rigidity is known as coherency point. Mass feeding is limited at these solid fractions and thus the displacement of grains away from each other by the application of a load cannot be accommodated by the inflow of liquid. The pressure drop between the intergranular liquid and grains can cause micro porosity. Further, an increase in thermal stress can cause hot tears. Hot tearing is prone to the solid fractions of 0.85–0.95. The alloy which



has higher chances of hot tearing are AA5182 and Al-4.5%Cu.

Generally, hot tearing occurs in the center of the ingot because of excessive tensile residual stresses. It is found that circumferential stresses and inelastic strains are tensile at the solidus temperature near the center of the ingot. During the start-up phase, these values reach maximum and this is favorable to hot crack formation. There are several methods proposed to reduce the hot tearing susceptibility. Through the application of a ramping procedure it is always possible to reduce the hot tearing susceptibility.

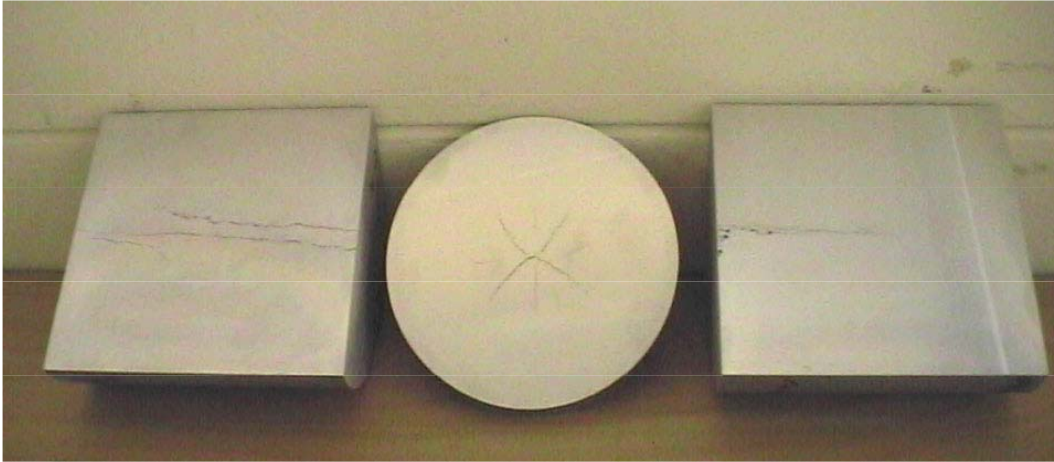
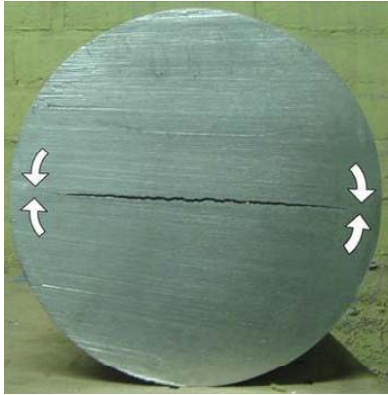


Figure 1.6: Typical hot tears which occur during pseudo steady state phase (Suyitno, 2005)

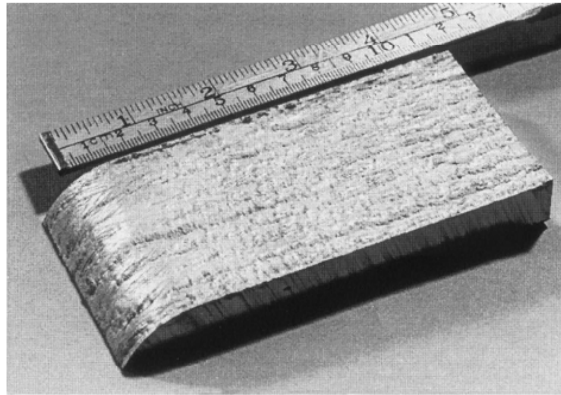
2. **Cold cracking:** It occurs in the fully solidified material below the solidus temperature. Generally cold cracks occur in the high strength alloys due to the higher thermal stresses built up during the casting and cooling to the atmospheric temperature [17]. The rapid propagation of such micro-cracks in tensile thermal stress fields can lead to catastrophic failure of ingots in the solid state. The 7xxx series aluminum alloys are more vulnerable to cracking mainly because of poor thermal and mechanical properties in the as-cast condition. Low thermal conductivity values compared to other aluminum alloys result in high-temperature gradients, which in turn lead to an accumulation of thermal stresses with different signs and magnitudes in different locations of the billets during DC casting. This kind of alloys loses its ductility below 200 °C and become extremely brittle, which can make the material prone to cold cracking [20]. As mentioned in the hot tearing case, the stress states are tensile in the center of the billet for all the time except the smaller region which is in contact with the bottom block. At the surface of the billet, on the other hand, stresses are tensile in the water impingement zone but

they turn to compressive upon further cooling. Even though there are chances of formation of cracks in the surface at the water impingement zone, in the later stages due to excessive compressive stresses it can be healed. This is not possible in the center. Similar to hot tearing, cold crack susceptibility is very high in the center of the billet. A typical cold crack which expands in radial direction in the center of the billet is shown in Fig. 1.7(a). The arrow region indicates that the direction of circumferential compressive stress which arrests the crack expansion.



Courtesy: Lalpoor, Eskin & Katgerman

(a)



Courtesy: Thevik, Asbjørn & Rusten

(b)

Figure 1.7: A typical (a) cold crack (Lalpoor *et al.*, 2009), and (b) exudation (Thevik *et al.* 1999)

3. **Macrosegregation:** Macrosegregation is an inhomogeneous distribution of alloying elements at the scale of solidified ingot. This can lead to nonuniform mechanical properties that affect the behavior of the metal during the subsequent processing and impair the quality of the final product [21]. Macrosegregation is a really serious problem because it cannot be eliminated during the downstream processing, unlike microsegregation, which can be removed relatively easily by high temperature annealing [22]. Macrosegregation occurs due to the transport of segregated alloying elements at the scale of a casting by the relative movement of liquid and solid phases. It is a direct consequence of the transport phenomena taking place during the solidification process. It is caused by advective solute transport primarily due to the flow of segregated liquid in the mushy zone. This laminar flow is a result of convection in the liquid part, driven by buoyancy forces due to thermal gradients (thermal natural convection), buoyancy forces due to concentration gradients (solutal natural convection), and inlet flow (bulk convection). Additionally, a feeding flow due to the density difference between the two phases (solidification shrinkage) is induced in the mushy zone [21].

In general, the advancing solidification front pushes the liquid enriched in the solute (in the case of partition coefficient less than 1) towards the hotter part of the casting, e.g., the center. As a result, after solidification, the center of the casting will contain more solute than the periphery of the casting. In reality the solute rich liquid should be transported toward the hot spot of the casting (in the direction of solidification). The driving force behind such transport is either convection or shrinkage-driven flow. There are two kinds of macrosegregation processes: (a) negative segregation - concentration of an element is lower than the average concentration in the alloy and (b) positive segregation. A positive segregation on the surface of the ingot is known as *exudation* [23]. Mostly, the thickness of an exudation layer is more than 1 mm as shown in Fig. 1.7(b) which can only be removed by machining.

4. **Ingot distortion:** Butt curl, butt swell, and rolling surface inward pull-in are the major ingot distortions which occur during the DC casting process. In the stationary stage, the solidified shell contracts inwards and the inhomogeneous distribution of the cooling jets results the rectangular ingot deform into *bone-shaped* as shown in Fig. 1.8(b). In an attempt to compensate this effect, molding collars have to be designed in convex shape, usually with three segments per quadrant instead of a rectangular one. Butt swell is the increase in cross-section nearby ingot butt.

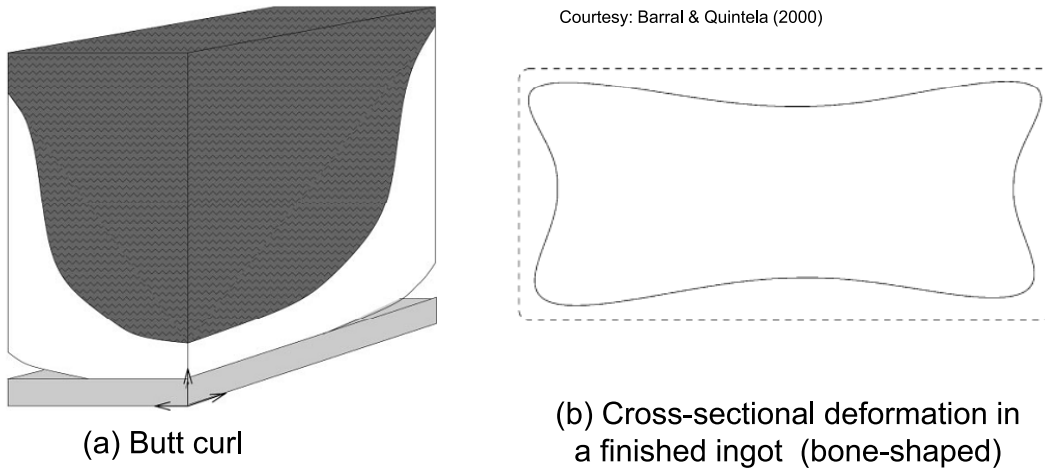


Figure 1.8: Butt curl and cross-sectional bone-shaped deformation of ingot (Barral and Quintela, 1999)

## 1.4 Problem definition

Experimental methods are highly important for the material characterizations, solving the inverse problems, and validating the numerical simulation results. Performing the

experiments in a real time DC casting plant is quite complicated and also not preferable. Therefore, a specially designed experimental set up which can reproduce the similar situation in the casting plant is highly essential for conducting the experimental study. Further, from the experiments only the thermo-kinematic quantities like temperature, displacement, etc. are measurable, whereas the kinetic quantities like heat flux, stress, etc. are obtained from the respective constitutive equations. Modeling the physical process is also equally important for the better understanding of the process, optimizing the parameters, and for the decision making. Due to the advancements in computer technology, it is feasible to simulate complex problems such as DC casting. Therefore, this work concentrates on the modeling of DC casting process and its numerical simulations. Experiments are only performed for the purpose of finding the secondary cooling boundary conditions.

Modeling the theromechanical behavior of the ingot during the DC casting process is a challenging task due to the complexities such as phase-change, latent heat release, moving interface, time-dependent domain, change in boundary conditions, rate-dependent material behavior, etc. There are different physical fields coupled to each other such as thermal, metallurgical, chemical, mechanical, etc. It is highly tedious to solve the coupled fields involving more than two or three. Furthermore, three dimensional problems consume larger computational time when compared to two dimensional problems. Apart from all these difficulties, the solution domain is time dependent and it grows in the direction of casting. Therefore, only three physical fields such as thermal, metallurgical and mechanical fields are considered and the attention is focused on the temperature and stress-strain evolutions.

In solidification modelling, thermal and metallurgical fields are strongly coupled due to the release of latent heat at the phase-change interval. Further, decoupling of these two fields may not produce accurate and reliable solutions when the phase-change interval is too small. The solutions of thermo-metallurgical fields strongly influences the mechanical field. The primary objective of this work is to capture the temperature evolution inside the ingot during the start-up and pseudo steady phases. This solidification problem itself complicated because of the moving solid-liquid interface where the thermal and mechanical properties change abruptly. The liquid flow is neglected and the liquid convection current due to the density difference is incorporated by means of increasing the thermal conductivity of the liquid phase. A fixed grid method with keeping the temperature as an independent variable is used to model the solidification problem. The primary and bottom block boundaries change continuously due to the solidification shrinkage of the ingot. The primary mold boundary has only two states: (a) contact, and (b) non-contact. During the contact case the ingot touches the mold and during the non-contact case an

air-gap between the mold and ingot develops. The bottom block boundary also has these two cases and additionally one more situation called as water intrusion also occurs. During the water intrusion, the cooling water enters the gap between ingot and bottom block. All these effects are included in the solidification model.

The secondary cooling boundary conditions are measured through experimental techniques. The objective of this experiment is to predict the boiling curve (temperature vs. heat flux). For this motive, a hot plate made up of casting material is quenched by an array of water jets which flow parallel to the plate in the direction of gravity. Even though this situation is not exactly the same as the DC casting secondary cooling, the boiling curve in both the cases are nearly similar. An infrared thermography is used to measure the temperature on the non-quenched side of the plate. Using the experimental temperature profile, an inverse 2-D heat conduction problem is solved to obtain the heat flux leaving on the quenched side. The ill-posed nature of the inverse problem demands sophisticated numerical techniques to avoid the numerical oscillations. Further, the inverse problems are highly sensitive to the experimental errors. A simple data noise filtering method is developed to reduce the level of error in the experimental measurements. The influence of the water velocity is studied in detail. Due to the absence of DC casting experimental facilities in our institute, an attempt is made to characterize the boiling curve using the available quenching unit. However, the explicit relation between the heat flux and quenching parameters such as water flow rate, water temperature, etc. is not established yet. For the sake of completeness, the modeling issues of an inverse problem are addressed in this work with the help of nickel and aluminum plate quenching. The experimental part of this work was carried by another research group in our institute.

There is a large amount of scraps to be remelted when the quality of the ingot is not satisfactory. The hot and cold cracks and the ingot deformations are the frequently encountered DC casting problems. Even though all the other casting defects are equally important, here the attention is only focused on these three defects. It is mandatory to know the history of the residual stress-strain development at every material point for the prediction of cracks. Further, the rate-dependent effects dominate in high temperature regions. Therefore, the mechanical behavior of ingot is modeled through the elastic-viscoplastic material model. The liquid phase is treated as a fictitious solid with a very small stiffness because it can not accommodate stresses. Within the mushy zone, there is a coherency point where the material starts sustaining the mechanical loads. From the coherency temperature to the solidus temperature, the mechanical behavior of the material is modeled by Norton's viscoplastic law. The solid phase is assumed to behave according to Garafalo's viscoplastic law. With these models, the stress-strain development near the mushy zone is carefully studied. And it is found that the nature of stresses in

the center of the billet are tensile, whereas at the surfaces it is compressive. The influence of casting speed, melt superheat, and secondary cooling boundary conditions is studied in detail.

Another important motive of this work is to understand and modify the secondary cooling HTC profile so that the magnitude of internal residual stresses can be minimized. To achieve this objective, it is necessary to develop a proper numerical technique and simulation software. There are large numbers of commercial packages such as ANSYS, ABAQUS, COMSOL, MSC.MARC, etc. which are available to simulate the industrial DC casting process. However, at a certain level, one has to enter the solver which is well known as *black box*<sup>1</sup> where there is a zero control. Therefore, an attempt is made to develop the finite element codes without using the commercial packages. This gives a complete insight of the problem from its starting to the end. Though, it demands more reengineering work but it is worthwhile once a well established code is developed. In this work, a MATLAB code is developed to solve the DC casting process.

## 1.5 Mathematical modeling of DC casting

In the real time industrial DC casting process, the bottom block is withdrawn with certain velocity, while the mold is kept stationary and the liquid melt is fed continuously from the top. However, in the DC casting model, the positions of ingot and bottom block are fixed, and the mold is allowed to move with the casting speed, and the melt feeding is achieved by the introduction of a new layer of materials which is an exact replica of an industrial DC casting process. This way of modeling eliminates the continuous change in spatial coordinates of a material point. The history of changes in the field variables such as temperature, stress, etc., at every material point can be tracked easily with this approach. Generally, in solid mechanics Lagrangian coordinate systems are more preferred rather than the Eulerian system. Based on this, the liquid phase is treated as a fictitious solid and its flow behavior is neglected.

The entire DC casting model is decomposed into two parts: (a) thermal model, and (b) mechanical/displacement model. The thermal model consists of solidification model, interface heat transfer model, and inverse model. The schematic representation of DC casting model is shown in Fig. 1.9. The temperature change may induce the phase transformation, and the phase transformation internally releases the latent heat which strongly affects the temperature change. Therefore, the heat conduction and phase fields have to be modeled simultaneously. Otherwise, the phenomena of latent heat release may not be

---

<sup>1</sup>A computer program into which users enter information and the system utilizes pre-programmed logic to return output to the user: <http://www.investopedia.com/terms/b/blackbox.asp>

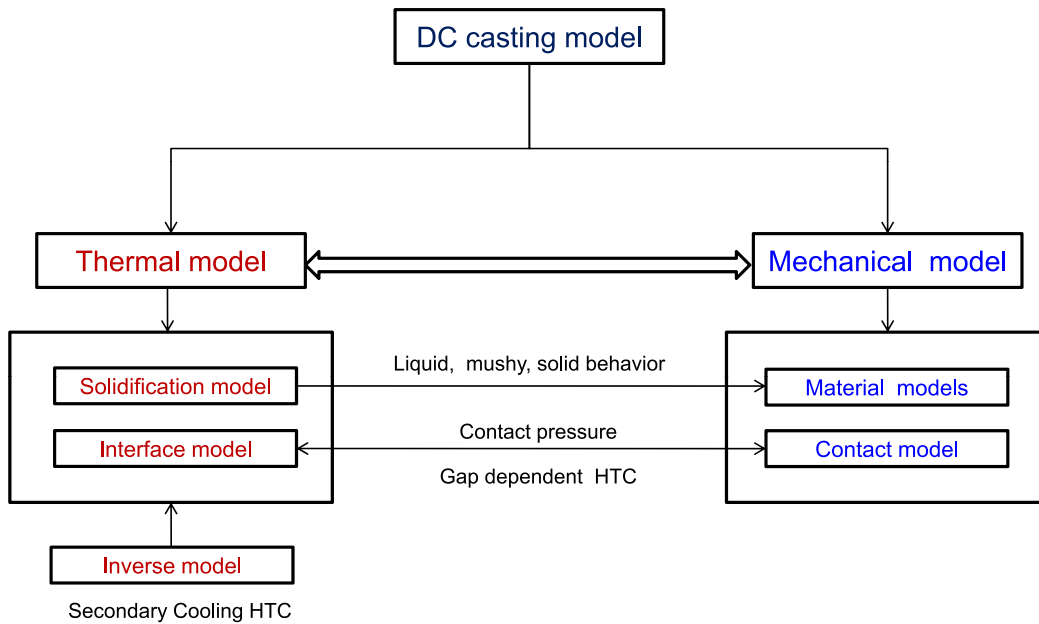


Figure 1.9: DC casting model

captured accurately. Generally in DC casting, different materials thermally interact at the boundaries such as casting or ingot, bottom block, and mold. The thermal interface model takes care of the ingot-bottom block and ingot-mold interfaces. In both of these interfaces, when the liquid metal starts solidifying, due to the thermal shrinkage, an air gap will be formed. The interfacial HTC is a function of normal gap between the interfaces. The inverse model provides the information about the secondary water cooling boundary conditions with the help of experiments. Even though the inverse model is a part of thermal model of DC casting, it can be handled as a separate problem. The solidification model and interface model are the integral part of a DC casting thermal model. As the interface HTC is prior known as a function of temperature, the thermal and mechanical problems can be solved independently.

The mechanical model of the DC casting problem is subdivided into a material model and a contact model. It is obvious that the material model and the contact model have to be inserted in a structural model with suitable boundary conditions which address the deformation of the ingot. Here, the attention is specifically focused on the material and contact models. A proper material model which can predict more accurately the behavior of mushy and solid phases is absolutely necessary for the realistic simulations. The ingot-bottom block and the ingot-mold mechanical contact determines the normal gap size which intern affects the thermal part.

From the knowledge of temperature change at every instant, the thermal strain can be computed which is the major driving force for the displacement field. In the case of casting, the heat transfer at the boundaries is strongly dependent on its displacement his-

tory. With a suitable coupling techniques, these two problems can be solved sequentially in a weakly coupled manner. The modeling details of both the thermal and mechanical problems, the numerical method used to solve the coupled field equations, and the coupling techniques are explained in detail in the following subsections.

### 1.5.1 Thermal model

The objective of modeling the thermal problem is to find the temperature evolution inside the ingot. To achieve this, the phase-change phenomena has to be modeled more accurately which strongly influences the heat conduction of the domain. Furthermore, the boundary conditions have to be well defined priorly. The thermal model takes care of all these effects and provides the information about the temperature change at any instant. Therefore, the thermal problem is described through the following subproblems such as solidification problem, interface problem and inverse problem which are discussed separately in detail.

#### Solidification model

A model which considers the heat conduction and the phase-change simultaneously is known as *solidification model*. Without assumptions, it is almost impossible to model any such physical processes. Therefore, the assumptions of the solidification model used in this work are described once again as follows:

1. The material is treated as an isotropic rigid heat conductor.
2. The liquid flow is neglected. Therefore, the liquid phase is treated as a fictitious solid.
3. Fixed grid method is followed. Therefore, the domain is not explicitly decomposed into solid, liquid, and mushy zones. The position of phase front and its kinetics are implicitly enforced in the energy balance.
4. The dissipation due to mechanical deformation is negligible when compared to the latent heat release. Therefore, the solidification and mechanical problems are decoupled within the time step.
5. The back diffusion effect is not considered. Therefore, the partition coefficient is taken as unity. The microsegregation is neglected.
6. The liquid convection is accounted in the form of increasing the thermal conductivity of the liquid phase by a factor of 5 from its original value.



7. The heat generation due to the frictional dissipation at the contact interface is assumed to be negligible.
8. There is no pore formation, i.e.  $f_s + f_l = 1$ . Where  $f_s$  and  $f_l$  are solid and liquid volume/phase fractions, respectively.

With the above mentioned assumptions, the energy balance is obtained based on the first law of thermodynamics. The latent heat phenomena are incorporated in the balance equation through the definition of the specific internal energy. This way of incorporating the latent heat is commonly known as temperature-based fixed grid method. The moving phase-front boundary condition is automatically satisfied and gets canceled once deriving the weak form of energy equation. A linear phase-change function is employed to capture the latent heat release.

The weak form of energy balance is discretized using the finite element method. A temperature-based finite element solution procedure proposed by Celentano *et al.* [24] is used to solve the discrete form of the energy equation. An isothermal phase-change introduces artificial numerical oscillations due to the exchange of field variables from temperature to enthalpy. Generally, enthalpy based methods are employed to solve the phase-change problems having a narrow solidification range. In this work, the existing temperature-based finite element method is suitably modified in such a way that we can handle any kind of phase-change problems with considerably less computational efforts. To achieve this, a line-search algorithm proposed by Fachinotti *et al.* [25] and Crisfield [26] is implemented within the Newton-Raphson iterations. A backward Euler time-stepping algorithm is used to discretize the rate equations.

## Interface model

The objective of the interface problem is to incorporate the influence of nearby material on the ingot. This is a kind of boundary condition which can not be solved independently. Therefore, the interface problem is an integral part of the thermal problem. In the DC casting, ingot-mold and ingot-bottom block are the two important interfaces which strongly affect the thermal behavior of ingot. As explained before, in both the interfaces contact and non-contact situations arise due to the thermal shrinkage of the solidified solid. In both cases, the interface heat transfer is assumed to occur mainly due to the combined heat convection and radiation. Even though the heat conduction is the predominant mode of heat transfer during the time of contact between the liquid ingot and nearby material, generally the heat conduction effect is incorporated through the definition of higher value of HTC. Therefore, a gap dependent HTC is defined for the interacting material boundaries. Alternatively, it is also possible to include the effect

of interface heat transfer by means of defining a temperature-dependent HTC. In this case, nearby material temperature is idealized to a mean temperature. Further, this method eliminates the mechanical dependent behavior of a heat conducting body. Both approaches are followed in this work.

A 4-noded interface element is developed based on the work of Lewis and Ravindran [27]. This introduces an additional matrix with a regular conductance matrix. The interface elements have no contribution for the regular capacitance matrix and force vector. The interface heat transfer coefficient is defined through the following relation as in Cervera *et al.* [28]

$$h(g_n) = \frac{k_a}{g_n + \frac{k_a}{h_o}} \quad (1.1)$$

where  $k_a$  is the thermal conductivity of air,  $h_o$  is the convection-radiation coefficient for the two surfaces in contact and  $g_n$  is the normal gap. Eq. (1.1) shows that the interfacial HTC depends on the normal gap and thermal conductivity of air. Thermal conductivity of air<sup>2</sup> varies from 0.02–0.05 W/mK which is 3–4 orders lesser than the metals.

## Inverse model

The inverse problem is defined as the estimation of boundary conditions using the experimental measurements. In DC casting, the secondary water cooling boundary conditions are estimated using an inverse problem. In this work, an inverse problem is solved by separately using the experimental temperature measurements made during the quenching of a hot plate by array of jets. It is assumed that the boiling curve obtained through the quenching experiments and the secondary cooling HTC of DC casting are nearly the same. An infrared thermography is used to measure the temperature evolution during the metal quenching process and the recorded temperature history is further processed using a 2-D inverse heat conduction model. The influence of the water velocity on the heat flux leaving at the boundary is analyzed based on the wetting front movement.

In this work, a non-iterative inverse finite element method proposed by Ling *et al.* [29] is suitably modified and successfully implemented for the 2-D domain. Due to non-iterative nature, the solution of the inverse problem is obtained in a single step. Generally, the inverse problems are solved iteratively to minimize the instantaneous error norm. To avoid the iterative process, the unknown force is written in a suitable form so that its derivative with respect to temperature yields a constant matrix which can be easily computed using the regular finite element method. This eliminates the repeated solving of direct problem.

---

<sup>2</sup>[http://www.engineeringtoolbox.com/air-properties-d\\_156.html](http://www.engineeringtoolbox.com/air-properties-d_156.html)

## 1.5.2 Mechanical model

The objective of modeling the mechanical problem is to find the evolution of displacement, residual stress and strain during the start-up and pseudo steady state phases of DC casting. The mechanical problem is also equally complex when compared to the thermal problem due to the following reasons: (a) rate-dependent material behavior, (b) mechanical contact between the objects, and (c) simultaneous handling of liquid, mushy and solid phases. The last issue is addressed through defining the material properties as a strong function of temperature. The coefficient of thermal expansion ( $\alpha$ ) and Young's modulus ( $E_y$ ) are the important material properties which control the displacement field. For the liquid phase,  $\alpha$  is taken as zero and  $E_y$  is taken as 3–4 orders less than a solid phase. Therefore, the liquid phase does not develop any stresses until it reaches a coherency temperature. The assumptions of the mechanical model used in this work can be stated as follows:

1. The material is treated as isotropic.
2. Small deformation theory is used to model the mechanical behavior of the ingot.
3. The interface between the ingot and mold and bottom block is decomposed into a pure contact problem in the normal direction, and the friction in the tangential direction is neglected.
4. The contribution of the metal shrinkage during solidification is neglected due to the constant liquid feeding within the mushy zone. The alloy is allowed to contract as soon as it reaches the coherency temperature [15].
5. The body force is neglected.
6. The liquid pressure on the solidified solid is not considered.

With these assumptions, the weak form of the linear momentum equation is discretized using the finite element method. The strain tensor is additively decomposed into three parts such as elastic, thermal, and inelastic. The volumetric nature of the thermal strain is the only external disturbance other than the contact conditions which continuously alters the other field variables such as stress, elastic strain, and inelastic strain. The inelastic strain can be either plastic or viscoplastic. Different integration algorithms are employed for the plastic and viscoplastic parts. The material model and contact model are discussed separately in the following subsections.

## Material model

The viscoplastic behavior of mushy zone is modeled using a Norton-Hoff law. Similarly, for the solid phase, the Garafalo viscoplastic rule is followed. The highly non-linear nature of these two viscoplastic laws demand sophisticated numerical schemes to integrate their rate forms. Therefore, a Newton-based implicit iterative integration scheme which is proposed by Saleeb *et al.* [30] is implemented for the integration point level computations. Furthermore, without the help of a line-search algorithm within a Newton's iteration, it is difficult to achieve the convergence. Due to the iterations at the integration point level, the computational time increases which can not be avoided in this kind of non-linear material behavior.

## Contact model

During the DC casting process, the ingot interacts not only thermally but also mechanically with the bottom block and mold. The relative motion between the bottom block and the ingot is relatively lower when compared to the ingot-mold contact. Therefore, it is reasonable to assume a frictionless smooth sliding contact between the bottom block and ingot. In the case of mold, even though there is a considerable relative motion exists with the ingot, due to the development of the air gap the major portion of mold loses the physical contact with the ingot. The prediction of the air gap is highly important because the interface thermal model computes the HTC based on the normal gap between the objects. Therefore, the contact between the objects in the normal direction is more important than the tangential direction. In this work, a coincident frictionless contact element is incorporated based on the method introduced by Vila Real *et al.* [31]. The mechanical contact between the ingot and bottom block is highly important for the exact prediction of the butt curl.

### 1.5.3 Coupling strategy

As discussed before, a thermo-mechano-metallurgical problem of the DC casting process is solved using the finite element method. Initially, the domain starts with few rows of elements, and continuously elements are added at the beginning of every time step according to the casting speed. Similarly, the thermal and mechanical boundary conditions are continuously updated. Non-linear coupled simultaneous equations obtained through FEM are solved using an *isothermal staggered algorithm* [32, 33]. Thermo-metallurgical and mechanical fields are solved sequentially in every time step in the following way:

1. The thermal and the metallurgical fields are solved simultaneously at a fixed configuration.

2. The mechanical field is solved at a constant temperature and phase fractions.

In each time step, first the transient temperature and metallurgical fields are solved simultaneously in an iterative manner, and finally the displacement field is computed iteratively using the full Newton-Raphson method. Armero and Simo [32] argued and proved that this kind of isothermal split of coupled problems are only conditionally stable. Therefore, a proper determination of the time step interval is essential for achieving the convergence. At the end of every time step, the thermo-mechanical interface contact conditions are updated.

## 1.6 Literature review

Mathematical modeling of DC casting process has evolved continuously over the past 35 years. A large number of research articles were published in the field of DC casting. Reviewing all the previously published works is almost impossible, and further it may lead to go out of the scope of this work. Therefore, only essential works which fall within the scope are critically reviewed. Firstly, the thermal aspects of DC casting model are discussed which includes the solidification phenomena, primary cooling and secondary cooling. Secondly, the mechanical aspects such as stress and strain development and material characterizations and its related modeling issues are addressed. Thirdly, the defect predictions such as hot tearing theories and cold cracking are presented. Finally, some general aspects of DC casting which do not come into the above-mentioned three categories are explained.

### 1.6.1 Thermal aspects of DC casting

Modeling the thermal field of DC casting is relatively complex because of the solidification phenomena and insufficient knowledge about the boundary conditions. With the help of advanced measuring techniques and modern computing facilities, researchers attempted to understand the thermal field of DC casting. The objective of the thermal field modeling is none other than predicting the temperature evolution. Even though the microstructure formation is equally important but without the knowledge of temperature, it is almost impossible to address other issues related to the DC casting process. Therefore, this section is dedicated to review the previous works related to the modeling of thermal field of DC casting.

## Solidification

The simulation of phase-change problems is highly important for achieving a high quality casting and to avoid difficult experimentations. During the phase-change, the latent heat release introduces a severe non-linearity and a local exchange of the field variables [34]. The finite element method (FEM) is one of the globally accepted numerical techniques for the simulation of coupled problems. A large number of phase-change problems are formulated, keeping the enthalpy as an independent variable [35], and the nodal temperatures are obtained from the enthalpy-temperature relations. Most of the commercial coupled field FE codes are based on the temperature-based formulation. Therefore, it is quite important to find a reasonable temperature-based formulation with improved convergence rate. In this work, a temperature-based finite element formulation is used to define the phase-change problem using the Celentano-Orate-Oller (COO) [24] method with an extra insertion of the line-search technique of Fachinotti *et al.* [25].

There are two different kinds of solidification / phase-change processes reported in the research community such as (a) isothermal solidification, and (b) non-isothermal solidification. Generally, pure metals and alloys of eutectic composition solidify at constant temperature known as *melting* or phase-change temperature. In contrast to pure metals, alloys solidify over a range of temperature known as phase-change interval. The solidification starts at a higher temperature known as *liquidus* temperature and ends at a lower temperature known as *solidus* temperature. In between the liquidus and solidus temperature, there exists a mixture of solid and liquid phases known as *mushy* phase. Apart from the physics of solidification, the mathematical modeling of a non-isothermal case is relatively simpler than the isothermal case. In contrast to the mathematical modeling, the physics of non-isothermal or alloy solidification is relatively complex and practically there are more changes of defect generation at the phase-change temperature interval.

There are two methods to model the phase-change phenomena using the finite element method: (a) fixed-grid method, and (b) front-tracking method. In the front tracking method [36], a deforming grid formulation is generally employed in order to adapt the mesh to the interface displacement. The solid and the liquid domains are treated as two separate domains and the latent heat release is treated as a special boundary condition relating the solid and the liquid domains [27]. Even though it predicts the latent heat release and the position of phase front more accurately, the major drawbacks of this method are the need to initialize the front location, the difficulty of dealing with appearing/disappearing phases, and multiple interfaces [24]. Further, this method is not suitable for alloys with a finite freezing range and complex geometries.

The fixed-grid methods are derived from a weak formulation that implicitly contains the moving interface condition [24]. Fixed grid methods treat both the solid and liquid

regions as one continuous region and the phase boundary is never explicitly determined. This eliminates the difficulties of mesh adapting and interface tracking. Within the framework of fixed grid methods, to account the latent heat effect, there are two options to choose a dependent variable as either *enthalpy* or *temperature*. In the enthalpy-based methods, the nodal enthalpy vector is obtained for each time step and the nodal temperatures can be computed using the well-known enthalpy-temperature relationship. The enthalpy-based method is a powerful tool to incorporate the latent heat effect but it needs a regularization to remove the discontinuity that appears at the phase front. The heat source method [37–39] and the effective specific heat method [40] are the other forms of enthalpy-based methods.

A large number of researchers worked on the fixed-grid phase-change problems and the interested readers are referred the following review articles [41–47]. Recently, the front-tracking fixed-grid methods [48, 49] is also emerging. Without the loss of generality, most of the above-mentioned methods perform extremely well for the non-isothermal solidification of alloys. When it comes to an isothermal solidification of pure metals, some of the computational methods introduce a numerical instability. This is mainly due to the local exchange of dependent variable from *temperature* to *enthalpy* during the isothermal latent heat release [34]. There exist quite a large number of enthalpy values at the isothermal phase-change temperature ( $\theta_m$ ). Due to this jump in enthalpy - temperature relation, the problem becomes highly nonlinear. Therefore, the classical Newton-Raphson method fails to converge to the solution.

Celentano *et al.* [24] proposed a temperature-based FEM for the phase-change problem which incorporates the latent heat release by means of an additional phase-change matrix and a latent heat vector. They derived an approximate jacobian matrix which preserves the numerical stability and gives a reasonable convergence rate. It does not need any explicit regularization and further coarser meshes and larger time steps (in comparison with other methods) can be used. The COO formulation performs extremely well for the isothermal phase-change with high Stefan numbers. Further, for low Stefan numbers, the temperature-based method fails to converge however small the time step might be. Therefore, Fachinotti *et al.* [25, 50] followed the COO’s temperature formulation, and introduced an element split technique along with a line-search algorithm. The Fachinotti *et al.* model is compatible with the COO model. Both models differ each other through the method of estimation of the latent heat vector ( $\Theta$ ) and the Jacobian contribution of latent heat matrix ( $\frac{\partial \mathbf{L}}{\partial \Theta}$ ).

Generally, there are two ways of estimating the element quantities such as integration point phase-fraction technique and element decomposition method. In the element decomposition method, a single element is divided into different regions based on the nodal

temperatures [25]. In each region, a single phase exists such as solid, mushy and liquid regions in the case of non-isothermal phase-change or solid and liquid regions if it is an isothermal. Therefore, an exact evaluation of the latent heat matrix is possible because of the absence of a discontinuous phase function in the isothermal case. This method does not demand any regularization of the integrands, assuring an accurate evaluation of the discrete balance equation. Unlike the element decomposition method, in the integration point phase-fraction method, the phase fractions are defined or computed at the integration points. This might appear to be trivial, because one may argue that a material point should be either liquid or solid. This question is reasonable and meaningful because even for the non-isothermal phase-change, the solid particle should start evolving at the liquidus temperature in the mushy zone. It means that mushy can be a physical mixture of solid and liquid but the material point should be either liquid or solid. Here, it should be indicated that for the computational purpose there is a compromise made between the reality and simulation. Even though, the integration point approach lacks this physical meaning, it saves a considerable amount of computational time and is compatible with the regular finite element method subroutines. Fachinotti *et al.* used a 3-noded triangular element and approximated the shape of the phase front as straight lines and evaluated the element quantities explicitly with out any Gauss quadrature kind of numerical integrations. Generally, this method is quoted in the research community as *non-standard spatial integration methods*.

In 1996, Celentano *et al.* [51] presented a coupled thermo-mechanical model for the solidification problem using a phenomenological approach which is an extension of their previous work. Saracibar *et al.* [33] extended the Celentano *et al.* work and introduced a thermo plasticity method using an isentropic split approach proposed by Armero and Simo [52]. A newly introduced thermal phase-change free energy function takes care of the latent heat release during the phase-change. In the coupled thermo-mechanical theory, an additive split of the local entropy into elastic and plastic parts is adopted, where the plastic entropy is viewed as an additional internal variable arising as a result of dislocation and lattice defect motion. The present work derives the method from the COO model and Fachinotti *et al.* [25] formulations, and attempts to generalize the temperature-based formulation even for low Stefan numbers.

## Primary cooling

As explained previously, the air gap develops once the interface material starts solidifying. Different authors proposed different methods to incorporate the interfacial heat transfer between the ingot and mold and bottom block. Mortensen [6] used a geometric mean of HTC's due to the air gap and the lubricating film in the primary cooling zone. Hao *et*



*al.* [53] used a temperature dependent HTC between the magnesium alloy ingot and mold. When the temperature of an interface material is above the liquidus temperature, the interfacial HTC is taken as 1500 W/m<sup>2</sup>K, and once the temperature drops to the solidus temperature a lower value of 75 W/m<sup>2</sup>K is assigned. In the phase-change interval, a linear variation is assumed. Katgerman *et al.* [54] directly used the solid fraction in the computation of primary cooling HTC given

$$h = h_{contact}^{(1-f_s)} h_{gap}^{f_s} \quad (1.2)$$

where  $f_s$  is the solid fraction, and  $h_{contact}$  and  $h_{gap}$  are the HTCs at the contact and non-contact situations, respectively. The values of  $h_{contact}$  and  $h_{gap}$  are taken as 4000 and 150 W/m<sup>2</sup>K respectively. Sengupta *et al.* [55] used the similar approach for an AA5182 alloy and modified the interfacial HTC as

$$h = h_{contact} (1 - f_s) + h_{gap} f_s \quad (1.3)$$

$h_{contact}$  might be in the range of 1000–2000 W/m<sup>2</sup>K, and similarly for  $h_{gap}$  it would be around 50–200 W/m<sup>2</sup>K. Suyitno *et al.* [56] idealized the primary cooling HTC as contact and non-contact cases. During the time of contact, HTC is taken as 1500 W/m<sup>2</sup>K, and in non-contact situation, the HTC is reduced to 300 W/m<sup>2</sup>K. Stangeland *et al.* [57] used the same approach, however they varied the HTC from 3000 W/m<sup>2</sup>K to 220 W/m<sup>2</sup>K for the same alloy of Al–Cu.

Wiskel [58] used a space-dependent HTC for the mold region. Drezet *et al.* [59] followed this approach and computed the HTC as a function of distance from the melt level through an inverse analysis of experimental measurements. Even though both authors investigated the same alloy such as AA5182, the magnitude changes a lot. According to Drezet *et al.*, the HTC at the melt level is around 1320 W/m<sup>2</sup>K and reaches a maximum of 2400 W/m<sup>2</sup>K at 10 mm from the melt level, and finally becomes 50 W/m<sup>2</sup>K at 60 mm from melt. This result is frequently used in the literature such as Williams *et al.* [60]. In this work, the Drezet *et al.* [59] method is used to account the primary cooling.

The bottom block boundary condition is similar to the primary mold boundary. Additionally, the secondary cooling water may enter the gap and changes the thermal behavior of the bottom block and the ingot base. This phenomena is known as water incursion. Suyitno *et al.* [5] incorporated the water incursion situation based on the amount of gap opening. During the time of water intrusion, the interfacial HTC is increased up to 3000 W/m<sup>2</sup>K at 200°C and gradually reduced to 1000 W/m<sup>2</sup>K at room temperature. Sengupta *et al.* [55] introduced a wetting factor which varies from 0 to 1 and represent the degree of wet. However, Droste *et al.* [61] argued that the intruded water might act

as a sink for both bottom block and ingot.

## Secondary cooling

The secondary cooling experienced by the ingot surfaces as they emerge from the mold, is governed by the boiling water heat transfer [62]. Fig. 1.10 shows the typical cooling water boiling curve as a function of ingot surface temperature. From the figure, it is easy to understand the four different boiling regimes such as the forced convection, nucleate boiling, transition boiling and film boiling. Generally, in DC casting, surface temperatures at the point of water contact, lie between the transition and film boiling regions. The temperature at which the vapor film collapses is known as Leidenfrost point (LFP). As the ingot is cooled by the direct chill water [58], the amount of heat extracted follows the transition portion of the cooling curve up to the maximum value, at a critical point shown in Fig. 1.10. With a further reduction in surface temperature, the intensity of nucleate boiling decreases until the surface temperature drops below the boiling point of water. Below this point, the heat is extracted by forced convective cooling [58].

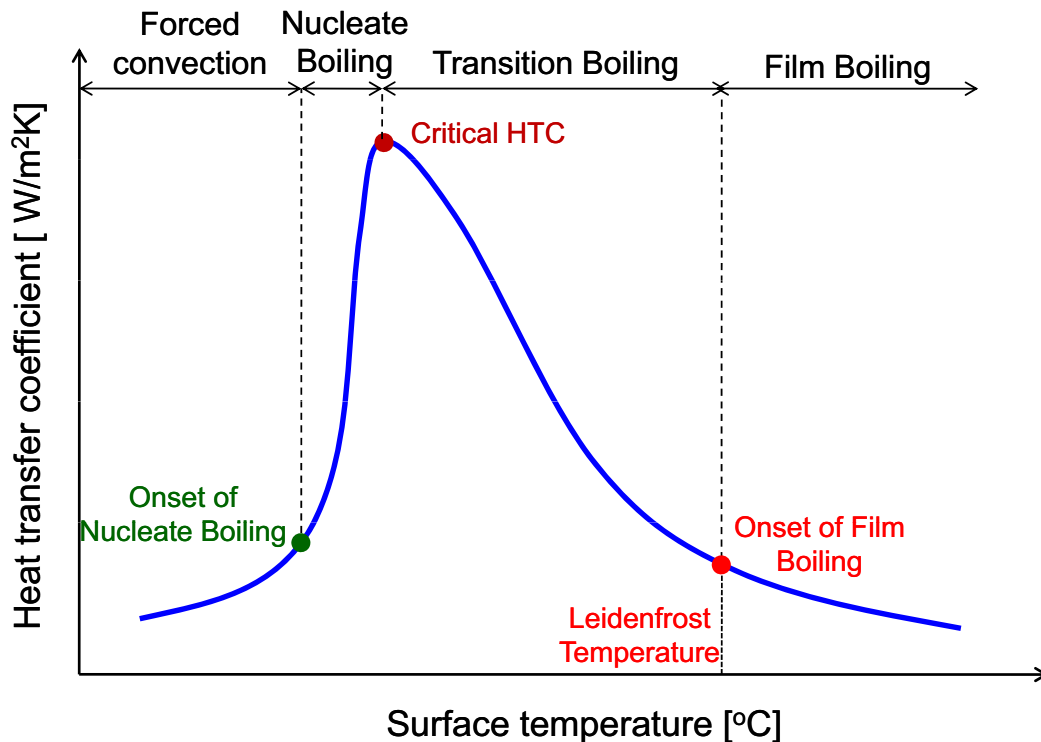


Figure 1.10: A typical boiling curve

Generally, based on the water flow, the secondary cooling ingot surface is divided into two different regions such as water impingement zone and free falling zone or downstream zone. In the water impingement zone, Opstelten and Rabenberg [63] presented a empirical

correlation for the heat flux and given as

$$\begin{aligned}
 q &= 27.3 \times 10^3 \theta - 1.27 \times 10^6 & \text{if } \theta < 120^\circ\text{C} \\
 q &= 94.3 \times 10^3 \theta - 9.24 \times 10^6 & \text{if } 120^\circ\text{C} \leq \theta < 150^\circ\text{C} \\
 q &= 12.3 \times 10^3 \theta - 3.06 \times 10^6 & \text{if } \theta \geq 150^\circ\text{C}
 \end{aligned} \tag{1.4}$$

In 1982, Weckman and Niessen [64] proposed a following correlation for the estimation of nucleate boiling HTC in the free falling region as,

$$h(\theta) = (-1.67 \times 10^5 + 704 \bar{\theta}) \left( \frac{Q}{\pi D} \right)^{1/3} + \frac{20.8}{\theta - \theta_{ref}} (\theta - 373.15)^3 \tag{1.5}$$

where  $\theta$  represents the billet surface temperature in Kelvin,  $\theta_{ref}$  is the bulk cooling water temperature in Kelvin,  $\bar{\theta}$  ( $= 0.5(\theta + \theta_{ref})$ ) is the mean temperature in Kelvin,  $Q$  is the water flow rate in  $\text{m}^3/\text{sec}$ , and  $D$  is the billet diameter in meter. The first term in Eq. (1.5) accounts for the convective heat transfer due to the one-phase free falling turbulent film of water, and the second term, which is taken into account only when  $\theta > 373.15$  K, models the subcooled nucleate boiling. However, the bulk temperature of the free falling water changes with respect to the billet height. Šarler and Mencinger [65] presented the method to calculate the increase in bulk temperature of cooling water as a function of billet height. Zuidema [4] slightly modified the Eq. (1.5) and did not verify that at all. Weckman and Niessen [64] mentioned the risk associated with increasing the casting speed from a steady state condition when cooling is by nucleate boiling. As the casting speed is increased, the surface temperature of the ingot will rise at the point where the secondary spray first hits. When this temperature surpasses the critical temperature, there will be a sudden switch into film boiling with its much lower heat extraction rates. Consequently, surface temperatures increase very rapidly causing more and more of the surface to enter the film boiling regime in a self-perpetuating manner. If heat extraction rates by film boiling are insufficient, to form a thick enough ingot shell, liquid metal breakout will occur. This sudden jump from nucleate boiling to film boiling may be responsible for liquid metal breakouts during the higher casting speeds.

Due to the film boiling, water ejection [55] may occur during the low water flow rate. Sengupta *et al.* [66] included the effect of water ejection in their model. Unfortunately, the information regarding the water ejection is not explained clearly. Sengupta *et al.* [12] extensively studied the secondary cooling of DC casting and compared it with the continuous casting of steel. They reported the following facts: (a) the maximum heat flux varies from 5 to 1 MW/m<sup>2</sup>, (b) the LFP varies from 250–350°C and increases with increasing water flow rate, and (c) rougher surfaces exhibit higher heat transfer rates.

Recently, Caron and Wells [67] presented a new two-dimensional inverse heat conduction (IHC) model which takes into account the effect of advanced cooling front phenomena during quenching tests. In their IHC model, the second derivative of the temperature with respect to time is computed to identify the progression of the wetting front along the sample surface. The initial sample temperature determines whether the film boiling takes place at the impingement point; it does not significantly affect the boiling curve for the free-falling zone. They found that the casting speed exerts a strong influence on the boiling curve if the initial temperature is above the Leidenfrost point for the impingement zone, else its effect is minimal. The cooling water flow rate influences the LFP and the rewetting temperature as well as the critical heat flux at the impingement point.

Mortensen [6] presented a model for the time-dependent heat and fluid flows during DC casting of aluminum alloy AA1050. They used a constant HTC of  $30 \text{ kW/m}^2\text{K}$  and estimated the length of the impingement zone as 10 mm. Drezet *et al.* [59] presented an inverse model using a maximum a posteriori (MAP) method developed by Rappaz *et al.* [68] and studied the secondary cooling of DC casting. They mentioned that the relationship between the surface temperature and the HTC is not unique between  $90^\circ\text{C}$  and  $110^\circ\text{C}$ . The reheating of the ingot surface below the water-impingement point associated with the water bounce-off produces a somewhat *skewed*, cooling curve around  $100^\circ\text{C}$ . Wiskel and Cockcroft [69, 70] investigated the secondary cooling of AA5182 alloy and presented an empirical relation for HTC as a function of temperature. The heat flow is influenced by the surface morphology and water flow conditions during the start-up phase. Opstelten and Rabenberg [63] showed that the classical description of a heat transfer coefficient or heat flux as a function of surface temperature alone does not accurately describe the thermal boundary condition for DC casting. The influences of water cooling on DC casting ingot was studied by Tsunekawa *et al.* [71], Grandfield *et al.* [72], and Maenner *et al.* [73]. Kiss *et al.* [74] showed the quality of water has the strongest influence on transition between the different boiling regimes and also on the character of the fluctuations of the surface temperature and heat flux. The influence of water flow rate and casting speed on the thermal boundary conditions of DC casting has been studied by Sabau *et al.* [75].

### 1.6.2 Mechanical aspects of DC casting

An excellent review of existing works related to the DC casting was presented by Sengupta *et al.* [16]. Barral and Quintel [2, 76] presented a 3-D numerical model for the accurate prediction of butt curl during the pseudo steady phase. They used a space and time dependent HTC profile for the lateral surfaces of the ingot. The details of the thermal model is not explained in detail but the mathematical aspects of the mechanical model

have been described in more detailed manner. The contact between the ingot and bottom block is modeled through the Lagrange multiplier method. To avoid non-linearities due to the contact condition and the viscoplastic law, they introduced a maximal monotone operator technique involving a contact multiplier and a viscoplastic multiplier. The liquid elements are treated as a purely elastic material.

### **Residual thermal stress-strain**

Fjær and Mo [77] presented a DC casting mathematical model known as ALSPEN using the finite element method. For the thermal model of AA6063, they used an established package known as ALSIM-2. They demonstrated the numerical method for computing the stress and strain using an axisymmetric circular billet. The advantage of their FEM model is the reduction of computational time by using a single integration point taken at the element center. Therefore, they introduced an initial stress concept for the newly incoming elements.

Williams *et al.* [60] simulated the 3-D DC casting of AA1201 alloy using a commercial package ANSYS. They used a modified Perzyna type viscoplastic law for the prediction of mechanical behavior of solid and mushy phases. They also incorporated the liquid flow. The material hardening effects and the initial free surface filling are not included in their model. They reported extremely higher values of stresses due to the inappropriate material model. Therefore, it is highly important to incorporate a proper material model. Drezet and Rappaz [15] and Katgerman and coworkers significantly contributed in the field of DC casting modeling.

Kaymak [78] investigated the development of residual stresses in a solid material subjected to quenching. In his work, the curvature of the quenched object is treated as a measure of distortion. To achieve this, a 2-D finite element model is developed using an elastic-plastic material model with isotropic hardening. He investigated the solid-solid phase transformation which generally occurs in steel. The thermal and metallurgical fields are decoupled within the time step. This may not be the case in liquid-solid phase transition problems due to the domination of latent heat release. He proposed the optimum cooling strategies to reduce the distortion and residual stresses [39, 79, 38]. With an enhanced cooling at the mass lumped region, and reduced cooling at the edges or less mass concentrated area, it is possible to reduce the residual stresses. His work is considered as a basis for the current investigation about the DC casting.

## Material characterization

Magnin *et al.* [80] performed tensile tests on an Al-4.5%Cu alloy in order to determine the rheology and ductility over a wide range of temperature moving from the room temperature to the dendritic coherency temperature. Based on their experimental observations, they come up with an elasto-viscoplastic law

$$\sigma = K (\dot{\epsilon}_p + \dot{\epsilon}_{po})^m (\epsilon_p + \epsilon_{po})^n \quad (1.6)$$

where  $K, m$ , and  $n$  are material parameters which are strongly dependent on temperature,  $\epsilon_p$  and  $\dot{\epsilon}_p$  are the plastic strain and plastic strain rate, and  $\epsilon_{po}$  and  $\dot{\epsilon}_{po}$  are the small constant plastic strain and strain rate respectively. Suyitno *et al.* [56] used the same law for the solid phase and proposed a different constitutive law for the mushy phase which is similar to the Garafalo law. However, they incorporated the solid fraction in the constitutive law of mushy which is not the case for the Garafalo law. According to them,

$$\sigma = \tilde{\sigma}_o e^{(\tilde{\alpha}f_s)} e^{\left(\frac{mQ}{R\theta}\right)} \dot{\epsilon}^m \quad (1.7)$$

Drezet and Rappaz [15] used the Garafalo law for the solid phase and Norton-Hoff law for the mushy phase. They investigated the AA1201 alloy and predicted the butt curl, butt swell and rolling faces inward pull-in. M'Hamdi *et al.* [81] used a complex viscoplastic law with more material parameters.

Depending on the fraction of liquid, the behavior of semisolid materials under stress has been described with rheological or creep-type laws. The critical temperature separating these two behaviors is defined as the dendrite *coherency temperature*. Above this temperature, the dendrites are free to move, and the material behaves as non-Newtonian viscous slurries. Just below the dendrite coherency temperature, the dendrites are in close proximity and interact as soon as a strain is applied. This causes the material to behave as a mush exhibiting a yield stress above which plastic flow occurs by grain boundary sliding [1].

Considering that a continuous domain of liquid exists in the mushy interval giving the possibility of sponge like behavior. Nguyen *et al.* [82] developed a two-phase isothermal model based on the theory of mixtures and the mechanics of continuous media. The model is able to characterize the compressibility and the hardening/softening behavior of the porous solid phase saturated with liquid, but fails to describe the tension-compression asymmetry representative of a real sponge like behavior when large strains are applied.

Benke and Laschet [83] experimentally investigated the behavior of A356 semi-solid alloy in tension, compression, and shear during equiaxed solidification. Their model is

based on the theory of porous media for a binary porous medium taking into account the mass exchange between the solid and the liquid due to the progressing solidification.

### 1.6.3 Hot tearing and cold cracking

A hot tear is a fracture formed during solidification due to the shrinkage and the hindered contraction, lack of feeding, and it initiates in the mushy zone [84]. Because of the complex mechanisms acting during the solidification of metals, the prediction of the hot tearing phenomenon is not an easy task. The complex nature of mushy properties adds additional difficulties while incorporating these in a hot tearing model. Therefore, it is important to understand the different stages of solidification before addressing the hot tearing theories. Suytino [5] categorized the alloy solidification process into four stages, based on the permeability of the solid network:

1. Stage-1: *Mass feeding*, in which both liquid and solid are free to move.
2. Stage-2: *Interdendritic feeding*, in which the remaining liquid has to flow through the dendritic network. After the dendrites have formed a solid skeleton, the remaining liquid has to flow through the dendritic network. A pressure gradient may develop across the mushy zone by solidification shrinkage occurring deeper in the mushy zone. However at this stage the permeability of the network is still large enough to prevent pore formation.
3. Stage-3: *Interdendritic separation*, in which the liquid network becomes fragmented and pore formation or hot tearing may occur. With increasing solid fraction, the liquid is isolated in pockets or immobilized by surface tension. When the permeability of the solid network becomes too small for the liquid to flow. Further thermal contraction of the solid will cause pore formation or hot tearing.
4. Stage-4: *Interdendritic bridging* or solid feeding, in which the ingot has developed a considerable strength and solid-state creep compensates further contraction. At the final stage of solidification ( $f_l < 0.1$ ), only isolated liquid pockets remain and the ingot has a considerable strength. Solid-state creep can now only compensate solidification shrinkage and thermal stresses.

At present, there are 8 hot tearing theories existing, and the detailed review of the related works can be found in Eskin *et al.* [85]. Generally, these theories can be classified based on *nonmechanical* aspects such as feeding behavior and *mechanical* aspects. A short description of the nonmechanical criteria are given below:

1. Feurer's criterion [86]: Feurer considers the transition from the second to third stage to be important for determining whether hot tears may initiate or not. The transition point is strongly dependent on the feeding pressure, length of porous network, volume fraction of liquid, dendrite arm spacing, tortuosity constant, viscosity of liquid, and density of solid and liquid. He stated that a hot tear occurs when the maximum volumetric flow rate through a dendritic network is lesser than the volumetric solidification shrinkage due to the density difference.
2. Clyne and Davies criterion [87]: Apart from the second and third stages, Clyne and Davies considered other transitions also in their criterion. In the last stage of solidification, it is difficult for the liquid to move freely so that the strains develop during this stage cannot be accommodated by mass and liquid feeding. Based on this, they defined the hot tearing susceptibility (HTS) as the vulnerable time period ( $t_V$ ) and the time available for the stress-relief process where mass feeding and liquid feeding occurs ( $t_R$ ) and is given as

$$\text{HTS} = \frac{t_V}{t_R} = \frac{t_{0.99} - t_{0.9}}{t_{0.9} - t_{0.4}} \quad (1.8)$$

where  $t_{0.99}, t_{0.9}$ , and  $t_{0.4}$  are the times when the solid fraction reach 0.99, 0.9, and 0.4 respectively. Due to the usage of constant values of the solid fraction for the transition limits, the influence of other parameters is neglected. This criterion is the simplest one to implement when compared to others.

3. Katgerman's criterion [88]: Katgerman combined the Feurer and Clyne and Davies criteria, and defined the HTS as,

$$\text{HTS} = \frac{t_{0.99} - t_{cr}}{t_{cr} - t_{coh}} \quad (1.9)$$

where  $t_{coh}$  is the time to reach coherency point, and  $t_{cr}$  is the time when feeding becomes inadequate. Generally,  $t_{cr}$  is computed based on the Feuer's criterion. This criterion is based on the first three stages of solidification.

The mechanical criteria are based on the rheological behavior of the mushy phase and its short descriptions are given below:

1. Prokhorov's criterion [89]: In this approach, hot cracking sensitivity is determined by the shrinkage and apparent strain rate in the mush in relation to the fracture strain.
2. Novikovs criterion [90]: According to this theory, hot cracking sensitivity is determined by shrinkage strains in the mush in relation to the fracture strain of the



mush.

3. Magnin *et al.* criteria [91]: It is based on the strain experienced during solidification in relation to the fracture strain in the last stage of solidification. The HTS is taken as the quotient of the circumferential plastic strain ( $\epsilon_{\theta\theta}^p$ ) at solidus temperature and the experimentally determined fracture strain ( $\epsilon_{fr}$ ) close to the solidus temperature. Thus, the sensitivity is taken as

$$\text{HTS} = \frac{\epsilon_{\theta\theta}^p}{\epsilon_{fr}} \quad (1.10)$$

This is also one of the simplest mechanical criterion. Even without the normalization with  $\epsilon_{fr}$ , according to this theory, it can be possible to say in which case hot cracks most likely occur.

4. Rappaz-Drezet-Gremaud (RDG) criterion [92]: According to them, the hot tear will form if the depression pressure in the mushy ( $\Delta P$ ) exceeds the critical depression pressure ( $\Delta P_{cr}$ ). The depression pressure is the sum of pressure due to the solidification shrinkage, deformation induced flow and metalostatic pressure.
5. Braccini *et al.* criterion [93]: They defined a critical strain rate which is used to represent the measure of the hot cracking sensitivity.

Suyitno *et al.* [84] extensively studied all the above mentioned existing criteria and discussed their finite element implementations. They analyzed all the criteria based on the following four aspects:(a) casting speed, (b) ramping procedure, (c) billet center, and (d) whether crack will form or not. And found that none of the eight criteria are able to correctly predict whether hot tear during DC casting will occur. The RDG criterion shows the greatest potential in this regard when used on a qualitative base. Further, they rated the different casting speed profiles based on the following parameters: (a) sump depth, (b) mushy zone length, and (c) stress near the mushy zone. Eskin and Katgerman [94] emphasized the importance and requirement for a hot tearing criteria. Farup and Mo [95] presented a two-phase continuum model for an isotropic mushy zone. They mentioned that due to the higher pressure in the solid phase than the liquid phase, tensile stress is necessary for the formation of hot tears. The hot tearing susceptibility increases with an increasing solidification interval and casting speed.

Paramatmuni *at el.* [96] studied the cracking resistance of Al2024 (AlCuMg) and Al3002 (AlMnMg) alloys and the microstructures formed at different locations of the ingot. Using the quench-cracking tests, they found that the increase in solidification rate increases the cracking resistance and decreases the grain size. This is due to the less

number of grain boundaries along which the crack has to pass resulting in absorption of a smaller amount of cracking energy, and thus the crack can easily pass through the coarse and continuous eutectic phases along the grain boundaries leading to an intergranular fracture. Conversely, the grain size and fraction of eutectics decreases when the cracking resistance increases.

Lalpoor *et al.* [97] investigated the microstructural features of intergranular brittle fracture and cold cracking in high strength aluminum alloys. It occurs mainly because of the continuous coverage of the grain boundaries and intergranular areas by brittle intermetallics and non-equilibrium eutectics formed at final stages of solidification. Weak bonding to the matrix and cleavage are the main reasons for the abrupt fracture, and brittle intermetallics are covering the fracture surfaces entirely. On the microscopic scale, however, micro cracks may form above the solidus temperature and preferably propagate through the intermetallics, making a river-like pattern. Thus they may not eventually get aligned normally to the maximum principal stress component, which is required for their propagation and eventually catastrophic failure.

The effect of porosity on hot tearing was investigated by Phillion *et al.* [98] using a semi-solid tensile deformation methodology combined with X-ray micro-tomography. They conducted tests on the commercial aluminum–magnesium alloy AA5182 in the as-cast state. With the help of hot isostatic pressing, they found that the semi-solid tensile strength and ductility of the material can be increased by reducing the number of pre-existing nucleation sites for strain accommodation. Further, they showed that the failure in this material is localized to the fracture surface with very little internal damage occurring in other areas.

M’Hamdi *et al.* [99, 81] made a comparison of experimental observations and computer simulations and showed that the trends in the occurrence and severity of center cracks in the DC cast ingots for the different casting speed profiles and explained using the changes in viscoplastic strain rate at the center. They investigated 5 different casting trials and demonstrated the importance of ramping. Further, they computed the pressure drops in the mushy zone using a simple model and showed that the mechanical contribution is larger than the shrinkage contribution during the critical stage of solidification. Their investigations are based on the following parameters: (a) strain accumulation in the vulnerable period, (b) stress in the normal direction of crack propagation, and (c) strain rate. In their later work [18], they proposed a new hot tearing theory based on the effective tearing strain known as accumulated viscoplastic strain in the vulnerable part of the mushy zone which exceeds the critical value.

Wu [100] argued that the major reason for the surface cracks in DC casting is the improper cooling given by the mold region. The air gap arises from the tendency of the

solidified shell to be pulled inward as a result of the contraction in the solidified ingot. The contraction stress and the metallostatic pressure may cause solidified shell cracking. Mao *et al.* [101] presented a fracture mechanics approach for the prediction of quench cracks. They found that the higher cooling rate results in lower cracking toughness under the same grain size structures. Martin *et al.* [102] investigated the fracture behavior in tension of the viscoplastic porous metal saturated with the liquid. Further, they extended their work [103] for the rheological behavior of mushy zone with moderate fraction of the solid. Lahaie and Bouchard [104] gave the importance of isothermal compressibility of the liquid phase for the formation of hot tears, and explained the need for the fracture based hot tearing theory. Due to the brittle nature of the mushy phase, once hot tear occurs, propagation of the crack will follow catastrophically until fracture.

Spittle and Cushway [105] reported that the increase in melt superheat increases the HTS based on the investigation of Al-Cu alloys. Eskin *et al.* [106] experimentally studied the effects of melt temperature and casting speed on the structure and defect formation during start-up and pseudo steady state phases of DC casting of an Al-2.8%Cu alloy. They varied the melt temperature from 660°C to 715°C. Increase in melt superheat increases the probability of bleed-outs during casting, deepens the sump, and results in the formation of a coarser structure. An increase in casting temperature decreases the vulnerability of the billet to hot tearing. This contradicts the work of Spittle and Cushway. Eskin *et al.* argued that the hot cracks are gradually substituted in the structure by microcracks, healed cracks, and pores. They mentioned that the increase in melt temperature increases the severity of subsurface segregation, whereas the macrosegregation in the rest of the billet remains virtually unaffected. Further, they reported that HTS is strongly diminished by an increased melt superheat.

#### 1.6.4 General aspects of DC casting

Drezet and Rappaz [15] predicted the ingot distortion using ABAQUS. They investigated the AA1201 alloy and optimized the shape of the mold. Specifically, they investigated the butt curl, butt swell and lateral faces inward pull-in. However, they did not discuss about the stress and viscoplastic strain evolutions. The material data for the present investigation are taken from this work. Suyitno [5] presented an FE model for the DC casting of round billet. They reported that during the start-up phase, all components of stresses in the mushy zone are tensile except the axial component. Further, they evaluated all the existing hot tearing criterion.

Mortensen [6] has presented a three-dimensional mathematical model for the transient evolution of the heat and fluid flows in DC casting of an AA1050 sheet ingot. His model is able to predict the complicated thermal history of the ingot in the start-up period of

the casting. The fluid flow has been shown to have a significant effect on how the solid shell solidifies against the bottom block and the mold.

Sengupta [62] conducted a 3-D simulation of DC casting using ABAQUS. He mainly focused on the thermal part of DC casting. Two different start-up conditions based on the secondary cooling are discussed in his work such as cold cast and hot cast. In the hot cast, a larger portion of the secondary cooling is subjected to film boiling, and therefore water ejection happens. The ingot is extremely hot during the hot cast. In the case of cold cast, the conditions are reversed and the billet is relatively colder. Based on the experimental results, they reported that the butt curl is higher in the cold cast than the hot cast. However, the information about the secondary cooling for the cold and hot cast are not explained except the water ejection phenomena. Further, they did not attempt the mechanical and hot crack part of the DC casting.

From the above-mentioned literature, it can be concluded that the influence of casting speed profile and melt superheat are investigated by several authors. However, very few authors focused their attention near the mushy zone. The mushy state of metal is the most important region in DC casting where the chances are high for the formation of hot tears. Further, the influence of secondary cooling parameters and its related studies are nowhere reported. Therefore, this work is dedicated to theoretically investigate the influence of casting speed profile, secondary cooling parameters, and melt superheat. The primary attention is focused on the mushy zone. From the stress and strain development near the mushy zone, the chances of hot tear formation are discussed in this work.

## 1.7 Thesis outline

Chapter 2 is dedicated to address the solidification problem. The mathematical formulation and the solution methodology are discussed in detail. To incorporate the pure metal solidification, more attention is devoted to the computational aspects of the problem. To validate the developed model, two different isothermal solidification problems are solved and the results are compared with the literature. The interfacial heat transfer is also addressed. In Chapter 3, the inverse problem associated with the secondary cooling of DC casting is investigated through the experimental observation of hot plate quenching. A mathematical formulation and the non-iterative solution procedures are discussed in detail. Two different materials such as nickel and aluminum alloy are investigated. The influence of water flow rate on the boiling curve is demonstrated through the combined experimental and finite element solutions.

The mechanical aspects of DC casting are discussed in Chapter 4. Two different types of inelastic strains and its time integration procedures are explained. The contact between

the interface materials are addressed. The importance of rate-dependent plastic behavior of metals are illustrated through the examples. Finally, an example thermo-mechanical problem is solved using the elastic-plastic and elastic-viscoplastic material laws and the results are compared. In Chapter 5, the simulation results of DC casting are presented. The problems associated with the start-up phase of DC casting is investigated through a constant casting speed of 120 mm/min. The influence of the casting speed is studied through different casting speed profiles and constant casting speeds. The influence of secondary cooling and other casting parameters are discussed.

## 1.8 Summary

The direct chill casting process is explained. Start-up and end phases of DC casting strongly depends on time. Primary, secondary, and bottom block are the three zones through which the ingot loses the heat. The air gap in the primary and bottom block zones significantly reduces the heat transfer. The importance of aluminum alloys and its classifications are addressed. The objective of this work is to develop a numerical model which can simulate the transient start-up phase of DC casting. The attention is focused on the temperature evolution and residual stress development. The assumptions of thermal and mechanical models are discussed. The importance of interfacial heat transfer and contact conditions are emphasized. The existing DC casting models are reviewed briefly.

# Chapter 2

## Modeling of Solidification Problem

This chapter presents the solidification model and its numerical solution techniques. A general governing differential equation is developed and then simplified according to the assumptions. The fixed grid method follows. The liquid phase is treated as a fictitious solid. The liquid flow and convection is neglected. The weak form of energy equation is derived using the variational principles. A temperature-based finite element technique is developed. The backward Euler time difference method is used to discretize the rate equation in time direction. The computational difficulty of isothermal phase-change is explained in detail. A line-search algorithm is introduced during the Newton's iterations. Two numerical examples are presented and the results are compared with the literature. This chapter is formulated based on the published work of Nallathambi *et al.* [107].

### 2.1 Definition

Let an open bounded domain  $\Omega \subset \mathbb{R}^{n_d}$  ( $n_d = 1,2,3$ ) be the configuration of a solidifying material body  $\mathcal{B}$  with particles defined by  $\vec{X} \in \tilde{\Omega}_0$ ,  $\Gamma = \partial\Omega$  its smooth boundary and the time interval of analysis  $t \in \Upsilon$  ( $\Upsilon \subset \mathbb{R}^+$ ). As usual,  $\tilde{\Omega} = \Omega \cup \Gamma$  and  $\Gamma = \Gamma_\theta \cup \Gamma_q$ . The *solidification* problem consists of finding the absolute temperature field  $\theta : \tilde{\Omega} \times \Upsilon \rightarrow \mathbb{R}^+$  such that [24]

$$-\nabla \cdot \vec{q} + \rho r_q + \mathcal{D}_{mech} = \rho \frac{\partial u}{\partial \theta} \left( \frac{\partial \theta}{\partial t} + \nabla \theta \cdot \vec{v} \right) \quad \text{in } \tilde{\Omega} \times \Upsilon \quad (2.1)$$

subject to the boundary conditions

$$\theta = \bar{\theta} \quad \text{in } \Gamma_\theta \times \Upsilon \quad (2.2)$$

$$\vec{q} \cdot \vec{n} = -q_{conv} - \bar{q} \quad \text{in } \Gamma_q \times \Upsilon \quad (2.3)$$

and the initial conditions

$$\theta(\vec{X}, t)|_{t=0} = \theta_0(\vec{X}) \quad \text{in } \Omega \quad (2.4)$$

$$f_{pc}(\vec{X}, t)|_{t=0} = 1 \quad \text{in } \Omega \quad (2.5)$$

$$\vec{v}(\vec{X}, t)|_{t=0} = 0 \quad \text{in } \Omega \quad (2.6)$$

Eq. (2.1) represents the energy balance of a continuum heat conductor. Where  $\vec{q}$  is the heat flux vector,  $\rho$  is the mass density,  $r_q$  is the specific internal heat source,  $\mathcal{D}_{mech}$  is the heat dissipation due to mechanical deformation,  $u$  is the specific internal energy, and  $\vec{v}$  is the velocity vector.

The first term in Eq. (2.1) is due to the heat conduction. The heat flux can be related to the temperature gradient through the well known Fourier's law of conduction as

$$\vec{q} = -\mathbf{K} \cdot \nabla\theta \quad (2.7)$$

where  $\mathbf{K}$  is the temperature-dependent conductivity second-rank tensor. As a consequence of the second law of thermodynamics, this tensor must be positive semidefinite. For an isotropic heat conductor,  $\mathbf{K}$  can be reduced to  $k \mathbf{I}$ .

The second term in the energy equation arises due to the internal heat generation. The third term arises due to the mechanical dissipation. If the heat conducting body is not assumed as a rigid one, the energy dissipation due to mechanical deformation has to be taken into account in the energy balance. The mechanical dissipation can be stated as

$$\mathcal{D}_{mech} = \mathbf{T} : \dot{\mathbf{E}}^{ie} \quad (2.8)$$

where  $\mathbf{T}$  is the Cauchy's stress tensor and,  $\dot{\mathbf{E}}^{ie}$  is the inelastic strain rate tensor. This is the only term which couples the mechanical field with the thermal field. In this kind of solidification problems, due to the domination of latent heat effect, this term becomes insignificant.

Eq. (2.2) represents the temperature prescribed essential boundary condition (EBC) on  $\Gamma_\theta$ , and Eq. (2.3) is the heat flux specified natural boundary condition (NBC) on  $\Gamma_q$  with unit outward normal  $\vec{n}$ . Heat flux can be applied in two ways: (a)  $\bar{q}$  is the prescribed normal heat flux and (b)  $q_{conv}$  is the heat flux due to convection-radiation phenomena. From Newton's law of cooling,

$$q_{conv} = -h (\theta - \theta_\infty) \quad (2.9)$$

where  $h$  is the temperature-dependent convection-radiation heat transfer coefficient

(HTC) and  $\theta_\infty$  is the atmospheric temperature.

The three initial conditions considered are: (a)  $\theta_0(\vec{X})$  is the initial temperature, (b)  $f_{pc}$  is the liquid phase fraction which is taken as one, and (c) zero initial velocity  $\vec{v}$ . The liquid flow field is not considered in this work. For the sake of completeness of the model, it is presented here.

The right hand side of the energy equation represents the rate of change of internal energy of the heat conducting body with respect to time. The rate of change of internal energy with respect to the temperature, represents the specific heat capacity. The material time derivative / total time derivative of temperature can be decomposed into (a) partial time derivative of temperature and (b) convective derivative of temperature. In this work, the liquid metal is treated as a fictitious solid and the velocity field is not taken into account. According to this assumption, the convective terms in the right hand side can be neglected. Therefore, the rate of change of internal energy with respect to time can be simplified as,

$$\dot{e} = \rho \frac{\partial u}{\partial \theta} \frac{\partial \theta}{\partial t} \quad (2.10)$$

The latent heat release during the phase-change can be incorporated in the specific internal energy term as in [24]

$$u = \int_{\theta_{ref}}^{\theta} C_p d\theta + L f_{pc} \quad (2.11)$$

where  $\theta_{ref}$  is the reference temperature,  $C_p$  is the specific heat capacity at constant pressure,  $L$  is the latent heat per unit mass.

The phase-change problem can be classified as (a) isothermal phase-change and (b) non-isothermal phase-change. During the isothermal phase-change, based on the temperature or the liquid fraction at every material point, the domain of the heat conducting body ( $\Omega$ ) can be decomposed into a liquid region ( $\Omega_l$ ) and a solid region ( $\Omega_s$ ) as shown in Fig. 2.1(a). The non-overlapping domain condition,  $\Omega = \Omega_l \cup \Omega_s$  has to be considered. The line which separates the two phases is called *phase front* on which the latent heat is released. The temperature of the phase front is exactly equal to the solidification temperature ( $\theta_s = \theta_l = \theta_m$ ) and the following Stefan condition should be satisfied on the phase front as

$$k_s \nabla \theta_s \cdot \vec{n}_s + k_l \nabla \theta_l \cdot \vec{n}_l - \rho L \vec{v}_p \cdot \vec{n}_l = 0 \quad (2.12)$$

where  $k_s$ ,  $\theta_s$ , and  $\vec{n}_s$  are the solid thermal conductivity, solidus temperature, and the unit outward normal vector on the solid domain nearby the phase front, respectively. Similarly,  $k_l$ ,  $\theta_l$  and  $\vec{n}_l$  are the same fields for the liquid domain. In Eq. (2.12),  $\vec{v}_p$  is the phase front velocity. The liquid phase fraction for the isothermal phase-change case can



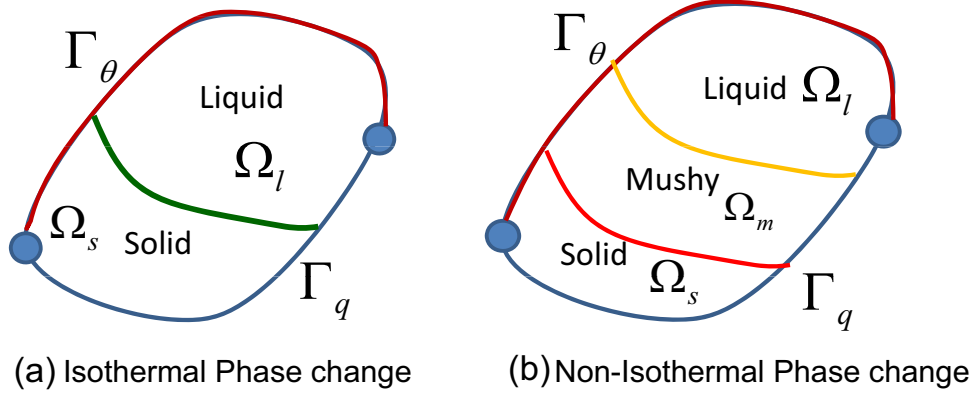


Figure 2.1: Domain of the heat conductor

be represented as

$$f_{pc}(\theta) = \begin{cases} 1, & \theta > \theta_m & \text{on } \Omega_l \\ 0, & \theta \leq \theta_m & \text{on } \Omega_s \end{cases} \quad (2.13)$$

Eq. (2.13) indicates the Heaviside step function  $H(\theta - \theta_m)$  which is schematically represented in Fig. 2.2(a).

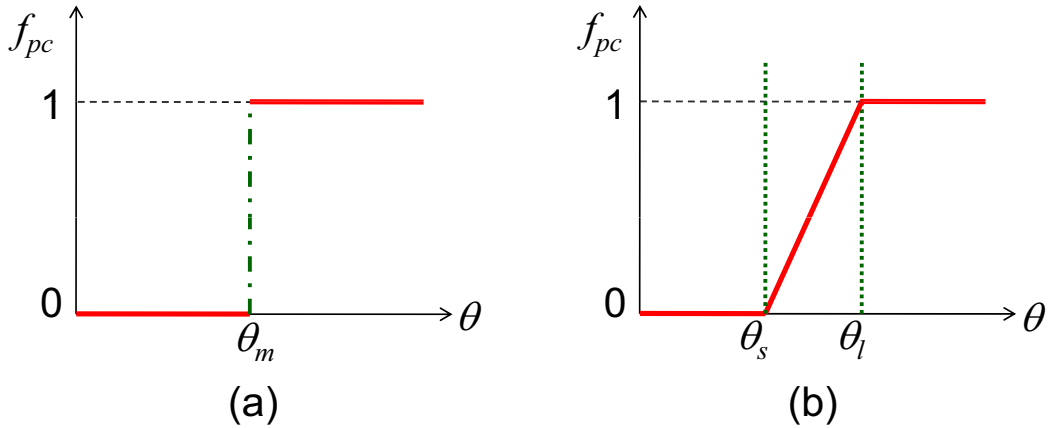


Figure 2.2: Phase-change function for: (a) isothermal case and (b) non-isothermal case

In non-isothermal phase-changes, there exists a *mushy zone* on which the phase fraction varies from zero to one, separating the liquid and solid domain as shown in Fig. 2.1(b). As usual,  $\Omega = \Omega_l \cup \Omega_m \cup \Omega_s$ . The phase fraction for the non-isothermal case can be stated as

$$f_{pc}(\theta) = \begin{cases} 1, & \theta > \theta_l & \text{on } \Omega_l \\ 0 < g(\theta) \leq 1, & \theta_s < \theta \leq \theta_l & \text{on } \Omega_m \\ 0, & \theta \leq \theta_s & \text{on } \Omega_s \end{cases} \quad (2.14)$$

where  $g(\theta)$  is the phase-change function which can be derived from the phase change kinetics. There are lot of choices for the selection of this function. A simple approximation

for this function is a linear one (Fig. 2.2(b)), given as

$$g(\theta) = \frac{\theta - \theta_s}{\theta_l - \theta_s}, \quad \theta_s < \theta \leq \theta_l \quad (2.15)$$

where  $\theta_s$  is the solidus temperature and  $\theta_l$  is the liquidus temperature.

For the isothermal case, Eq. (2.11) shows that the specific internal energy presents a discontinuity across the moving interface. This fact makes the problem highly non-linear. For the non-isothermal case, it can be observed that the latent heat effect appears only in the domain of mushy zone ( $\Omega_m$ ). In the solid and liquid regions, the classical definition of the specific heat capacity, i.e.  $C_p = \frac{\partial u}{\partial \theta}$  is recovered because the temperature derivative  $f_{pc}$  is zero in those regions for both cases.

After simplification and substitution of Eq. (2.11), and Eq. (2.7) in Eq. (2.1), the final form becomes

$$\nabla \cdot (k \nabla \theta) + \rho r_q = \rho \left( C_p + L \frac{\partial f_{pc}}{\partial \theta} \right) \dot{\theta} \quad (2.16)$$

Eq. (2.16) is the final form of the Governing Differential Equation (GDE) for the phase-change problem using the effective heat capacitance method [24]. The GDE with initial and boundary conditions of the solidification problem can be summarized as

GDE:	$\nabla \cdot (k \nabla \theta) + \rho r_q = \rho \left( C_p + L \frac{\partial f_{pc}}{\partial \theta} \right) \dot{\theta}$	in $\tilde{\Omega} \times \Upsilon$
EBC:	$\theta = \bar{\theta}$	in $\Gamma_\theta \times \Upsilon$
NBC:	$\vec{q} \cdot \vec{n} = -q_{conv} - \bar{q}$	in $\Gamma_q \times \Upsilon$
IC:	$\theta(\vec{X}, t) _{t=0} = \theta_0(\vec{X})$	in $\Omega$

## 2.2 Solution Methodology

In general, the closed form solutions for the non-linear problems is highly difficult and almost impossible. Therefore, one has to choose an efficient numerical solution procedure which can handle the non-linearity issues in an easy manner. The well established numerical techniques are the finite volume method, finite element method, boundary element method, meshless methods, etc. The Finite Element Method (FEM) is employed for the numerical solution of the GDE because of its robustness. From the GDE, the weak form is derived using the variational principles. The weak form of GDE is discretized by large number of elements where the field variable is represented in terms of nodal values using an appropriate shape functions. The element matrices and vectors are assembled according to the nodal connectivities to get the global matrices and vectors.

### 2.2.1 Weak form

For an arbitrarily chosen temperature distribution  $\tilde{\theta}$ , the thermal equilibrium condition in Eq. (2.16) has to satisfy the following integral based on the virtual temperature principle as

$$\int_{\Omega} \left[ \nabla \cdot (k \nabla \theta) + \rho r_q - \rho \left( C_p + L \frac{\partial f_{pc}}{\partial \theta} \right) \dot{\theta} \right] \tilde{\theta} d\Omega = 0 \quad (2.17)$$

By using the property of the divergence operator,

$$\nabla \cdot (\tilde{\theta} k \nabla \theta) = (k \nabla \theta) \cdot \nabla \tilde{\theta} + \nabla \cdot (k \nabla \theta) \tilde{\theta} \quad (2.18)$$

Therefore, Eq. (2.17) can be written as

$$\int_{\Omega} \left[ \nabla \cdot (\tilde{\theta} k \nabla \theta) - (k \nabla \theta) \cdot \nabla \tilde{\theta} + \rho r_q \tilde{\theta} - \rho C_p \dot{\theta} \tilde{\theta} - \rho L \frac{\partial f_{pc}}{\partial \theta} \dot{\theta} \tilde{\theta} \right] d\Omega = 0 \quad (2.19)$$

Unlike the EBC, the NBC has to be incorporated in the formulation itself. The EBC are applied at the end before solving the global algebraic equations. Applying the Gauss divergence theorem on the natural thermal boundary condition Eq. (2.3), the first term in Eq. (2.19) becomes,

$$\int_{\Omega} \left[ \nabla \cdot (\tilde{\theta} k \nabla \theta) \right] d\Omega = \int_{\Gamma_q} \left[ \vec{n} \cdot (\tilde{\theta} k \nabla \theta) \right] d\Gamma_q = \int_{\Gamma_q} [q_{conv} + \bar{q}] \tilde{\theta} d\Gamma_q \quad (2.20)$$

substituting Eq. (2.20) in Eq. (2.19) and becomes

$$\begin{aligned} \int_{\Omega} \left[ (k \nabla \theta) \cdot \nabla \tilde{\theta} \right] d\Omega + \int_{\Omega} \rho C_p \dot{\theta} \tilde{\theta} d\Omega + \int_{\Omega} \rho L \frac{\partial f_{pc}}{\partial \theta} \dot{\theta} \tilde{\theta} d\Omega = \dots \\ \int_{\Gamma_q} [q_{conv} + \bar{q}] \tilde{\theta} d\Gamma_q + \int_{\Omega} \rho r_q \tilde{\theta} d\Omega \end{aligned} \quad (2.21)$$

where it should be noted that in the isothermal phase-change case, the temperature derivative of  $f_{pc}$  is equal to Dirac delta  $\delta(\theta - \theta_m)$  function. For the sake of computational simplicity,  $\frac{\partial f_{pc}}{\partial \theta} \dot{\theta}$  is replaced by  $\frac{\partial f_{pc}}{\partial t}$ . After the substitution of Newton's law of cooling, the final weak form of GDE becomes,

$$\begin{aligned} \int_{\Omega} \left[ \nabla \tilde{\theta} \cdot (k \nabla \theta) \right] d\Omega + \int_{\Omega} \rho C_p \tilde{\theta} \dot{\theta} d\Omega + \int_{\Omega} \rho L \frac{\partial f_{pc}}{\partial t} \tilde{\theta} d\Omega + \dots \\ \int_{\Gamma_q} h \tilde{\theta} \theta d\Gamma_q = \int_{\Gamma_q} h \theta_{\infty} \tilde{\theta} d\Gamma_q + \int_{\Gamma_q} \bar{q} \tilde{\theta} d\Gamma_q + \int_{\Omega} \rho r_q \tilde{\theta} d\Omega \end{aligned} \quad (2.22)$$

This weak form automatically cancels the Stefan condition Eq. (2.12) especially for the fixed domain methods. Eq. (2.22) has to be satisfied over the entire domain and sub-

domains like liquid, solid and mushy for an arbitrary temperature distribution  $\tilde{\theta}$ .

## 2.2.2 Finite Element Technique

The entire domain can be decomposed into an assemblage of finite elements. Over each element, the temperature field is interpolated from the nodal temperatures. Using a standard FEM as in [108], the nodal temperature and the gradient of temperature for a typical element can be given as

$$\begin{aligned}\theta^e &= \mathbf{N}^T \Theta^e = \Theta^{eT} \mathbf{N} \\ \nabla \theta^e &= \mathbf{B}^T \Theta^e = \Theta^{eT} \mathbf{B}\end{aligned}\quad (2.23)$$

where the subscript  $e$  denotes the  $e^{th}$  element and  $\Theta^e$  is the vector of all nodal point temperatures of the  $e^{th}$  element with  $n$ -nodes.  $\mathbf{N}$  and  $\mathbf{B}$  are functions of local co-ordinates and known as the shape function vector and gradient operator, respectively. Therefore, the weak form of a single element becomes

$$\begin{aligned}& \int_{\Omega_e} \left[ \tilde{\Theta}^{eT} \mathbf{B} k \mathbf{B}^T \Theta^e \right] d\Omega_e + \int_{\Omega_e} \left[ \tilde{\Theta}^{eT} \rho C_p \mathbf{N} \mathbf{N}^T \dot{\Theta}^e \right] d\Omega_e + \dots \\ & \int_{\Omega_e} \left[ \tilde{\Theta}^{eT} \rho L \frac{\partial f_{pc}}{\partial t} \mathbf{N} \right] d\Omega_e + \int_{\Gamma_{qe}} \left[ \tilde{\Theta}^{eT} h \mathbf{N} \mathbf{N}^T \Theta^e \right] d\Gamma_{qe} = \dots \quad (2.24) \\ & \int_{\Gamma_{qe}} \left[ \tilde{\Theta}^{eT} h \theta_\infty \mathbf{N} \right] d\Gamma_{qe} + \int_{\Gamma_{qe}} \left[ \tilde{\Theta}^{eT} \bar{q} \mathbf{N} \right] d\Gamma_{qe} + \int_{\Omega_e} \left[ \tilde{\Theta}^{eT} \rho r_q \mathbf{N} \right] d\Omega_e\end{aligned}$$

After arranging the terms, the total potential to be minimized can be written as

$$\Phi^e \left( \tilde{\Theta}^e \right) = \tilde{\Theta}^{eT} \mathbf{F}^e - \tilde{\Theta}^{eT} \mathbf{K}^e \Theta^e - \tilde{\Theta}^{eT} \mathbf{C}^e \dot{\Theta}^e - \tilde{\Theta}^{eT} \mathbf{L}^e \quad (2.25)$$

where the element matrices and vectors are

$$\begin{aligned}\mathbf{K}^e &= \int_{\Omega_e} \mathbf{B} k \mathbf{B}^T d\Omega_e + \int_{\Gamma_q^e} h \mathbf{N} \mathbf{N}^T d\Gamma_q^e \\ \mathbf{C}^e &= \int_{\Omega_e} \rho C_p \mathbf{N} \mathbf{N}^T d\Omega_e \\ \mathbf{L}^e &= \int_{\Omega_e} \mathbf{N} \rho L f_{pc} d\Omega_e \quad (2.26) \\ \mathbf{F}^e &= \int_{\Omega_e} \mathbf{N} \rho r_q d\Omega_e + \int_{\Gamma_q^e} \mathbf{N} h \theta_\infty d\Gamma_q^e + \int_{\Gamma_q^e} \mathbf{N} \bar{q} d\Gamma_q^e\end{aligned}$$

From the element quantities, the global matrices and vectors can be obtained based

on the element-nodal mappings. Therefore, the total global potential can be written as

$$\Phi(\tilde{\Theta}) = \tilde{\Theta}^T \mathbf{F} - \tilde{\Theta}^T \mathbf{K} \Theta - \tilde{\Theta}^T \mathbf{C} \dot{\Theta} - \tilde{\Theta}^T \dot{\mathbf{L}} \quad (2.27)$$

where  $\mathbf{K}$  is the global thermal conductance matrix,  $\mathbf{C}$  is the global capacitance matrix,  $\mathbf{L}$  is the global latent heat vector,  $\mathbf{F}$  is the global force vector, and  $\Theta$  is the global nodal temperature vector. From the total potential, the residual vector ( $\mathbf{R}$ ) can be obtained as

$$\mathbf{R} = \frac{\partial \Phi}{\partial \tilde{\Theta}} = \mathbf{F} - \mathbf{K} \Theta - \mathbf{C} \dot{\Theta} - \dot{\mathbf{L}} \quad (2.28)$$

At a finite time, there exist a unique temperature profile for which the residual vector becomes zero and it becomes

$$\boxed{\mathbf{K} \Theta + \mathbf{C} \dot{\Theta} + \dot{\mathbf{L}} = \mathbf{F}}$$

Due to the presence of time derivatives, a proper time integration is required to solve this equation. Before solving this equation, EBC has to be imposed which can be implemented by eliminating corresponding rows and columns.

### 2.2.3 Iterative incremental scheme

The rate equation can be integrated using an Euler backward method for obtaining the unconditionally stable numerical scheme. Assume  $\Theta^n$  is the known temperature vector at time  $t_n$  which is the previous time step. Similarly,  $\Theta^{n+1}$  is the current time step ( $t_{n+1} = t_n + \Delta t$ ) temperature vector and  $\Delta t$  is the time interval. The time derivative of temperature and latent heat vector can be approximated as

$$\dot{\Theta}^{n+1} = \frac{\Theta^{n+1} - \Theta^n}{\Delta t} \quad \text{and} \quad \dot{\mathbf{L}}^{n+1} = \frac{\mathbf{L}^{n+1} - \mathbf{L}^n}{\Delta t} \quad (2.29)$$

The residual vector at the current time step can be written as

$$\mathbf{R}(\Theta^{n+1}) = \mathbf{F} \Delta t + \mathbf{C} \Theta^n - (\mathbf{L}^{n+1} - \mathbf{L}^n) - (\mathbf{C} + \mathbf{K} \Delta t) \Theta^{n+1} \quad (2.30)$$

This equation is implicit and highly non-linear in nature. Therefore, an iterative scheme is required to solve this system of equations. To recover the quadratic convergence, Newton-Raphson method is adopted. The temperature at the  $(i+1)^{\text{th}}$  iteration can be written as

$$\Theta_{i+1}^{n+1} = \Theta_i^{n+1} + \delta \Theta \quad (2.31)$$

where  $\Theta_i^{n+1}$  is the previous iteration temperature and  $\delta\Theta$  is the current iterative-increment temperature. Therefore, Eq. (2.30) can be modified as

$$\mathbf{R}(\Theta_i^{n+1}) = \mathbf{F} \Delta t + \mathbf{C} \Theta^n - (\mathbf{L}_i^{n+1} - \mathbf{L}^n) - (\mathbf{C} + \mathbf{K} \Delta t) \Theta_i^{n+1} \quad (2.32)$$

Using a Taylor series expansion of the residual vector without higher order terms,

$$\begin{aligned} \mathbf{R}_{i+1}^{n+1} &= \mathbf{R}_i^{n+1} + \frac{\partial \mathbf{R}_i^{n+1}}{\partial \Theta_i^{n+1}} d\Theta + \dots \\ &\cong \mathbf{R}_i^{n+1} + \mathbf{J}(\Theta_i^{n+1}) \delta\Theta + \dots \end{aligned} \quad (2.33)$$

Therefore, the Jacobian matrix can be derived as

$$\mathbf{J}(\Theta_i^{n+1}) = \left. \frac{\partial \mathbf{R}}{\partial \Theta} \right|_i^{n+1} = -\mathbf{K} \Delta t - \mathbf{C} - \left. \frac{\partial \mathbf{L}}{\partial \Theta} \right|_i^{n+1} \quad (2.34)$$

where the derivative of the latent heat vector with respect to the temperature is denoted as *phase-change matrix*  $\mathbf{C}_{pc}$  as in [24]. The elemental form of the phase-change matrix is given as in [24]

$$\mathbf{C}_{pc}^e = \frac{\partial \mathbf{L}}{\partial \Theta} = \int_{\Omega^e} \mathbf{N} \rho L \frac{\partial f_{pc}}{\partial \theta} \mathbf{N}^T d\Omega^e \quad (2.35)$$

For the isothermal phase-change case, the temperature derivative of the phase fraction

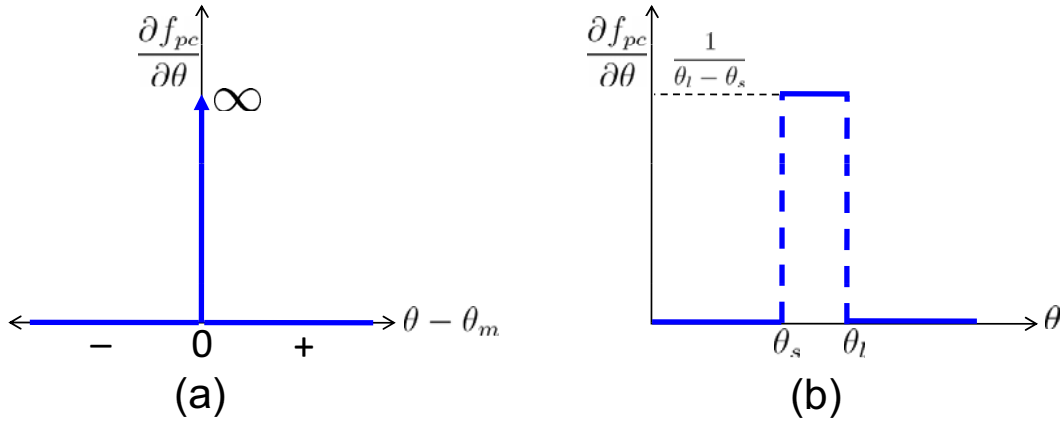


Figure 2.3: Derivative of phase-change function with respect to temperature: (a) isothermal case and (b) non-isothermal case (linear phase-change function)

function  $f_{pc}$  becomes the Dirac delta function  $\delta(\theta - \theta_m)$  as shown in Fig. 2.3(a). The infinite slope at the phase-change temperature increases the computational difficulty of isothermal case. In contrast to isothermal, a finite slope is obtained for the non-isothermal phase-change as shown in Fig. 2.3(b). To recover the numerical stability, the derivative of the phase fraction with respect to temperature at every iteration is calculated as in

[24]

$$\left. \frac{\partial f_{pc}}{\partial \theta} \right|_i^{n+1} = \frac{f_{pc_i}^{n+1} - f_{pc}^n}{\theta_i^{n+1} - \theta^n} \quad \text{and} \quad \left. \frac{\partial f_{pc}}{\partial \theta} \right|_1^{n+1} = 0 \quad (2.36)$$

The error in the evaluation of  $\frac{\partial f_{pc}}{\partial \theta}$ , forces the Jacobian matrix becomes an approximate one. This can be compensated by the exact evaluation of the residual vector R. Finally, the incremental temperature vector can be calculated from the Jacobian Eq. (2.34), by forcing the residual vector Eq. (2.33) to reach zero as

$$\delta \Theta = - [\mathbf{J}(\Theta_i^{n+1})]^{-1} \mathbf{R}(\Theta_i^{n+1}) \quad (2.37)$$

The convergence criterion at the current iteration is evaluated using the current temperature vector, the residual vector, and the conductance matrix as stated in [24]

$$\left. \frac{\mathbf{R}^T \mathbf{R}}{(\mathbf{K}\Theta)^T (\mathbf{K}\Theta)} \right|_{i+1}^{n+1} < \epsilon \quad (2.38)$$

where  $\epsilon$  is the computational zero and taken as  $10^{-3}$ . The above mentioned iterative-increment scheme can be summarized as:

1. Set  $\Theta_1^{n+1} = \Theta^n$ ,  $L_1^{n+1} = L^n$ ,  $i = 1$ .
2. Compute  $\mathbf{K}_i^{n+1}$ ,  $\mathbf{C}_i^{n+1}$ ,  $\mathbf{C}_{pc_i}^{e\ n+1}$ ,  $L_i^{n+1}$  and  $F_i^{n+1}$
3. Assign:  $\mathbf{M}_i^{n+1} = \mathbf{K}_i^{n+1} \Delta t + \mathbf{C}_i^{n+1}$
4.  $\mathbf{R}_i^{n+1} = F_i^{n+1} \Delta t + \mathbf{C}_i^{n+1} \Theta^n + L^n - L_i^{n+1} - \mathbf{M}_i^{n+1} \Theta_i^{n+1}$
5.  $\mathbf{J}_i^{n+1} = \mathbf{M}_i^{n+1} + \mathbf{C}_{pc_i}^{e\ n+1}$
6. Find  $\delta \Theta = (\mathbf{J}_i^{n+1})^{-1} \mathbf{R}_i^{n+1}$
7. Update  $\Theta_{i+1}^{n+1} = \Theta_i^{n+1} + \delta \Theta$ ,  $i = i + 1$
8. Check convergence criteria using Eq. (2.38).
9. If step.8 is true goto step.1 else goto step.2.

## 2.3 Computational difficulty

Non-isothermal phase-change problems are relatively simpler than the isothermal phase-change problems. The major reason for the simplicity is due to the continuity of  $f_{pc}$  and  $\frac{\partial f_{pc}}{\partial \theta}$  with respect to the temperature. Therefore, the latent heat vector and matrix can be easily evaluated for the non-isothermal phase-change problems without much difficulties (even for a linear phase-change function). When the phase-change interval decreases, the computational difficulties increase. If the interval reaches zero, the problem becomes isothermal phase-change and the temperature-based methods fail to converge to the solution due to the local exchange of field variable from temperature to enthalpy [34].

This fact can be clearly understood through the following example.

Let us consider a one-dimensional isothermal solidification with equal solid-liquid material properties ( $\rho_s = \rho_l = \rho$ ,  $C_{ps} = C_{pl} = C_p$ ,  $k_s = k_l = k$ ), the GDE Eq. (2.16) can be reduced as

$$k \frac{\partial^2 \theta}{\partial x^2} = \rho C_p \frac{\partial \theta}{\partial t} + \rho L \frac{\partial f_{pc}}{\partial t} = \rho \frac{\partial h(\theta)}{\partial t} \quad (2.39)$$

where  $h(\theta)$  is the enthalpy of the solidifying body which can be defined as a function

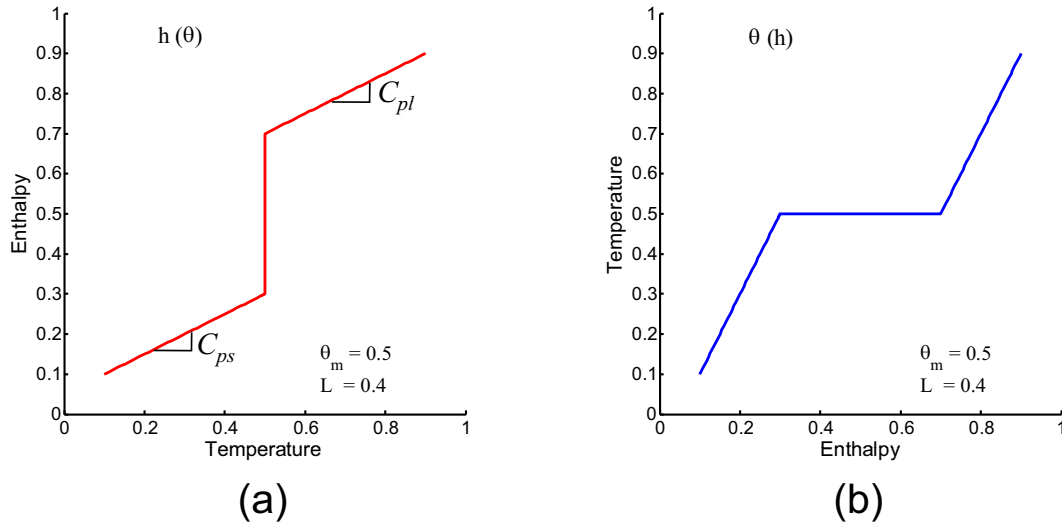


Figure 2.4: Isothermal phase-change (Knoll *et al.*, 1999) (a) Enthalpy as a function of temperature and (b) Temperature as a function of enthalpy

of temperature as  $h = C_p \theta + f_{pc} L$ . Eq. (2.39) is known as the temperature form of the energy equation. The main difficulty with this temperature form is evident in Fig. 2.4(a), where a pure-material enthalpy-temperature relation is depicted. It is clear that there exists a range of possible values for  $h$  at  $\theta_m$ , i.e., there is not a unique  $h(\theta_m)$ . The temperature version of the energy equation at the front is therefore ill-posed because  $h(\theta_m)$  is not single-valued. At the front,  $\theta$  is constant and  $f_{pc}$  is a function of enthalpy through the relationship  $h - C_p \theta_m = f_{pc} L$ . This non-uniqueness is avoided in standard implicit methods by fixing the temperature  $\theta$  at  $\theta_m$ , whereby the energy equation is solved for  $f_{pc}$  with the time derivative of temperature set to zero. This is equivalent to solve the energy equation for  $h$  at the front. Substituting  $h - C_p \theta_m = f_{pc} L$  in Eq. (2.39) making  $\frac{\partial \theta}{\partial t} = 0$ , the energy equation at the front becomes [34],

$$k \frac{\partial^2 \theta}{\partial x^2} = \rho \frac{\partial h}{\partial t} \quad (2.40)$$

This represents a local exchange in dependent variables at the front from  $\theta$  to  $h$ , and requires one to fix the front position over a nonlinear iteration within a time step [34].



This artificial *fixing* of the front position may restrict the time step size for the nonlinear convergence and accuracy. In employing enthalpy as the dependent variable on the entire grid, we need to evaluate  $\theta$  as a function of  $h$ , which is depicted in Fig. 2.4(b) for a pure material. Here we can clearly see that temperature is a unique, single-valued function of enthalpy form. Due to this fact, the isothermal phase-change problems are formulated in the enthalpy. But most of the commercial FE codes are based on the temperature-based formulation. Therefore, we need to develop a proper numerical algorithm which can handle the isothermal phase-change problem without much difficulty.

In this work, the temperature is chosen as a dependent variable and during the isothermal phase-change, the above-mentioned difficulty is handled by means of approximating the Heaviside and Dirac delta functions.  $f_{pc}$  (Heaviside function as shown in Fig. 2.2(a)) and  $\frac{\partial f_{pc}}{\partial \theta}$  (Dirac delta function) are approximated for the isothermal phase-change by

$$f_{pc} = \lim_{a \rightarrow 0} \frac{1}{\pi} \tan^{-1} \left( \frac{\theta - \theta_m}{a} \right) + \frac{1}{2} \quad (2.41)$$

$$\frac{\partial f_{pc}}{\partial \theta} = \lim_{a \rightarrow 0} \frac{a}{\pi} \frac{1}{a^2 + (\theta - \theta_m)^2} \quad (2.42)$$

where  $a$  is the numerical zero. For two different values of  $a$ , the Heaviside and the Dirac delta functions are plotted in Fig. 2.5. The physical meaning of this type of approximation is simply to introduce an artificial phase-change interval, which is a reasonable assumption if we choose a very small value of  $a$  in Eq. (2.41) and Eq. (2.42).

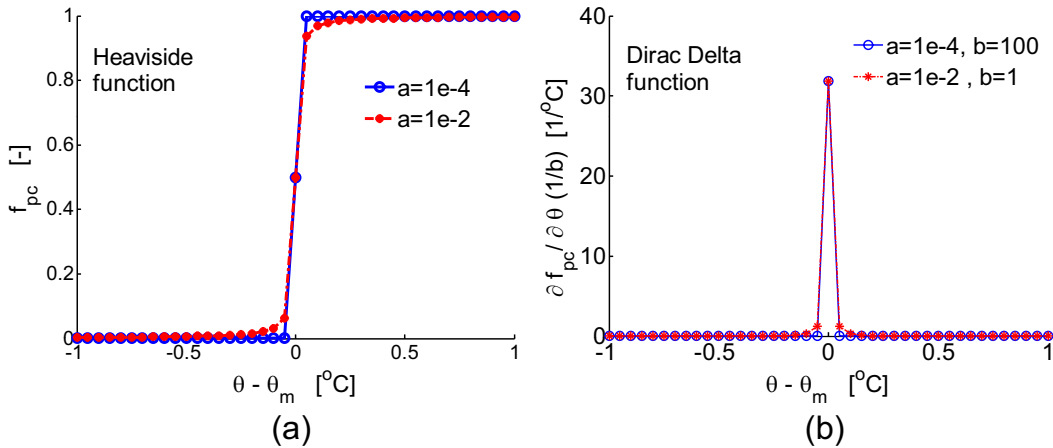


Figure 2.5: Liquid phase fraction function for an isothermal phase change: (a) Heaviside function and (b) Dirac delta function

Further, the non-convergence in Newton's iteration occurs for the phase-change problems with lower Stefan number. The Stefan number ( $St$ ) is defined as the ratio of specific heat to the latent heat. Irrespective of the formulation, for the lower Stefan number problems the Newton's method produces divergence. This issue is addressed in the next

section.

## 2.4 Line-Search Algorithm

One more computational difficulty in the phase-change problem is mentioned as follows: If  $\theta^{n+1}$  is not in the neighborhood of  $\theta^n$ , the classical Newton iterative method fails to converge. Therefore, a line-search algorithm is introduced to recover the quadratic convergence of Newton iterations. The FEM attempts to minimize the total potential  $\Phi$  which is defined as

$$\Phi(\Theta) = \Theta^T \mathbf{F} - \Theta^T \mathbf{K} \Theta - \Theta^T \mathbf{C} \dot{\Theta} - \Theta^T \dot{\mathbf{L}} \quad (2.43)$$

From the total potential  $\Phi$ , as explained in Section 2.2.3, the residual vector  $\mathbf{R}$ , the Jacobian matrix  $\mathbf{J}$ , and the iterative-increment temperature vector  $\Delta\Theta$  can be written as

$$\mathbf{R} = \frac{\partial\Phi}{\partial\Theta} \quad ; \quad \mathbf{J} = \frac{\partial^2\Phi}{\partial\Theta^2} \quad \text{and} \quad \delta\Theta = -\mathbf{J}^{-1}\mathbf{R}$$

Instead of updating the temperature vector as given in Eq. (2.31), the modified temperature update in every iteration can be given by

$$\Theta_{i+1}^{n+1} = \Theta_i^{n+1} + \eta \delta\Theta \quad (2.44)$$

where  $\eta$  is the scalar multiplier which is generally known as *step length*. When the  $\eta$  reaches unity, the classical Newton method is recovered. We use the Taylor expansion about the solution at  $\eta$  as in [26]

$$\begin{aligned} \Phi(\eta + \delta\eta)|_{i+1}^{n+1} &= \Phi(\eta)|_{i+1}^{n+1} + \frac{\partial\Phi}{\partial\Theta} \frac{\partial\Theta}{\partial\eta} \delta\eta + \dots \\ &= \Phi|_{i+1}^{n+1} + \delta\Theta^T \mathbf{R}(\eta) \delta\eta + \dots \end{aligned} \quad (2.45)$$

To reach a stationary value at  $\eta$ , we need

$$s(\eta) = \delta\Theta^T \mathbf{R}(\eta)|_{i+1}^{n+1} = 0 \quad (2.46)$$

The physical meaning of Eq. (2.46) is that the search direction ( $\Delta\Theta$ ) and the residual vector are orthogonal to each other as in [25]. One has to find the step-size  $\eta$  which minimizes  $s(\eta)$  within the iteration loop. Assuming  $i + 1$  as the current iteration,  $m$  is the line-search index,  $\delta\Theta = \delta\Theta_{i+1}^{n+1}$  is the fixed search direction with in the current

iteration, the following quantities can be computed as in [25]

$$\begin{aligned}
 m \leftarrow 1, \quad \eta_1 \leftarrow 0, \quad r_1 &= \frac{s_1}{s_1} = 1, \quad s_1 = \delta\Theta^T R(\Theta_i^{n+1}) \\
 m \leftarrow 2, \quad \eta_2 \leftarrow 1, \quad r_2 &= \frac{s_2}{s_1}, \quad s_2 = \delta\Theta^T R(\Theta_i^{n+1} + \delta\Theta)
 \end{aligned}$$

It is assumed that  $r_2$  is always less than  $r_1$ . The approximate value of  $\eta$  can be calculated using linear interpolation and extrapolation until the convergence criterion of  $r < 0.8$  gets satisfied. Due to the severe non-linear nature of the  $s$ , a highly efficient algorithm is required to avoid dangerous extrapolations as mentioned in Crisfield [26]. The different types of interpolation and extrapolation operations which arises during the line-search are schematically shown in Fig. 2.6. Fig. 2.7 represents the Crisfield's line-search algorithm. The line search parameters are set as follows:  $\eta_{\max a} = 20$ ,  $\eta_{\min a} = 0$ ,  $\text{amp} = 10$ , and  $\text{ct} = 0$ . The algorithm is as follows

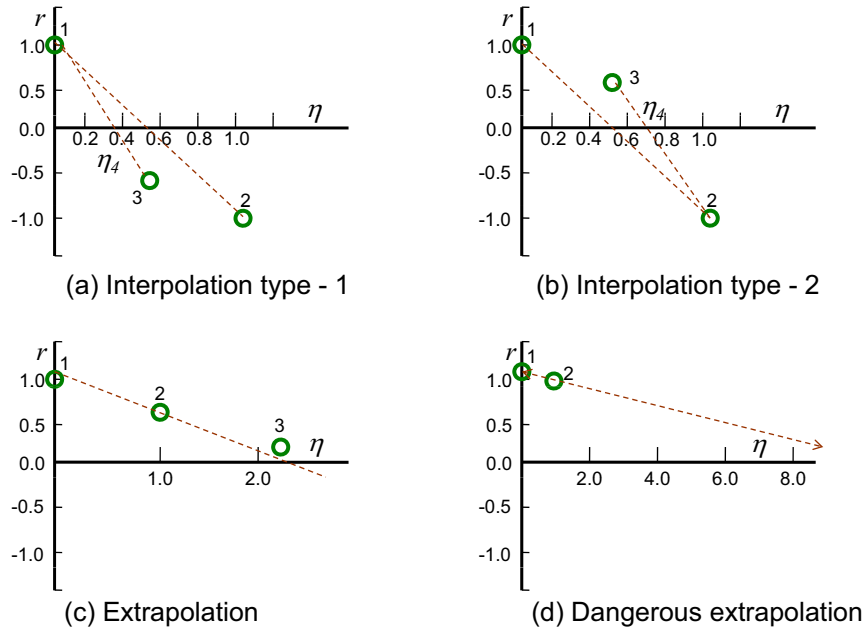


Figure 2.6: Possible choices of interpolation and extrapolation during line-search (Crisfield, 1991)

- **Step-1:** If  $\text{ct} > 2$ , end the line-search loop, else go to **Step-2**.
- **Step-2:** Using linear interpolations / extrapolations, find a minimum  $\eta$ ,  $\eta_-$  for which  $r$  should be negative. If negative  $r_-$  exists for  $\eta_-$ , goto **Step-3** else goto **Step-4**.
- **Step-3:** Find a largest  $\eta$ ,  $\eta_+$  for which  $r$  is positive ( $r_+$ ) and also  $\eta_+$  should be less than the previous positive  $r$ ,  $r_+$ . Perform interpolation between  $\eta_+$  and  $\eta_-$  and

named as  $\eta_a$ . Calculate  $\eta_b = \eta_+ + 0.2(\eta_- - \eta_+)$ . Set  $\eta_{m+1} = \max(\eta_a, \eta_b)$ ,  $ct = ct+1$ ,  $m = m + 1$ . Goto Step-1.

- Step-4: Find a maximum previous  $\eta$  and named as  $\eta_{\max}$ . Extrapolate between  $\eta_m$  and  $\eta_{m-1}$  and store in  $\eta_{m+1}$ . If  $\eta_{m+1} < 0$  or  $\eta_{m+1} > \text{amp} \times \eta_{\max}$ , change  $\eta_{m+1}$  as  $\text{amp} \times \eta_{\max}$ . Set  $ct = ct+1$ ,  $m = m+1$ . Goto Step-1.

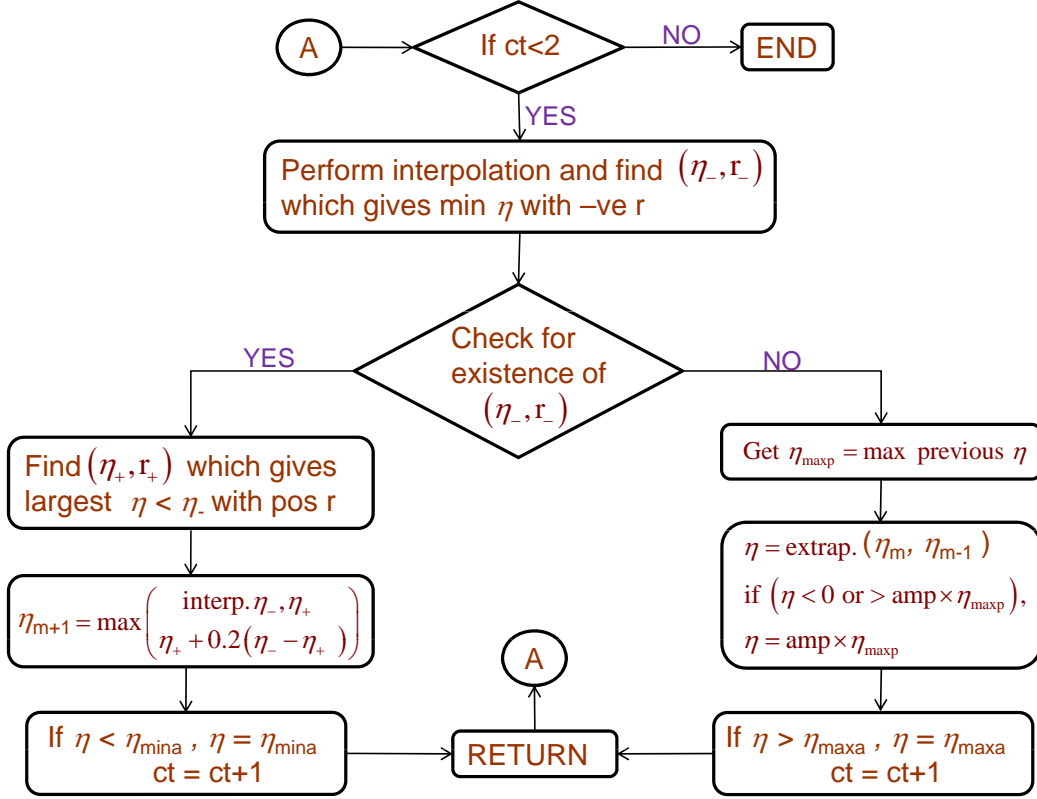


Figure 2.7: Line-search Algorithm (Crisfield, 1991)

The computational cost of performing a line-search in every Newton iteration is very high. Therefore, one has to check whether the line-search is required for the current iteration or not through checking the value of  $r$ . If the absolute value of  $r$  exceeds 0.8, performing a line-search significantly improves the Newton iteration. During the line-search, the element matrices have to be calculated more often, which increases the computational cost.

## 2.5 Element computations

When compared to 3-D analysis, 2-D analyses are simpler and the results can be interpreted easily. Therefore, a generalized 2-D element is developed which can handle the

following phase-change problems: (a) plane problems and (b) axisymmetric problems. Using an isoparametric element formulation, the global co-ordinates of the element and the temperature inside the element can be give as

$$\{x \ y\} = \mathbf{N}^T \{X \ Y\} \quad \text{and} \quad \theta^e = \mathbf{N}^T \Theta^e \quad (2.47)$$

where  $\mathbf{N}$  is the shape function vector,  $\{X \ Y\}$  is the element nodal co-ordinates matrix in which  $X$  and  $Y$  are nodal  $x$  and  $y$  co-ordinates vector,  $\Theta^e$  is the element nodal temperature vector. The shape function vector for a 4-noded quadrilateral element as

$$\mathbf{N} = \frac{1}{4} \begin{Bmatrix} (1+\xi)(1+\eta) \\ (1-\xi)(1+\eta) \\ (1-\xi)(1-\eta) \\ (1+\xi)(1-\eta) \end{Bmatrix} \quad (2.48)$$

where  $\xi$  and  $\eta$  are the local co-ordinates as shown in Fig. 2.8. Using the chain rule of

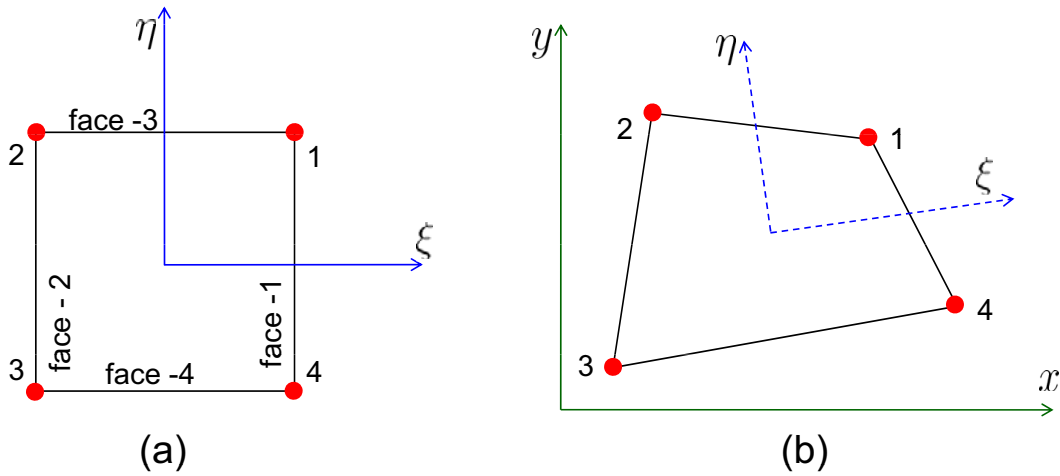


Figure 2.8: 4-noded quadrilateral element: (a) parent element and (b) typical element

differentiation,

$$\left\{ \frac{\partial}{\partial \xi} \quad \frac{\partial}{\partial \eta} \right\} = \left\{ \frac{\partial}{\partial x} \quad \frac{\partial}{\partial y} \right\} \begin{bmatrix} \frac{\partial x}{\partial \xi} & \frac{\partial x}{\partial \eta} \\ \frac{\partial y}{\partial \xi} & \frac{\partial y}{\partial \eta} \end{bmatrix} = \left\{ \frac{\partial}{\partial x} \quad \frac{\partial}{\partial y} \right\} \tilde{\mathbf{J}} \quad (2.49)$$

where the Jacobian matrix  $\tilde{\mathbf{J}}$  is defined as

$$\tilde{\mathbf{J}} = \begin{bmatrix} \frac{\partial x}{\partial \xi} & \frac{\partial x}{\partial \eta} \\ \frac{\partial y}{\partial \xi} & \frac{\partial y}{\partial \eta} \end{bmatrix} = \left\{ \frac{\partial \mathbf{N}}{\partial \xi} \quad \frac{\partial \mathbf{N}}{\partial \eta} \right\}^T \{X \ Y\} \quad (2.50)$$

The temperature gradient can be represented as

$$\begin{aligned}\nabla\theta_e &= \left\{ \frac{\partial\theta_e}{\partial x} \quad \frac{\partial\theta_e}{\partial y} \right\} = \left\{ \frac{\partial}{\partial x} \quad \frac{\partial}{\partial y} \right\}^T \mathbf{N}^T \Theta^e \\ &= \tilde{\mathbf{J}}^{-T} \left\{ \frac{\partial N}{\partial \xi} \quad \frac{\partial N}{\partial \eta} \right\}^T \Theta^e \\ &= \mathbf{B}^T \Theta^e\end{aligned}\tag{2.51}$$

where  $\mathbf{B}$  is the derivative of shape function with respect to global co-ordinates and also known as gradient operator of size  $4 \times 2$

$$\mathbf{B} = \left\{ \frac{\partial N}{\partial \xi} \quad \frac{\partial N}{\partial \eta} \right\} \tilde{\mathbf{J}}^{-1}\tag{2.52}$$

In 2-D finite elements, the infinitesimal volume for the volume integrals is obtained by multiplying the area with the thickness in the perpendicular direction,

$$d\Omega_e = b \, dx \, dy = b \, |\tilde{\mathbf{J}}| \, d\xi \, d\eta\tag{2.53}$$

Similarly, the infinitesimal area for the surface integrals is

$$d\Gamma_e = \begin{cases} b \left( \sqrt{\tilde{\mathbf{J}}(1,2)^2 + \tilde{\mathbf{J}}(2,2)^2} \right) d\eta & \text{on faces 1 \& 2} \\ b \left( \sqrt{\tilde{\mathbf{J}}(1,1)^2 + \tilde{\mathbf{J}}(2,1)^2} \right) d\xi & \text{on faces 3 \& 4} \end{cases}\tag{2.54}$$

the scalar  $b$  in Eq. (2.53) and Eq. (2.54) can be defined as

$$b = \begin{cases} b \quad \textit{real thickness} & \text{if plane case} \\ x \quad \textit{radius} & \text{if axisymmetric (1 rad is considered)} \end{cases}.\tag{2.55}$$

The faces define the four boundaries of the element. According to the node numbering in Fig. 2.8, the left and right sides are called faces 1 and 2, and top and bottom sides are called faces 3 and 4, respectively.

## 2.6 Thermal interface

Generally, the solidifying substance known as casting is kept inside a mold. It is important to account the heat transport from the casting to the mold. During the time of contact, the heat transfer between the surfaces takes place through heat conduction. However, in the later stages, there is an air gap which exists between these two surfaces. Therefore, a jump or discontinuity in the temperature profile occurs due to the lower

thermal conductivity of air. The interfacial heat transfer can be simply idealized as a pure convection and the energy balance at the interface can be given as,

$$\vec{q}_c \cdot \vec{n}_c = \vec{q}_m \cdot \vec{n}_m = h_{\text{int}} (\theta_c - \theta_m) \quad (2.56)$$

where the subscripts  $c$  and  $m$  denotes the casting and mold, and  $h_{\text{int}}$  is the temperature or gap-dependent interfacial heat transfer coefficient (IHTC). In the finite element aspect, this equation can be easily incorporated as an additional conductance matrix. A typical 4-noded interfacial element is shown in Fig. 2.9. Therefore, the interfacial conductance

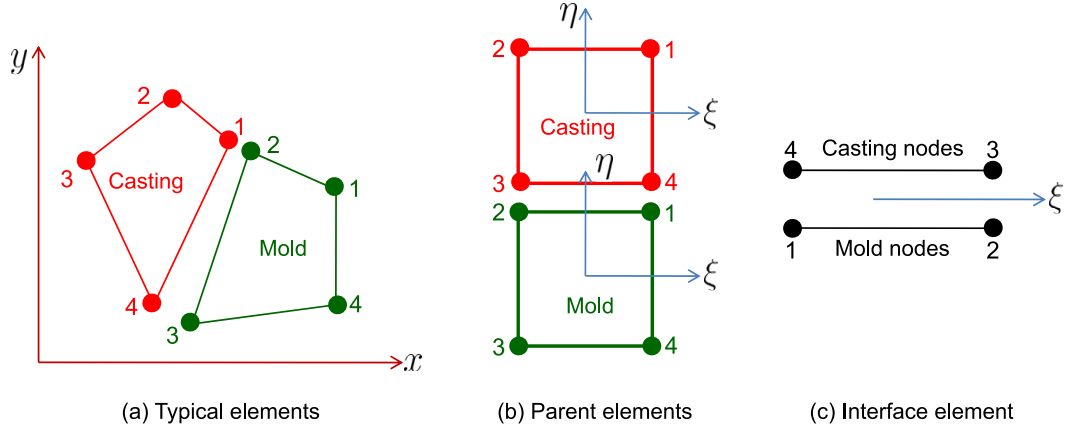


Figure 2.9: Thermal interface element

matrix is explicitly given as in [27],

$$\mathbf{K}_{\text{int}} = \frac{b h_{\text{int}} L_{\text{ele}}}{6} \begin{bmatrix} 2 & 1 & -2 & -1 \\ 1 & 2 & -1 & -2 \\ -2 & -1 & 2 & 1 \\ -1 & -2 & 1 & 2 \end{bmatrix} \quad (2.57)$$

where  $L_{\text{ele}}$  is the length of interfacial element, and  $b$  is defined in Eq. (2.55).

## 2.7 Numerical results

The developed temperature-based finite element technique is applied to two different isothermal solidification problems. Firstly, a one dimensional solidification of a semi infinite slab is analyzed for the validation, checking the accuracy and computational advantages of the numerical technique. Due to the low Stefan number, the line-search algorithm plays a crucial role in this problem. Secondly, an isothermal solidification of aluminum in a permanent steel mold is considered. The interface between the mold and

casting is modeled by the introduction of an additional conductance matrix along with the regular matrices.

Table 2.1: Material properties for 1-D isothermal phase-change problem

Density ( $\rho_s = \rho_l$ )	1	kg/m <sup>3</sup>
Thermal conductivity ( $k_s = k_l$ )	1.08	W/mK
Specific heat capacity ( $C_{ps} = C_{pl}$ )	1	J/kgK
Latent heat ( $L$ )	70.26	J/kg
Phase-change temperature ( $\theta_m$ )	-0.1	°C
Initial temperature ( $\theta_o$ )	0.0	°C

### 2.7.1 Isothermal solidification of 1-D bench-mark problem

A bench-mark isothermal phase-change problem of a 1-D semi-infinite slab with  $St = 0.625$  is considered [109, 24, 25]. As specified in [24, 25], 32 equally spaced 4-noded rectangular elements of 0.125 m width (Fig. 2.10) and time step  $\Delta t = 0.2$  s are used. The material properties are given in Table. 2.1. The dimensionless temperature of the problem is defined as in [25]

$$\theta^* = \frac{\theta_o - \theta_m}{\theta_m - \theta_w} = 2 \times 10^{-3} \quad (2.58)$$

The Stefan number governs the temperature gradient discontinuity, while the dimensionless temperature is related to the magnitude of this gradient next to the wall. The solution process performance uses to deteriorate when  $St$  or  $\theta^*$  decreases. The Stefan number is also a measure of the solid-liquid interface velocity. A smaller value of  $St$  indicates that the interface movement will be slower due to the large amount of latent heat [27]. The above-mentioned values lead to a critical circumstance wherein enthalpy models fail to converge. This problem is frequently analyzed in the literature for checking the efficiency of the computation technique.

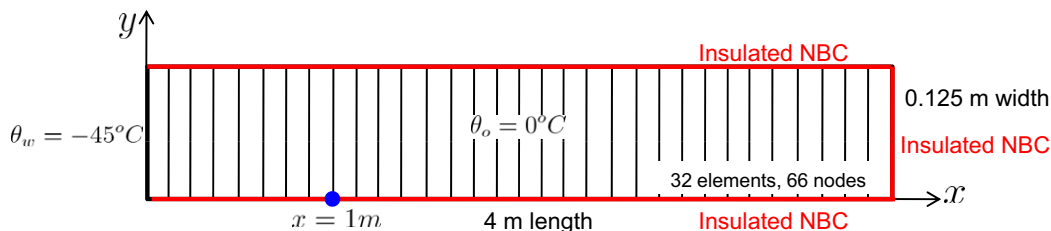


Figure 2.10: 1-D semi infinite slab: Domain with boundary conditions



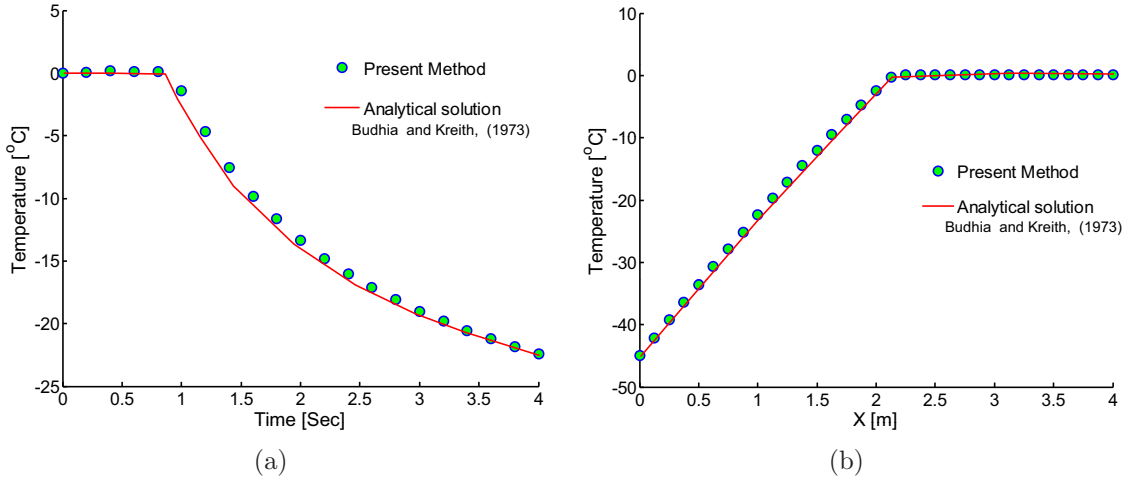


Figure 2.11: 1-D semi infinite slab: (a) temperature evolution at  $x = 1$  m and (b) temperature distribution at  $t = 4$  s

The temperature evolution at  $x = 1$  m is shown in Fig. 2.11(a). The temperature distribution at  $t = 4$  s, and the phase front evolution are shown in Fig. 2.11(b) and Fig. 2.12(a), respectively. Here, the line-search loop plays an important role. Without the line-search loop, the solution never converges how small the time step size might be. Fig. 2.12(b) shows the number of iterations, and the number of times the line search loop is executed in every time step for the same meshing and time step. It is observed that for every time step, an average of 8.1 iterations are carried out, and an average of 4 line-search loops out of 8.1 iterations for the convergence of the solution as shown in Fig. 2.12(b). Within the line search loop, the element matrices are computed at an average of 3–5 times. Therefore, the computational cost is high, but for this kind of isothermal solidification problems with a low Stefan number, it is unavoidable. Further, without the help of line search algorithm, it is almost impossible to use the temperature-based FE for the isothermal solidification problems with a low Stefan number.

## 2.7.2 Isothermal solidification of aluminum in a steel mold

A cylindrical casting of pure aluminum in a steel mold is analyzed. The dimensions of the mold and casting and its finite element mesh is shown in Fig. 2.13. Due to low  $St$ , an artificial phase-change interval of  $3^\circ\text{C}$  is introduced, and a relatively higher time-step interval (2.5 Sec) is used to obtain the solution. Nishida *et al.* [110] experimentally measured the interfacial HTC and air gap. Celentano *et al.* [24] solved the thermal part of the same problem and verified their results with a temperature-dependent interfacial HTC. Further, Celentano *et al.* [51] extended their model with a gap-dependent interfacial HTC. Therefore, a comparison between the experimental results, the present formulation,

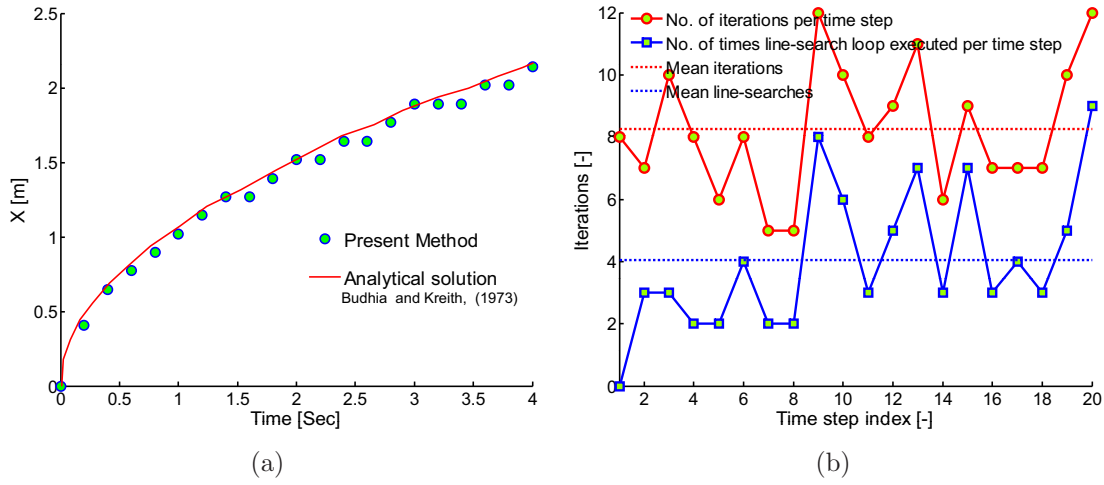


Figure 2.12: 1-D semi infinite slab: (a) interface evolution and (b) number of iterations and mean line search per iteration

and the results of Celentano *et al.* is made. The parameters used in this problem are given in Table. 2.2. The top of the casting and outer boundaries of mold are assumed to be perfectly insulated. An elastic-plastic material model with a frictionless contact model is used to solve the displacement field which is explained in Chapter 4. The bottom of the mold is fixed and the casting is free to move axially upward.

At the interface, coincident nodes are considered. The computational procedures to calculate the gap between the interface nodes are given in Chapter 4. The interface HTC is computed based on Eq. (1.2). The evolution of temperature at the four different locations (Fig. 2.13) taken in the middle cross-section is shown in Fig. 2.14(a). The release of latent heat at the center of the casting is clearly visible because the temperature at that location remains in isothermal phase-change temperature for a period of 15 s. During this period, the inner surface of the mold suddenly get heated upto 340°C. Due to high heat transfer at the surface of the casting, the solidification starts from the casting-mold interface and proceeds toward center. After 15 s, the air gap forms between the surfaces, and the HTC decreases drastically. Therefore, the slope of the casting temperature curve decreases. Due to the existence of the air gap, the mold inner surface temperature reaches a steady state much faster. However, the temperature at the outer surface of the mold increases gradually.

The results are in good agreement with the experimental results of Nishida *et al.* However, the present method slightly over predicts the temperature of the casting after 40 s. Due to the very low Stefan number for the first 7 time steps, the convergence is achieved at an average of 8.2 iterations and 4 local line-search iterations, which are similar to the previous problem. The evolution of the air gap between the points B and C is given in Fig. 2.13. Even though the results agree with Celentano *et al.*, due to the

Table 2.2: Parameters used in solidification of pure aluminum inside a steel mold (Celentano *et al.* 1996)

	Aluminum	Steel
Density(kg/m <sup>3</sup> )	2650	7850
Latent heat (kJ/kg)	395.1	—
Melting temperature (°C)	660	—
Specific heat capacity (J/kgK)		
≤ 100 °C	955.2	552.3
200°C	995.4	
300°C	1036.0	
400°C	1077.8	
500°C	1118.0	
≥600°C	1158.5	552.3
Thermal conductivity (W/mK)		
≤ 100°C	234.3	45.6
200°C	225.9	
400°C	221.8	
600°C	217.6	
659.9°C	209.2	
660.1°C	92.0	
>800°C	96.2	45.6
Young's modulus (GPa)		
25 °C	69.3	194
800 °C	35.4	194
Poissons ratio	0.37	0.30
Coefficient of thermal expansion (×10 <sup>-6</sup> /°C)		
25°C	23.19	12
300°C	27.86	
400°C	30.23	
659.9°C	30.36	
660.1°C	30.12	12
Yield stress (MPa)		
25°C	49.3	210
660°C	0.01	210
Hardening modulus (GPa)	0	0
Initial casting temperature – 670°C		
Initial mold temperature – 200°C		
HTC at contact condition( $h_c$ ) – 2929 W/m <sup>2</sup> K		
Contact normal stiffness( $k_n$ ) – 1×10 <sup>12</sup> MPa/m		

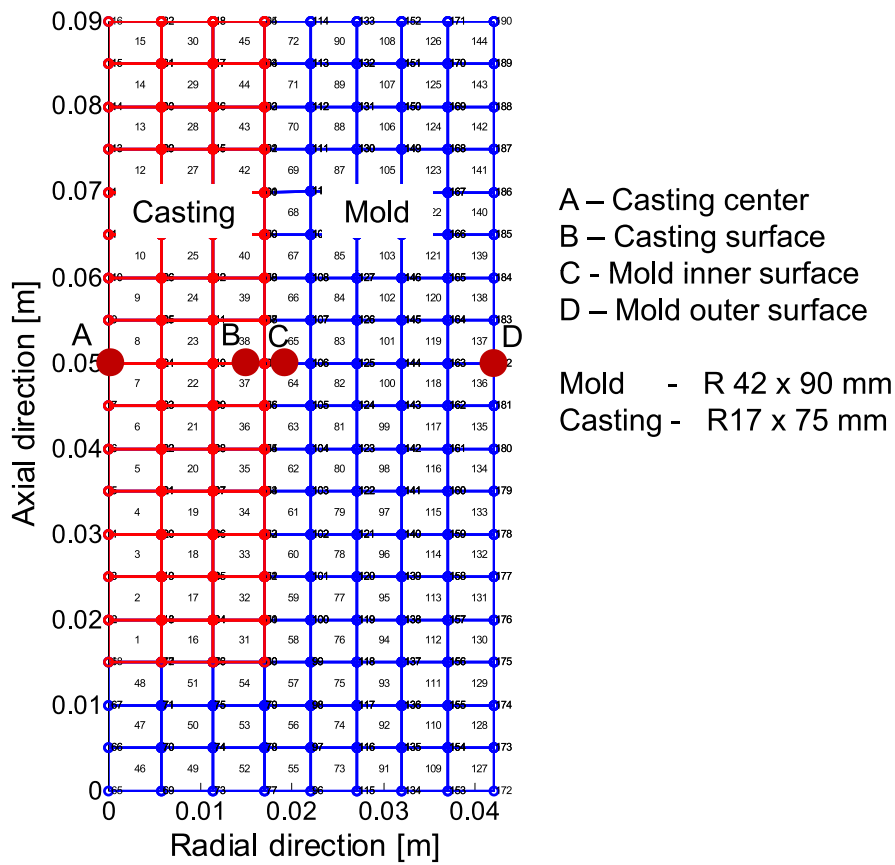


Figure 2.13: Pure aluminum solidification in steel mold (Celentano *et al.*, 1996): FE mesh

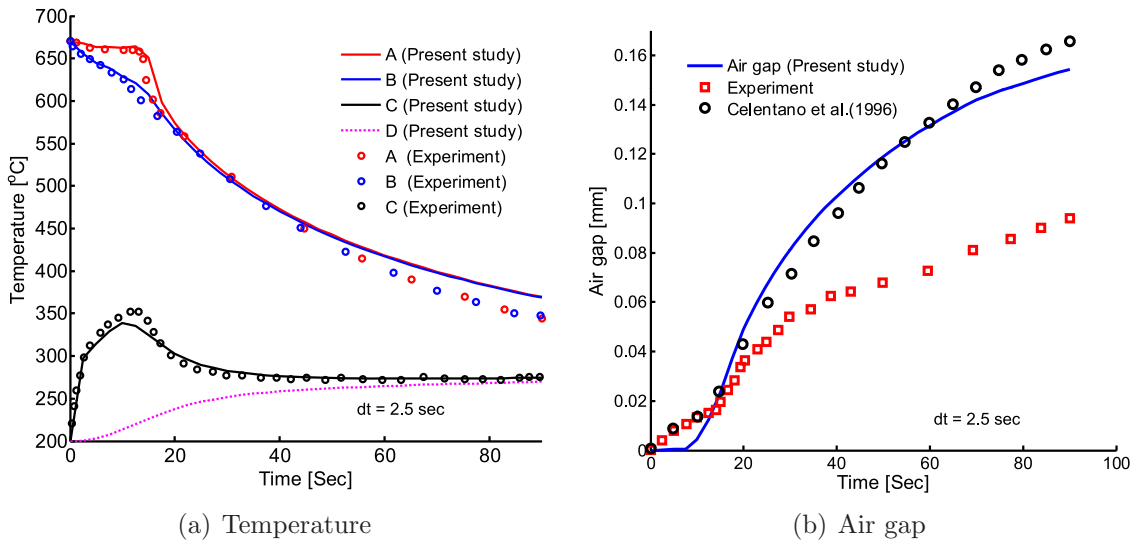


Figure 2.14: Pure aluminum solidification in steel mold (Celentano *et al.* 1996): (a) temperature evolution at different locations and (b) evolution of air gap

inappropriate material model (*elastic-perfectly plastic*), the experimental results are not matching with the simulation results.

## 2.8 Summary

The phase-change phenomenon is modeled and the computation techniques are explained in detail. A temperature-based fixed grid finite element method is developed for the phase-change problem. While solving the energy equation, the temperature is treated as a dependent variable instead of enthalpy. Even though, the enthalpy-based methods handle the isothermal phase-change problems more efficiently, when it comes to problems with a low Stefan number, it produces numerical oscillations during the Newton's iterations. The difficulty associated with the isothermal phase-change problem is explained in detail. A temperature-based formulation along with the line-search algorithm handles the isothermal phase-change problems with a low Stefan number in an efficient manner. Two different isothermal phase-change problems are solved for the validation of the model. The results of numerical examples show that the developed solidification model and the numerical method followed are strong enough to handle any kind of isothermal phase-change problem. With this notion, the solidification of DC casting can be easily solved with out any modifications.

# Chapter 3

## Inverse Problem

In Direct Chill (DC) non-ferrous metal casting, water is used as a cooling medium to extract the heat from the solidified outer layer of the ingot which supports the inner molten metal. This chapter presents the combined experimental and numerical technique to estimate the heat flux in the secondary cooling region of DC casting. The secondary cooling in DC casting is similar to the quenching of hot plate by an array of jets. Experimental techniques are explained for the measurement of temperature. A two-dimensional Inverse Heat Conduction Problem (IHCP) is solved by the non-iterative finite element method using the experimental temperature data. The wetting front which separates the film boiling and nucleate boiling zone, changes the order of the heat flux. Maximum heat flux position and its propagation velocity are plotted as a function of time. It is demonstrated that the water velocity and the maximum heat flux are not having a linear relationship. This chapter is formulated based on the published work of Nallathambi and Specht [111].

### 3.1 Secondary cooling in DC casting

In DC casting, heat transfer from the molten metal to the cooling water takes place through the outer solidified layer as show in Fig. 3.1(a). The outer solid layer which is in direct contact with cooling water, plays a major role for the ingot quality. Therefore, proper understanding of the heat transfer mechanism in the outer solid layer is required. Performing experiments at the real time DC casting plant is highly difficult and also expensive. Reproducing the similar operating conditions in a simplistic way will eliminate the intricacies in the experimentation of DC casting plant. Therefore, water quenching of a thin hot rectangular plate made of DC casting material from higher temperature is introduced to mimic the real time cooling of DC casting outer solid layer.

When the hot solid surface is exposed to the cooling water, there can be two different identifiable zones: (a) wet zone and (b) dry zone. The heat transfer mechanism in these

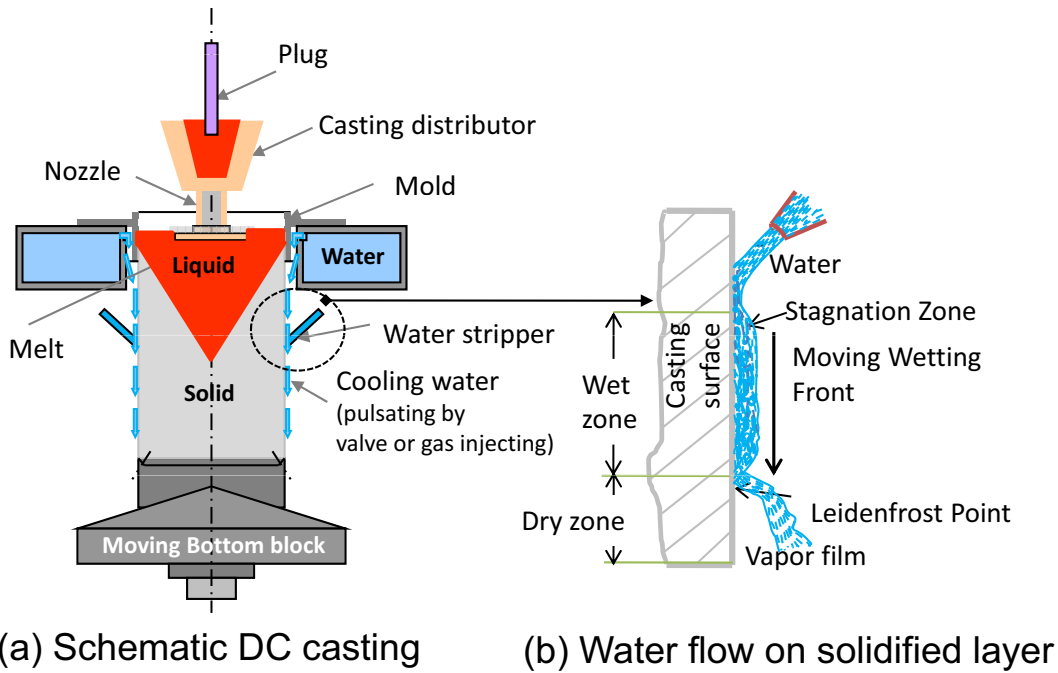


Figure 3.1: Secondary cooling in DC casting

two zones are entirely different. In the wet zone, water wets the surface of the solid, nucleate and transition boiling, and forced convection heat transfer dominates. During the nucleate boiling, the heat flux reaches the maximum. In the case of the dry zone, film boiling dominates and a thin film of water vapor is formed on the surface of the solid and it acts like an insulator which reduces the heat transfer. A visible thin wetting front separates these two regions, and within this front, the heat flux reaches its global maximum [112]. Also, this wetting front propagates in the coolant flow direction with a certain velocity.

A large number of researchers studied the quenching of hot plate, and some of the important related works are reviewed briefly: Elias and Yadigaroglu [113] developed an analytical one-dimensional model for the rewetting of a hot plate and predicted the wetting front velocity. They emphasized the importance of axial heat conduction. The limits of the unsteady-state quenching method was discussed by Peyayopanukul and Westwater [114]. Carbajo [115] conducted a detailed study on the rewetting temperature and critically reviewed the existing models. Surface effects in boiling heat transfer have been studied by Roy Chowdhury and Winterton [116], and Shoji *et al.* [117]. The influence of plate thickness on the boiling curve was carried by Westwater *et al.* [118] and stated that if the thickness of the plate is too small, the estimated critical heat flux will also be too small. Guo and El-Genk [119], and El-Genk and Guo [120] conducted experiments on the inclined surfaces with a downward flow and reported that the nucleate boiling heat

flux decreases as the angle of inclination is increased. Further, El-Genk and Glebov[121] studied the influence of curved surfaces and proved that through the curved surface, heat extraction can be maximized. Klinzing *et al.* [122] developed the film and transition boiling correlations for quenching of hot surfaces with water sprays. El-Genk and Guo[123] performed the sensitivity analysis and shown that the thermal diffusivity of the material has strong influence on the pool boiling curve. Without the help of precision experimental instrumentations, it is almost impossible to capture the influence of the kind of coolant, coolant flow characteristics, and surface condition of the specimen on the wetting front movement. Jeschar *et al.* [124] reported that there is no correlation between the water quality and the cooling process. Hall *et al.* [125, 126], and Mozumder *et al.* [127] studied the quenching of metals by an impingement of jet, and Puschmann *et al.* [128] performed experiments on spray quenching.

The pioneering work in water cooling of DC casting was done by Wiskel and Cockcroft [69, 70], Drezet *et al.* [59], and Zuidema *et al.* [129]. In contrast to the present observation about nickel plates, Wells *et al.*[130] observed the increase in heat flux when the water flow rate increases, and also studied the influences of surface morphology and starting temperature in DC aluminum casting. Mozumder *et al.* [131] studied the delay of wetting front propagation during jet impingement quenching and concluded that the value of maximum heat flux is 5–60 times higher than the heat transfer value just before the wetting front movement. Recently, Akmal *et al.* [132] studied the influence of initial surface temperature, water temperature and jet velocity on curved surfaces exposed to an impinging water jet.

The estimation of Heat Flux (HF) demands the solution of the IHCP [133]. Using the Laplace transform, Monde [134] solved the inverse heat conduction problem analytically for a one-dimensional (1-D) heat conductor. Ijaz and coworkers [135] have presented an adaptive state estimator for the estimation of input heat flux and measurement sensor bias in two-dimensional (2-D) inverse heat conduction problems. Continuous-time analogue Hopfield neural network based inverse solution algorithm has been proposed by Deng and Hwang [136]. The conjugate gradient method for the estimation of the surface heat flux has been used by Huand and Wu [137] and Xue and Yang [138]. A non-iterative least square minimization technique along with FEM proposed by Ling *et al.* [29] simplifies the inverse problem computation and produces consistent results.

In this work, the heat flux leaving from the water quenched rectangular plate as a function of space and time is estimated using the combined experimental and finite element technique through the inverse analysis. Ling *et al.*'s non-iterative technique is used to solve the inverse problem. The location of Maximum Heat Flux (MaxHF) is identified and plotted as a function of time. The effect of water velocity on the surface



heat flux is analyzed and it is demonstrated that the increase in water velocity always may not increase the surface HF.

## 3.2 Experimental arrangements

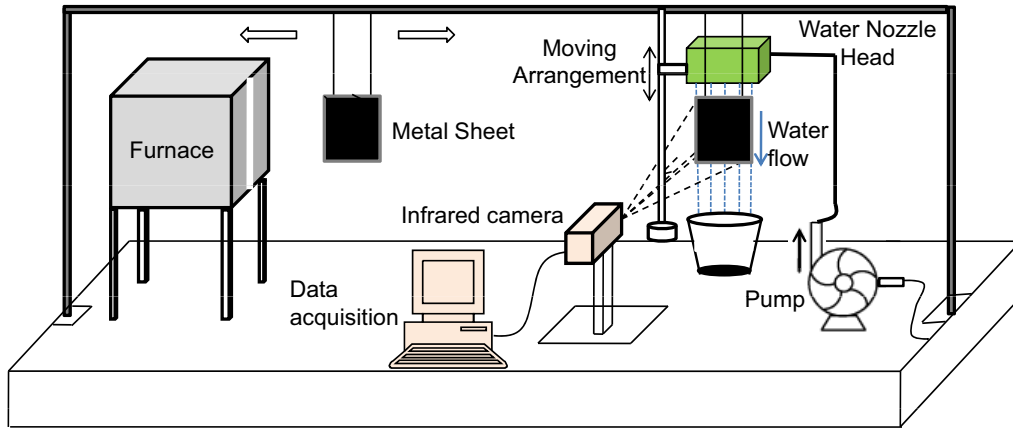


Figure 3.2: Experimental arrangement for water quenching of hot plate

The experimental arrangement for the quenching of the hot plate is shown in Fig. 3.2. There are three major groups of components in this arrangement: (a) furnace unit, (b) temperature data acquisition unit and (c) quenching unit. In the furnace unit, the sample (rectangular plate) is electrically heated into the higher temperature before quenching. There are provisions in the furnace, to set the final temperature of the plate. The infrared camera is used for measuring the surface temperature of the plate from its back side. The infrared camera has a lot of advantages over the other temperature measuring instruments like thermocouple. Before heating the plate in the furnace, it is prepared with one side black coating which improves the emissivity of the plate. The emissivity of the coating has to be determined for the calibration of the infrared camera. The temperature change in the plate can be sensed by the infrared camera and the complete quenching program is recorded in the data acquisition system. The frequency of the infrared camera is 150 Hz and it can measure the temperature with an accuracy of  $\pm 0.1$  K. The measurement range of the infrared camera for this experimental setup is 50–650°C.

The quenching unit has two important components: nozzle head with moving arrangements and hydraulic pump. Totally 10 orifices are provided in the nozzle head and it is attached with a moving arrangements. The nozzle head delivers the jets of coolant with an inclination of  $45^\circ$  to the sample. The details of the nozzle head are as follows: the dimensions are 200 mm  $\times$  125 mm  $\times$  100 mm, the size of the single orifice is 4.78 mm, the

distance between two orifices is 10 mm, the orifices are provided in the 125 mm side, and the head is made up of aluminum alloys with a wall thickness of 10 mm. The horizontal distance between the sample and the nozzle head is 23 mm, and the nozzle head is located vertically 20 mm from the top of the sample. Only 8 out of 10 orifices are allowed to supply the coolant. Otherwise, the coolant will flow on the backside of the plate which might affect the temperature recordings in the infrared camera. A hydraulic pump with a flow regulating device delivers the cooling water to the nozzle head. The nozzle head supplies the cooling water to the hot rectangular plate. De-ionized water is used as a coolant, and supplied with a constant temperature of 20°C.

### 3.3 Mathematical formulation

In the case of Direct Heat Conduction Problem (DHCP), the boundary conditions are well known and one has to solve the Governing Differential Equation (GDE) to find the interior domain solution. In the Inverse Heat Conduction Problem (IHCP), the boundary conditions are unknown, and some part of the domain solution is known through experiments. Using this experimental temperature data, it is required to solve the GDE for the estimation of the boundary conditions. The FEM is used to solve the IHCP using experimental data and DHCP temperature solution. In this section, the mathematical aspects of the DHCP and IHCP are explained separately in detail.

#### 3.3.1 Direct Heat Conduction Problem (DHCP)

As discussed in the solidification problem, the *metal quenching* problem consists of finding the absolute temperature field  $\theta : \bar{\Omega} \times \Upsilon \rightarrow \mathbb{R}^+$  such that [24]

$$\nabla \cdot k \nabla \theta = \rho c_p \dot{\theta} \quad \text{in } \Omega \times \Upsilon \quad (3.1)$$

subject to the boundary conditions

$$\theta = \bar{\theta} \quad \text{in } \Gamma_\theta \times \Upsilon \quad (3.2)$$

$$k \nabla \theta \cdot \vec{n} = q \quad \text{in } \Gamma_q \times \Upsilon \quad (3.3)$$

and the initial condition

$$\theta(\vec{X}, t)|_{t=0} = \theta_0(\vec{X}) \quad \text{in } \Omega \quad (3.4)$$

Eq. (3.1) represents the energy balance obtained from the first law of thermodynamics and Fourier's law of heat conduction, where  $\rho$  is the density,  $c_p$  is the specific heat

capacity, and  $k$  is the thermal conductivity which are functions of temperature, and  $q$  is the temperature and space dependent normal heat flux due to convection-radiation phenomenon.

Applying the variational principle and Euler backward time difference method as discussed in the solidification problem, the final form of the FEM equation at the current time step  $n + 1$  is given as [139]

$$(\mathbf{C} + \Delta t \mathbf{K}) \Theta^{n+1} = \mathbf{C} \Theta^n + \Delta t \mathbf{F}^{n+1} \quad (3.5)$$

where the capacitance matrix ( $\mathbf{C}$ ), the conductance matrix ( $\mathbf{K}$ ) and the force vector ( $\mathbf{F}$ ) are given in elemental form as

$$\begin{aligned} \mathbf{C}^e &= \int_{\Omega_e} \rho c_p \mathbf{N} \mathbf{N}^T d\Omega^e \\ \mathbf{K}^e &= \int_{\Omega_e} \mathbf{B} k \mathbf{B}^T d\Omega^e \\ \mathbf{F}^e &= \int_{\Gamma_q^e} \mathbf{N} q d\Gamma_q^e \end{aligned} \quad (3.6)$$

### 3.3.2 Inverse Heat Conduction Problem (IHCP)

Let an interior of the domain  $\Omega$  bounded by the curve  $\Gamma = \Gamma_\theta \cup \Gamma_q$ , where  $\Gamma_\theta$  is the temperature described boundary, and  $\Gamma_q$  is the unknown heat flux boundary due to the water cooling. Using the standard finite element discretization technique, the convective heat flux vector  $\tilde{\mathbf{q}}^{n+1}$  at the current time step on the boundary  $\Gamma_q$  is represented as

$$\tilde{\mathbf{q}}^{n+1} = [\tilde{q}_1^{n+1}, \tilde{q}_2^{n+1}, \dots, \tilde{q}_J^{n+1}]^T \quad (3.7)$$

where  $J$  is the total number of nodes on  $\Gamma_q$ . In order to determine the vector  $\tilde{\mathbf{q}}^{n+1}$ , we assume that instantaneous time-varying temperature measurements,  $\tilde{\mathbf{Y}}^{n+1}$ , are available at  $I$  measurement site nodes

$$\tilde{\mathbf{Y}}^{n+1} = [\tilde{Y}_1^{n+1}, \tilde{Y}_2^{n+1}, \dots, \tilde{Y}_I^{n+1}]^T \quad (3.8)$$

where  $I$  is the total number of nodes on the measurement site. The objective of the IHCP is to estimate the surface heat flux at the quenched site using the measurement site temperature data. Assume that  $\tilde{\Theta}^{n+1}$  is the calculated temperature vector using inverse FEM at the  $I$  measurement site nodes. Therefore, the instantaneous error norm is defined as in [29]

$$S = (\tilde{\mathbf{Y}}^{n+1} - \tilde{\Theta}^{n+1})^T (\tilde{\mathbf{Y}}^{n+1} - \tilde{\Theta}^{n+1}) \quad (3.9)$$

Using a non-iterative technique proposed by [29] while minimizing the error norm with respect to the surface heat flux ( $\partial S/\partial \tilde{q} = 0$ , called as *matrix normal equation*), yields the *sensitivity coefficient matrix*  $\tilde{\mathbf{X}}$  as in [29]

$$\tilde{X}_{ij} = \frac{\partial \tilde{\theta}_i^{n+1}}{\partial \tilde{q}_j^{n+1}} \quad (3.10)$$

where superscript on  $\tilde{X}_{ij}$  is suppressed. Exploiting the advantage of FEM, the force vector as mentioned in Eq. (3.5) and Eq. (3.6) is modified as in [29]

$$\mathbf{F}^{n+1} = \tilde{\mathbf{D}} \tilde{\mathbf{q}}^{n+1} + \mathbf{c} \quad (3.11)$$

where  $\mathbf{c}$  is determined by the known temperature distribution on  $\Gamma_\theta$  and  $\tilde{D}_{Pj} = \partial \mathbf{F}_P^{n+1}/\partial \tilde{q}_j^{n+1}$ , is a constant matrix of dimension  $N \times J$ .  $N$  is the total number of nodes on  $\bar{\Omega}$ , and  $P$  is the global node number. From the DHCP (Eq. (3.5)), the temperature vector is rewritten as in [29]

$$\Theta^{n+1} = \Psi^n + \Delta t \mathbf{U} \mathbf{F}^{n+1} \quad (3.12)$$

$\Psi^n$  and  $\mathbf{U}$  in Eq. (3.12) is given as in [29]

$$\begin{aligned} \mathbf{U} &= (\mathbf{C} + \Delta t \mathbf{K})^{-1} \\ \Psi^n &= \mathbf{U} \mathbf{C} \Theta^n \end{aligned} \quad (3.13)$$

Substituting Eq. (3.11) in Eq. (3.12), the measurement site calculated temperature vector  $\tilde{\Theta}^{n+1}$  is given as in [29]

$$\tilde{\Theta}^{n+1} = \tilde{\Psi}^n + \Delta t \tilde{\mathbf{U}} [\tilde{\mathbf{D}} \tilde{\mathbf{q}}^{n+1} + \mathbf{c}] \quad (3.14)$$

where  $\tilde{U}_{iP} = U_{GP}$  and  $\tilde{\Psi}_i^n = \Psi_G^n$  are mapped from the global nodes to the nodes on the quenched boundary  $\Gamma_q$ . The sensitivity coefficient matrix is explicitly rewritten from Eq. (3.10), and Eq. (3.14)

$$\tilde{\mathbf{X}}^{n+1} = \Delta t \tilde{\mathbf{U}} \tilde{\mathbf{D}} \quad (3.15)$$

Finally, from the minimization of the error norm, the unknown surface heat flux is given as

$$\tilde{\mathbf{q}}^{n+1} = \left( \tilde{\mathbf{X}}^T \tilde{\mathbf{X}} \right)^{-1} \tilde{\mathbf{X}}^T (\tilde{\mathbf{Y}}^{n+1} - \tilde{\Psi}^n - \Delta t \tilde{\mathbf{U}} \mathbf{c}) \quad (3.16)$$

The inverse solution algorithm is summarized as follows: (i)  $\Theta^n$ ,  $\mathbf{C}$ ,  $\mathbf{K}$  and  $\mathbf{c}$  are known from the previous time step.  $\tilde{\mathbf{Y}}^{n+1}$  is the known current experimental temperature vector.

Using these quantities,  $\tilde{q}^{n+1}$  can be determined from Eq. (3.16). (ii) the force vector  $F^{n+1}$  has to be determined using the current  $\tilde{q}^{n+1}$  according to the relation given in Eq. (3.11). (iii) the global temperature vector  $\Theta^{n+1}$  can be determined by substituting  $F^{n+1}$  in Eq. (3.12).

### 3.3.3 Element computations

The computation of the conductance and capacitance matrices and force vector are as similar to the solidification problem. The only unknown matrix to be addressed in the inverse problem is the  $\mathbf{D}$  matrix. It can be defined as the derivative of the force vector with respect to the nodal heat flux vector. Assuming  $c = 0$ , the force vector can be written as

$$F^{n+1} = \mathbf{D} \mathbf{q}^{n+1} = \tilde{\mathbf{D}} \tilde{\mathbf{q}}^{n+1} \quad (3.17)$$

from  $\mathbf{D}$  and  $\mathbf{q}$ ,  $\tilde{\mathbf{D}}$  and  $\tilde{\mathbf{q}}$  can be computed from the global to local mappings as explained before. In Eq. (3.6), the element force vector can be modified by substituting the unknown heat flux  $q$  as  $q = \mathbf{N}^T \mathbf{q}^e$  and becomes

$$F^e = \int_{\Gamma_q^e} \mathbf{N} \mathbf{N}^T \mathbf{q}^e d\Gamma_q^e \quad (3.18)$$

where  $\mathbf{q}^e$  is the element unknown nodal heat flux vector. Now the element form of  $\mathbf{D}$  matrix can be given as

$$\mathbf{D}^e = \frac{\partial F^e}{\partial \mathbf{q}^e} = \int_{\Gamma_q^e} \mathbf{N} \mathbf{N}^T d\Gamma_q^e \quad (3.19)$$

This matrix becomes constant due to the absence of material properties. This can be easily computed without much difficulty.

## 3.4 Quenching of nickel plate

A rectangular nickel plate (pure nickel - Ni200) having the geometry and constant material properties as given in Table. 3.1 is heated to an initial temperature of approximately  $600^\circ C$  and is quenched by the cooling water with two different velocities and flows are as follows: 1 m/s with 517 litre/hr, and 1.5 m/s with 777 litre/hr. The effective length ( $L_m$ ) of the plate considered for the analysis is 156 mm, and 44 mm is allowed for the water jet to strike the plate parallel to its length as shown in Fig. 3.3.

To evaluate the heat flux, the non-iterative FEM method described in Section 3.3 is applied to the 2-D structure as show in Fig. 3.3. It is assumed that there is no variation in the cooling characteristics of the plate in the width direction. The 2-D model of

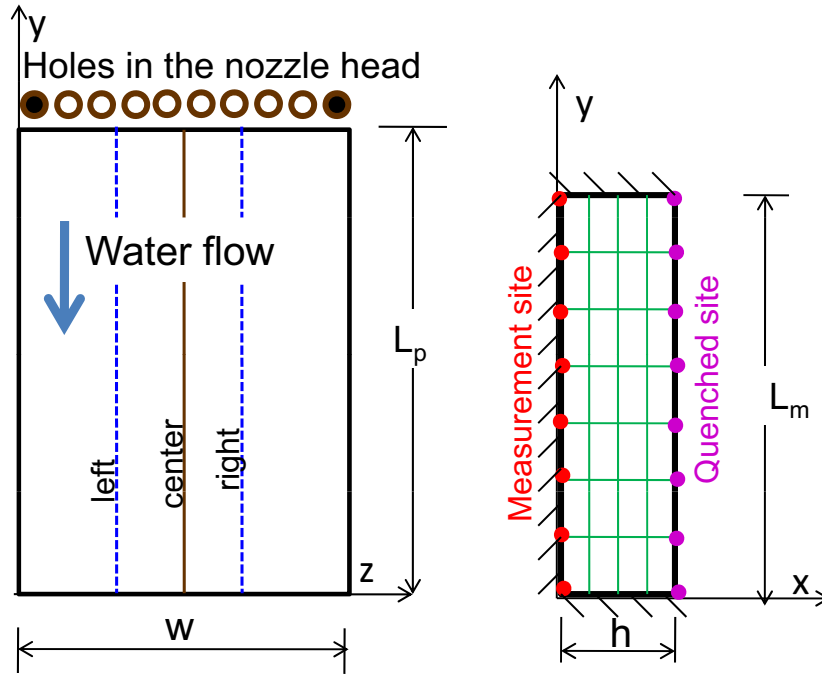


Figure 3.3: Schematic representation of plate and finite element model

Table 3.1: Geometry and Material Details

<b>Plate</b> length	$L_p$	200 mm
Width	$w$	110 mm
Thickness	$h$	2 mm
<b>Nickel 200</b> Density	$\rho$	8908 kg/m <sup>3</sup>
Thermal conductivity	$\lambda$	90.9 W/mK
Specific heat	$c_p$	444 J/kgK

2×156 mm dimension having 4×67 elements is schematically represented in Fig. 3.3. Apart from the quenched surface, all thermal boundaries are assumed to be insulated for the sake of simplicity. A uniform time step of magnitude numerically equal to the diffusive time of the structure is used and it is defined as in Ling *et al.* [29]

$$\text{Diffusive time} = \frac{(\text{Distance bet. measured \& quenched surface})^2}{\text{Thermal diffusivity}} \quad (3.20)$$

The diffusive time of the nickel plate considered for the analysis is 0.174 seconds which is treated as a simulation time interval.

### 3.4.1 Validation

Before examining the influence of water velocity, the accuracy of the developed inverse algorithm, and the repeatability of the experimental setup are verified. To validate the inverse FEM, the aforementioned material and the mesh is considered for the numerical experiment. A temperature-dependent HTC is given as an input to the DHCP and the temperature vector at the measurement site is estimated. Using this temperature history, an IHCP is solved and the HTC as a function of the quenched surface temperature is plotted at the center point as shown in Fig. 3.4. Due to the absence of noise in the input

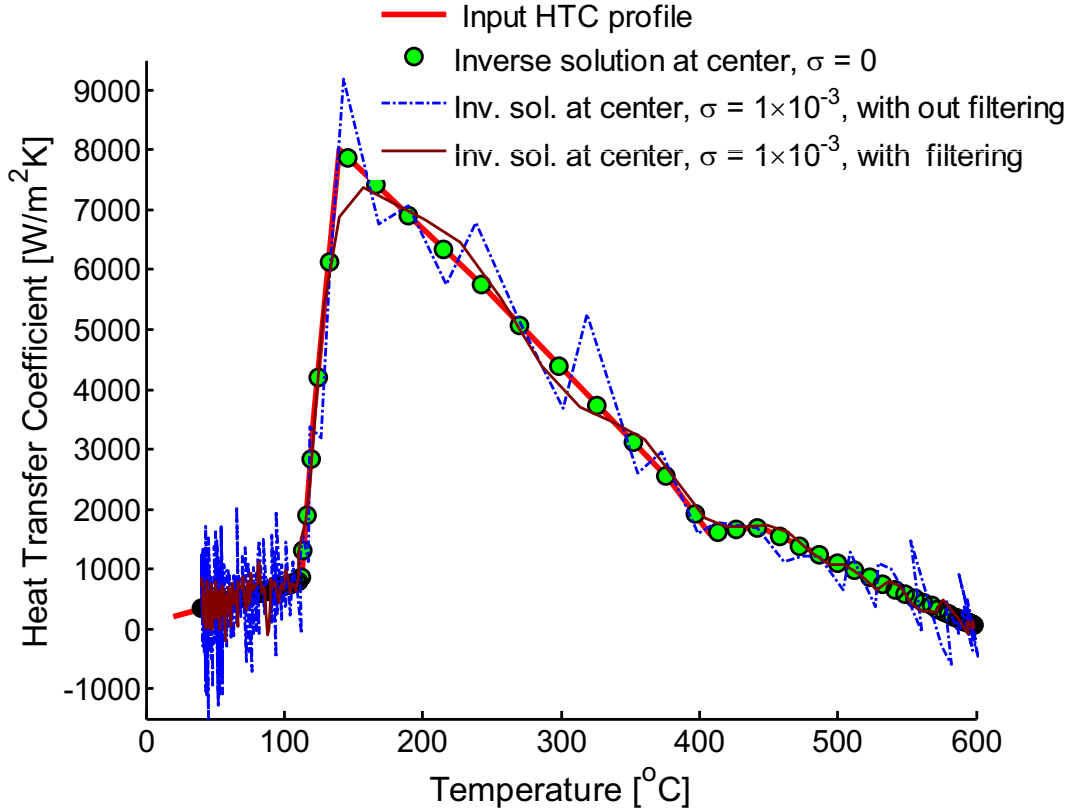


Figure 3.4: Validation of inverse algorithm: HTC vs. Temperature

temperature history, the estimated HTC profile exactly matches with the input profile. It is impossible to perform the experiments, without the inherent noises. Therefore, a random noise is artificially generated and added to the input temperature history as in [29, 140]

$$\text{noisy } \tilde{\mathbf{Y}}_i^{n+1} = \tilde{\mathbf{Y}}_i^{n+1} + \bar{\sigma} \tilde{\epsilon}_i^{n+1}, \quad \text{and} \quad \tilde{\epsilon}_i^{n+1} = \sum_{j=1}^{12} RN_j - 6.0 \quad (3.21)$$

where  $RN$  is a random number uniformly distributed between 0 and 1,  $i$  is the measurement site node index, and  $\bar{\sigma}$  is the noise controlling parameter. A noise with  $\bar{\sigma} = 1 \times 10^{-3}$

is introduced with the input temperature profile, and the solution of the IHCP is plotted as shown in Fig. 3.4. Hernandez *et al.* [141] showed that filtering the raw experimental data prior to the inverse analysis greatly improved the estimates of surface heat flux and heat transfer coefficient. A simple noise filtering technique is developed, and the filtered  $\theta$  vs. HTC is shown in Fig. 3.4. The results show that, even for a very high noise, using a filtering technique, the shape of the HTC profile is preserved but slightly under predict the maximum input HTC.

The repeatability of the experiment is verified through the sequence of experiments, and the temperature profiles at the center of solution domain (77 mm from top of solution domain or 121 mm from top of the plate) at the central cross-section are plotted as shown in Fig. 3.5. Three experiments were performed for each water velocity, and the two experiments with similar temperature history are selected and averaged for further processing.

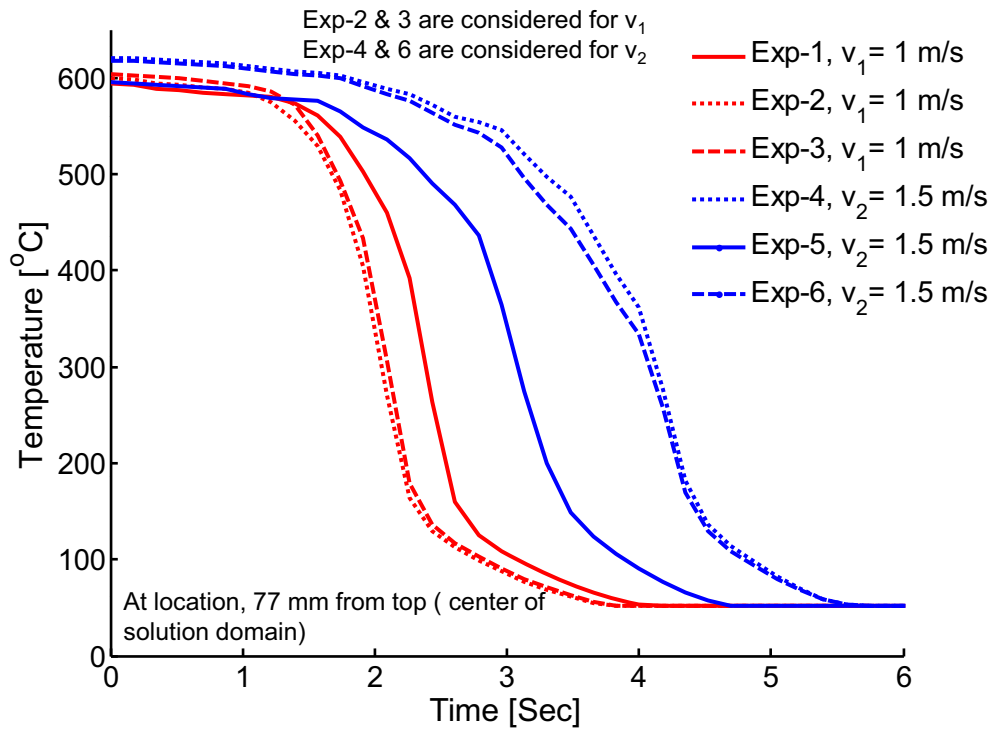


Figure 3.5: Repeatability of the experimental setup: Temperature profiles

### 3.4.2 Temperature profiles

The temperature profiles extracted at four different locations along the central line of the plate are plotted as shown in Fig. 3.6. The solid line represents the water velocity of 1 m/s and dashed line represents the water velocity of 1.5 m/s. At all locations (9, 56, 103, and 150 mm from the top of solution domain at central cross-section), the temperature of the



lower velocity case decreases much faster than the higher velocity case. The temperature profiles itself indicates the influence of coolant velocity on the cooling rate.

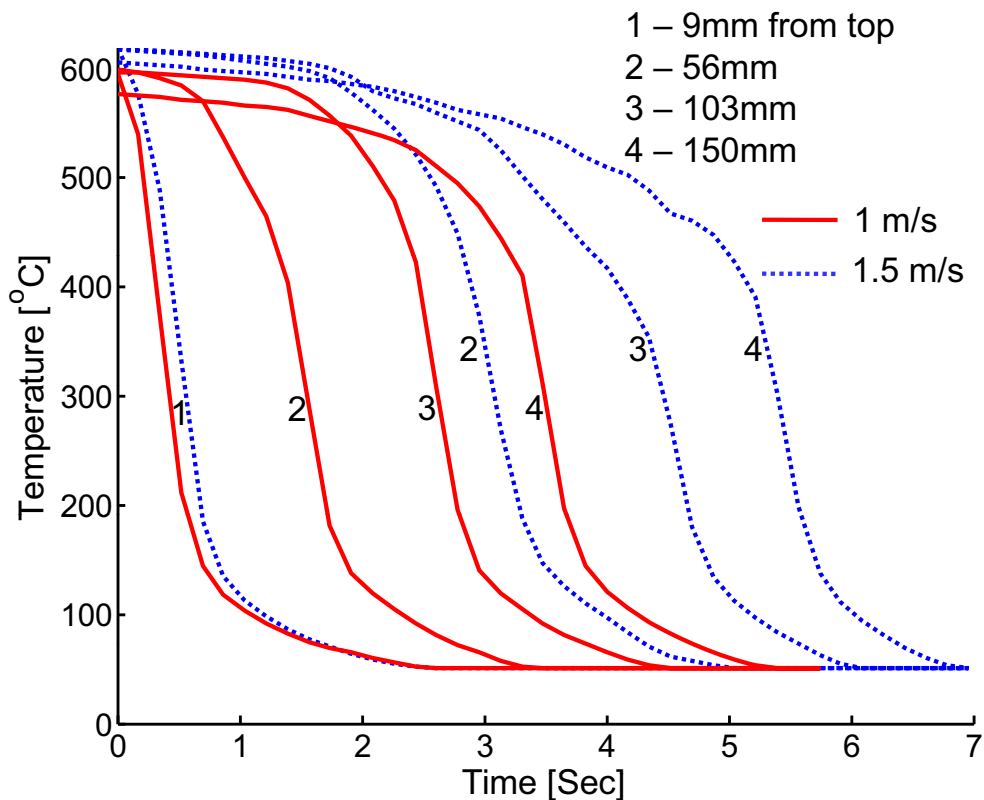


Figure 3.6: Nickel: experimental temperature profile at center line

### 3.4.3 Estimated heat flux

The instantaneous heat flux distribution along the length of the plate for two different velocities of water at two different time is represented in Fig. 3.7(a). Due to the presence of noise in the experimental data, the vector regularization [133] is required to get a reasonable heat flux profile. In this work, a simple three point averaging type of regularization is carried out with giving more weight on the point at which heat flux is required. From Fig. 3.7(a), it is observed that the heat flux attains a maximum at a particular location and also its position shifts toward the bottom of the plate with respect to time. This fact indicates that, while the cooling water flows along the length of the plate, the wetting front which separates the film and nucleate boiling, moves continuously along the water flow direction. Mozumder *et al.* [112] proved that the position of MaxHF lies within the wetting front. In this work, the wetting front position and the MaxHF position are assumed to be the same. At 1.7 s, the MaxHF (wetting front) for the lower water velocity occurs at 0.06 m, and for the higher velocity the MaxHF occurs at 0.04 m. Similarly at 3.5 s, the higher velocity MaxHF occurs at 0.07 m and the lower velocity

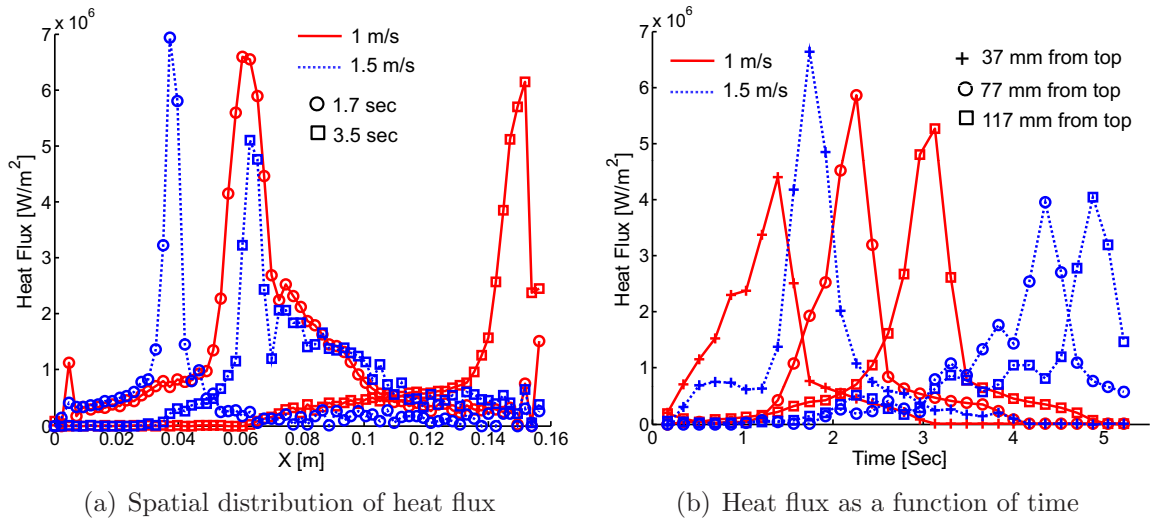


Figure 3.7: Nickel: heat flux distribution

MaxHF occurs at 0.15 m. This result explicitly proves that the water velocity highly influences the location of instantaneous MaxHF and its magnitude. Similarly, the heat flux as a function of time at three different locations taken at the central cross-section is shown in Fig. 3.7(b). For the lower velocity case, at the center point of the solution domain, the heat flux reaches its maximum at 2.2 s, and for the higher velocity case the maximum occurs at 4.3 s as shown in Fig. 3.7(b). But at the location of 37 mm from top of solution domain, the heat flux for the higher velocity case reaches a maximum value of 6.5 MW/m<sup>2</sup> which is higher than the lower velocity case of 4.5 MW/m<sup>2</sup>.

### 3.4.4 Maximum heat flux propagation

When the wetting front starts moving, the surface temperature drops sharply, a consequence of which the surface heat flux increases dramatically and the heat flux reaches its maximum value [112]. Fig. 3.8(a) represents the position of MaxHF at different time for the two different water velocities. In the initial stage, the higher water velocity curve leads the lower velocity curve and afterward it always lags behind the lower velocity curve. The wetting front reaches the bottom of the plate much faster in the case of the lower water velocity. This fact can be further verified through the velocity of MaxHF propagation.

To determine the MaxHF propagation velocity, the MaxHF position data are fitted by the least-squares method to a suitable polynomial (as shown in Fig. 3.8(a) by a dotted line) and then the polynomial equation is differentiated. Fig. 3.8(b) represents the MaxHF propagation velocity as a function of time. Even though both the higher and lower water velocity curves follow the same trend, their peaks and the time at which they reach this

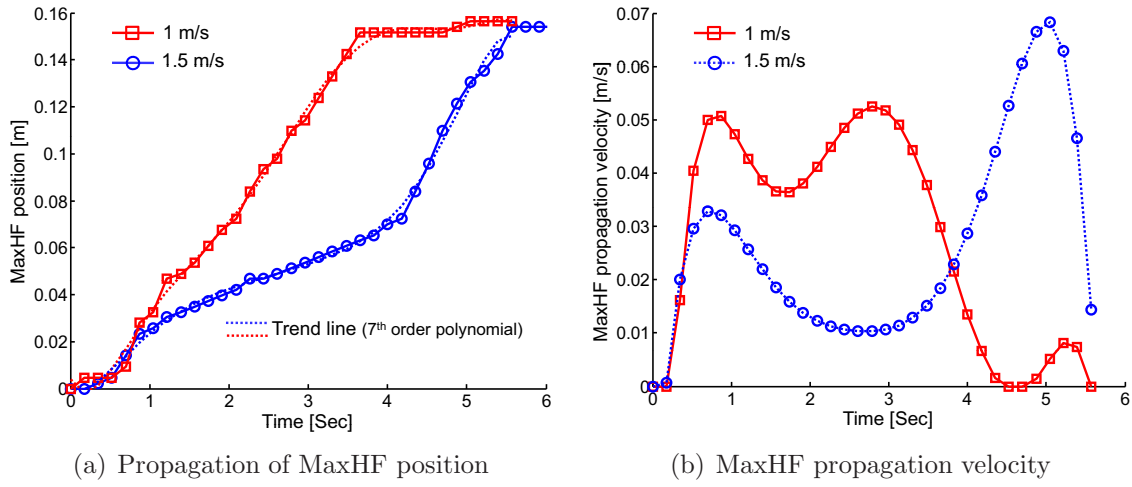


Figure 3.8: Nickel: propagation of MaxHF

peak vary drastically. This figure reveals the effect of water velocity on the MaxHF propagation. The wetting front reaches the bottom of the plate at 3.6 s in the case of 1 m/s water velocity and for the water velocity of 1.5 m/s takes nearly 5.5 s. Increase in water velocity delays the MaxHF propagation.

### 3.4.5 Surface heat flux vs. temperature

Increase in water velocity delays the MaxHF propagation. To understand this fact quantitatively, an attempt is made to plot the surface heat flux as a function of temperature (boiling curve). For that, 20 mm left to the central line and 20 mm right to the central line of plate is modeled along with the central line as shown in Fig. 3.3. From the above three mentioned simulations, all nodes except 4 nodes in each end of the FEM mesh are considered for the heat flux vs. temperature plot as shown in Fig. 3.9. A trend line has been fitted for the two different velocities of water as shown in Fig. 3.10(a). The film boiling (above 400°C), nucleate and transition boiling (190 - 400°C), and forced convection (below 190°C) regions can be easily recognized from the Fig. 3.10(a). Increase in the water velocity, decreases the MaxHF. For water velocity of 1.5 m/s, the heat flux curve shifts toward the lower temperature side and also shrinks when compared to the heat flux curve for a water velocity of 1 m/s. The heat flux in the nucleate boiling and film boiling zone is higher for lower water velocity. But in the forced convection zone, heat flux in higher water velocity is greater than the lower water velocity case. Therefore, increase in water velocity and flow does not increase the heat extraction from the hot surface. The temperature at which the heat flux reaches a maximum value lies around 180–190°C, and also its independent of water velocity [112]. Similar kind of results are reported in Li and Wells [142]. However, Mozumder *et al.* [112] reported that the maximum heat flux

occurs at  $145^{\circ}\text{C}$ . An attempt is made to plot HTC as a function of temperature as shown in Fig. 3.10(b), and the maximum HTC occurs around  $150\text{--}160^{\circ}\text{C}$ .

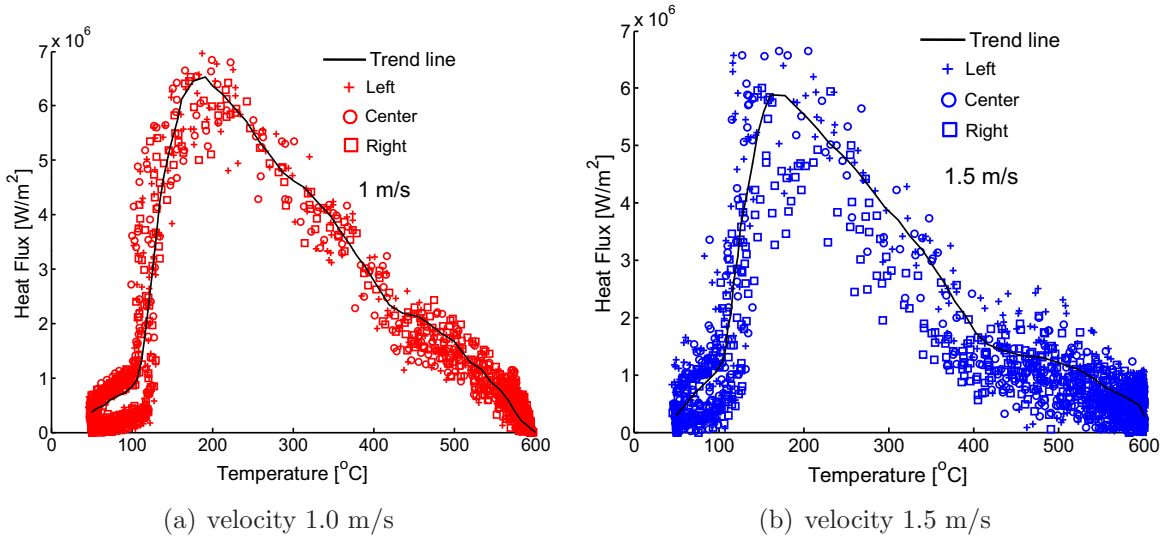


Figure 3.9: Nickel: Heat flux vs. Temperature

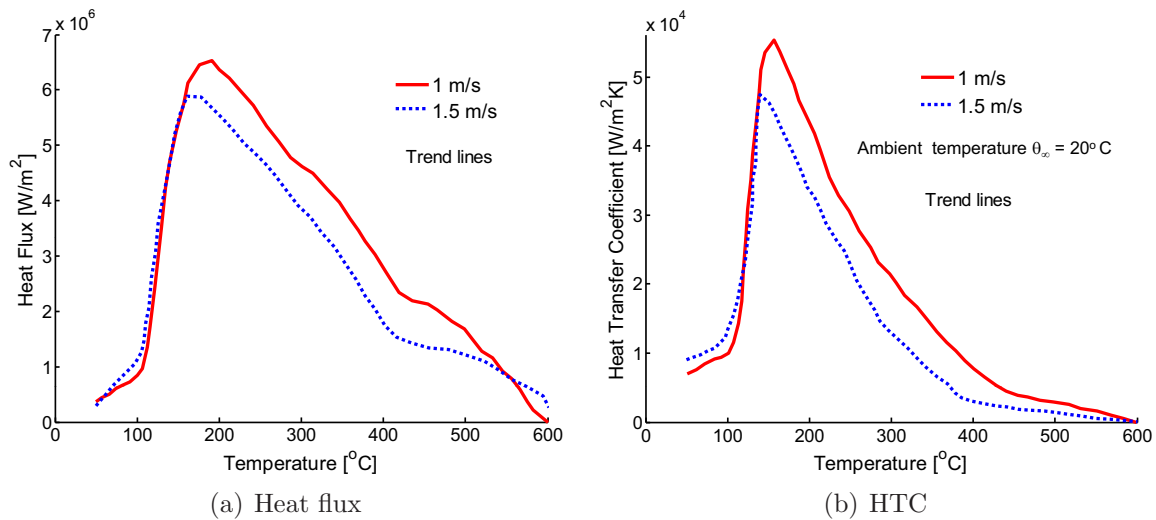


Figure 3.10: Nickel: Heat flux and HTC as a function of temperature

To further verify the potential of the inverse algorithm, HTC as a function of space and time for the higher velocity case is plotted as shown in Fig. 3.11. This HTC history is taken as a time-dependent convective boundary condition, the direct problem is solved and the temperature profiles are compared with the experimental results as shown in Fig. 3.12. The developed inverse algorithm predicts the temperature with an accuracy of  $\pm 10^{\circ}\text{C}$ .

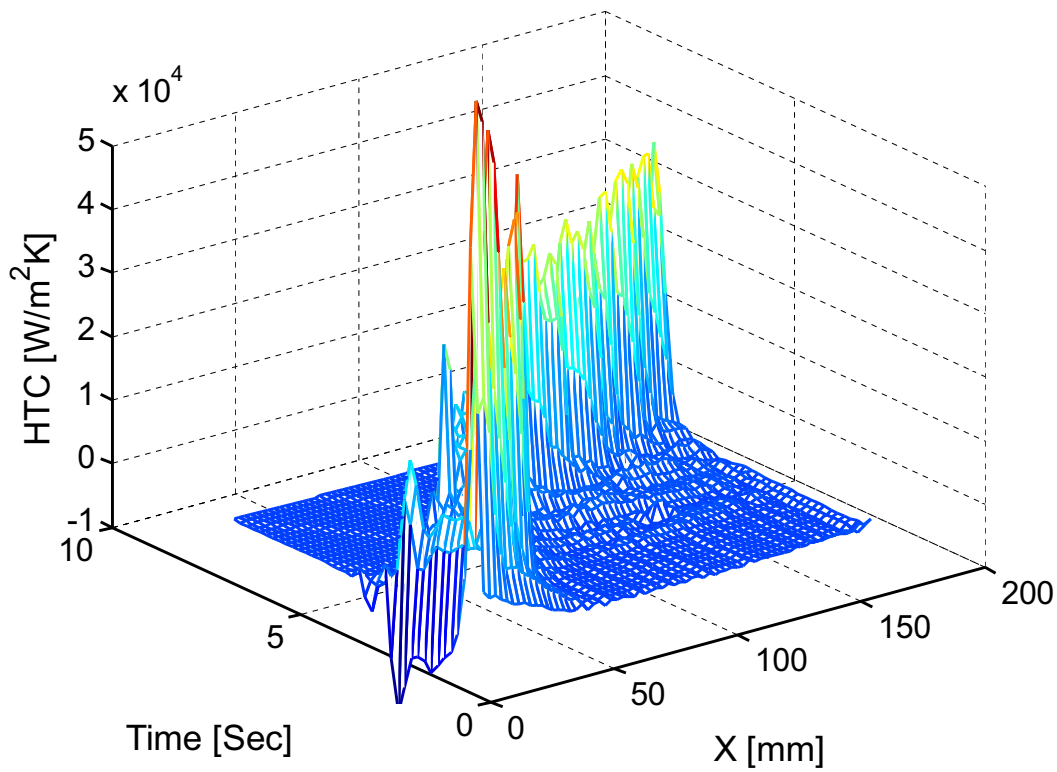


Figure 3.11: Verification of Inverse algorithm: HTC as a function of space and time for  $v = 1.5$  m/s

### 3.5 Quenching of aluminum plates

Similar to the nickel, quenching of aluminum plates (AA2024/AL2024) are investigated for 4 different water velocities such as 0.9, 1.2, 1.5, and 1.8 m/s. The dimensions of the plate, quenching unit, and other quenching parameters are the same as before. The material properties of AA2024 are given in Table. 3.2. Initially, the plates are heated up to 520°C. To study the influence of the water velocity, experiments are carried out under almost similar quenching conditions except the water flow rate. To further ensure the repeatability, several experiments are performed for the same water flow rate and the temperature profiles are averaged.

Table 3.2: Aluminum AA2024 alloy - Material properties

Density	2770 kg/m <sup>3</sup>
Thermal conductivity	177 W/mK
Specific heat	875 J/kgK

The position of the wetting front / MaxHF is shown in Fig. 3.13. Completely opposite behavior is observed. Here, the increase in water velocity increases the wetting front

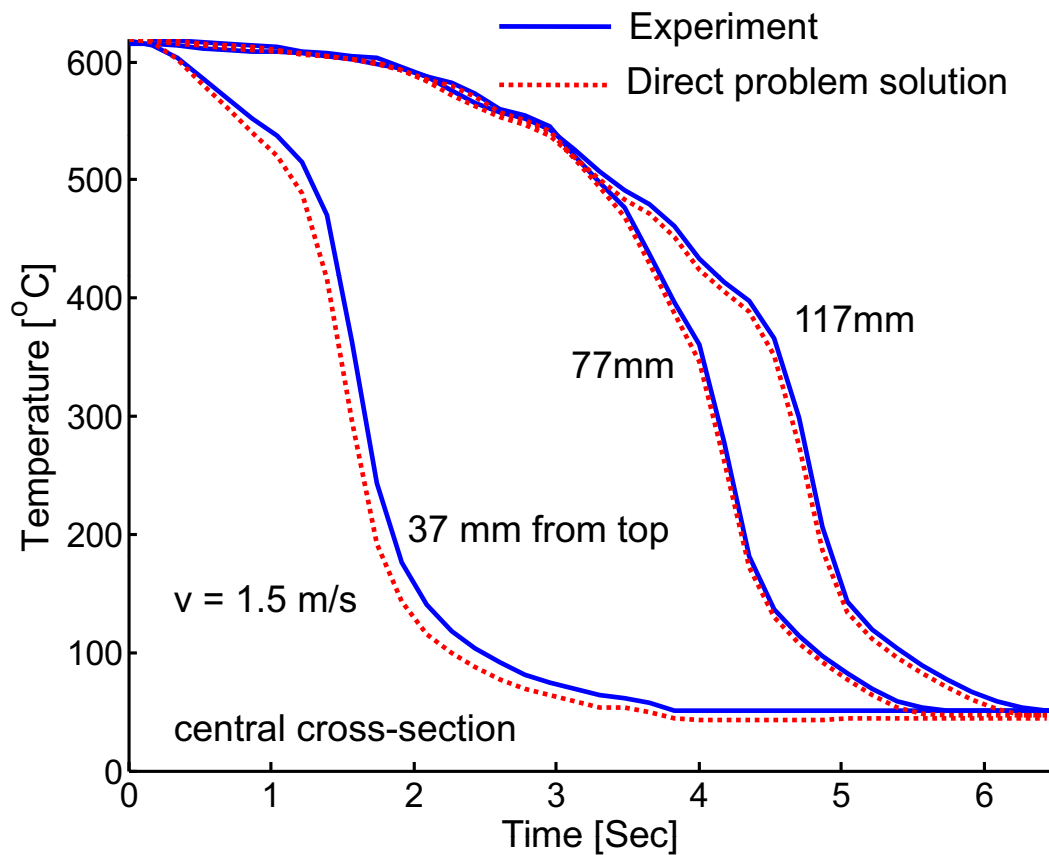


Figure 3.12: Verification of Inverse algorithm: Comparison of temperature profiles

movement. In the lowest velocity case (0.9 m/s), the wetting front movement is slower than the others. Surprisingly, for the lower velocity cases (1.2 and 1.5 m/s), the maximum speed of wetting front is observed. Further increase in water velocity, does not promote the speed of the wetting front. Even though, in the case of 1.5 m/s, the speed of the wetting front is relatively higher than the lowest water velocity case, it is much lower than 1.2 and 1.5 m/s. It indicates the fact that the relation between the water velocity and wetting front movements are not exactly linear. However, at this moment, the physical meaning behind this fact is not well understood.

The boiling curve for AA2024 is shown in Fig. 3.14. Here, the increase in water velocity promotes the heat flux leaving on the surface of the plate. Fig. 3.14 shows that the increase in water velocity expands the boiling curve. In all the velocities, the maximum heat flux occurs at 180–185°C which is similar to that of nickel. Increase in water velocity, significantly improves the film boiling and transition boiling. There is no much difference observed in nucleate boiling zone. The maximum heat fluxes for all the cases lie around 2.1–2.8 MW/m<sup>2</sup> which is lower than the nickel.

The objective of this study is to get a HTC as a function of temperature. To achieve this motive, the heat flux values are normalized with the surface temperature difference,

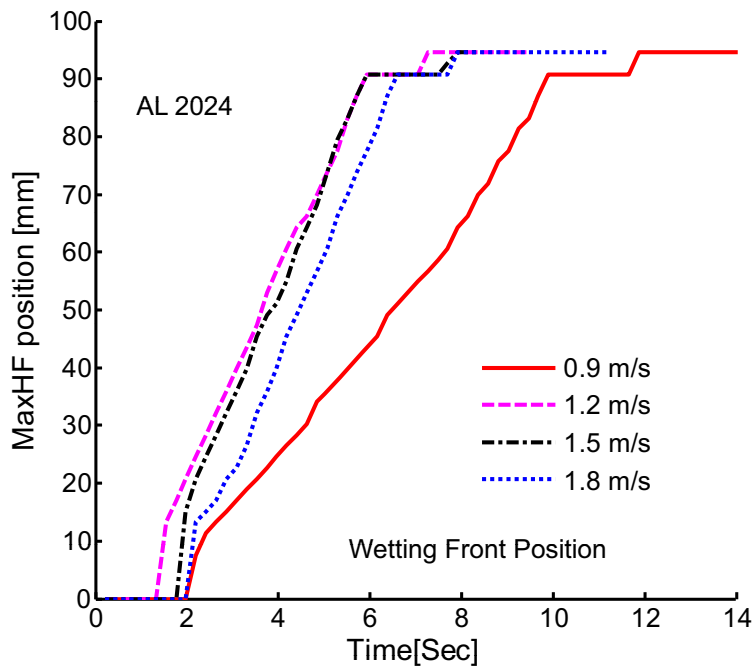


Figure 3.13: Quenching of aluminum: wetting front movement

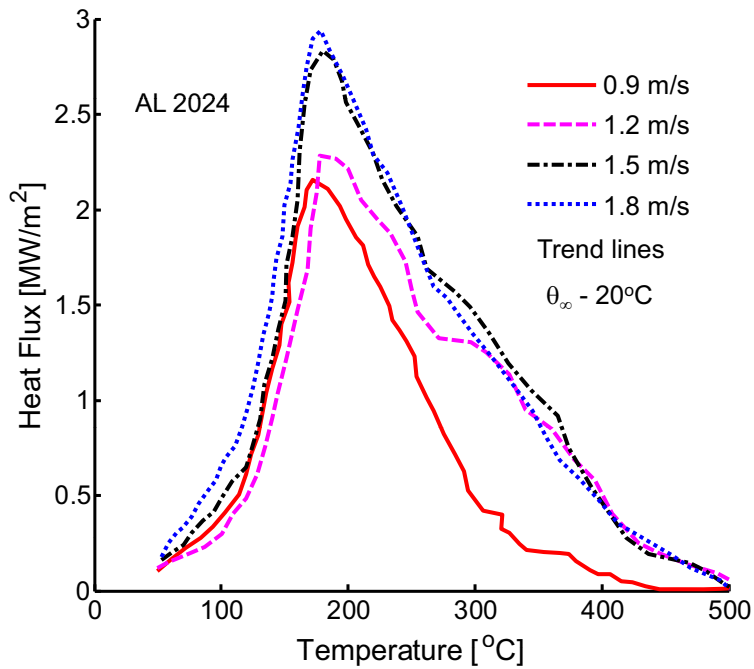


Figure 3.14: Quenching of aluminum: heat flux vs. temperature

and the HTC profiles are shown in Fig. 3.15. The LFP in the case of aluminum is lower than the nickel and increases with increase in water velocity. In all the cases, the maximum HTC is around 1.3–1.8 kW/m<sup>2</sup>K.

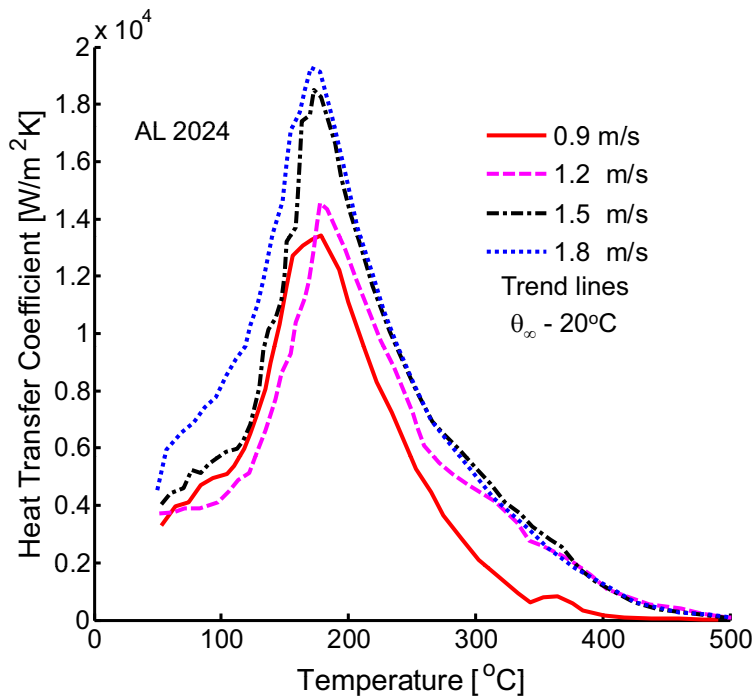


Figure 3.15: Quenching of aluminum: HTC vs. temperature

### 3.6 Other considerations

The temperature dependency of the thermal properties has to be taken into account which may significantly change the present observations. The wetting front and the position of the maximum heat flux are assumed to coincide. The shape of the wetting front along the width direction is assumed as straight. The influence of the water velocity on the wetting front movement may not be linear, therefore more experiments have to be done with different water velocities. The stability of the developed inverse algorithm is not discussed in this article. The trend curve fitting in heat flux vs. temperature plot (Fig. 3.9) is heuristic in nature. The increase in the cooling water temperature is not taken in to account when computing the HTC. The initial temperature distribution of the plates under different water velocities are not exactly equal. The experimental setup does not mimic the secondary cooling of DC casting. Therefore, it may not be completely applicable to the DC casting. In the case of DC casting, the liquid metal continuously supply the heat, and the ingot moves with certain velocity. These effects are not taken into account in the present analysis. Due to the limitations of thermography, it is not possible to cover the entire zone of boiling. Therefore, the observations made on the film boiling zone is not accurate.



### 3.7 Summary

The experimental setup for studying the secondary cooling in DC casting is established. Water is treated as a coolant and it is supplied through the nozzle head which can produce a maximum of 10 jets. A rectangular plate with an initial temperature of 500–600°C is quenched at the front side and the temperature of the plate at the back side is recorded using an infrared camera. From the measured temperature, the heat flux is estimated by solving the IHCP. A non-iterative finite element method developed by Ling *et al.* [29] is employed to solve the IHCP. The accuracy of the inverse solution, and the repeatability of the plant are verified. The influence of the cooling water velocity and the quantity of flow on the heat flux is analyzed. It is observed that the increase in water velocity and flow and the heat extraction from the hot surface is not linear. This fact is verified through the maximum heat flux (MaxHF) propagation and its velocity on time. Increase in water velocity may not always increase the MaxHF propagation and the MaxHF. Nickel and aluminum plates are investigated, and the heat flux in the case of nickel is 3–4 times higher than the aluminum. Increase in water velocity promotes the film boiling and increase the Leidenfrost point.

# Chapter 4

## Modeling of Displacement Field

In DC casting, the liquid metal is solidified under strong thermal gradients. During the solidification, the material develops stress and strain due to the nonuniform thermal forces. This chapter presents the mathematical modeling of displacement field. The finite element method is used to solve the momentum equation. Small deformation theory is used. The strain tensor is additively decomposed into elastic, thermal and inelastic strain tensors. Elasto-plastic and elasto-viscoplastic constitutive relations are implemented. Two numerical examples are presented for the validation of finite element solution approach.

### 4.1 Mathematical formulation

A thermo-elasto-plastic / thermo-elasto-viscoplastic continuous body  $\mathcal{B}$  with interior  $\Omega \subset \mathbb{R}^{n_d}$  ( $n_d = 1,2,3$ ) and displacement boundary  $\Gamma_u$ , traction boundary  $\Gamma_t$ ,  $\Gamma = \Gamma_u \cup \Gamma_t$ , together as mentioned in thermal field as  $\tilde{\Omega} = \Omega \cup \Gamma$  and the time interval of analysis  $t \in \Upsilon$  ( $\Upsilon \subset \mathbb{R}^+$ ), has to satisfy the equilibrium equation at the current spatial configuration  $\vec{X} \in \tilde{\Omega}$ . The equilibrium equation which yields the displacement solution  $\vec{u}$  is given as in [52]

$$\nabla \cdot \mathbf{T} + \vec{b}_f = \vec{0} \quad \text{in } \tilde{\Omega} \times \Upsilon \quad (4.1)$$

subject to the boundary conditions

$$\vec{u} = \vec{u}_s \quad \text{in } \Gamma_u \times \Upsilon \quad (4.2)$$

$$\mathbf{T} \cdot \vec{n} = \vec{t}_f \quad \text{in } \Gamma_t \times \Upsilon \quad (4.3)$$

where  $\mathbf{T} = T_{ij} \vec{e}_i \otimes \vec{e}_j$  is the stress tensor,  $\vec{b}_f = b_{fi} \vec{e}_i$  is the body force vector,  $\vec{u}_s$  is the prescribed displacement vector and  $\vec{t}_f$  is the prescribed traction vector with unit outward normal  $\vec{n}$ .

The total deformation observed in the DC casting is less than 4%. Therefore, using the advantage of small deformation theory, the total strain  $\mathbf{E}$  can be additively decomposed into three components as

$$\mathbf{E} = \frac{1}{2} [\nabla \vec{u} + (\nabla \vec{u})^T] = \mathbf{E}^e + \mathbf{E}^t + \mathbf{E}^{ie} \quad (4.4)$$

where  $\mathbf{E}^e$  is the elastic strain tensor (tensorial),  $\mathbf{E}^t$  is the thermal strain tensor, and  $\mathbf{E}^{ie}$  is the inelastic strain tensor (tensorial). The inelastic strain might be either plastic strain or viscoplastic strain. Once estimating the inelastic and the thermal strain tensors, the elastic strain tensor can be obtained from the total strain tensor, and its methods of estimation are discussed in the subsequent subsections in detail. Using the elastic part of the strain tensor  $\mathbf{E}^e$ , stress tensor  $\mathbf{T}$  can be determined from the constitutive law of the material as

$$\mathbf{T} = \mathbb{C} : \mathbf{E}^e = \kappa \text{tr}(\mathbf{E} - \mathbf{E}^t) \mathbf{I} + 2\mu (\mathbf{E}' - \mathbf{E}^{ie}) \quad (4.5)$$

where  $\mathbb{C}$  is the fourth-order elasticity tensor,  $\mathbf{I} = \delta_{ij} \vec{e}_i \otimes \vec{e}_j$  is the second-order identity tensor,  $\kappa$  is the bulk modulus, and  $\mu$  is the shear modulus which are functions of temperature and phase fractions. Further, the elasticity tensor can be defined as,

$$\mathbb{C} = 3\kappa \mathbb{P}_1 + 2\mu \mathbb{P}_2 \quad (4.6)$$

where  $\mathbb{P}_1$  and  $\mathbb{P}_2$  are the fourth-order volumetric and deviatoric projectors, respectively, are defined as

$$\mathbb{P}_1 = \frac{1}{3} (\mathbf{I} \otimes \mathbf{I}) \quad \implies \mathbb{P}_{1ijkl} = \frac{1}{3} \delta_{ij} \delta_{kl} \vec{e}_i \otimes \vec{e}_j \otimes \vec{e}_k \otimes \vec{e}_l \quad (4.7)$$

$$\mathbb{P}_2 = \mathbb{I} - \frac{1}{3} (\mathbf{I} \otimes \mathbf{I}) \quad \implies \mathbb{I}_{ijkl} = \frac{1}{2} (\delta_{ik} \delta_{jl} + \delta_{il} \delta_{jk}) \vec{e}_i \otimes \vec{e}_j \otimes \vec{e}_k \otimes \vec{e}_l \quad (4.8)$$

where  $\mathbb{I}$  is the fourth-order symmetric identity tensor. By the definition of  $\mathbb{P}_2$ , the deviatoric part of total strain tensor can be defined as

$$\mathbf{E}' = \mathbb{P}_2 : \mathbf{E} \quad \implies \quad \mathbf{E}'_{ij} = \mathbb{P}_{2ijkl} \mathbf{E}_{kl} \vec{e}_i \otimes \vec{e}_j \quad (4.9)$$

### 4.1.1 Thermal strain

When the hot metal is allowed to cool under the absence of external mechanical loads, the dimensions of the material shrinks. Similarly, while heating the material expands. Therefore, a reversible strain is always associated with the heat treatment process. Such a strain is known as thermal strain. This strain is volumetric in nature. The thermal strain can be computed in any one of the two ways: (a) density approach, or (b) coeffi-

cient of thermal expansion approach. In both methods, one has to define the reference temperature ( $\theta_{ref}$ ) where the thermal strain is zero. In this work, the thermal strain is determined using the linearized coefficient of thermal expansion ( $\alpha$ ) as

$$\mathbf{E}^t = \alpha (\theta - \theta_{ref}) \mathbf{I} \quad (4.10)$$

where  $\theta$  is the current temperature. For the liquid phase,  $\alpha$  becomes zero. The time rate of thermal strain can be give as

$$\dot{\mathbf{E}}^t = \alpha \dot{\theta} \mathbf{I} \quad (4.11)$$

Alternatively, the density based estimation of thermal strain can be given as in Kaymak [78] and Pietzsch *et al.* [79],

$$\mathbf{E}^t = \left( \sqrt[3]{\frac{\rho_R}{\rho}} - 1 \right) \mathbf{I} \quad (4.12)$$

where  $\rho_R$  is the reference density, and  $\rho$  is the current density. Both the methods produce the same results.

### 4.1.2 Plastic strain

The inelastic strain may be either a rate-independent plastic strain or a rate-dependent viscoplastic strain. The plastic strain can be defined through the classical rate-independent plasticity theory. When the equivalent stress exceeds the yield stress, plastic strain occurs. Using a classical rate-independent, isotropic, thermo-plastic material model with the temperature and the phase fraction-dependent constitutive law and systematically employing the yield criterion, loading criterion, flow rule, hardening rule and consistency condition which are discussed separately in detail, the plastic strain rate ( $\dot{\mathbf{E}}^p$ ) can be estimated. This section is formulated based on the published work of Nallathambi *et al.* [38]. The stress-rate can be expressed as [78],

$$\dot{\mathbf{T}} = \mathbb{C} : \left( \dot{\mathbf{E}} - \dot{\mathbf{E}}^t - \dot{\mathbf{E}}^p \right) = \mathbb{C}^{ep} : \dot{\mathbf{E}} \quad (4.13)$$

where  $\mathbb{C}^{ep}$  is the tangent elasto-plastic operator. Fig. 4.1 shows the plastic loading occurs at a point  $\mathbf{T}$  in the direction normal to yield surface because of the strain increment  $\dot{\mathbf{E}}$ .

1. **Yield criterion:** The material starts yielding when the yield criterion is satisfied. The von-Mises yield criteria has the special feature of the smooth surface with convexity which is more suitable for pressure-independent ductile materials and

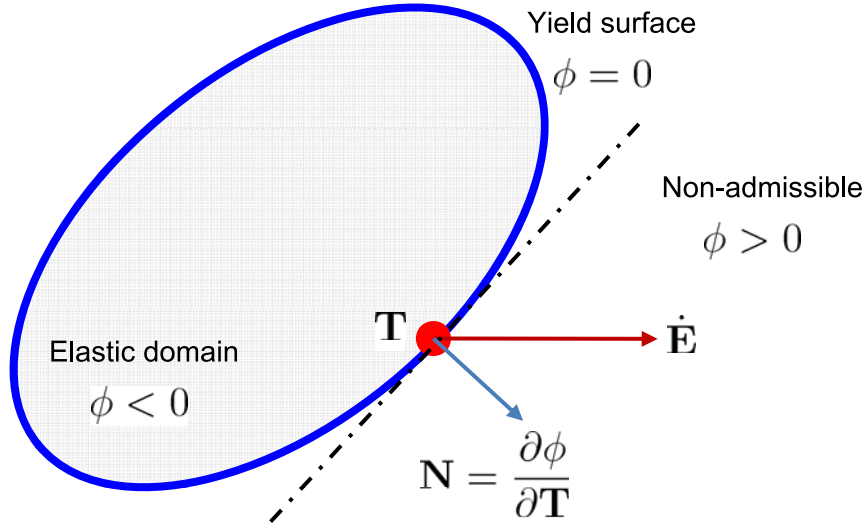


Figure 4.1: Plasticity: plastic loading at  $\mathbf{T}$

given as [78]

$$\phi(\mathbf{T}', \epsilon^p, \theta, f_{pc}) = \|\mathbf{T}'\| - \sqrt{\frac{2}{3}} \sigma_y(\epsilon^p, \theta, f_{pc}) \quad (4.14)$$

where  $\mathbf{T}'$  is the deviatoric stress tensor,  $\epsilon^p$  is the effective plastic strain which is used as a strain hardening internal variable, and  $\sigma_y$  is the temperature and phase fractions dependent yield strength.  $\mathbf{T}'$  and  $\|\mathbf{T}'\|$  can be defined as [78],

$$\mathbf{T}' = \mathbb{P}_2 : \mathbf{T} \quad \text{and} \quad \|\mathbf{T}'\| = \sqrt{\mathbf{T}' : \mathbf{T}'} \quad (4.15)$$

2. **Loading criterion:** The loading criterion can be stated as in [143],

$$\begin{aligned} \phi = 0 \quad \text{and} \quad \dot{\phi}|_{\epsilon^p = \text{const}} &> 0 && \text{loading} \\ \phi = 0 \quad \text{and} \quad \dot{\phi}|_{\epsilon^p = \text{const}} &= 0 && \text{neutral loading} \\ \phi = 0 \quad \text{and} \quad \dot{\phi}|_{\epsilon^p = \text{const}} &< 0 && \text{unloading} \end{aligned}$$

where,  $\dot{\phi} = \frac{\partial \phi}{\partial \mathbf{T}'} : \dot{\mathbf{T}}' + \frac{\partial \phi}{\partial \theta} \dot{\theta} + \frac{\partial \phi}{\partial \epsilon^p} \dot{\epsilon}^p + \frac{\partial \phi}{\partial f_{pc}} \dot{f}_{pc}$

3. **Flow rule:** An associated flow rule is employed and given as in [143]

$$\dot{\mathbf{E}}^P = \dot{\lambda} \frac{\partial \phi}{\partial \mathbf{T}} = \dot{\lambda} \frac{\mathbf{T}'}{\|\mathbf{T}'\|} = \dot{\lambda} \tilde{\mathbf{N}} \quad (4.16)$$

where  $\dot{\lambda}$  and  $\tilde{\mathbf{N}}$  are the plastic multiplier and the flow surface normal or stress deviator direction, respectively. Plastic deformations of metals are incompressible in nature. Therefore, the trace of the plastic strain tensor is zero. Mathematically,

$$\mathbb{P}_1 : \mathbf{E}^P = \mathbf{0} \quad \text{or} \quad \text{tr}(\mathbf{E}^P) = 0$$

4. **Hardening rule:** A linear isotropic hardening rule is considered, and the yield strength is stated as in [143]

$$\sigma_y(\epsilon^p, \theta, f_j) = \sigma_{y_0}(\theta, f_j) + H(\theta, f_j) \epsilon^p \quad (4.17)$$

where  $\sigma_{y_0}$  is the yield strength at the virgin state, and  $H$  is the plastic modulus. The hardening state variable is integrated from the plastic multiplier

$$\epsilon^p = \sqrt{\frac{2}{3}} \dot{\lambda} \quad (4.18)$$

5. **Consistency condition:** In general, the consistency condition ( $\dot{\phi} = 0$ ) yields the value of plastic multiplier  $\dot{\lambda}$ . The isothermal staggered algorithm [32] suggests that the temperature and phase fractions are kept constant (i.e.,  $\dot{\theta} = 0$  and  $\dot{f}_{pc} = 0$ ), the computation of the plastic multiplier [52] reduces to

$$\dot{\lambda} = \frac{\tilde{\mathbf{N}} : \dot{\mathbf{E}}}{1 + \frac{H}{3\mu}} \quad (4.19)$$

The continuum tangential elasto-plastic material operator  $\mathbb{C}^{ep}$  for fixed temperature and phase fractions can be given as in [78],

$$\mathbb{C}^{ep} = \frac{\partial \dot{\mathbf{T}}}{\partial \dot{\mathbf{E}}} = \mathbb{C} - \frac{2\mu}{1 + \frac{H}{3\mu}} \tilde{\mathbf{N}} \otimes \tilde{\mathbf{N}} \quad (4.20)$$

### 4.1.3 Viscoplastic strain

In metals, for instance, the phenomenological effects of time-dependent mechanisms become apparent typically at absolute temperatures higher than around one third of the melting point [144]. This fact is illustrated through the uniaxial tension test with metallic bars at higher temperatures are shown in Fig. 4.2. Fig. 4.2(a) shows the stress-strain curve for various strain rates. In general, the elasticity modulus is independent of the rate of loading but, clearly, the initial yield limit as well as the hardening curve depend strongly on the rate of straining. This rate-dependence is also observed at low temperatures, but usually becomes significant only at higher temperatures. Another aspect of time-dependence is the phenomenon of creep. Fig. 4.2(b) shows the evolution of plastic strains over time in experiments where tensile specimens have been loaded to different stress levels and left at constant stress during long periods of time. The material experiences a continuous plastic flow that is accelerated for higher stress levels.

The strains generated by creep are physically indistinguishable from those result-

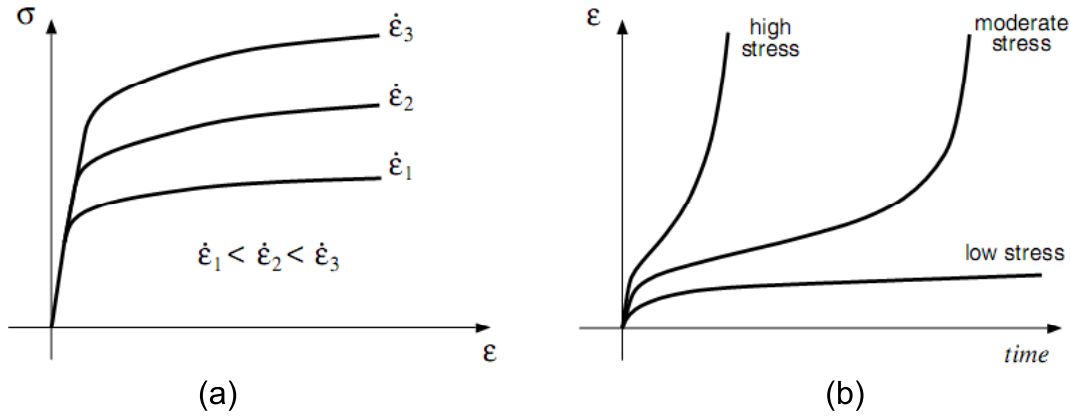


Figure 4.2: Viscoplasticity (Neto *et al.*, 2008): (a) Strain rate dependence: uniaxial tests at different strain rates and (b) Creep: plastic flow at constant stress

ing from the quasi-time-independent plastic flow, particularly at elevated temperatures. Therefore, the plastic and creep deformations can be collectively treated as viscoplastic strain [15]. Viscoplastic models can be grouped into two categories: (a) models with yield surface and (b) models without yield surface. The viscoplastic models with yield surface are conceptually similar to that of the classical rate-independent plasticity except the consistency condition. Therefore, the stress state outside the yield surface, e.g., Perzyna model. In fact, particularly at higher temperatures, many materials can be modeled as flowing whenever under stress; that is, the yield stress is effectively zero. In such cases, a yield surface and a corresponding elastic domain need not to be introduced in the formulation of the theory. Norton's law and Garafalo's law are examples of viscoplastic models without a yield surface which have been widely used .

Similar to the plastic deformation, the viscoplastic deformation is incompressible. Irrespective of the model, the viscoplastic strain rate tensor ( $\dot{\mathbf{E}}^{vp}$ ) can be written in terms of a scalar viscoplastic strain rate ( $\dot{\epsilon}^{vp}$ ) as in [15]

$$\dot{\mathbf{E}}^{vp} = \frac{3}{2} \dot{\epsilon}^{vp} \frac{\mathbf{T}'}{\sigma_{\text{eff}}} = \dot{\epsilon}^{vp} \tilde{\mathbf{N}} \quad (4.21)$$

where  $\tilde{\mathbf{N}}$  is the flow direction,  $\sigma_{\text{eff}}$  is the von Mises equivalent stress, and  $\dot{\epsilon}^{vp}$  is the equivalent viscoplastic strain rate. The flow direction which is defined in the plasticity section is slightly modified in the viscoplastic case for the suitability with all the models of viscoplasticity. Therefore, the flow direction, the equivalent stress, and the equivalent viscoplastic strain are given as

$$\tilde{\mathbf{N}} = \frac{3}{2} \frac{\mathbf{T}'}{\sigma_{\text{eff}}} \quad \text{and} \quad \sigma_{\text{eff}} = \sqrt{\frac{3}{2} \mathbf{T}' : \mathbf{T}'} \quad \text{and} \quad \dot{\epsilon}^{vp} = \sqrt{\frac{2}{3} \dot{\mathbf{E}}^{vp} : \dot{\mathbf{E}}^{vp}} \quad (4.22)$$

The scalar viscoplastic strain rate can be defined by any one of the following models.

### Perzyna model

In the Perzyna model, the excess stress is directly related to the viscoplastic strain rate through the proportionality constant which is known as viscosity ( $\eta$ ). Therefore, the viscoplastic strain rate can be stated as

$$\dot{\epsilon}^{vp} = \frac{1}{\eta} \left\langle \tilde{\phi}(\mathbf{T}) \right\rangle \quad (4.23)$$

where  $\tilde{\phi}$  is the yield function and,  $\langle x \rangle$  is the ramp function which can be defined as

$$\tilde{\phi} = \sigma_{\text{eff}} - \sigma_y(\epsilon^{vp}) \quad \text{and} \quad \langle x \rangle := \frac{x + |x|}{2} \quad (4.24)$$

where  $\sigma_y$  can be defined like isotropic hardening discussed in the plasticity case. When  $\eta \rightarrow 0$ , one can recover the rate-independent case but the problem becomes unconstrained regularization problem which is ill-posed in nature. Further, the closed form solution can be obtained like in plasticity case, with the introduction of the relaxation time ( $\tau = \frac{\eta}{2\mu}$ ) as explained in [52].

### Garafalo law

In DC casting, the solidified metal behavior can be well captured by the Garafalo law which has no concept of yield surface. The Garafalo law can be defined as

$$\dot{\epsilon}^{vp} = A \left[ \sinh \left( \frac{\sigma_{\text{eff}}}{\tilde{\sigma}_o} \right) \right]^{\tilde{n}} e^{-\left(\frac{Q}{RT}\right)} \quad (4.25)$$

where  $A$ ,  $\tilde{\sigma}_o$ , and  $\tilde{n}$  are the material-dependent constants,  $Q$  is the apparent creep activation energy,  $R$  is the universal gas constant, and  $T$  is the absolute temperature. Due to the presence of the temperature term in Eq. (4.25), the evolution of the viscoplastic strain strongly depends on temperature. The exponential term in Eq. (4.25) represents the well known Arrhenius law [144].

### Norton-Hoff law

The Norton-Hoff law is the one of the simplest classical viscoplastic model. The mechanical behavior of mushy can be well modeled by the Norton-Hoff law. This can be stated as

$$\dot{\epsilon}^{vp} = \tilde{k} \left( \frac{\sigma_{\text{eff}}}{\tilde{\sigma}_o} \right)^{\tilde{n}} \quad (4.26)$$



where  $\tilde{k}$ ,  $\tilde{\sigma}_o$ , and  $\tilde{n}$  are temperature-dependent material constants. In the literature, this Norton law is often called *power law*.

## 4.2 Solution Methodology

The finite element method is used to solve the governing differential equation. The stress equilibrium equation has to be put in a more convenient form before using it in finite element formulations. Firstly, the weak form of GDE is derived. Secondly, the FEM is employed to discrete the GDE, and the element matrices and vectors are derived. Finally, the time integration of the constitutive equation at the integration point level is explained separately for elasto-plastic and elasto-viscoplastic cases.

### 4.2.1 Weak form

The higher order mechanical GDE is reduced to lower order with the help of principle of virtual displacement and the direct substitution of natural boundary conditions (NBC). Following the same arguments as used in the solidification problem, for an arbitrary displacement field  $\vec{u}$ , the mechanical equilibrium condition Eq. (4.1) has to satisfy the following integral equation

$$\int_{\Omega} \left[ \nabla \cdot \mathbf{T} + \vec{b}_f \right] \cdot \vec{u} \, d\Omega = 0 \quad (4.27)$$

This is apparently satisfied because the bracket in the integral is zero vector as per Eq. (4.1). By using the property of the divergence operator,

$$\nabla \cdot \left( \mathbf{T} \cdot \vec{u} \right) = (\nabla \cdot \mathbf{T}) \cdot \vec{u} + \mathbf{T} : \nabla \vec{u} \quad (4.28)$$

substituting the above relation in Eq. (4.27) and becomes

$$\int_{\Omega} \nabla \cdot \left( \mathbf{T} \cdot \vec{u} \right) \, d\Omega - \int_{\Omega} \left( \mathbf{T} : \nabla \vec{u} \right) \, d\Omega + \int_{\Omega} \vec{b}_f \cdot \vec{u} \, d\Omega = 0 \quad (4.29)$$

Applying the Gauss divergence theorem on the natural boundary condition Eq. (4.3), the first term in Eq. (4.29) becomes,

$$\int_{\Omega} \nabla \cdot \left( \mathbf{T} \cdot \vec{u} \right) \, d\Omega = \int_{\Gamma_t} \vec{n} \cdot \left( \mathbf{T} \cdot \vec{u} \right) \, d\Gamma_t = \int_{\Gamma_t} \vec{t}_f \cdot \vec{u} \, d\Gamma_t \quad (4.30)$$

The second term in Eq. (4.29) can be represented as,

$$\begin{aligned}
\mathbf{T} : \nabla \vec{u} &= \mathbf{T} : \left( \frac{1}{2} \left[ \nabla \vec{u} + (\nabla \vec{u})^T \right] + \frac{1}{2} \left[ \nabla \vec{u} - (\nabla \vec{u})^T \right] \right) \\
&= \mathbf{T} : \frac{1}{2} \left[ \nabla \vec{u} + (\nabla \vec{u})^T \right] \\
&= \mathbf{T} : \tilde{\mathbf{E}}
\end{aligned} \tag{4.31}$$

where  $\tilde{\mathbf{E}}$  is the second-order tensorial strain tensor. Due to the symmetry of the stress tensor (conservation of angular momentum), only the symmetric part of displacement gradient becomes non-zero during the scalar product. Further, the symmetric part of displacement gradient is the tensorial strain tensor as defined in Eq. (4.4). Substituting Eq. (4.30) and Eq. (4.31) in Eq. (4.29) and it becomes,

$$\int_{\Omega} \mathbf{T} : \tilde{\mathbf{E}} \, d\Omega = \int_{\Gamma_t} \vec{t}_f \cdot \vec{u} \, d\Gamma_t + \int_{\Omega} \vec{b}_f \cdot \vec{u} \, d\Omega \tag{4.32}$$

This is the final weak form of GDE. The engineering strain tensor  $\mathbf{E}_{\text{eng}}$  can be obtained from the tensorial strain tensor  $\mathbf{E}$  by multiplying the shear components by a factor of 2.

## 4.2.2 Finite element method

Before applying FEM to the weak form, the matrix conversion of tensor quantities has to be established. Due to the symmetry, the fourth-order tensors can be simplified in a matrix form and, similarly, the second-order tensors can be represented in a vector form. Therefore, the fourth-order identity tensor ( $\mathbb{I}$ ), and second-order identity tensor ( $\mathbf{I}$ ) are represented as,

$$\mathbf{I} = \begin{bmatrix} 1 & 0 & 0 & 0 & 0 & 0 \\ 0 & 1 & 0 & 0 & 0 & 0 \\ 0 & 0 & 1 & 0 & 0 & 0 \\ 0 & 0 & 0 & 1 & 0 & 0 \\ 0 & 0 & 0 & 0 & 1 & 0 \\ 0 & 0 & 0 & 0 & 0 & 1 \end{bmatrix} \quad \text{and} \quad \mathbf{I} = \left\{ \begin{array}{c} 1 \\ 1 \\ 1 \\ 0 \\ 0 \\ 0 \end{array} \right\} \tag{4.33}$$

With the help of Eq. (4.33), the fourth-order projectors in Eq. (4.7) & (4.8) can be simplified as

$$\mathbf{P}_1 = \frac{1}{3} \begin{bmatrix} 1 & 1 & 1 & 0 & 0 & 0 \\ 1 & 1 & 1 & 0 & 0 & 0 \\ 1 & 1 & 1 & 0 & 0 & 0 \\ 0 & 0 & 0 & 0 & 0 & 0 \\ 0 & 0 & 0 & 0 & 0 & 0 \\ 0 & 0 & 0 & 0 & 0 & 0 \end{bmatrix} \quad \text{and} \quad \mathbf{P}_2 = \frac{1}{3} \begin{bmatrix} 2 & -1 & -1 & 0 & 0 & 0 \\ -1 & 2 & -1 & 0 & 0 & 0 \\ -1 & -1 & 2 & 0 & 0 & 0 \\ 0 & 0 & 0 & 3 & 0 & 0 \\ 0 & 0 & 0 & 0 & 3 & 0 \\ 0 & 0 & 0 & 0 & 0 & 3 \end{bmatrix} \quad (4.34)$$

The fourth-order elasticity tensor in Eq. (4.6) can be simplified as

$$\mathbf{C} = \begin{bmatrix} \kappa + \frac{2\mu}{3} & \kappa - \frac{\mu}{3} & \kappa - \frac{\mu}{3} & 0 & 0 & 0 \\ \kappa - \frac{\mu}{3} & \kappa + \frac{2\mu}{3} & \kappa - \frac{\mu}{3} & 0 & 0 & 0 \\ \kappa - \frac{\mu}{3} & \kappa - \frac{\mu}{3} & \kappa + \frac{2\mu}{3} & 0 & 0 & 0 \\ 0 & 0 & 0 & \mu & 0 & 0 \\ 0 & 0 & 0 & 0 & \mu & 0 \\ 0 & 0 & 0 & 0 & 0 & \mu \end{bmatrix} \quad (4.35)$$

Eq. (4.35) is not exactly equivalent form of Eq. (4.6). While writing in matrix form, the elasticity tensor is written in a slightly modified form as,

$$\mathbf{C} = 3 \kappa \mathbf{P}_1 + 2 \mu \mathbf{P}_2 \mathbf{L}^{-1} \quad (4.36)$$

where  $\mathbf{L}$  is the constant matrix which can be defined as,

$$\mathbf{L} = \begin{bmatrix} 1 & 0 & 0 & 0 & 0 & 0 \\ 0 & 1 & 0 & 0 & 0 & 0 \\ 0 & 0 & 1 & 0 & 0 & 0 \\ 0 & 0 & 0 & 2 & 0 & 0 \\ 0 & 0 & 0 & 0 & 2 & 0 \\ 0 & 0 & 0 & 0 & 0 & 2 \end{bmatrix} \quad (4.37)$$

The reason for the insertion of  $\mathbf{L}^{-1}$  in Eq. (4.36) is that the engineering strain is used while writing the constitutive equation Eq. (4.5). Therefore, the engineering strain tensor  $\mathbf{E}_{\text{eng}}$ , and stress tensor  $\mathbf{T}$  can be written in vector form as,

$$\begin{aligned} \mathbf{E}_{\text{eng}} = \mathbf{L} \mathbf{E} &= \{ \epsilon_{xx} \quad \epsilon_{yy} \quad \epsilon_{zz} \quad 2\epsilon_{xy} \quad 2\epsilon_{xz} \quad 2\epsilon_{yz} \}^T \\ \mathbf{T} &= \{ \sigma_{xx} \quad \sigma_{yy} \quad \sigma_{zz} \quad \tau_{xy} \quad \tau_{xz} \quad \tau_{yz} \}^T \end{aligned} \quad (4.38)$$

where  $\mathbf{E}$  is the vector form of tensorial strain tensor. The double contraction or scalar product of two tensor quantities can be written in matrix form as,

$$\mathbf{T} : \mathbf{E} := \mathbf{T}^T \mathbf{L} \mathbf{E} = \mathbf{T}^T \mathbf{E}_{\text{eng}} = \mathbf{E}_{\text{eng}}^T \mathbf{T} \quad (4.39)$$

For the sake of simplicity, now onwards  $\mathbf{E}_{\text{eng}}$  is denoted as  $\mathbf{E}$ . With this notion, the weak form of GDE for a single element can be written as

$$\int_{\Omega^e} \tilde{\mathbf{E}}^{eT} \mathbf{T}^e d\Omega^e = \int_{\Gamma_t^e} \tilde{\mathbf{U}}^{eT} \mathbf{T}_f^e d\Gamma_t^e + \int_{\Omega^e} \tilde{\mathbf{U}}^{eT} \mathbf{B}_f^e d\Omega^e \quad (4.40)$$

where  $\hat{\mathbf{U}}^e$ ,  $\mathbf{T}_f^e$ , and  $\mathbf{B}_f^e$  are the element displacement, traction, and body force vectors respectively. This can be stated as

$$\hat{\mathbf{U}}^e = \{u^e \ v^e \ w^e\}^T \quad , \quad \mathbf{T}_f^e = \{t_{fx}^e \ t_{fy}^e \ t_{fz}^e\}^T \quad , \quad \mathbf{B}_f^e = \{b_{fx}^e \ b_{fy}^e \ b_{fz}^e\}^T \quad (4.41)$$

Eq. (4.40) is in the suitable form for the application of the finite element method. Therefore, the  $x$ ,  $y$  and  $z$  components of the element nodal displacements are given as

$$u^e = \mathbf{N}^T \bar{\mathbf{U}}^e \quad , \quad v^e = \mathbf{N}^T \bar{\mathbf{V}}^e \quad , \quad w^e = \mathbf{N}^T \bar{\mathbf{W}}^e \quad (4.42)$$

where  $\bar{\mathbf{U}}^e$ ,  $\bar{\mathbf{V}}^e$ , and  $\bar{\mathbf{W}}^e$  are element nodal displacements in  $x$ ,  $y$  and  $z$  directions respectively. Therefore, the element displacement vector  $\hat{\mathbf{U}}^e$  can be written as

$$\hat{\mathbf{U}}^e = \Psi^e \mathbf{U}^e \quad (4.43)$$

where  $\Psi^e$  and  $\mathbf{U}^e$  are the element interpolation matrix and element nodal displacement vector respectively. Considering  $n$  as the number of nodes per element, the above mentioned quantities can be stated as,

$$\Psi^e = \begin{bmatrix} \mathbf{N}_1 & 0 & 0 & \mathbf{N}_2 & 0 & 0 & \cdots & \mathbf{N}_n & 0 & 0 \\ 0 & \mathbf{N}_1 & 0 & 0 & \mathbf{N}_2 & 0 & \cdots & 0 & \mathbf{N}_n & 0 \\ 0 & 0 & \mathbf{N}_1 & 0 & 0 & \mathbf{N}_2 & \cdots & 0 & 0 & \mathbf{N}_n \end{bmatrix} \quad (4.44)$$

and

$$\mathbf{U}^e = \{\bar{\mathbf{U}}_1^e \ \bar{\mathbf{V}}_1^e \ \bar{\mathbf{W}}_1^e \ \bar{\mathbf{U}}_2^e \ \bar{\mathbf{V}}_2^e \ \bar{\mathbf{W}}_2^e \ \cdots \ \bar{\mathbf{U}}_n^e \ \bar{\mathbf{V}}_n^e \ \bar{\mathbf{W}}_n^e\}^T \quad (4.45)$$

The element strain can be given as,

$$\mathbf{E}^e = \begin{bmatrix} \frac{\partial}{\partial x} & 0 & 0 & \frac{\partial}{\partial y} & \frac{\partial}{\partial z} & 0 \\ 0 & \frac{\partial}{\partial y} & 0 & \frac{\partial}{\partial x} & 0 & \frac{\partial}{\partial z} \\ 0 & 0 & \frac{\partial}{\partial z} & 0 & \frac{\partial}{\partial x} & \frac{\partial}{\partial y} \end{bmatrix}^T \begin{Bmatrix} u^e \\ v^e \\ w^e \end{Bmatrix} = \Pi \hat{\mathbf{U}}^e \quad (4.46)$$

Finally, the element strain vector becomes,

$$\mathbf{E}^e = \mathbf{B} \mathbf{U}^e \quad \text{where} \quad \mathbf{B} = \Pi \Psi^e \quad (4.47)$$

where  $\mathbf{B}$  is the strain-displacement matrix and  $\Pi$  is the derivative operator. Substituting Eq. (4.47) in the weak form Eq. (4.40) and becomes,

$$\int_{\Omega^e} \left[ \tilde{\mathbf{U}}^{eT} \mathbf{B}^T \mathbf{T}^e \right] d\Omega^e = \int_{\Gamma_t^e} \left[ \tilde{\mathbf{U}}^{eT} \Psi^{eT} \mathbf{T}_f^e \right] d\Gamma_t^e + \int_{\Omega^e} \left[ \tilde{\mathbf{U}}^{eT} \Psi^{eT} \mathbf{B}_f^e \right] d\Omega^e \quad (4.48)$$

Substituting the elastic constitutive relation  $\mathbf{T}^e = \mathbf{C} \mathbf{E}^e$ , the total potential to be minimized can be written as

$$\Phi^e(\tilde{\mathbf{U}}^e) = \tilde{\mathbf{U}}^{eT} \mathbf{F}^e - \tilde{\mathbf{U}}^{eT} \mathbf{K}^e \mathbf{U}^e \quad (4.49)$$

where the element quantities are

$$\mathbf{K}^e = \int_{\Omega^e} \left[ \mathbf{B}^T \mathbf{C} \mathbf{B} \right] d\Omega^e \quad (4.50)$$

$$\mathbf{F}^e = \int_{\Gamma_t^e} \left[ \Psi_e^T \mathbf{T}_f^e \right] d\Gamma_t^e + \int_{\Omega^e} \left[ \Psi_e^T \mathbf{B}_f^e \right] d\Omega^e \quad (4.51)$$

From the element quantities, the global matrices and vectors can be obtained based on the element-nodal mappings. Therefore, the total global potential can be written as

$$\Phi(\tilde{\mathbf{U}}) = \tilde{\mathbf{U}}^T \mathbf{F} - \tilde{\mathbf{U}}^T \mathbf{K} \mathbf{U} \quad (4.52)$$

From the total potential, the residual vector ( $\mathbf{R}$ ) can be obtained as

$$\mathbf{R} = \frac{\partial \Phi}{\partial \tilde{\mathbf{U}}} = \mathbf{F} - \mathbf{K} \mathbf{U} \quad (4.53)$$

There exists a unique displacement profile for a particular external force  $\mathbf{F}$  which makes the residual zero and it becomes

$$\boxed{\mathbf{K} \mathbf{U} = \mathbf{F}}$$

Once applying the EBC, the equation has to be solved for the displacement. The material law considered is an elastic one. When it comes to elasto-plastic or elasto-viscoplastic, the constitutive relation exist only in the incremental form. These issues are discussed elaborately in the next section.

### 4.2.3 Iterative incremental scheme

Treating  $t_n$  as the previous time,  $\Delta t$  is the time interval or time step size, and  $t_{n+1} = t_n + \Delta t$  is the current time time. Further,  $\Delta U$  is the time-increment of displacement vector at  $(n + 1)^{\text{th}}$  time step, and  $\delta U$  is the current iterative displacement vector at  $(i + 1)^{\text{th}}$  iteration. The total displacement, and incremental displacement can be written as

$$U^{n+1} = U^n + \Delta U \quad (4.54)$$

$$\Delta U_{i+1} = \Delta U_i + \delta U \quad (4.55)$$

Combining the two equations and the total displacement at the current time-step and the current iteration becomes

$$U_{i+1}^{n+1} = U_i^{n+1} + \delta U \quad (4.56)$$

The Newton-Raphson method is already well explained in the solidification problem. Following the same argument,

$$\begin{aligned} \delta E^e &= \mathbf{B} \delta U^e & (4.57) \\ \delta T^e &= \mathbf{C}_i^{epn+1} \delta E^e = \mathbf{C}_i^{epn+1} \mathbf{B} \delta U^e \\ E_{i+1}^{en+1} &= E_i^{en+1} + \delta E^e \\ T_{i+1}^{en+1} &= T_i^{en+1} + \mathbf{C}_i^{epn+1} \mathbf{B} \delta U^e \end{aligned} \quad (4.58)$$

where  $\mathbf{C}^{ep}$  is elemental consistent elasto-plastic/elasto-viscoplastic operator. At the beginning of the current time step, the following initialization is adopted:

$$\begin{aligned} E_1^{en+1} &= E^{en} + \Delta E^{et} \\ T_1^{en+1} &= T^{en} \end{aligned} \quad (4.59)$$

where  $\Delta E^{et}$  is the elemental increment thermal strain. The final form of mechanical equilibrium equation becomes

$$\mathbf{K}_i^{n+1} \delta U = F^{n+1} - R_i^{n+1} \quad (4.60)$$

where  $\mathbf{K}$  is the global tangent stiffness matrix,  $F$  is the global external force vector, and  $R$  is the global internal force vector from the previous iteration. The elemental forms of matrices and vectors are given as in [139]

$$\begin{aligned} \mathbf{K}_i^{en+1} &= \int_{\Omega^e} [\mathbf{B}^T \mathbf{C}^{epn+1} \mathbf{B}] d\Omega^e \\ F^{en+1} &= \int_{\Gamma_t^e} [\Psi_e^T T_f^{en+1}] d\Gamma_t^e + \int_{\Omega^e} [\Psi_e^T B_f^{en+1}] d\Omega^e \\ R_i^{en+1} &= \int_{\Omega^e} [\mathbf{B}^T T_i^{en+1}] d\Omega^e \end{aligned} \quad (4.61)$$

The convergence criteria at the current iteration is evaluated using the current iterative displacement vector, and the current total displacement vector as

$$\left( \frac{\delta U^T \delta U}{U^T U} \right) < \epsilon \quad (4.62)$$

where  $\epsilon$  is the computational zero and taken as  $10^{-6}$ . The above mentioned iterative-increment scheme can be summarized as:

Table 4.1: Displacement field: Global iterative-increment scheme

- |   |
|---|
| <ol style="list-style-type: none"> <li>1. Set <math>U_1^{n+1} = U^n</math>, <math>\Delta U_1 = 0</math>, <math>i = 1</math>.</li> <li>2. Compute <math>\mathbf{K}_i^{n+1}</math>, <math>F^{n+1}</math>, and <math>R_i^{n+1}</math> by using <math>U_i^{n+1}</math></li> <li>3. Find <math>\delta U = (\mathbf{K}_i^{n+1})^{-1} [F^{n+1} - R_i^{n+1}]</math></li> <li>4. Update <math>U_{i+1}^{n+1} = U_i^{n+1} + \delta U</math>, <math>\Delta U_{i+1} = \Delta U_i + \delta U</math>, <math>i = i + 1</math></li> <li>5. Check convergence criteria using Eq. (4.62).</li> <li>6. If step.5 is true goto step.1 else goto step.2.</li> </ol> |
|---|

#### 4.2.4 Integration of plastic constitutive relation

In the finite element procedure as discussed in the previous section, the determination of the tangent stiffness matrix and internal reaction vector demands the integration of constitutive relations. Different procedures are followed for the integration of elasto-plastic and elasto-viscoplastic constitutive relations. The plastic multiplier in the elastic-

plastic case can be expressed in a closed form. In contrast to the elasto-plastic case, the iterative procedure is followed for the integration of the rate equation in the elasto-viscoplastic case which is discussed in a more detailed manner in the next section.

From the global iterations,  $U_i^{n+1}$  is the known displacement vector at the beginning of the  $n + 1^{th}$  time step and  $i + 1^{th}$  iteration. Using  $U_i^{n+1}$ , the components of total strain at the integration point can be computed using the relation  $E_i^{n+1} = \mathbf{B} U_i^{n+1}$ . The thermal strain ( $E^{t^{n+1}}$ ) at the current time step can be computed using Eq. (4.10). It is assumed that the previous plastic strain ( $E_{i-1}^{p^{n+1}}$ ) at the integration point is known. Therefore, the trial stress can be stated as,

$$\mathbf{T}_i^{n+1 trial} = \mathbf{T}^{trial} = \mathbf{C} \left( E_i^{n+1} - E^{t^{n+1}} - E_{i-1}^{p^{n+1}} \right) \quad (4.63)$$

From the trial stress, the final stress can be computed as

$$\begin{aligned} \mathbf{T}_i^{n+1} = \mathbf{T} &= \mathbf{C} \left( E_i^{n+1} - E^{t^{n+1}} - \left[ E_{i-1}^{p^{n+1}} + \dot{E}^p \Delta t \right] \right) \\ &= \mathbf{T}^{trial} - \mathbf{C} \dot{E}^p \Delta t \end{aligned} \quad (4.64)$$

The engineering plastic strain rate can be approximated using the flow rule stated in Eq. (4.16) as

$$\begin{aligned} \left( \dot{E}^p \right)_i^{n+1} &= \frac{E_{i-1}^{p^{n+1}} - E_{i-1}^{p^n}}{\Delta t} = \frac{\delta E^p}{\Delta t} = \frac{\lambda_i^{n+1} - \lambda_i^n}{\Delta t} \mathbf{L} \tilde{N}_i^{n+1} \\ &= \frac{\delta \lambda}{\Delta t} \mathbf{L} \tilde{N}_i^{n+1} \end{aligned} \quad (4.65)$$

where  $\delta \lambda$  is the iterative plastic multiplier, and  $\tilde{N}$  is the trial stress deviator direction. The trial stress deviator and its direction can be stated as

$$\mathbf{S}^{trial} = \mathbf{P}_2 \mathbf{T}^{trial} \quad \text{and} \quad \tilde{N} = \frac{\mathbf{S}^{trial}}{\|\mathbf{S}^{trial}\|} \quad \text{where} \quad \|\mathbf{S}^{trial}\| = \sqrt{(\mathbf{S}^{trial})^T \mathbf{L} \mathbf{S}^{trial}} \quad (4.66)$$

substituting Eq. (4.65) and Eq. (4.66) in Eq. (4.64),

$$\begin{aligned} \mathbf{T} &= \mathbf{T}^{trial} - \mathbf{C} \delta \lambda \mathbf{L} \tilde{N} \\ \mathbf{S} &= \mathbf{S}^{trial} - 2\mu \delta \lambda \mathbf{L}^{-1} \mathbf{L} \tilde{N} \\ \|\mathbf{S}\| &= \|\mathbf{S}^{trial}\| - 2\mu \delta \lambda \end{aligned} \quad (4.67)$$

It is assumed that the trail deviatoric direction and final deviatoric stress direction are assumed to coincide. Eq. (4.64) does not contain any time terms due to the assumption



of rate-independency. The trial yield function can be stated as

$$\phi^{trial} = \|\mathbf{S}^{trial}\| - \sqrt{\frac{2}{3}} (\sigma_{yo} + H \epsilon^{pn+1}) \quad (4.68)$$

The plastic flow occurs when  $\phi^{trial} > 0$  in such a manner that  $\phi = 0$ . This gives the expression for the plastic multiplier in an explicit manner as in [52],

$$\delta\lambda = \frac{\phi^{trial}}{2\mu \left(1 + \frac{H}{3\mu}\right)} \quad (4.69)$$

The consistent tangent elasto-plastic operator can be obtained as

$$\begin{aligned} \mathbf{C}^{ep} &= \frac{\partial \mathbf{T}_i^{n+1}}{\partial \mathbf{E}_i^{n+1}} = \mathbf{C} - \mathbf{C} \mathbf{L} \frac{\partial (\delta\lambda \tilde{\mathbf{N}})}{\partial \mathbf{E}_i^{n+1}} \\ &= \mathbf{C} - \mathbf{C} \mathbf{L} \left( \tilde{\mathbf{N}} \left\{ \frac{\partial \delta\lambda}{\partial \mathbf{E}} \right\}^T + \delta\lambda \frac{\partial \tilde{\mathbf{N}}}{\partial \mathbf{E}} \right) \end{aligned} \quad (4.70)$$

This expression is slightly different from the continuum elasto-plastic operator Eq. (4.20) because of the algorithm followed. The derivative in Eq. (4.70) can be obtained as

$$\begin{aligned} \frac{\partial \delta\lambda}{\partial \mathbf{E}} &= \frac{\partial \delta\lambda}{\partial \mathbf{S}^{trial}} \frac{\partial \mathbf{S}^{trial}}{\partial \mathbf{E}} = \left( \frac{1}{1 + \frac{H}{3\mu}} \right) \tilde{\mathbf{N}} \\ \frac{\partial \tilde{\mathbf{N}}}{\partial \mathbf{E}} &= \frac{\partial \tilde{\mathbf{N}}}{\partial \mathbf{S}^{trial}} \frac{\partial \mathbf{S}^{trial}}{\partial \mathbf{E}} = \frac{2\mu}{\|\mathbf{S}^{trial}\|} \left( \mathbf{P}_2 \mathbf{L}^{-1} - \tilde{\mathbf{N}} \tilde{\mathbf{N}}^T \right) \end{aligned} \quad (4.71)$$

substituting Eq. (4.71) in Eq. (4.70), we obtain

$$\mathbf{C}^{ep} = \mathbf{C} - \left( \frac{2\mu}{1 + \frac{H}{3\mu}} \right) \tilde{\mathbf{N}} \tilde{\mathbf{N}}^T - \frac{4\mu^2 \delta\lambda}{\|\mathbf{S}^{trial}\|} \left( \mathbf{P}_2 \mathbf{L}^{-1} - \tilde{\mathbf{N}} \tilde{\mathbf{N}}^T \right) \quad (4.72)$$

The stress, plastic strain, and equivalent plastic strain can be updated as

$$\begin{aligned} \mathbf{T}_i^{n+1} &= \mathbf{T}^{trial} - 2\mu \delta\lambda \tilde{\mathbf{N}} \\ \mathbf{E}_i^{pn+1} &= \mathbf{E}_{i-1}^{pn+1} + \delta\lambda \mathbf{L} \tilde{\mathbf{N}} \\ \epsilon_i^{pn+1} &= \epsilon_{i-1}^{pn+1} + \sqrt{\frac{2}{3}} \delta\lambda \end{aligned} \quad (4.73)$$

Once determined  $\mathbf{T}_i^{n+1}$ , and  $\mathbf{C}^{ep}$ , the internal reaction vector and tangent stiffness matrix has to be computed according to Eq. (4.61). The iterative stress and iterative-incremental plastic strain are computed based on the previous iteration, not from the previously

converged time-step. However, use of an iterative scheme based on the intermediate non converged values is questionable for a problem which is physically path-dependent. In addition, if *unloading* within the iterative process occurs, a new iteration is necessary which starts from the converged stresses state  $\mathbf{T}^n$ .

#### 4.2.5 Integration of viscoplastic constitutive relation

In contrast to the plastic case,  $\Delta U_i$  is used for the computation of element quantities. From  $\Delta U_i$ ,  $\Delta E_i$  can be obtained from the relation  $\Delta E_i = \mathbf{B} \Delta U_i$ . The subscript  $i$  is the global iteration index which is disregarded for the sake of simplicity.

The fully implicit backward Euler integration scheme is employed for the derivation of necessary equations. Therefore, the stress update in the local integration point level is stated as

$$\mathbf{T}^{n+1} = \mathbf{T}^n + \Delta \mathbf{T} \quad (4.74)$$

where  $\mathbf{T}^n$  is the known previous time-step equilibrium stress. The incremental stress  $\Delta \mathbf{T}$  can be expressed by the thermo-elasto-viscoplastic constitutive relation as

$$\Delta \mathbf{T} = \mathbf{C} (\Delta \mathbf{E} - \Delta \mathbf{E}^t - \Delta \mathbf{E}^{vp}) \quad (4.75)$$

The viscoplastic strain can be approximated using the backward Euler time difference and substituting Eq. (4.21) as

$$\left( \dot{\mathbf{E}}^{vp} \right)^{n+1} = \frac{(\mathbf{E}^{vp})^{n+1} - (\mathbf{E}^{vp})^n}{\Delta t} = \frac{\Delta \mathbf{E}^{vp}}{\Delta t} = (\dot{\epsilon}^{vp})^{n+1} \tilde{\mathbf{N}}^{n+1} \quad (4.76)$$

where  $\tilde{\mathbf{N}}$  is flow direction vector which can be given as,

$$\tilde{\mathbf{N}} = \frac{3}{2 \sigma_{\text{eff}}} \mathbf{L} \mathbf{S} = \sqrt{\frac{3}{2}} \left( \frac{1}{\sqrt{\mathbf{S}^T \mathbf{L} \mathbf{S}}} \right) \mathbf{L} \mathbf{S} \quad (4.77)$$

where  $\mathbf{S} = \mathbf{P}_2 \mathbf{T}$  is the stress deviator. Therefore, the current stress becomes

$$\mathbf{T}^{n+1} = \mathbf{T}^n + \mathbf{C} \left( \Delta \mathbf{E} - \Delta \mathbf{E}^t - \Delta t (\dot{\epsilon}^{vp})^{n+1} \tilde{\mathbf{N}}^{n+1} \right) \quad (4.78)$$

This equation is implicit in nature, therefore the iterative scheme is adopted. Keeping  $k$  as the previous local iteration counter, the residual can be stated as in [30],

$$\bar{\mathbf{R}}_k^{n+1} = \mathbf{T}_k^{n+1} - \mathbf{T}^n - \mathbf{C} \left( \Delta \mathbf{E} - \Delta \mathbf{E}^t - \Delta t (\dot{\epsilon}^{vp})_k^{n+1} \tilde{\mathbf{N}}_k^{n+1} \right) \quad (4.79)$$

Thus, consider a first-order Taylor series expansion of the residual vector,

$$\bar{\mathbf{R}}_{k+1}^{n+1} = \bar{\mathbf{R}}_k^{n+1} + \frac{\partial \bar{\mathbf{R}}_k^{n+1}}{\partial \mathbf{T}_k^{n+1}} d\mathbf{T} \quad (4.80)$$

where  $d\mathbf{T}$  is the local iterative-increment of stress vector at integration point. Forcing  $\bar{\mathbf{R}}_{k+1}^{n+1}$  to reach zero,

$$d\mathbf{T} = - \left[ \frac{\partial \bar{\mathbf{R}}_k^{n+1}}{\partial \mathbf{T}_k^{n+1}} \right]^{-1} \bar{\mathbf{R}}_k^{n+1} = - \bar{\mathbf{K}}^{-1} \bar{\mathbf{R}}_k^{n+1} \quad (4.81)$$

where the Jacobian matrix  $\bar{\mathbf{K}}$  can be derived from Eq. (4.79) as

$$\bar{\mathbf{K}} = \mathbf{I} + \mathbf{C} \Delta t \left( \frac{\partial \dot{\epsilon}^{vp}}{\partial \mathbf{T}} \tilde{\mathbf{N}}^T + \dot{\epsilon}^{vp} \frac{\partial \tilde{\mathbf{N}}}{\partial \mathbf{T}} \right)_k^{n+1} \quad (4.82)$$

$\dot{\epsilon}^{vp}$ , and  $\tilde{\mathbf{N}}$  are functions of current local iterative stress vector  $\mathbf{T}_k^{n+1}$ . Therefore

$$\begin{aligned} \left. \frac{\partial \dot{\epsilon}^{vp}}{\partial \mathbf{T}} \right|_k^{n+1} &= \frac{\partial \dot{\epsilon}^{vp}}{\partial \sigma_{\text{eff}}} \left[ \frac{\partial \mathbf{T}'}{\partial \mathbf{T}} \right] \left\{ \frac{\partial \sigma_{\text{eff}}}{\partial \mathbf{T}'} \right\} = \frac{\partial \dot{\epsilon}^{vp}}{\partial \sigma_{\text{eff}}} \tilde{\mathbf{N}} \\ \left. \frac{\partial \tilde{\mathbf{N}}}{\partial \mathbf{T}} \right|_k^{n+1} &= \frac{\partial \tilde{\mathbf{N}}}{\partial \mathbf{T}'} \left[ \frac{\partial \mathbf{T}'}{\partial \mathbf{T}} \right] = \frac{3}{2 \sigma_{\text{eff}}} \left( \mathbf{P}_2 \mathbf{L} - \frac{2}{3} \tilde{\mathbf{N}} \tilde{\mathbf{N}}^T \right) \end{aligned} \quad (4.83)$$

substituting Eq. (4.83) in Eq. (4.82)

$$\bar{\mathbf{K}} = \mathbf{I} + 2\mu \Delta t \left[ \left( \frac{\partial \dot{\epsilon}^{vp}}{\partial \sigma_{\text{eff}}} - \frac{\dot{\epsilon}^{vp}}{\sigma_{\text{eff}}} \right) \mathbf{L}^{-1} \tilde{\mathbf{N}} \tilde{\mathbf{N}}^T + \frac{3}{2} \frac{\dot{\epsilon}^{vp}}{\sigma_{\text{eff}}} \mathbf{P}_2 \right]_k^{n+1} \quad (4.84)$$

The iterative form of stress update becomes

$$\mathbf{T}_{k+1}^{n+1} = \mathbf{T}_k^{n+1} + d\mathbf{T} \quad (4.85)$$

Finally, the consistent tangent elasto-viscoplastic operator may be derived directly from the integration scheme and is defined as

$$\mathbf{C}^{ep} = \bar{\mathbf{K}}^{-1} \mathbf{C} \quad (4.86)$$

Once determined  $\mathbf{C}^{ep}$ , and  $\mathbf{T}_i^{n+1}$ , the tangent stiffness matrix and the residual vector can be computed using the Eq. (4.61). It is well known that the Newton-Raphson method exhibits its fast rate of convergence and stability only when the trial solution is close to the converged value. In reality, for highly nonlinear problems the trial solution may be far

away from the real solution. Thus, applying a full step-size correction in the iteration, the updated vector may actually be detrimental to the solution, causing convergence difficulties. Therefore, a line-search algorithm is implemented within each iteration to overcome the divergence difficulty. The line-search algorithm is well explained in the solidification problem. The above-mentioned integration point computations for the elasto-viscoplastic problem can be summarized as follows:

Table 4.2: Displacement field: Local integration point computation for elasto-viscoplastic problem

- |  |
|--|
| <ol style="list-style-type: none"> <li>1. input: <math>\Delta U_i</math>, <math>\Delta E^t</math>, and <math>T^n</math>. Set <math>T_1^{n+1} = T^n</math>, and <math>k = 1</math>.</li> <li>2. Compute <math>\bar{R}_k^{n+1}</math>, and <math>\bar{K}</math> by using Eq. (4.79) and Eq. (4.82).</li> <li>3. Find <math>dT = \bar{K}^{-1} \bar{R}_k^{n+1}</math>; <math>s_1 = dT^T \bar{R}_k^{n+1}</math>, <math>r_1 = 1</math>, <math>\eta_1 = 0</math>, <math>m = 1</math></li> <li>4. Update <math>T_{k2}^{n+1} = T_k^{n+1} + dT</math>. Find <math>\bar{R}(T_{k2}^{n+1})</math>; <math>s_2 = dT^T \bar{R}_{k2}^{n+1}</math>, <math>r_2 = s_2/s_1</math>, <math>\eta_2 = 1</math>, <math>m = 2</math></li> <li>5. Call line search algorithm <b>if</b> <math> r_2  &gt; 0.8</math> and find <math>\eta</math>. <b>else</b> <math>\eta = 1</math>.</li> <li>6. Update <math>T_{k+1}^{n+1} = T_k^{n+1} + \eta dT</math>, and <math>k = k + 1</math>.</li> <li>7. <b>if</b> <math>\ dT\  &gt; \text{tol}</math>, go to step.2 <b>else</b> go to next step.</li> <li>8. Find <math>C^{ep} = \bar{K}^{-1} C</math> and compute <math>K_i^{n+1}</math>.</li> <li>9. Compute <math>R_i^{n+1}</math> using <math>T_k^{n+1}</math> and update <math>T_k^{n+1}</math> as <math>T_i^{n+1}</math></li> </ol> |
|--|

### 4.3 Element computations

As discussed in the solidification problem, a generalized 2-D mechanical element is developed which can handle the following problems: (a) plane strain problems and (b) axisymmetric problems. Using an isoparametric element formulation, the global coordinates and the displacement field inside the element can be given as

$$\{x \ y\} = N^T \{X \ Y\} \quad \text{and} \quad u^e = N^T \bar{U}^e \quad , \quad v^e = N^T \bar{V}^e \quad (4.87)$$

where  $N$  is the shape function vector,  $\{X \ Y\}$  is the element nodal coordinates matrix in which  $X$  and  $Y$  are nodal  $x$  and  $y$  coordinates vector,  $\bar{U}^e$ , and  $\bar{V}^e$  are the element nodal displacements in  $x$ , and  $y$  directions, respectively.

The total strain is the derivative of the displacement field. Therefore, a linear total strain field is obtained for the 9-noded element. In order to have a linear stress field, the thermal strains must also be linear. Since the thermal strains are linear functions of temperature, the thermal field must also be linear. Such a linear thermal field can be provided by 4-noded elements. This is the reason for the selection of 4-noded thermal element and 9-noded mechanical element. The layout of a typical mechanical element is

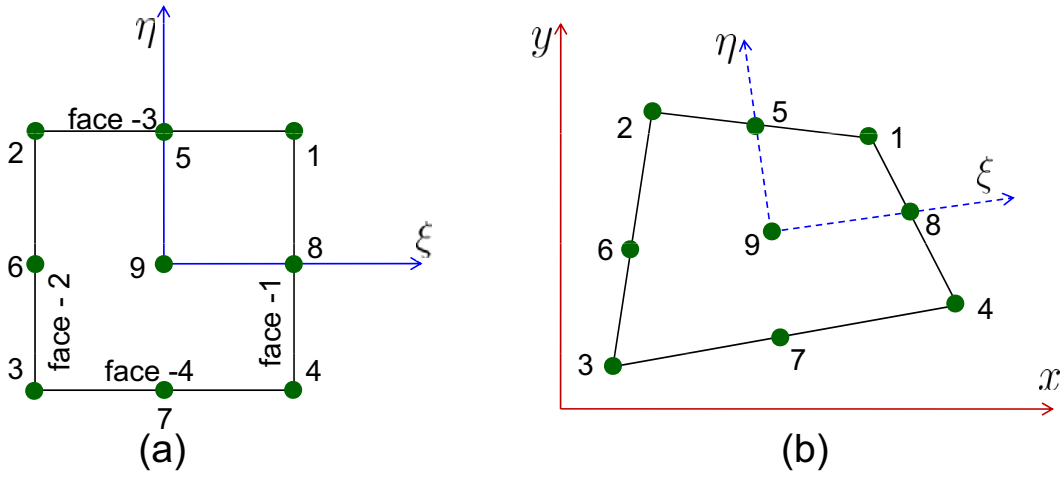


Figure 4.3: 9-noded quadrilateral element: (a) parent element and (b) typical element

indicated in Fig. 4.3. The shape function vector for a 9-noded quadrilateral element is stated as

$$\mathbf{N} = \begin{Bmatrix} N_1 \\ N_2 \\ N_3 \\ N_4 \\ N_5 \\ N_6 \\ N_7 \\ N_8 \\ N_9 \end{Bmatrix} = \begin{Bmatrix} 0.25 (\xi^2 + \xi) (\eta^2 + \eta) \\ 0.25 (\xi^2 - \xi) (\eta^2 + \eta) \\ 0.25 (\xi^2 - \xi) (\eta^2 - \eta) \\ 0.25 (\xi^2 + \xi) (\eta^2 - \eta) \\ 0.5 (1 - \xi^2) (\eta^2 + \eta) \\ 0.5 (\xi^2 - \xi) (1 - \eta^2) \\ 0.5 (1 - \xi^2) (\eta^2 - \eta) \\ 0.5 (\xi^2 + \xi) (1 - \eta^2) \\ (1 - \xi^2) (1 - \eta^2) \end{Bmatrix} \quad (4.88)$$

where  $\xi$  and  $\eta$  are the local coordinates as shown in Fig. 4.3. Therefore, the element displacement vector  $\hat{\mathbf{U}}^e$  can be written as,

$$\hat{\mathbf{U}}^e = \Psi^e \mathbf{U}^e \quad (4.89)$$

where  $\Psi^e$  and  $\mathbf{U}^e$  are the element interpolation matrix and the element nodal displacement vector, respectively. The above mentioned quantities can be stated as

$$\Psi^e = \begin{bmatrix} N_1 & 0 & N_2 & 0 & \cdots & N_9 & 0 \\ 0 & N_1 & 0 & N_2 & \cdots & 0 & N_9 \end{bmatrix} \quad (4.90)$$

and

$$\mathbf{U}^e = \{\bar{\mathbf{U}}_1^e \quad \bar{\mathbf{V}}_1^e \quad \bar{\mathbf{U}}_2^e \quad \bar{\mathbf{V}}_2^e \quad \cdots \quad \bar{\mathbf{U}}_9^e \quad \bar{\mathbf{V}}_9^e\}^T \quad (4.91)$$

Using the chain rule of differentiation

$$\left\{ \frac{\partial}{\partial \xi} \quad \frac{\partial}{\partial \eta} \right\} = \left\{ \frac{\partial}{\partial x} \quad \frac{\partial}{\partial y} \right\} \begin{bmatrix} \frac{\partial x}{\partial \xi} & \frac{\partial x}{\partial \eta} \\ \frac{\partial y}{\partial \xi} & \frac{\partial y}{\partial \eta} \end{bmatrix} = \left\{ \frac{\partial}{\partial x} \quad \frac{\partial}{\partial y} \right\} \tilde{\mathbf{J}} \quad (4.92)$$

where the Jacobian matrix  $\tilde{\mathbf{J}}$  is defined as

$$\tilde{\mathbf{J}} = \begin{bmatrix} \frac{\partial x}{\partial \xi} & \frac{\partial x}{\partial \eta} \\ \frac{\partial y}{\partial \xi} & \frac{\partial y}{\partial \eta} \end{bmatrix} = \left\{ \frac{\partial \mathbf{N}}{\partial \xi} \quad \frac{\partial \mathbf{N}}{\partial \eta} \right\}^T \{ \mathbf{X} \quad \mathbf{Y} \} \quad (4.93)$$

The plane strain case is treated as the standard one. The gradient operator ( $\Pi$ ) for the standard case can be represented as

$$\Pi = \begin{bmatrix} \frac{\partial}{\partial x} & 0 \\ 0 & \frac{\partial}{\partial y} \\ \frac{\partial}{\partial y} & \frac{\partial}{\partial x} \end{bmatrix} = \begin{bmatrix} \frac{\partial}{\partial \xi} & 0 \\ 0 & \frac{\partial}{\partial \eta} \\ \frac{\partial}{\partial \eta} & \frac{\partial}{\partial \xi} \end{bmatrix} \tilde{\mathbf{J}}^{-1} \quad (4.94)$$

The strain-displacement operator for the standard case ( $\mathbf{B}_{\text{std}}$ ) can be obtained as,

$$\mathbf{B}_{\text{std}} = \Pi \Psi^e = \begin{bmatrix} \frac{\partial}{\partial \xi} & 0 \\ 0 & \frac{\partial}{\partial \eta} \\ \frac{\partial}{\partial \eta} & \frac{\partial}{\partial \xi} \end{bmatrix} \tilde{\mathbf{J}}^{-1} \begin{bmatrix} \mathbf{N}_1 & 0 & \mathbf{N}_2 & 0 & \cdots & \mathbf{N}_9 & 0 \\ 0 & \mathbf{N}_1 & 0 & \mathbf{N}_2 & \cdots & 0 & \mathbf{N}_9 \end{bmatrix} \quad (4.95)$$

The dimensions of  $\mathbf{B}_{\text{std}}$  matrix is  $3 \times 18$ . When it comes to the axisymmetric problem, one additional row of size  $1 \times 18$  has to be added with the standard case for accounting the circumferential strain or hoop strain. Therefore,

$$\mathbf{B}_{\text{axs}} = \begin{bmatrix} \mathbf{B}_{\text{std}} \\ \mathbf{B}_{\text{add}} \end{bmatrix}, \text{ where } \mathbf{B}_{\text{add}} = \begin{bmatrix} \frac{\mathbf{N}_1}{x} & 0 & \frac{\mathbf{N}_2}{x} & 0 & \cdots & \frac{\mathbf{N}_9}{x} & 0 \end{bmatrix} \quad (4.96)$$

In 2-D finite elements, the infinitesimal volume for the volume integrals is obtained by multiplying the area with the thickness in the perpendicular direction,

$$d\Omega_e = b \, dx \, dy = b \, |\tilde{\mathbf{J}}| \, d\xi \, d\eta \quad (4.97)$$

Similarly, the infinitesimal area for the surface integrals is

$$d\Gamma_e = \begin{cases} b \left( \sqrt{\tilde{\mathbf{J}}(1,2)^2 + \tilde{\mathbf{J}}(2,2)^2} \right) d\eta & \text{on faces 1 \& 2} \\ b \left( \sqrt{\tilde{\mathbf{J}}(1,1)^2 + \tilde{\mathbf{J}}(2,1)^2} \right) d\xi & \text{on faces 3 \& 4} \end{cases} \quad (4.98)$$

the scalar  $b$  in Eq. (4.97) and Eq. (4.98) can be defined as

$$b = \begin{cases} b \text{ real thickness} & \text{if plane strain case} \\ x \text{ radius} & \text{if axisymmetric (1 rad is considered)} \end{cases} . \quad (4.99)$$

The faces define the four boundaries of the element. According to the node numbering in Fig. 4.3, the left and right sides are called faces 1 and 2, and top and bottom sides are called faces 3 and 4, respectively.

The volumetric and deviatoric projectors, and  $\mathbf{L}$  matrix for the standard plane strain case is given as,

$$\mathbf{P}_1 = \frac{1}{3} \begin{bmatrix} 1 & 1 & 0 \\ 1 & 1 & 0 \\ 0 & 0 & 0 \end{bmatrix}, \quad \mathbf{P}_2 = \frac{1}{3} \begin{bmatrix} 2 & -1 & 0 \\ -1 & 2 & 0 \\ 0 & 0 & 3 \end{bmatrix} \quad \text{and} \quad \mathbf{L} = \begin{bmatrix} 1 & 0 & 0 \\ 0 & 1 & 0 \\ 0 & 0 & 2 \end{bmatrix} \quad (4.100)$$

Similarly for the axisymmetric case,

$$\mathbf{P}_1 = \frac{1}{3} \begin{bmatrix} 1 & 1 & 0 & 1 \\ 1 & 1 & 0 & 1 \\ 0 & 0 & 0 & 0 \\ 1 & 1 & 0 & 1 \end{bmatrix}, \quad \mathbf{P}_2 = \frac{1}{3} \begin{bmatrix} 2 & -1 & 0 & -1 \\ -1 & 2 & 0 & -1 \\ 0 & 0 & 3 & 0 \\ -1 & -1 & 0 & 2 \end{bmatrix} \quad \text{and} \quad \mathbf{L} = \begin{bmatrix} 1 & 0 & 0 & 0 \\ 0 & 1 & 0 & 0 \\ 0 & 0 & 2 & 0 \\ 0 & 0 & 0 & 1 \end{bmatrix} \quad (4.101)$$

## 4.4 Contact model

During the metal casting, the solidifying metal and mold interacts thermo-mechanically. The interfacial HTC is a strong function of the air gap formed between these two surfaces. Therefore, it is important to address the problem of interfacial contact. In this work, the interface problem is decomposed into a pure contact problem in the normal direction and the zero frictional resistance in the tangential direction of the interface. The behavior of the interface elements is characterized by the relation between the relative displacements of the surfaces in contact at the interface. As similar to regular elements, an isoparametric formulation is used and the elements have zero thickness with coincident nodes. In this work, the interface element is based on the joint element developed by Vila Real *et al.* [31]. For the sake of completeness, the relative displacement in the tangential direction is modeled and finally substituted with zero tangential stiffness ( $k_t$ ).

The relative displacement at any point along the element represented in Fig. 4.4 is given as

$$\epsilon^{e*} = \begin{Bmatrix} \gamma^* \\ \epsilon_n^* \end{Bmatrix} = \begin{Bmatrix} t_{x'} - b_{x'} \\ t_{y'} - b_{y'} \end{Bmatrix} \quad (4.102)$$

where  $\gamma^*$  and  $\epsilon_n^*$  are the relative displacements in the direction of the local axis  $x'$  and  $y'$  respectively. Further,  $t$  refers to the top side of the element and  $b$  to the bottom side. Therefore,  $t_{x'}$  and  $b_{x'}$  represent the displacement in the local  $x'$ -axis direction at the top side of the element and bottom side of the element. The displacement at any point of

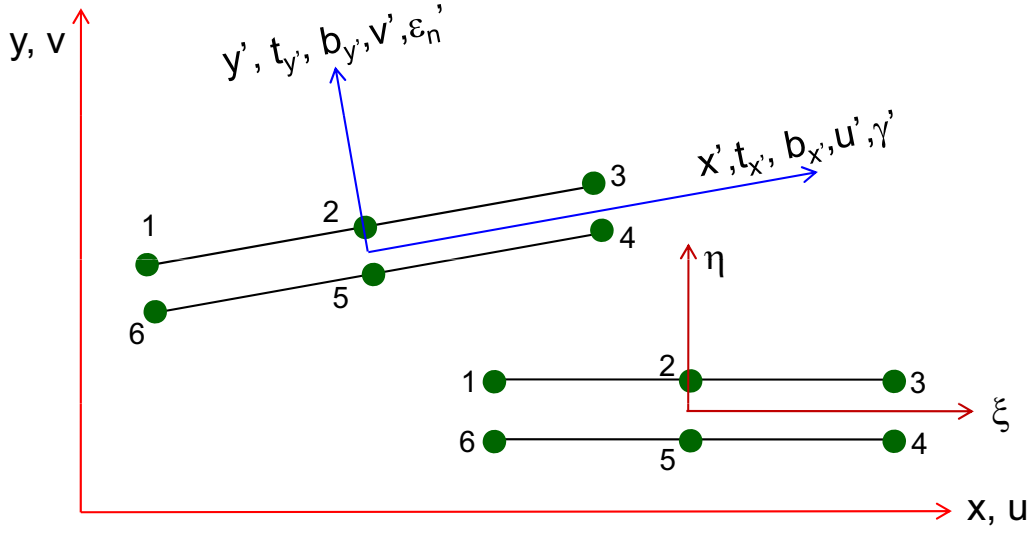


Figure 4.4: Schematic representation of interface contact element

the 6-noded element represented in Fig. 4.4 are given in terms of the shape functions as

$$\begin{aligned}
 t_{x'} &= \mathbf{N}^T \bar{\mathbf{U}}^{e'} & \text{and} & & t_{y'} &= \mathbf{N}^T \bar{\mathbf{V}}^{e'} \\
 b_{x'} &= \bar{\mathbf{N}}^T \bar{\mathbf{U}}^{e'} & \text{and} & & b_{y'} &= \bar{\mathbf{N}}^T \bar{\mathbf{V}}^{e'}
 \end{aligned} \quad (4.103)$$

where  $\mathbf{N}$  and  $\bar{\mathbf{N}}$  are shape function vectors,  $\bar{\mathbf{U}}^{e'}$  and  $\bar{\mathbf{V}}^{e'}$  are nodal displacement vectors along the local  $x'$  and  $y'$  axis respectively. The above mentioned quantities can be expanded as follows:  $\mathbf{N}^T = \{N_1 \ N_2 \ N_3\}$ ,  $\bar{\mathbf{N}}^T = \{N_3 \ N_2 \ N_1\}$ ,  $\mathbf{U}^{e'T} = \{U_1^{e'} \ U_2^{e'} \ U_3^{e'}\}$ , and  $\mathbf{V}^{e'T} = \{V_1^{e'} \ V_2^{e'} \ V_3^{e'}\}$ . Further the shape function vector can be given as

$$\mathbf{N} = \begin{Bmatrix} N_1 \\ N_2 \\ N_3 \end{Bmatrix} = \begin{Bmatrix} \frac{r^2-r}{2} \\ 1-r^2 \\ \frac{r^2+r}{2} \end{Bmatrix} \quad (4.104)$$

where  $r$  is a local coordinate which varies from -1 to +1. Substituting Eq. (4.103) in Eq. (4.102) the elemental form of relative displacement can be written as

$$\epsilon^{e*} = \tilde{\Psi}^e \mathbf{U}^{e'} \quad (4.105)$$

in which

$$\tilde{\Psi}^e = \begin{bmatrix} N_1 & 0 & N_2 & 0 & N_3 & 0 & -N_3 & 0 & -N_2 & 0 & -N_1 & 0 \\ 0 & N_1 & 0 & N_2 & 0 & N_3 & 0 & -N_3 & 0 & -N_2 & 0 & -N_1 \end{bmatrix} \quad (4.106)$$

and

$$\mathbf{U}^{e'T} = \left[ \bar{\mathbf{U}}_1^{e'} \ \bar{\mathbf{V}}_1^{e'} \ \bar{\mathbf{U}}_2^{e'} \ \bar{\mathbf{V}}_2^{e'} \ \dots \ \bar{\mathbf{U}}_6^{e'} \ \bar{\mathbf{V}}_6^{e'} \right] \quad (4.107)$$



The element local displacements and global displacements can be related through the well-known transformation matrix ( $\mathbf{Q}$ ) as,

$$\mathbf{U}^{e'} = \mathbf{Q} \mathbf{U}^e \quad (4.108)$$

where  $\mathbf{U}^e$  is the elemental form of the nodal global displacement vector. Therefore, Eq. (4.105) is represented as

$$\epsilon^{e*} = \tilde{\Psi}^e \mathbf{U}^{e'} = \tilde{\Psi}^e \mathbf{Q} \mathbf{U}^e = \mathbf{B}_{\text{con}} \mathbf{U}^e \quad (4.109)$$

where  $\mathbf{B}_{\text{con}} = \tilde{\Psi}^e \mathbf{Q}$  is the strain displacement matrix for the contact element. The stiffness matrix for an interface contact element is defined in the standard FEM which is discussed above as [31]

$$\mathbf{K}_{\text{con}}^e = \int_{\Gamma_c^e} \mathbf{B}_{\text{con}}^T \mathbf{D} \mathbf{B}_{\text{con}} d\Gamma_c^e \quad (4.110)$$

where  $\Gamma_c$  is the contact surface and  $\mathbf{D}$  is the matrix which relates the stresses and the relative displacement in the local coordinate system, so that the incremental contact stress vector can be given as in [31]

$$\Delta \mathbf{T}_{\text{con}}^e = \begin{Bmatrix} \Delta \tau^e \\ \Delta \sigma_n^e \end{Bmatrix} = \begin{bmatrix} k_t & 0 \\ 0 & k_n \end{bmatrix} \begin{Bmatrix} \Delta \gamma^* \\ \Delta \epsilon_n^* \end{Bmatrix} = \mathbf{D} \Delta \epsilon^{e*} = \mathbf{D} \mathbf{B}_{\text{con}} \mathbf{U}^e \quad (4.111)$$

where  $k_t$  and  $k_n$  are tangential and normal contact stiffness. Generally,  $k_n$  is chosen as an arbitrary large number for numerical convergence. Here, it should be noted that only compressive stresses are allowed, i.e.  $\sigma_n \leq 0$ . Finally, the contact stiffness matrix and its corresponding residual vector are added to regular matrices and vectors before solving. The normal gap between the contact nodes can be easily computed from the vertical displacement of nodes in the local coordinate system using Eq. (4.109).

## 4.5 Numerical examples

For the purpose of validation, two numerical examples are presented in this section. Firstly, the stress-strain curve for different constitutive laws are obtained using the 2-D axisymmetric case and the results are compared with the 1-D model. For this purpose, the displacement controlled uniaxial tensile test is simulated by the numerical experiments. Further, the significance of the rate effect is explained through this example. Secondly, a 2-D axisymmetric problem with the purely thermal load is analyzed using the rate-dependent Perzyna law and rate-independent plasticity. The results of the two models

are compared.

### 4.5.1 Mechanical loading

The stress-strain curve obtained by the simple 1-D case is compared with the 2-D case. For this purpose, a cylinder with dimensions of  $50 \times 200$  mm is considered. One end of the cylinder is assumed to be hinged. Due to symmetry, the problem is simplified as an axisymmetric case which is shown in Fig. 4.5. The displacement is specified on the another end of the cylinder. With this prescribed displacement, an uniform strain-rate is maintained throughout the cylinder. The thermal strain in this case is treated as zero. The material properties are given in Table. 4.3. The equivalent stress and equivalent strain at the point A (Fig. 4.5) is plotted and compared with the 1-D model for various material models. A simple 1-D model is developed for the verification of the constitutive

Table 4.3: Material properties - Mechanical loading problem

Perzyna model and rate-independent plasticity		
Young's modulus ( $E_y$ )	210	GPa
Poisson's ratio ( $\nu$ )	0.3	
Yield stress ( $\sigma_{yo}$ )	3	MPa
Hardening modulus ( $H$ )	1	GPa
Viscosity ( $\eta$ )	1	GPa.s
Norton-Hoff law		
$\tilde{k}$	$2.1 \times 10^{-6}$	/s
$\tilde{n}$	4.76	
$\tilde{\sigma}_o$	1	MPa
Garafalo law		
$A$	$28.2 \times 10^{25}$	/s
$Q$	400	kJ/mol
$\tilde{n}$	7.13	
$\tilde{\sigma}_o$	1	MPa

law. In this model, the scalar incremental total strain ( $\Delta\epsilon$ ) is supplied and the scalar incremental stress ( $\Delta\sigma$ ) is computed based on the constitutive law. The total strain is additively decomposed into elastic and inelastic strain. The inelastic strain can be obtained from the rate-independent plasticity case or rate-dependent viscoplastic case. The Young's modulus ( $E_y$ ) in the 1-D case is multiplied by a factor of  $\frac{3}{2(1+\nu)}$  for the purpose of comparing with the 2-D axisymmetric results.

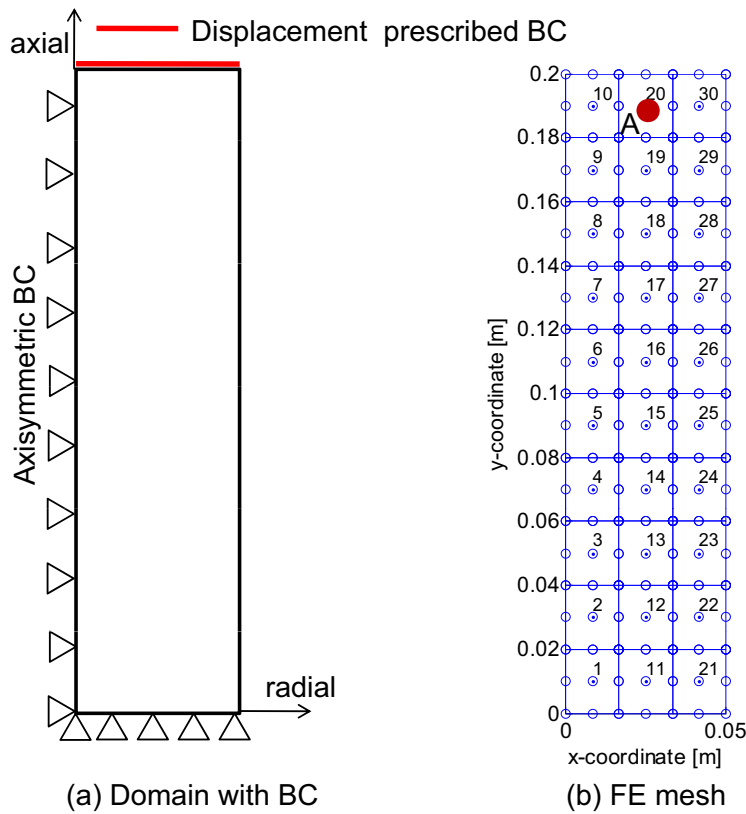


Figure 4.5: Mechanical loading: (a) axisymmetric domain with boundary conditions and (b) finite element mesh

Firstly, the rate-independent elasto-plastic constitutive law is simulated. This case coincides with the Perzyna elasto-viscoplastic case when the strain rate is less than  $1 \times 10^{-5} /s$  as shown in Fig. 4.6. Secondly, the Perzyna type elasto-viscoplastic constitutive law for various strain rates are simulated and the stress-strain curves are plotted as shown in Fig. 4.6. When the strain rate increases the stress-strain curve shifts upward, i.e. the yield limit increases. The 2-D results are in good agreement with the 1-D case.

Thirdly, the stress-strain curves are obtained by using the Norton-Hoff law and plotted as shown in Fig. 4.7(a). Due to the absence of yield stress, there is no lower bound for the stress-strain curve. This is not possible in the Perzyna type viscoplasticity. Further, there is no hardening kind of behavior in the stress-strain curve. This resembles the rate-independent plasticity case with zero hardening.

Finally, the Garafalo law is used to obtain the stress-strain curve for various strain rates which are shown in Fig. 4.7(b). The temperature used for the computation is 773 K. For a very high strain rate material behaves like a perfectly elastic one. This fact can be clearly observed from the stress-strain curves. The 2-D axisymmetric case results exactly match with the 1-D case. Therefore, the accuracy of the 2-D model is assured.

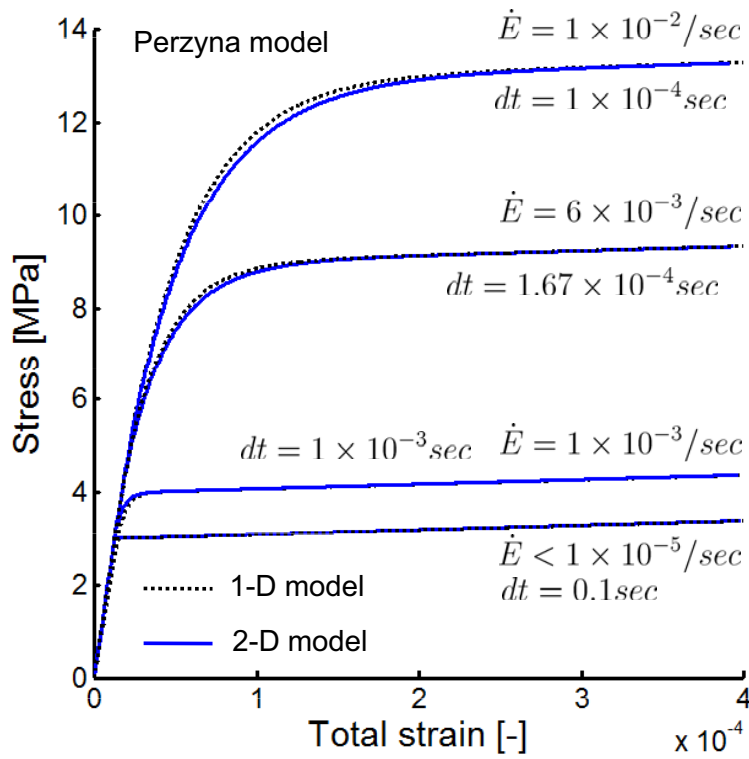


Figure 4.6: Stress-strain curve: Perzyna model

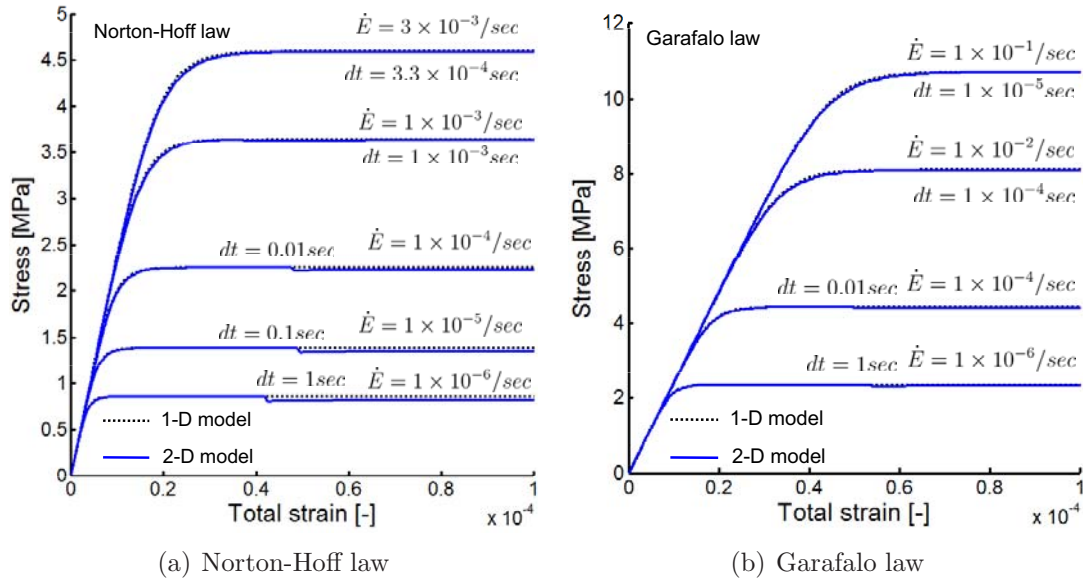


Figure 4.7: Stress-strain curve: Norton-Hoff and Garafalo law

## 4.5.2 Thermal loading

An axisymmetric cylinder as discussed in the previous section is exposed to the convective heat transfer coefficient of  $500 \text{ W/m}^2\text{K}$  on its longer surface while keeping the other sides insulated (Fig. 4.8). The material properties are given in Table. 4.4 as a function of temperature. The mechanical and thermal boundary conditions are shown in Fig. 4.8(a).

The finite element mesh used for the computation is given in Fig. 4.8(b). The thermal strain is computed by the density approach. The temperature change can be predicted by the 2-D axisymmetric solidification model without the phase-change effect.

Table 4.4: Material properties [pure aluminum] - Thermal loading problem

$\theta$ $^{\circ}C$	$E_y$ GPa	$\nu$	$\sigma_{yo}$ MPa	$H$ GPa	$k$ W/mK	$\rho$ kg/m <sup>3</sup>	$C_p$ J/kgK	$\eta$ GPa.sec
50	69.29	0.33	11.49	0.45	238.82	2694	912.4	1
100	67.60	0.33	10.58	0.43	240.08	2685	939.7	1
150	65.82	0.33	9.67	0.40	239.33	2675	964.0	1
200	63.94	0.33	8.76	0.37	237.46	2665	986.2	1
250	61.92	0.33	7.85	0.34	235.05	2654	1007.3	1
300	59.76	0.34	6.94	0.32	232.37	2643	1028.3	1
350	57.44	0.35	6.03	0.29	229.53	2632	1050.1	1
400	54.94	0.36	5.12	0.26	226.49	2620	1073.8	1
450	52.24	0.37	4.21	0.23	223.20	2608	1100.3	1
500	49.32	0.39	3.30	0.21	219.60	2595	1130.5	1
550	46.17	0.41	2.40	0.18	215.76	2582	1165.6	1

The initial temperature of the cylinder is considered as 500°C. Fig. 4.9 shows the temperature evolution at the locations A and B shown in Fig. 4.8(b). Within 100 seconds, the material cools down to 250°C. The rate-independent plasticity model and Perzyna type viscoplastic material models are used to compute the displacement field. The evolution of stresses at the center (location A) is plotted as shown in Fig. 4.10(a). Due to sudden cooling, the axial, radial and circumferential stresses immediately reach the tensile maximum, and in the later stages of cooling, the stresses become compressive in nature. The shear stress is very low and tensile in nature. Both the models predict nearly the same stress pattern. Fig. 4.10(b) shows the stresses evolution at the outer surface (location B). The circumferential stress is compressive in nature with relatively high magnitude when compared to axial and radial stresses. The shear stress is almost null in both the material models. In the case of circumferential stress, the Perzyna model predicts lesser value when compared to rate-independent plasticity model.

The distributions of von Misses equivalent stress at time  $t = 250$  s are plotted for both the models as shown in Fig. 4.11. Similar pattern with nearly same magnitude is observed in both the models. The equivalent stress is maximum in regions close to the outer surface and the axial center of central surface. The minimum stress is also observed in a certain portion of central surface. The distributions of all components of stresses for the viscoplastic case is shown in Fig. 4.12. The axial and circumferential stresses are compressive at the outer surface and tensile at the inner surface. The radial stress is

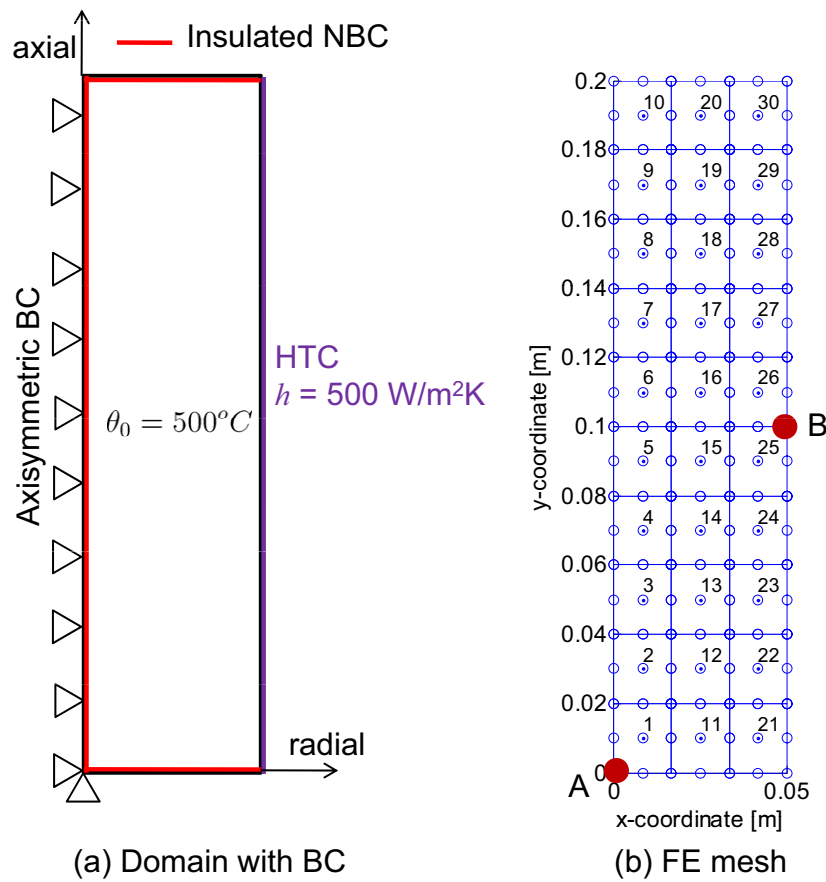


Figure 4.8: Thermal loading: (a) axisymmetric domain with boundary conditions and (b) finite element mesh

nearly zero at the outer and tensile at the inner. The shear stress is compressive in the lower half and tensile in the upper half.

These two numerical examples show the potential of the developed numerical techniques. Three different viscoplastic laws predict the rate effect considerably well. With this mechanical model, the thermo-mechanical effects of DC casting can be studied easily.

## 4.6 Summary

In this chapter, the finite element method for the computation of the stress-strain field is explained. Firstly, the weak form of the momentum equation is derived. Using a small deformation theory, the strain tensor is approximated as the symmetric part of displacement gradient. Further, the strain tensor is additively decomposed into elastic, thermal, and inelastic parts. The thermal strain can be computed using the density approach or the thermal expansion approach. The inelastic strain can be either plastic strain or viscoplastic strain. The Perzyna, Norton-Hoff, and Garafalo law are the three

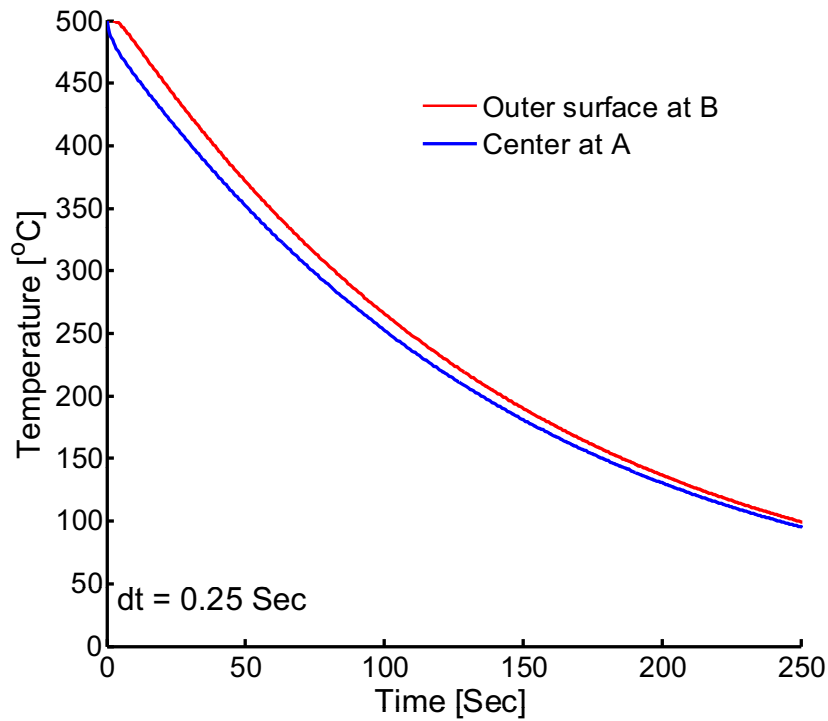


Figure 4.9: Thermal loading: Temperature evolution

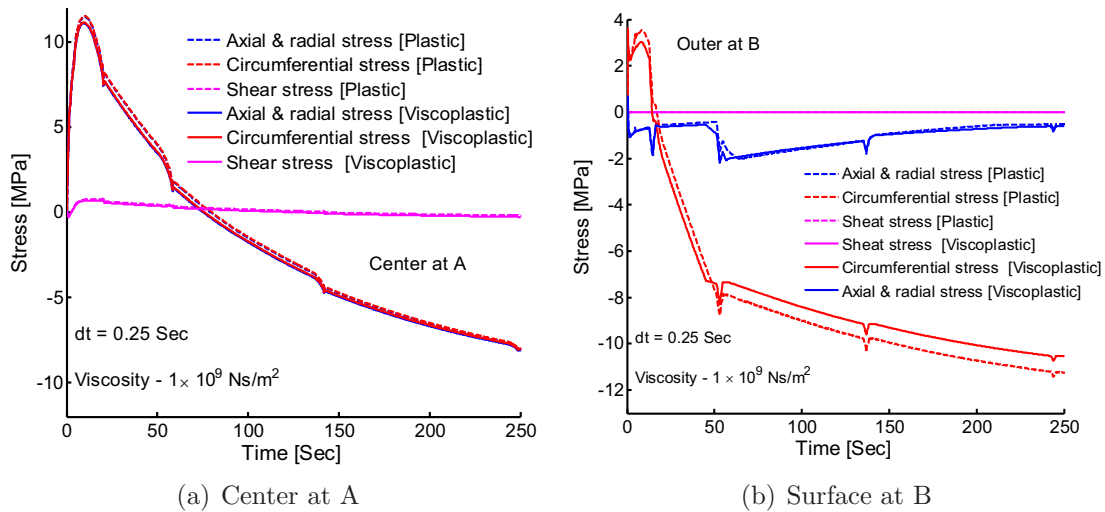


Figure 4.10: Thermal loading: Evolution of stresses at center (A) and outer(B)

important viscoplastic material models suitable for the aluminum alloys used in DC casting. Two different kinds of integration techniques are followed for the integration of the constitutive law. The incorporation of contact conditions between the surfaces are explained. The accuracy of the displacement model is verified by two numerical examples. With this notion, the mechanical effects of DC casting can be studied without any major modifications.

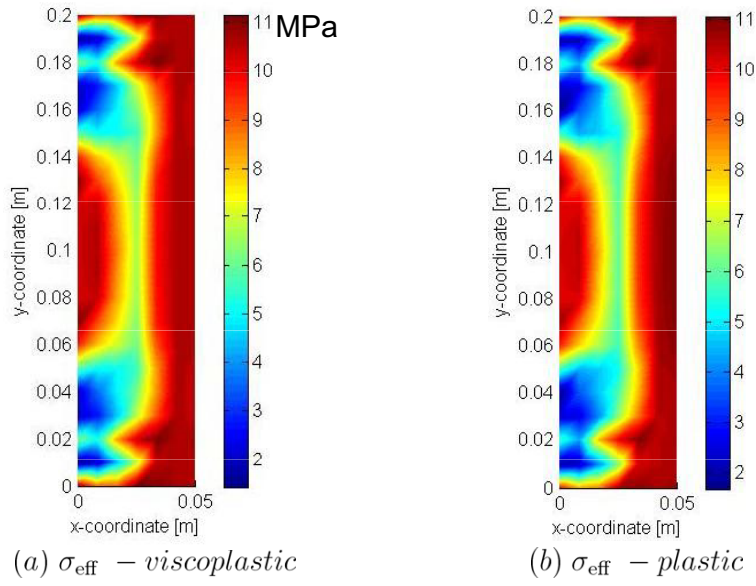


Figure 4.11: Thermal loading: Distribution of von Mises equivalent stress at  $t = 250$  s (a) Perzyna model and (b) rate-independent plasticity

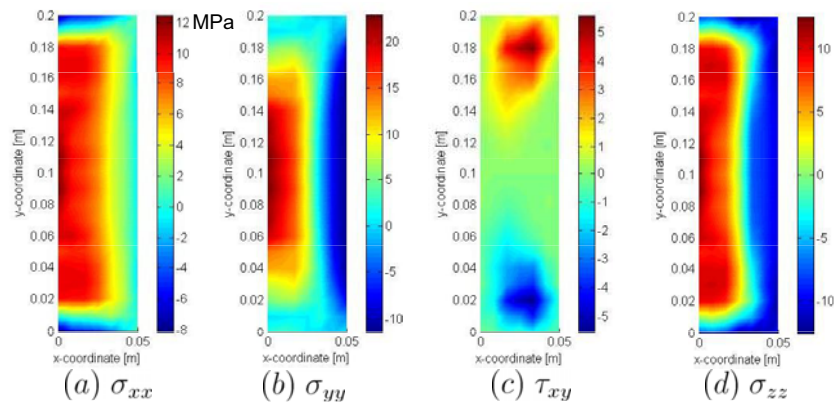


Figure 4.12: Thermal loading: Distribution of stresses at  $t = 250$  s (a) radial ( $\sigma_{xx}$ ), (b) axial ( $\sigma_{yy}$ ), (c) shear ( $\tau_{xy}$ ), and (d) circumferential ( $\sigma_{zz}$ )



# Chapter 5

## Numerical simulation of DC casting

### 5.1 Description of DC casting Model

The real time DC casting process is suitably transformed and reproduced by proper assumptions: the position of the bottom block and ingot/billet is fixed and the ingot/billet grows vertically upward, and the associated boundary conditions move with a casting speed. To simplify the computations, the bottom block and mold are neglected for the analysis. The attention is only focused on the casting, and the interactions of casting with the bottom block and mold are suitably applied.

In this work, a cylindrical extrusion billet of radius 100 mm is considered for the study which is schematically represented in Fig. 5.1. Due to the rotational symmetry, only a rectangular domain is considered for the analysis. Further, the  $x$ -axis represents the radial direction and the  $y$ -axis represents the axial direction and axis of symmetry. The height of mold is taken as 60 mm. The billet height is considered as a function of time and increases in the  $y$  direction according to the casting speed. The initial height of the billet is taken as 10 mm with 2 rows of elements which is the computational domain for the first time step. For the next time step, an additional row of liquid elements is added in the  $y$  direction. Fig. 5.2 shows the computational domain at time  $t$  and  $t + \Delta t$ . The element growth in the  $y$  direction represents the liquid feeding from the furnace.

The thermal boundaries of the billet is divided into five regions which are non-overlapping.  $\Gamma_1$  represents the symmetry axis where the heat flux leaving in the normal direction is considered as zero, i.e. insulated BC.  $\Gamma_1$  extends along with the element growth.  $\Gamma_2$  is the temperature described essential BC which mimics the liquid feeding.  $\Gamma_2$  is assigned with a melt temperature which does not vary with time. The size of the  $\Gamma_2$  BC is fixed but it shifts in the positive  $y$ -direction along the element growth as shown in Fig. 5.2. The interaction of the billet with bottom block is represented through  $\Gamma_3$  convection BC. The size of  $\Gamma_3$  is fixed and the HTC is assumed to vary with temperature.

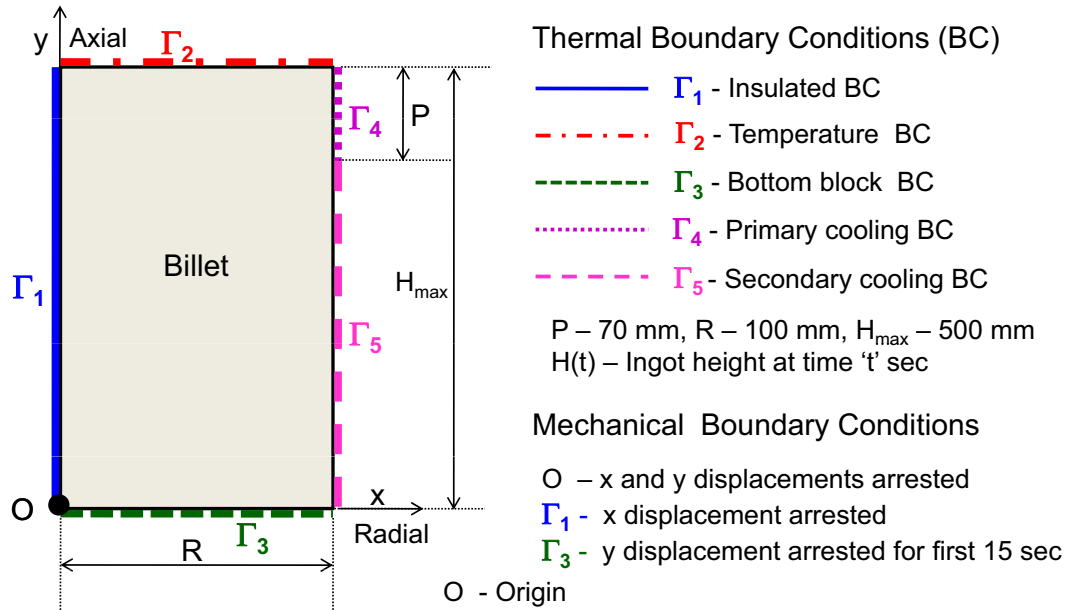


Figure 5.1: Computational domain of DC casting billet with thermal and mechanical boundary conditions

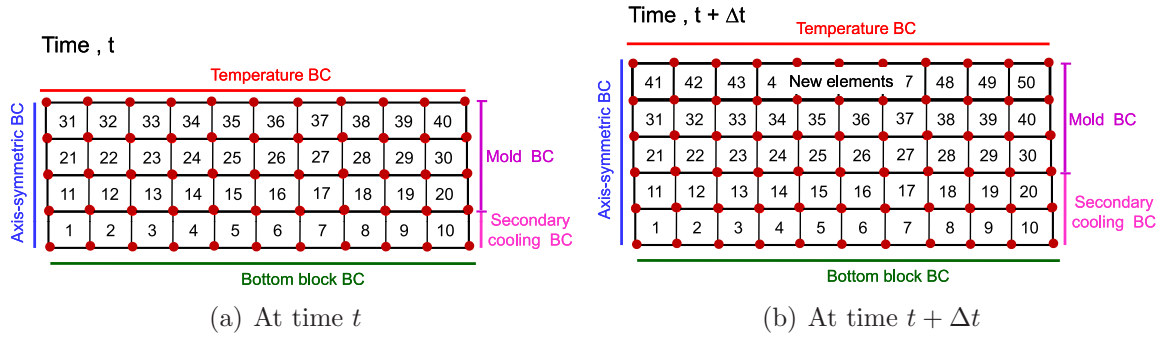


Figure 5.2: Computational domain of DC casting billet at time  $t$  and  $t + \Delta t$

The air gap formation and water intrusion cases are imposed on the HTC. Fig. 5.3(a) shows the bottom block HTC as a function of temperature which is taken from Williams *et al.* [60]. The temperature of the bottom block is treated as constant with a value of  $100^\circ\text{C}$  [15].

$\Gamma_4$  represents the primary mold cooling regions with a fixed length and moves upward in the  $y$ -direction during the element growth. This boundary condition is always referred from the top of the melt. Drezet *et al.* [59] performed experiments and found the HTC as a function of position from the top which is shown in Fig. 5.3(b). A small portion of size 10 mm is added along with the mold BC which represents the gap between the mold and water impingement zone known as air cooling zone. The HTC of this air cooling zone is taken as  $50 \text{ W/m}^2\text{K}$ . The temperature of the mold is taken as  $100^\circ\text{C}$ . The secondary water cooling zone is represented by  $\Gamma_5$  which changes its size during the element growth.

Generally, in the simulation of DC casting, the secondary cooling boundary is the most complicated one due to the lot of controlling parameters such as water flow rate, surface temperature, cooling water quality, etc. In this work, the secondary cooling HTC is taken from Williams *et al.* [60] and shown in Fig. 5.4 as a function of temperature. Further, different boiling zone temperatures and HTCs are clearly mentioned in the figure.

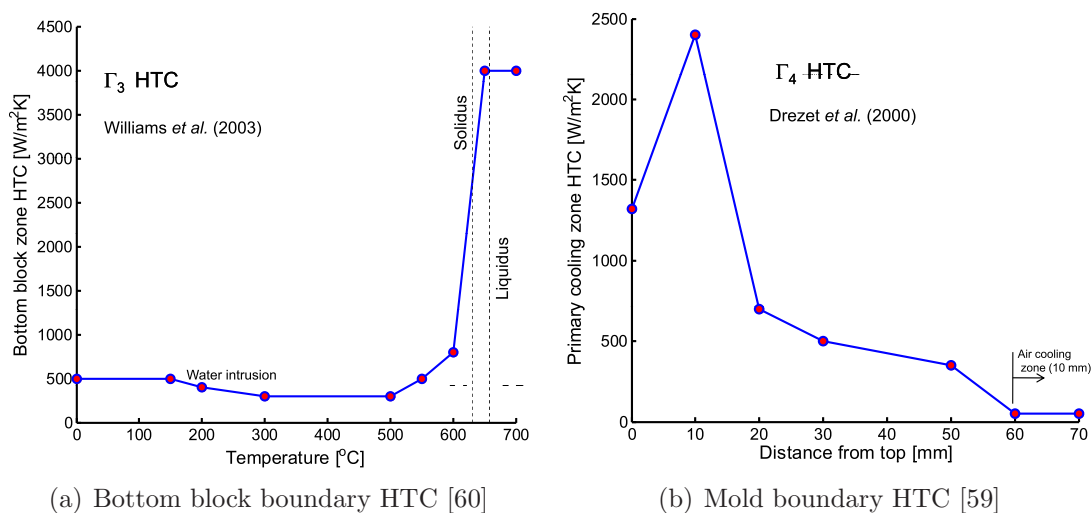


Figure 5.3: Bottom block and mold boundary HTCs

The mechanical boundary conditions can be classified into three: (a) axisymmetric boundary conditions are assigned on the  $\Gamma_1$  regions, (b) to avoid the rigid body motion, the origin of the billet is fixed, and (c) to avoid the penetration of the billet on bottom block,  $\Gamma_3$  is fixed for the first 15 seconds and then released. Therefore, the contact model is not incorporated in the following simulations. It is obvious that the contact conditions are applicable on the region  $\Gamma_3$ . However, the contact problem increases the number of equilibrium iterations of the mechanical problem. Generally, the mechanical boundary conditions associated with the bottom block have less influence for the extrusion billets having smaller cross-sections. On the other hand, for the prediction of butt curl in the case of rolling ingots, the contact between ingot and bottom block has to be incorporated carefully. The air gap between the bottom block and the billet can be considered as the vertical displacement of the nodes on  $\Gamma_3$  regions.

The computational domain includes the liquid metal, the mushy zone, and the solid part. The material is assumed to be an AA1201 alloy. The thermophysical and thermo-mechanical properties of the alloy are taken from Drezet *et al.* [15] and given in Table. 5.1. Linear approximations are used to calculate the material properties at intermediate temperatures. Above the coherency temperature ( $\theta_c$ ), the alloy is assumed to behave as a liquid. The Young's modulus, thermal conductivity, and the coefficient of thermal expansion are strong functions of temperature. The thermal conductivity of the liquid phase

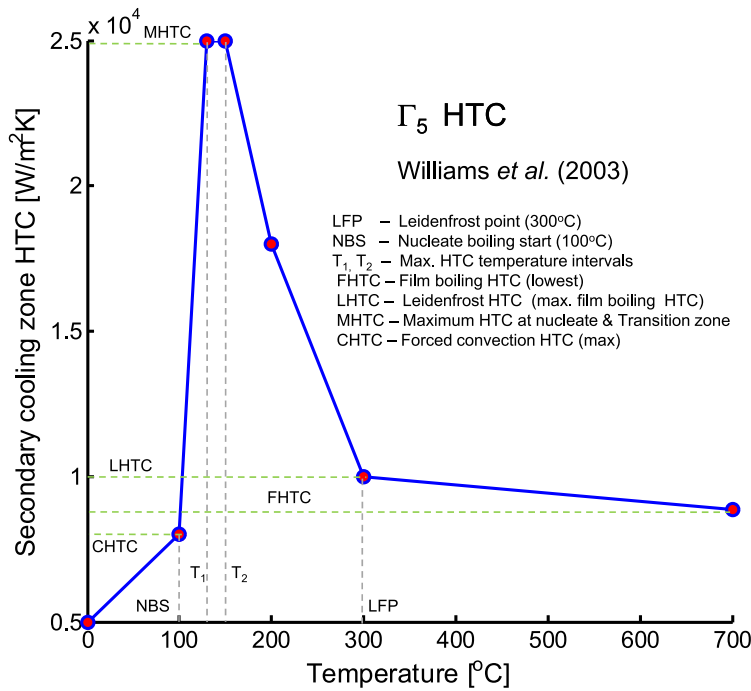


Figure 5.4: Secondary water cooling region HTC (Williams *et al.* 20003) as a function of temperature

is increased to 400 W/mK so as to account for the liquid convection in the sump. The density of the metal is treated as constant. Therefore, the contribution of metal shrinkage during the solidification is neglected as a result of constant liquid feeding within the mushy zone. For the computational purpose, a very small non-zero value is assigned to the Young's modulus above the coherency temperature. Through this, the stress development in the liquid phase is almost eliminated. There is no mixture rule employed for the computation of material properties in the mushy state. Further, the mixture rules are not necessary if the material properties are known as a function of temperature. In between the coherency temperature (temperature at liquid fraction of 0.714) and 5°C above the solidus temperature, the creep behavior of mushy is modeled using the Norton-Hoff law, and its parameters as a function of temperature are separately given in Table. 5.2. Below 635°C, the Garafalo law is used to describe the mechanical behavior of the solid phase. To ensure the liquid incompressibility, the value of Poisson's ratio is increased to 0.49 above  $\theta_c$ .

A 4-noded quadratic element is used for the thermal field computations. The element matrices are computed using a 4-point Gauss quadrature rule. To make the thermal strain compatible with the mechanical strains such as elastic and viscoplastic strains, a 9-noded quadratic element is used for the mechanical field computations. Therefore, a linear strain field is obtained within the element. Generally, for a 9-noded element, 4 integration points are not sufficient because of the large number of non-zero or complex eigenvalues arise

Table 5.1: Material properties of **AA1201**

Solidus temperature	630 °C		Young's Modulus	68.2 GPa	$\leq 25$ °C
Liquidus temperature	658 °C			60.6 GPa	200 °C
Coherency temperature	650 °C			51.8 GPa	400 °C
Solid & liquid density	2650 kg/m <sup>3</sup>			41.8 GPa	630 °C
Latent heat	358 kJ/kg			40.0 GPa	650 °C
Thermal conductivity	227	$\leq 27$ °C		0.1 MPa	650.1°C
(W/mK)	230	127 °C		1.0 kPa	658°C
	227	227 °C		0.1 kPa	$\geq 700$ °C
	222	327 °C	Poisson's ratio	0.37	$\leq 650.1$ °C
	216	427 °C		0.49	$> 650.1$ °C
	210	527 °C	Thermal expansion	23.20	$\leq 25$ °C
	203	630 °C	( $\times 10^{-6}$ /°)C	25.20	200 °C
	90	$\geq 658$ °C		30.23	400 °C
Specific heat	905	$\leq 27$ °C		34.30	630 °C
(J/kgK)	950	127 °C		38.40	650 °C
	998	227 °C		0.0	$\geq 650.1$ °C
	1043	327 °C	Garafalo law		$< 635$ °C
	1090	427 °C	A ( $s^{-1}$ )	$28.2 \times 10^{25}$	
	1135	527 °C	Q (KJ/gmol)	400	
	1181	630 °C	$\tilde{n}$	7.13	
	1086	$\geq 658$ °C	$\tilde{\sigma}_o$ (MPa)	13.6	

Table 5.2: Parameters of Norton-Hoff law (**AA1201**)

$\theta$ (°C)	$\tilde{k}(s^{-1})$	$\tilde{n}$	$\tilde{\sigma}_o$ (MPa)
635	$2.1 \times 10^{-6}$	4.76	1.0
640	$6.9 \times 10^{-6}$	3.85	1.0
645	$1.36 \times 10^{-4}$	3.5	1.0
650	$1.15 \times 10^{-3}$	3.4	1.0

for an element matrix. Therefore, 9 integration points are chosen for the mechanical computations. A home made MATLAB program is used to generate the meshes and to solve the thermal and mechanical field non-linear equations iteratively. To accelerate the convergence in the global level, a line-search algorithm is used within the Newton-Raphson iterations. Further, in the integration point level, the constitutive equations are integrated iteratively again using the line-search algorithm within the Newton-Rahphson iterations. The flow chart of the algorithm used to solve the DC casting problem is shown in Fig. 5.5.

Thermal and mechanical problems are solved sequentially using an isothermal staggered approach. Within the time step, first the thermal problem is solved and the time increment of temperature at the nodal and integration points are found. The influence of the mechanical solution on the thermal problem is nullified because the interfacial HTC is defined as a function of temperature instead of the normal gap between the surfaces. Therefore, the interface model is not included in the following simulations. Generally, implicit Euler backward scheme is independent of the time step size except in very few cases. Therefore larger time step is used for the thermal field computations. In the case of larger time steps, due to the relatively high temperature gradient, the mechanical problem encounters the convergence problem. Therefore, within a global time step, the mechanical problem is solved repeatedly using a locally smaller time increment. The thermal force is the only external disturbance which induces the mechanical deformation because the body force and the liquid pressure on the solidified layer in the mushy zone are neglected. The influence of thermal solution on the mechanical problem is very high.

## 5.2 Simulation of DC casting

A constant casting speed of 120 mm/min is investigated. For reducing the computational time, only 8 elements are taken in the radial direction, and the time step size is considered as 3 seconds. During the start-up phase, 8 local time steps are used in the mechanical field computations. Similarly, for the pseudo steady state, 5 local time steps are introduced. Fig. 5.6 shows the evolution of temperature at 5 different positions nearby the bottom of the billet. It can be clearly perceived that the cooling is effective in the surface of the billet rather than the center. Even before the water strikes the surface of the billet, the cooling rate is relatively higher in the butt of the billet due to the simultaneous cooling effect provided by the mold and the bottom block. Therefore, the solidification fronts first start from the billet butt and moves towards the center. At the time of 33 s, the water first starts striking the butt and the rapid change in the temperature occurs from 553°C to 147°C within a short duration of 24 seconds. Unlike the butt, the temperature

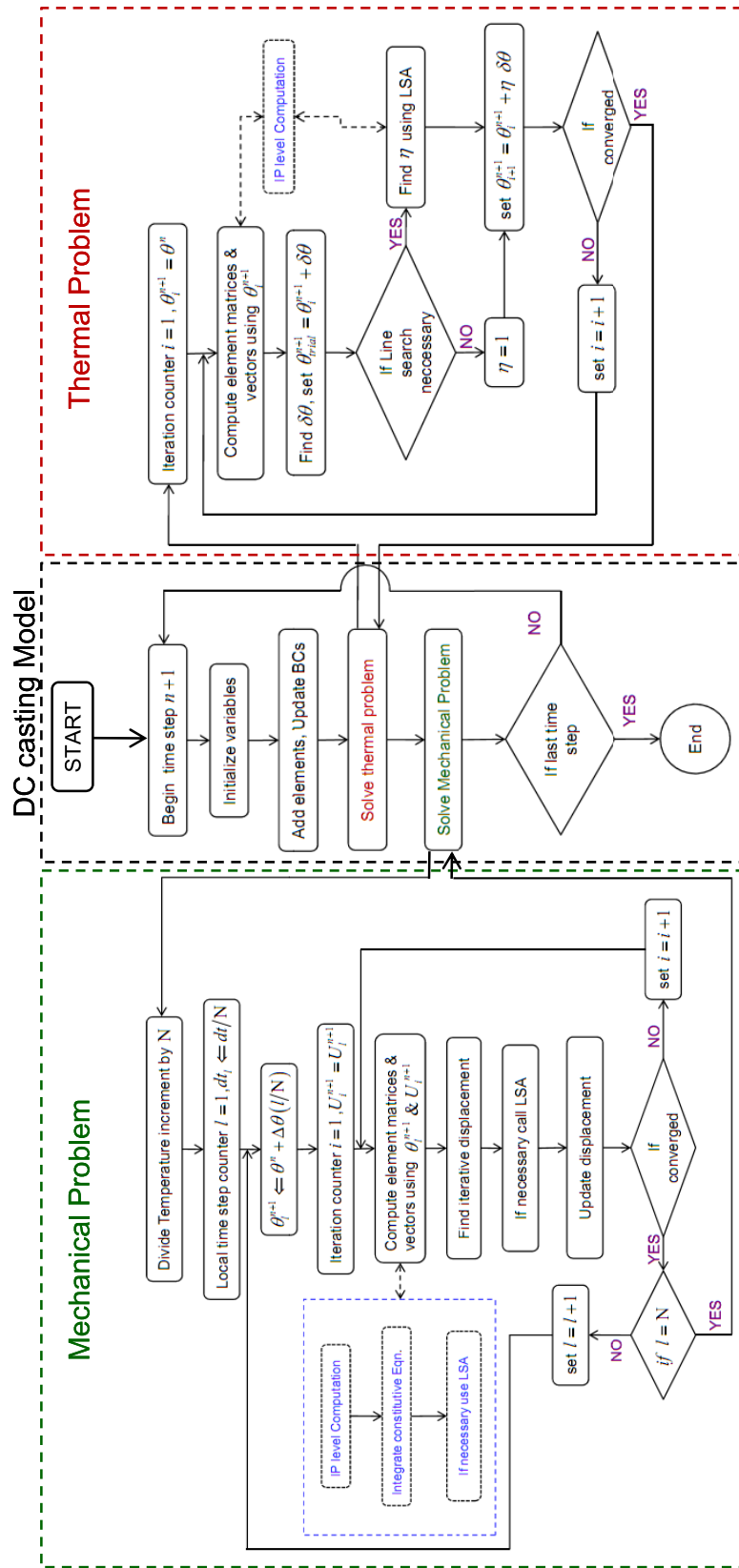


Figure 5.5: Flowchart of DC casting model algorithm

at the center of billet remains above the solidus temperature until the butt temperature drops to 147°C.

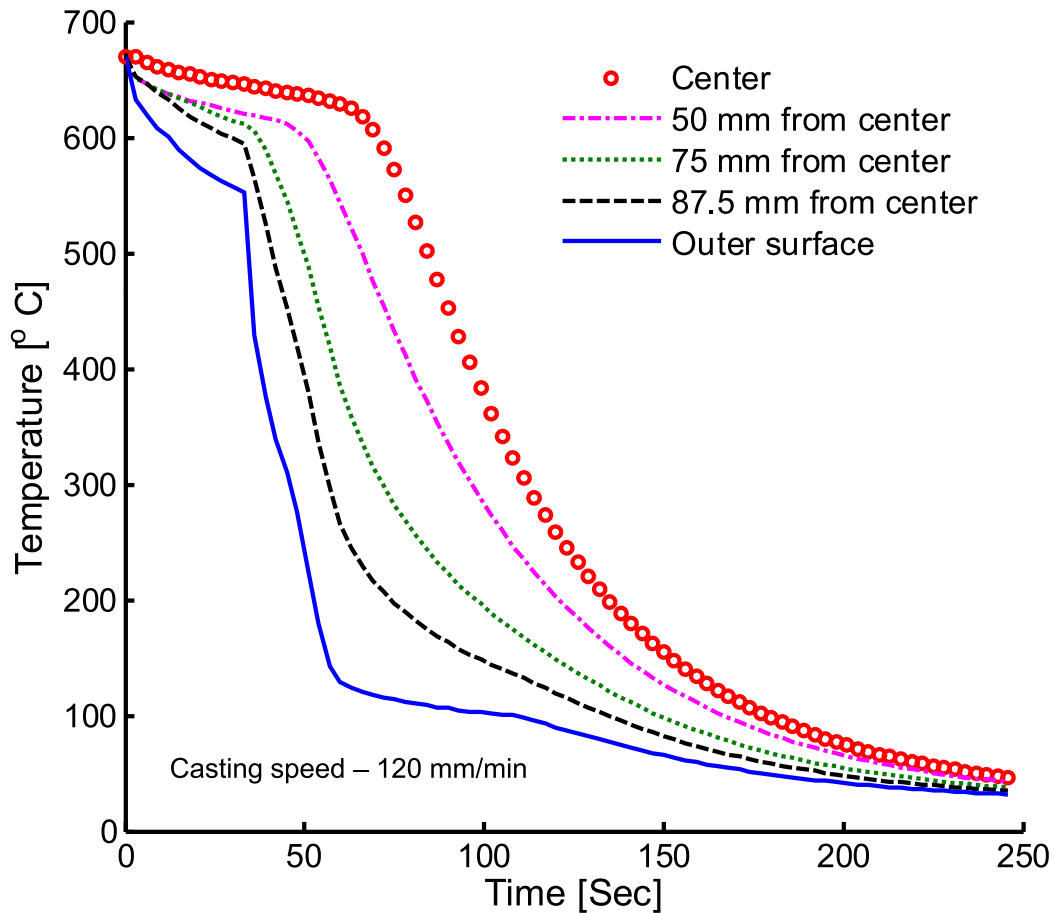


Figure 5.6: Casting speed 120 mm/min: Temperature evolution nearby bottom block

To understand the movement of solidus and liquidus lines in the early stages of the start-up phase, the temperature contours are plotted just before and after 24 seconds of the water impingement as shown in Fig. 5.7. During this stage, the phase fronts move faster in the axial direction rather than in the radial direction. This fact can be verified through the Fig. 5.7. The axial movement of the solidus line increases the solidified shell thickness and provides enough strength to support the inner liquid melt. Further, due to the high casting speed, the solidus line just falls nearby the bottom of the mold which is dangerous due to the chances of mushy bleed out. Fig. 5.7 also indicates that the isotherms propagate from the butt toward the center of the melt.

The temperature contours are plotted for three different stages of DC casting as shown in Fig. 5.8. Fig. 5.8(a) shows the temperature contours at 78 seconds from the start of casting, and the billet height at this moment is 160 mm. The position of the solidus line with respect to the melt level indicates the sump depth. The sump depth at this stage is 127 mm in the center. Fig. 5.8(b) shows temperature contours at the end of the start-up



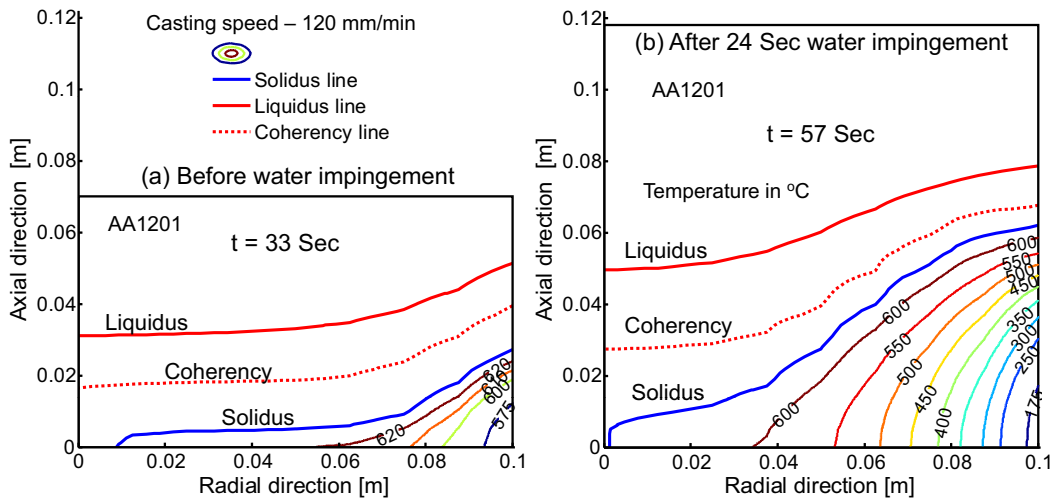


Figure 5.7: Casting speed 120 mm/min: Temperature contours at before and after water impingement

phase. The sump depth slightly decreases when compared to the previous stage. The pseudo steady state temperature contours are shown in Fig. 5.8(c). There is no change in sump depth observed after this stage. Nearly, half of the billet temperature is less than  $150^{\circ}\text{C}$ .

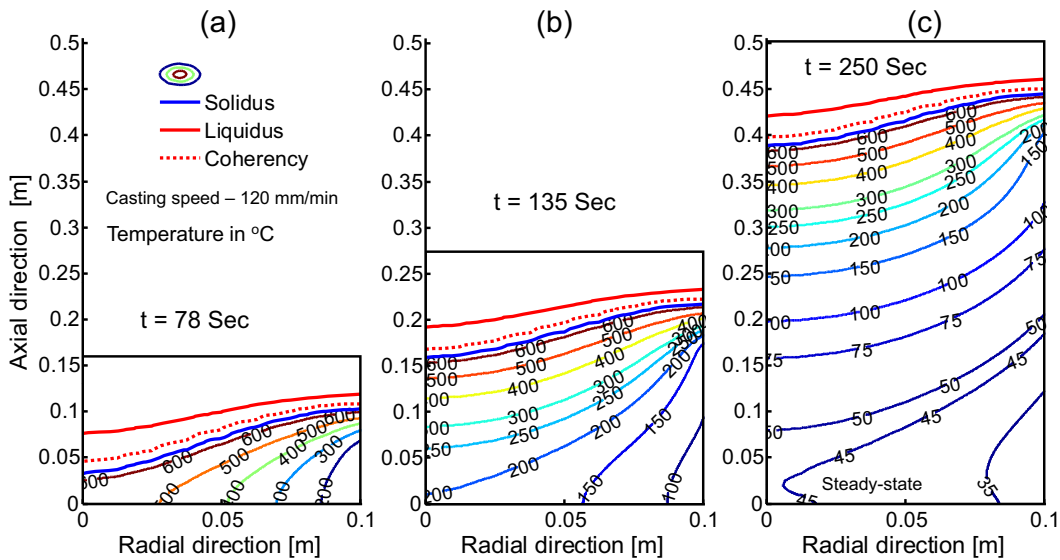


Figure 5.8: Casting speed 120 mm/min: Temperature contours at different stages of DC casting: (a) during start-up phase, (b) end of start-up phase, and (c) pseudo steady state

To understand the evolution of sump depth and length of the mushy zone, Fig. 5.9 is plotted. The sump depth is defined by the distance between the location of the solidus and the melt level. The length of the mushy zone is defined as the distance between the solidus and liquidus. It can be observed that the sump depth and mushy length are maximum at the center rather than at the surface. Fig. 5.9(a) shows that the sump depth

increases steadily and reaches a maximum of 128 mm at 75 s and then decreases to a constant value of 115 mm at the center. However, the length of the mushy zone at the center reaches a maximum of 50 mm at 57 s and decreases to a steady state value of 33 mm as shown in Fig. 5.9(b). The time lag between the maximum sump depth and the maximum mushy zone length is due to the faster advancement of melt level when compared to the phase-fronts movement. Once the solidus reaches the center, the mushy zone length will start decreasing, but this is not the case for the sump depth. To validate the evolution of the sump depth, the results are compared with the results of Suyitno *et al.* [56]. Here, it should be noted that the casting speed for both the cases are the same but the material is different. Suyitno *et al.* simulated for the Al-4.5%Cu alloy with the nearly similar thermal boundary conditions of the present case. However, the present results of AA1201 alloy are in excellent agreement with them. This fact indicates that the sump depth is independent of the material but strongly depends on casting speed and boundary conditions. However, the same is not true for the mushy length because different alloys may have different freezing ranges.

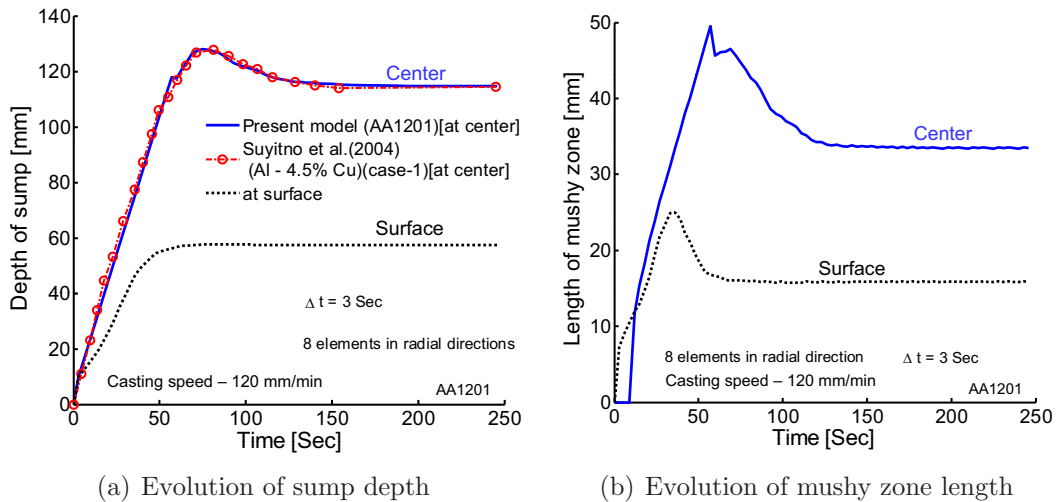


Figure 5.9: Casting speed 120 mm/min: evolution of sump depth and mushy zone

Some authors refer the *pseudo steady state* as the *steady state*. Therefore, it should be noted that both names refer the same state. The steady state sump depth and the mushy zone length along the radial direction are presented in Fig. 5.10. In the center of the billet, the sump depth and the mushy length are higher than near the edge of the billet. This is due to the rapid cooling near the surface. Almost double the value of the sump depth and mushy length is obtained at the center when compared to the surface. This can not be generalized for all kinds of alloys. Suyitno *et al.* [56] reported that the mushy zone length at the billet surface is slightly higher than the subsurface. However, in the present simulation, this effect is not observed.

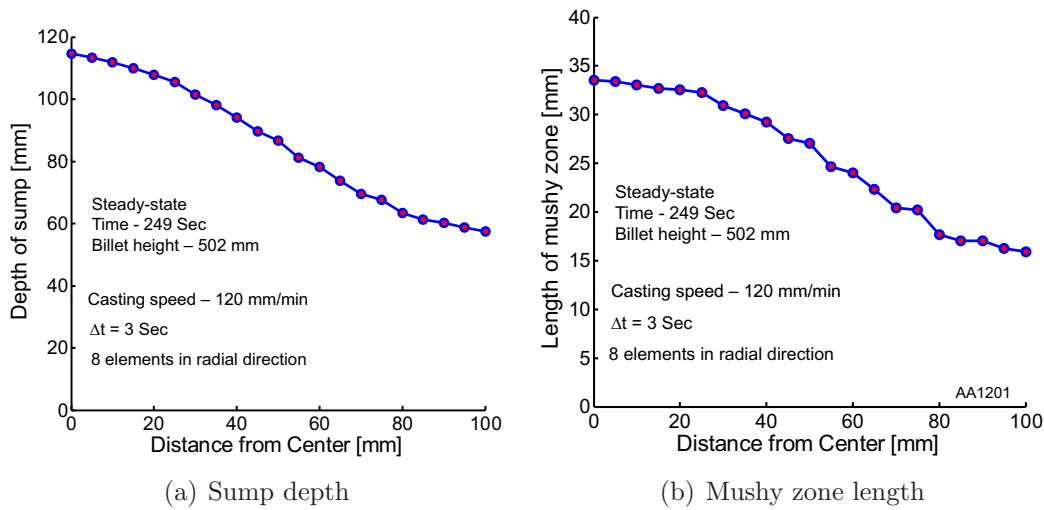
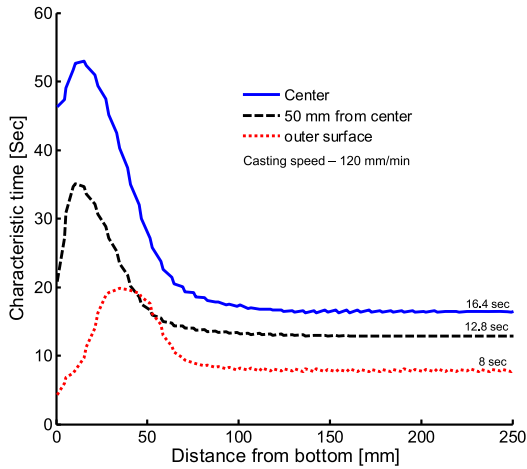


Figure 5.10: Casting speed 120 mm/min: radial distribution of sump depth and mushy zone at steady state

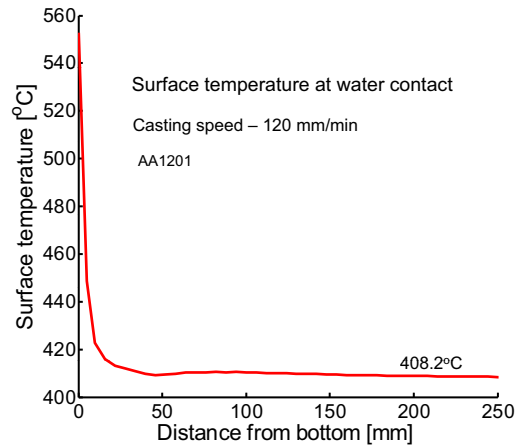
The mushy state is the most vulnerable state where more likely hot tears may occur. Therefore, the characteristic time (CT) which is known as the time spent in mushy state is computed and plotted as a function of billet height as shown in Fig. 5.11(a). Three different locations are considered such as the center, 50 mm from center, and outer surface of the billet. For all the locations, the CT increases and reaches a maximum value and then decreases to a steady state value. The CT is higher at the center, and the maximum occurs at a height of 10–12 mm from the bottom which corresponds to the start-up phase. This fact indicates that the center of the billet is the most critical region in the DC casting. Therefore, there are more chances of hot tearing to form near the center of the billet. And also, this is more likely to occur during the start-up phase. Further, the steady state CT at the surface is only half of the center.

The proper understanding of secondary cooling of DC casting is highly essential because nearly 80% of casting heat is extracted through this zone. Therefore, an attempt is made to analyze the temperature of the billet surface at which water starts striking initially. Fig. 5.11(b) shows the surface temperature of the billet vs. the distance from the bottom at which water starts impinging. Within a very short span of 50 mm from the bottom, the surface temperature of the billet decreases from 553°C to 410°C. After that, the temperature slightly increases and then decreases to a steady state value of 408°C which is nearly 100°C above the Leidenfrost temperature. Therefore, it can be clearly understood that the film boiling is the dominant mechanism of heat transfer in the water impingement zone. It is quite interesting to know the length of different boiling zones.

Fig. 5.12 shows the length of film, transition, and nucleate boiling zones vs. billet height. The steady state length of all the three boiling zones are around 14.3, 21.8,

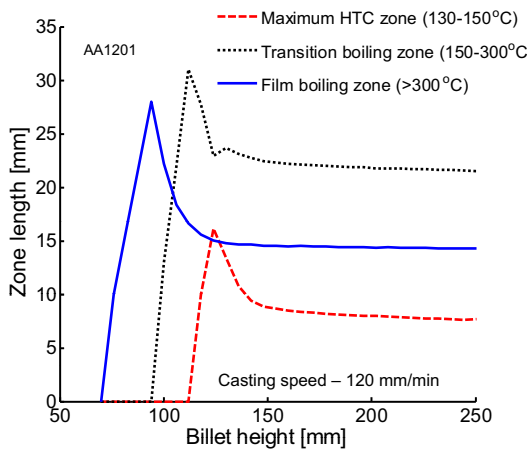


(a) Characteristic time

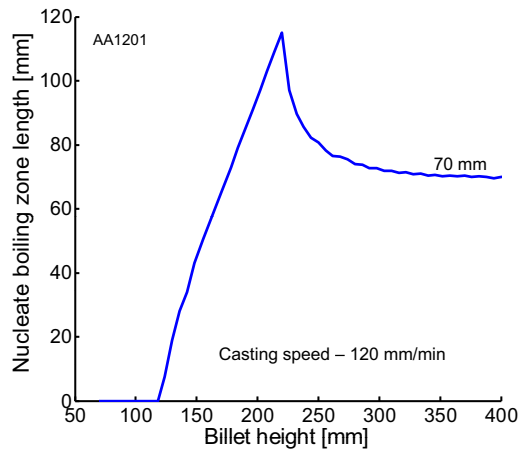


(b) surface temperature

Figure 5.11: Casting speed 120 mm/min: Characteristic time and surface temperature of billet at which water strikes first vs. distance from bottom of the billet



(a)



(b)

Figure 5.12: Casting speed 120 mm/min: different boiling zone length as a function of billet height

and 70 mm respectively. Further, the length of the maximum heat flux or HTC zone can be crudely approximated as the thickness of wetting front. In this case, the steady state wetting front thickness lies around 7.8 mm which is practically reasonable. These informations are very useful for altering the cooling strategy.

The evolution of radial, axial, and circumferential stresses at the center and the subsurface (90 mm from center in the radial direction) of the billet are plotted as shown in Fig. 5.13. Near the bottom of the billet, the influence of the boundary condition is very high. Therefore, the cross-section considered for the analysis is taken at 50 mm from the bottom. Further, the element integration points are located within the elements and not on the element boundaries. The stress and strain are computed only in the integration points. Even though, it is possible to bring the integration point quantities to the nodal level through the inverse mapping but this is not more accurate to make the decisions. Due to this reason, the nearest integration points are considered for the study. Due to the symmetry, the radial and circumferential components of stresses are equal at the center. In the center, all the stress components are tensile in nature. However, near the subsurface, the axial and circumferential stresses are compressive. It can be seen that stresses become constant after certain time. The higher value of tensile stresses near the center of the billet can easily open the existing cracks.

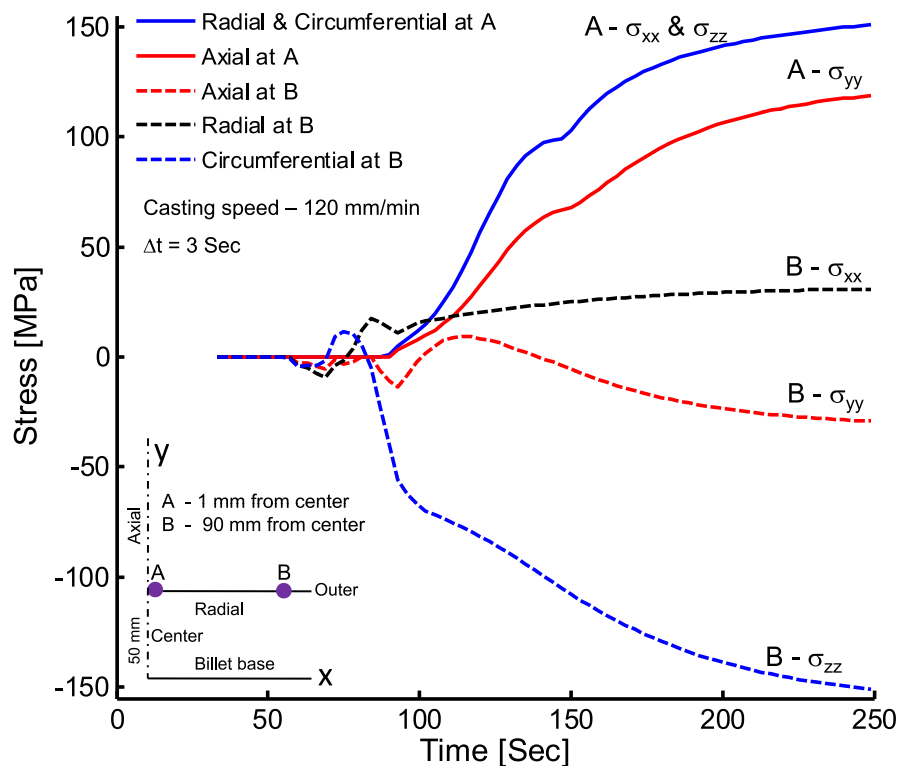
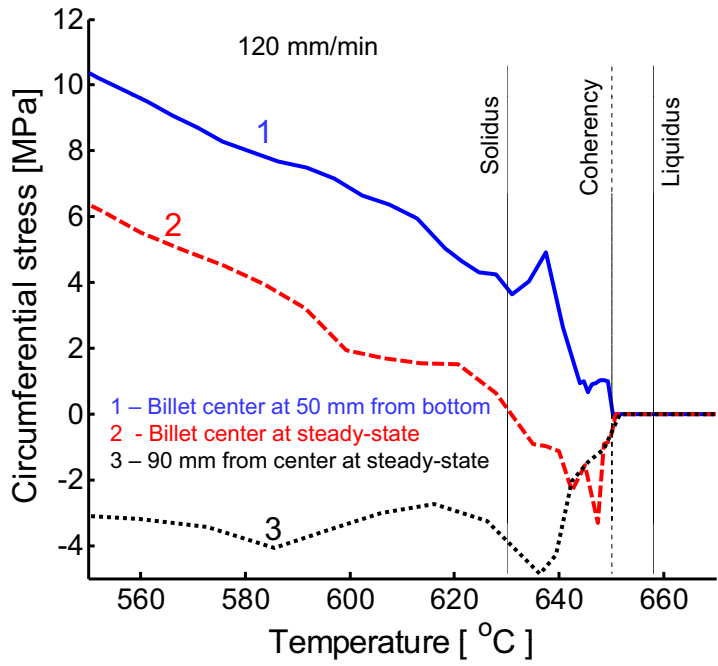


Figure 5.13: Casting speed 120 mm/min: evolution of stress at center and a radial distance of 90 mm (50 mm from bottom)

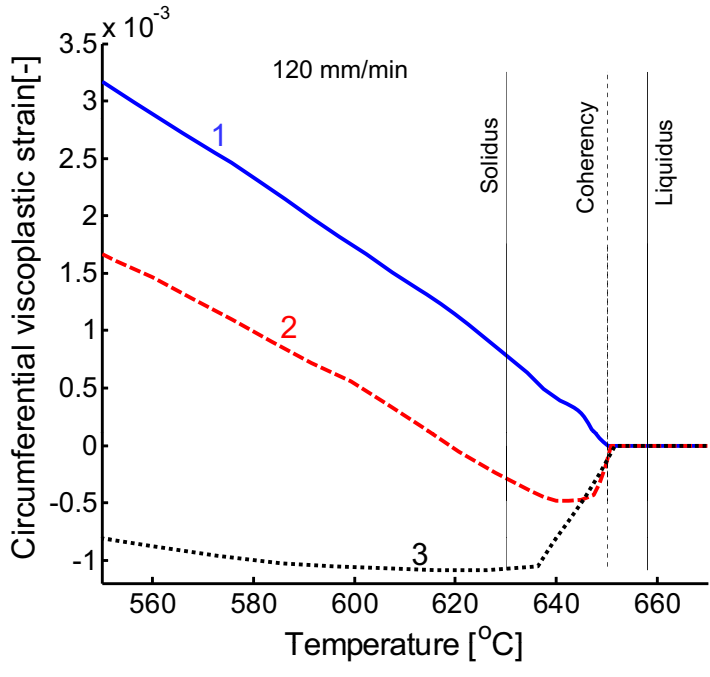
It is commonly believed that in order for a hot tear to form, the stress or inelastic strain must exceed a critical limit. Since the starting cracks in the center of the billet may propagate in the radial or axial direction, it is of interest to analyze the stress or inelastic strain component in the direction perpendicular to the crack direction. The circumferential component of stress/strain is the one which can open the crack in both the axial and radial directions. Further, the hot tear may form during the last stage of solidification in the start-up phase. Fig. 5.14 shows the circumferential stress and viscoplastic strain as a function of temperature. Three locations are selected such as the center of the billet at start-up phase (1), center of the billet at pseudo steady state (2), and subsurface of the billet at pseudo steady state (3). Until the coherency temperature, there is no accumulation of stress and viscoplastic strain at all the locations. From the coherency to the solidus, the location (1) which corresponds to the start-up phase, the stress and viscoplastic strain are tensile in nature. However for the location (2) and (3), the nature of stress and strain are compressive in the mushy state. Below the solidus temperature, the nature of stress and strain at the locations (1) and (2) are tensile but for the location (3), it is compressive. Overall, the start-up phase stress and strain are higher when compared to the steady state for all temperatures. This tensile nature of stress and strain in the mushy zone is the most favorable situation for the development of hot tear.

Similarly, the axial components of stresses and viscoplastic strains are plotted in Fig. 5.15. The trend of the axial stress is similar to the circumferential stress with slightly lesser magnitude. However, the axial stress and axial viscoplastic strain behave in an opposite manner. At the billet center, the axial stresses are tensile and the axial viscoplastic strains are compressive both in the start-up and steady state. The situation is again reversed at the subsurface during the steady state. The reason for such a behavior of axial viscoplastic strain is not yet clear. Similar results are reported in Suyitno *et al.* [56]. The tensile nature of axial stress can easily open the existing cracks in the radial direction. However, the radial crack can not reach the outer surface due to high compressive stress.

The components of stresses and viscoplastic strains at the solidus temperature are shown in Fig. 5.16 at the center of the billet along the axial direction. Plotting this graph is little trivial due to the large temperature gradient at the end of solidification. The temperature may not exactly reach the solidus temperature. Therefore, a linear interpolation is performed between the upper and the lower solidus point. Further, the stresses and strains are taken at different time intervals. The circumferential and radial stresses at the solidus temperature reaches a maximum of 5 MPa at a location of 45–55 mm from bottom and, then decreases to a steady state value of 1.7 MPa. Similar

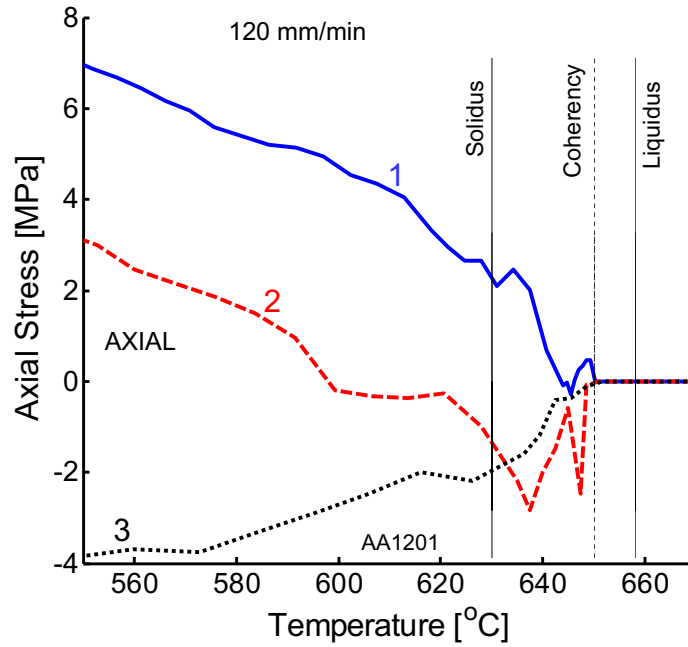


(a) Circumferential stress

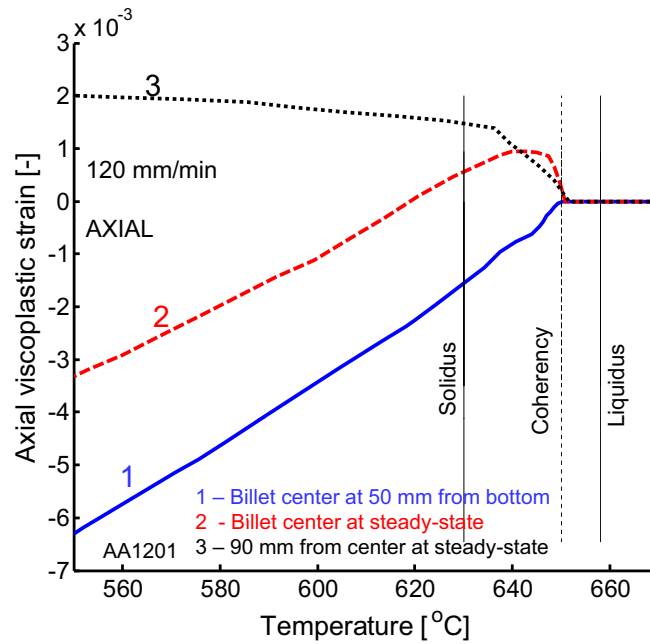


(b) Circumferential viscoplastic strain

Figure 5.14: Casting speed 120 mm/min: circumferential stress and viscoplastic strain as a function of temperature



(a) Axial stress



(b) Axial viscoplastic strain

Figure 5.15: Casting speed 120 mm/min: axial stress and viscoplastic strain as a function of temperature

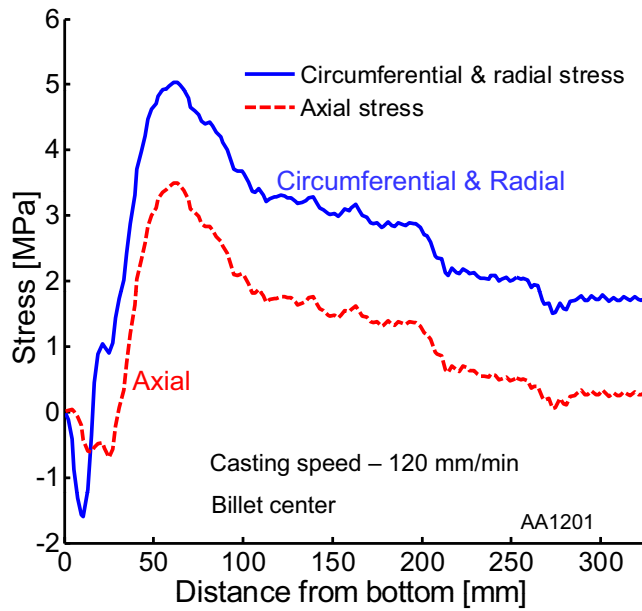


trends are observed for the axial stress. All the components of stresses at the center of the billet along the axial direction are tensile in nature except in a smaller region nearby the bottom block. Further, the stresses are maximum during the start-up phase. Therefore, one can conclude that the start-up phase is the most critical phase in DC casting and the hot tear may form near the center of the billet where the regions close to lower mushy. However, the viscoplastic strains at the solidus temperature behave little different and contracting with the results of Suyitno *et al.* [56]. The circumferential and axial components of viscoplastic strains follow an opposite pattern. The circumferential viscoplastic strain reaches a compressive maximum of 0.011 at 20 mm from the bottom and then changes the nature to tensile. Similarly, the axial viscoplastic strain is tensile near the bottom block zone and then becomes compressive. This may be due to the influence of boundary conditions chosen.

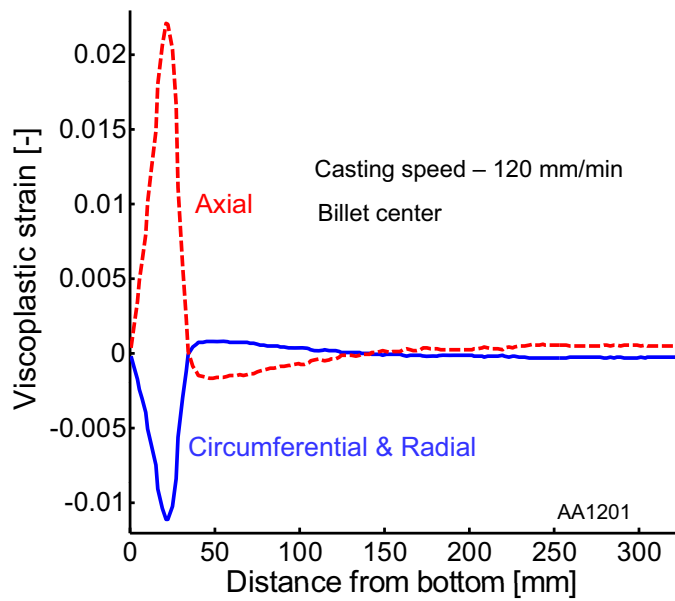
The contours of the radial, axial, and circumferential stresses during the steady state casting are shown in Fig. 5.17. It can be perceived that the stresses start developing in the mushy zone in the vicinity of the coherency. The radial stress is tensile at all positions except a smaller region nearby the water impingement. The axial and circumferential stresses are compressive close to the edge and tensile in the center of the billet. In the water impingement zone, the axial stress is relatively higher and tensile in nature. Nearby solidus, the stress state is tensile which is in good agreement with Suyitno *et al.* [56]. The stress contours nearby bottom block regions is little complex.

The contours of radial, axial, and circumferential viscoplastic strains during the steady state casting are shown in Fig. 5.18. The radial viscoplastic strain is compressive near the subsurface of the billet and tensile in the center. This observation is a little contradicting with the Suyitno *et al.* [56]. In contrast with the axial stress, the axial viscoplastic strain is compressive near the center and tensile in the edge which is in good agreement with Suyitno *et al.* [56]. The circumferential viscoplastic strain is compressive near the edge of the billet and tensile in the center of the billet. The radial and circumferential viscoplastic strains in the mushy state close to the solidus and nearby center are tensile whereas it will become compressive near the edge. However, the axial viscoplastic strain behaves oppositely. The influence of bottom block boundary on strain contours are higher than the stress.

The equivalent stress distribution along with the deformed shape of the billet is shown in Fig. 5.19. The nodal displacement components are multiplied by a factor of 5. The equivalent stress is higher near the edge and lower at the center. Near the mushy and higher temperature regions, the equivalent stress is almost zero. In the butt region, the equivalent stress reaches a global maximum. To understand the butt deformation, Fig. 5.20 is plotted. It shows the evolution of butt curl and temperature. Until water



(a) Circumferential stress



(b) Circumferential viscoplastic strain

Figure 5.16: Casting speed 120 mm/min: circumferential stress and viscoplastic strain at solidus temperature as a function of distance from bottom of the billet

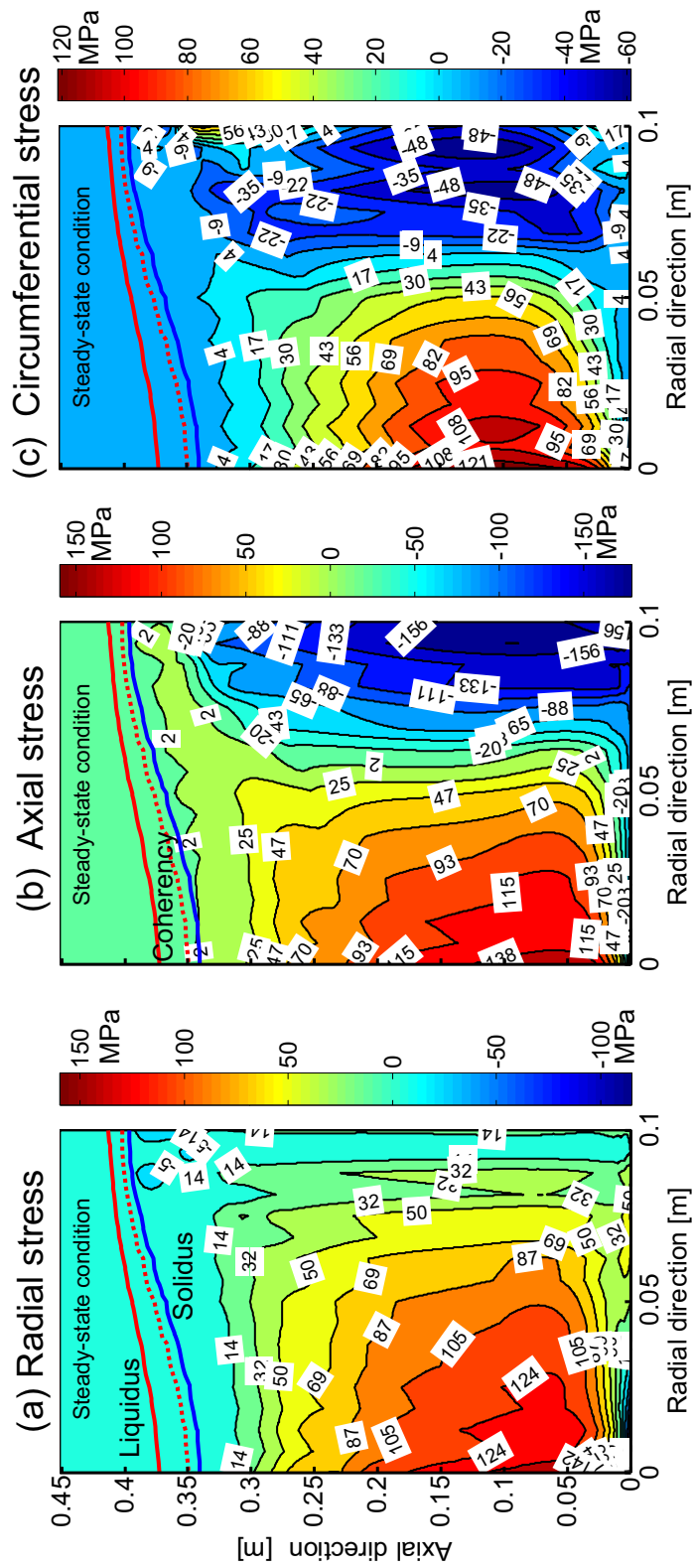


Figure 5.17: Casting speed 120 mm/min: stress contours at pseudo steady state



touches the butt, the displacement is relatively low and then it suddenly shoots up to a maximum of 1.6 mm at 140°C. After that, the thermal gradients are not sufficient to induce further deformation. Therefore, it relaxes to a steady state value of 0.9 mm.

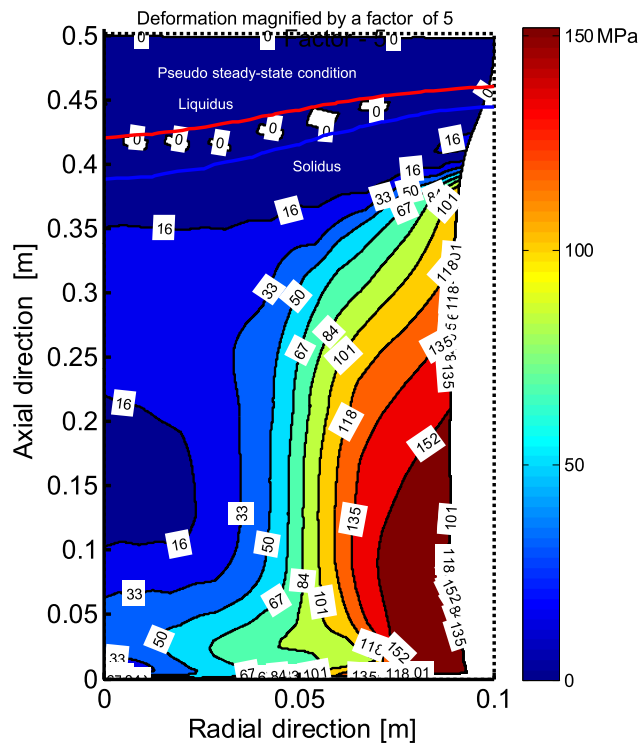


Figure 5.19: Casting speed 120 mm/min: deformed shape with equivalent stress distribution at pseudo steady state

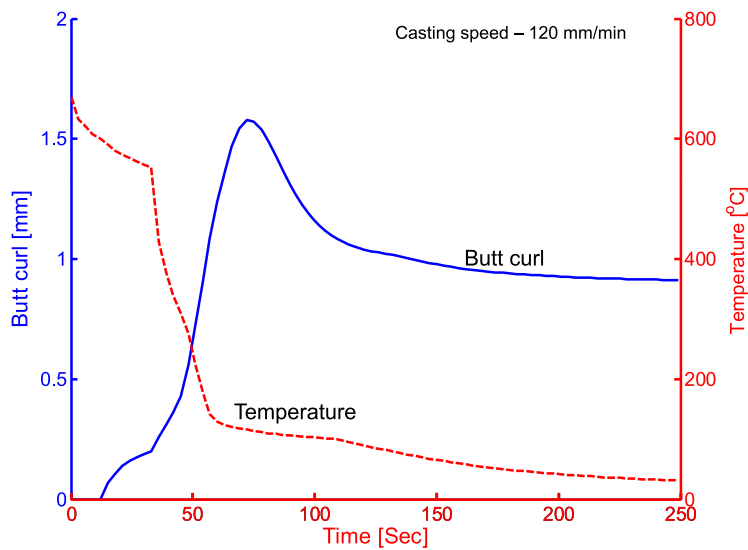


Figure 5.20: Casting speed 120 mm/min: butt curl evolution

## 5.3 Influence of casting speed

The influence of the casting speed is studied in two ways: (a) different casting speed profiles, and (b) constant casting speed with different magnitudes. Firstly, six different casting speed profiles are considered which are given as a function of billet height as shown in Fig. 5.21. In all the cases, during the steady state condition, the casting speed is maintained constant. However, the start-up phase casting speed is different for all the cases. The case-1 is initially started with a speed of 100 mm/min and increased to 120 mm/min when the billet height reaches 29 mm, and afterwards the same speed is maintained throughout the casting. The case-2 is similar to the case-1 but the casting speed is gradually increased from 100 to 120 mm/min when the billet height reaches 300 mm. In case-3, a constant casting speed of 150 mm/min is used for the entire casting. The case-4 is similar to the case-2 but a casting speed of 150 mm/min is reached at a height of 300 mm. All the above mentioned four cases are exactly the same as Suyitno *et al.* [56]. Additionally, case-5 and case-6 are considered to illustrate the importance of the start-up phase ramping procedure which are taken from M'Hamdi *et al.* [81]. These two cases are similar after a billet height of 50 mm. However, the initial casting speed is different. In case-5, the casting speed of 80 mm/min is maintained constantly until the height of the billet reaches 150 mm and then suddenly increased to a higher speed of 110 mm/min. In contrast to case-5, the case-6 is started with 130 mm/min and then suddenly decreased to 80 mm/min at a billet height of 50 mm. The case-6 is not exactly the same as M'Hamdi *et al.* [81] because they increased the speed gradually to 110 mm/min after a height of 50 mm. However, the case-5 is same as M'Hamdi *et al.* [81]. Secondly, four different constant casting speeds are considered such as 80, 120, 150, and 180 mm/min.

### 5.3.1 Thermal field

The steady state temperature distribution for the cases 1 and 3 is shown in Fig. 5.22. When compared to case-1, the billet is relatively hotter in case-3. Even though these two cases are plotted at two different times, the sump depth and mushy dimensions at center are relatively lower for case-1. Similar temperature contours are obtained for the cases 2 and 4, i.e. 1 and 2 are similar and 3 and 4 are similar. Further, the steady state temperature distribution for the cases 5 and 6 is also similar. Therefore, it can be concluded that the steady state temperature distribution is independent of the ramping procedure. However, the time at which the steady state is reached and the billet height differ from each other.

The sump depth and the mushy dimensions are used as a criterion for the hot tearing

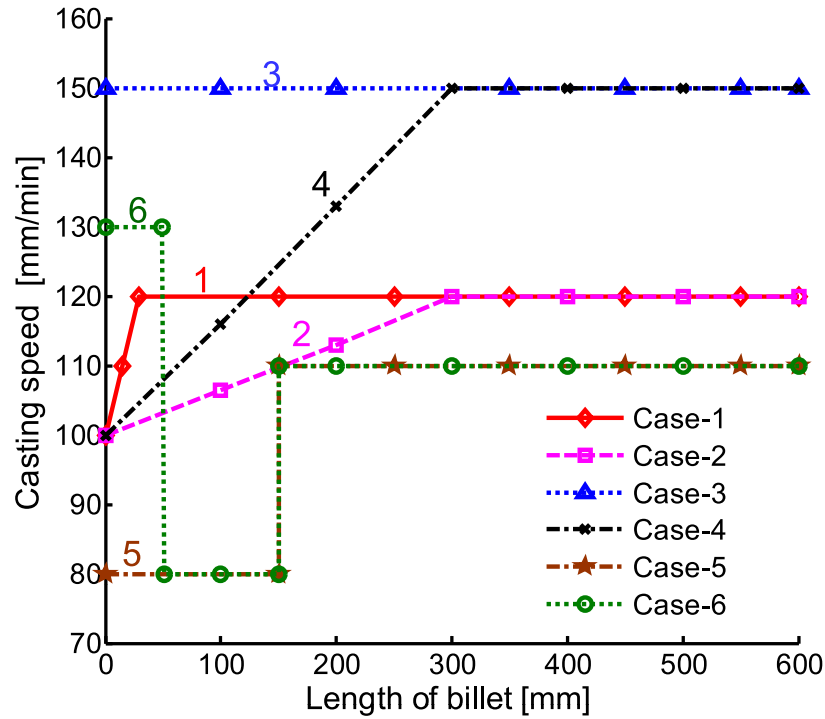


Figure 5.21: Casting speed profiles vs. length of billet

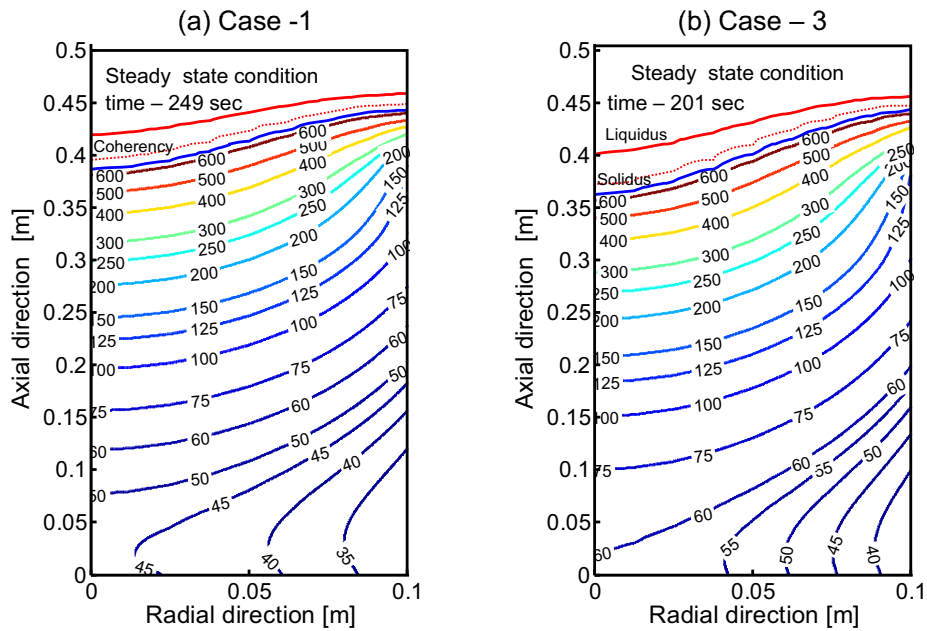
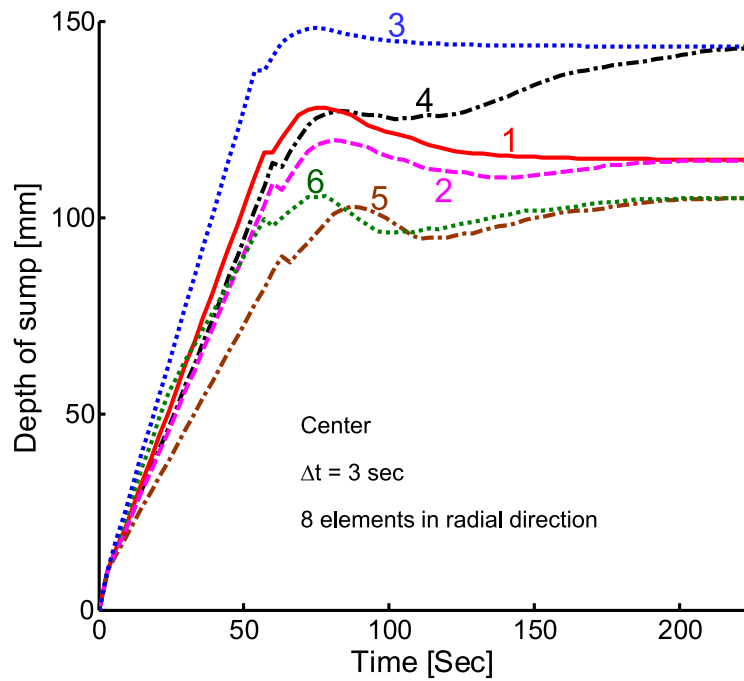


Figure 5.22: Influence of casting speed profile: steady state temperature distribution for (a) case-1 and (b) case-3

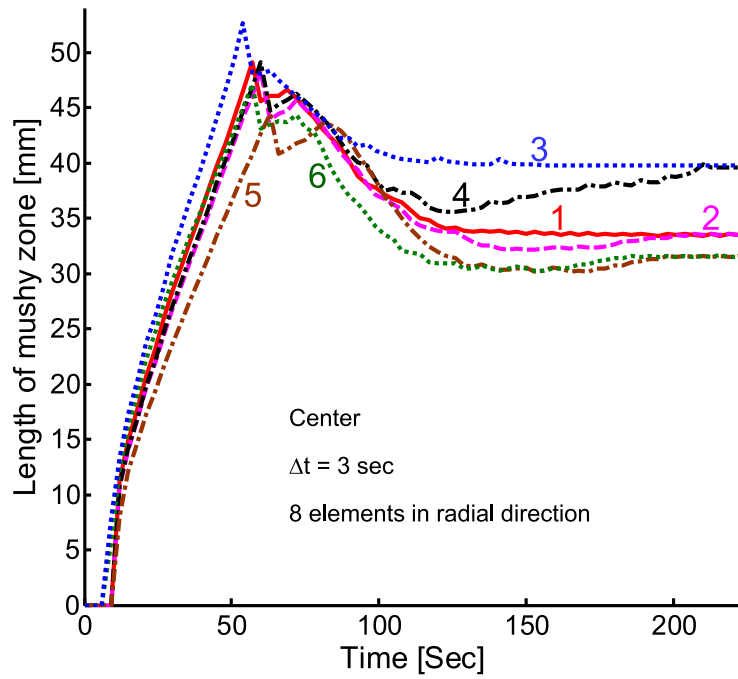
development [56]. Therefore, it is important to analyze these two parameters. For the six casting profiles considered, the evolution of sump depth and mushy zone length are plotted (Fig. 5.23) at the center of the billet where the values are critical. In case-1 and 3, the sump depth increases steadily and reaches a maximum at 78 s after then decrease to a steady state value. However, in case-3, there is not much decrease in sump depth after the peak, and further it reaches the steady state much faster than in the other cases which is shown in Fig. 5.23(a). This contradicts the results of Suyitno *et al.* [56] because they reported that the higher the casting speed, the longer is the time to reach the steady state. All the remaining cases (2, 4, 5, and 6), after reaching a peak value, the sump depth decreases and then increases to reach a steady state value. The steady state is obtained for case-1 at 144 s (billet height - 285 mm), case-2 at 195 s (360 mm), case-3 at 111 s (273 mm), case-4 at 225 s (495 mm), case-5 at 210 s (314 mm), and case-6 at 210 s (339 mm). From these results, it is clear that the ramping procedure delays the time and increases the billet height to reach a steady state. Even though a lower casting speed is used in the cases 5 and 6, due to the improper ramping method, the steady state is reached at a slightly longer time. Therefore, it can be concluded that the sudden change in casting speed increases the time to reach a steady state. While comparing the cases 5 and 6, the sump depth evolves faster in case-6 than in case-5. Only 3 mm difference in sump depth is observed between case-6 and case-5 at the peak. From the start-up phase sump depth evolutions, it can be rated that the probability of hot tear formation for the casting profiles considered as in the descending order as 3-4-1-2-6-5. This means that case-3 has higher chances and case-5 has lower.

The evolution of mushy zone length (MZL) is nearly similar as that of sump depth for all the cases as show in Fig. 5.23(b). However, the cases 5 and 6 behave in a slightly different manner. Before reaching the peak value, the MZL evolution rate is higher for case-6 when compared to case-5. Similarly, after the peak, for case-6, the MZL evolution rate decreases faster than case-5. Therefore, it is easy to rate the cases starting from 1 to 4 as 3-4-1-2 but for the cases 5 and 6, it is not possible based on the MLZ evolution. It is concluded that the steady state sump depth and MZL are independent of the ramping procedure. To understand the influence of the casting speed, the steady state sump depth and MZL are plotted as a function of radial position for the different constant casting speeds as shown in Fig. 5.24. It shows that the sump depth and MZL are maximum at the center and the magnitude increases with increase in casting speed. However, in the surface, the MZL decreases with increase in casting speed. In the subsurface of distance 80 mm from the center, the mushy dimension is independent of casting speed. Similarly, for the casting speed of 150 and 180 mm/min, the sump depth at the surface is nearly equal. The percentage increase in casting speed is same as the percentage increase in





(a) Evolution of sump depth



(b) Evolution of mushy zone length

Figure 5.23: Influence of casting speed profile: evolution of sump depth and mushy zone at center

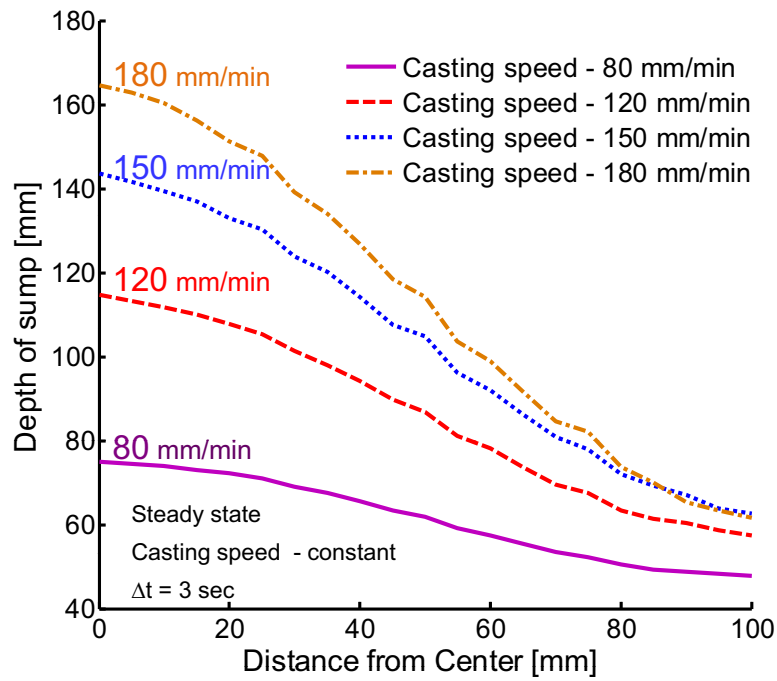
sump depth at the center. However, the percentage increase in MZL is slightly lower.

### 5.3.2 Mechanical field

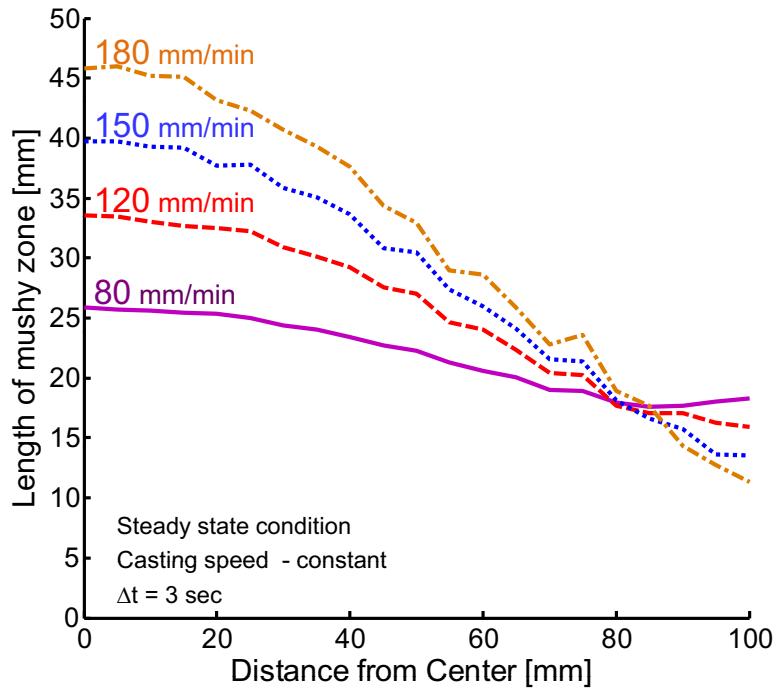
Due to the tensorial nature of stress and strain, analyzing the displacement field results are relatively complex when compared to that of the thermal field. According to the thermal analysis, case-3 has the highest and case-5 has the lowest chances of hot tearing formation. During the steady state condition, almost similar behavior is observed for the cases 5 and 6. Therefore, the steady state distribution of circumferential stress ( $\sigma_{zz}$ ) and circumferential viscoplastic strain ( $\epsilon_{zz}^{vp}$ ) are plotted for the cases 6 and 3 as shown in Fig. 5.25 and Fig. 5.26. The stress and strain concentrations nearby the bottom block area are higher for case-3 compared to case-6. Higher tensile stress and strain are induced in case-3 when compared to case-6. However, near the water impingement and butt areas, the tensile viscoplastic strain region is larger in case-6 than in case-3. A higher tensile stress is induced near the solidus line at the center in case-3. Therefore, case-3 has the higher chances of hot tear formation than case-6.

The evolution of circumferential stresses at the center of the billet (56 mm from bottom) is plotted as shown in Fig. 5.27(a) for all the 6 casting profiles. Due to the symmetry, these curves also represent the radial stress evolution. Without doubt, the rating is the same as before. The ramping procedure has a positive influence on the stress evolution. Similarly, the circumferential stresses at the billet subsurface (56 mm from bottom) are plotted as shown in Fig. 5.27(b) for four different constant casting speeds. The higher the casting speed, the higher the stress at subsurface.

The development of circumferential stress and viscoplastic strain as a function of temperature is studied through the Fig. 5.28. Here, the location is selected at a distance of 50 mm from bottom close to center of the billet. Even though the stresses are tensile in nature at the end of the solidification for all the casting profiles, the chances of hot tear formation are more for the cases 1, 3, and 4 when compared to the cases 2, 5, and 6. This is due to the development of compressive stress before reaching the solidus for the cases 2, 5, and 6. Further, for the cases 5 and 6, the viscoplastic strains are compressive even at the end of the solidification. Therefore, case-5 and case-6 has no chances of developing hot tear if the viscoplastic strain is the deciding criteria. This is not the case for the stress because the nature of stresses are tensile at the end of solidification for all the cases. While comparing case-5 with case-6, the chances of crack formation are more for case-6 than case-5. Not only hot tears, the chances of cold crack formation are also higher at the billet center where the regions correspond to the start-up phase. The rating is same as before, however, it is difficult to say when it comes to case-1 and case-4 due to the similar behavior.



(a) sump depth



(b) Mushy zone length

Figure 5.24: Influence of casting speed: radial distribution of sump depth and mushy zone at steady state

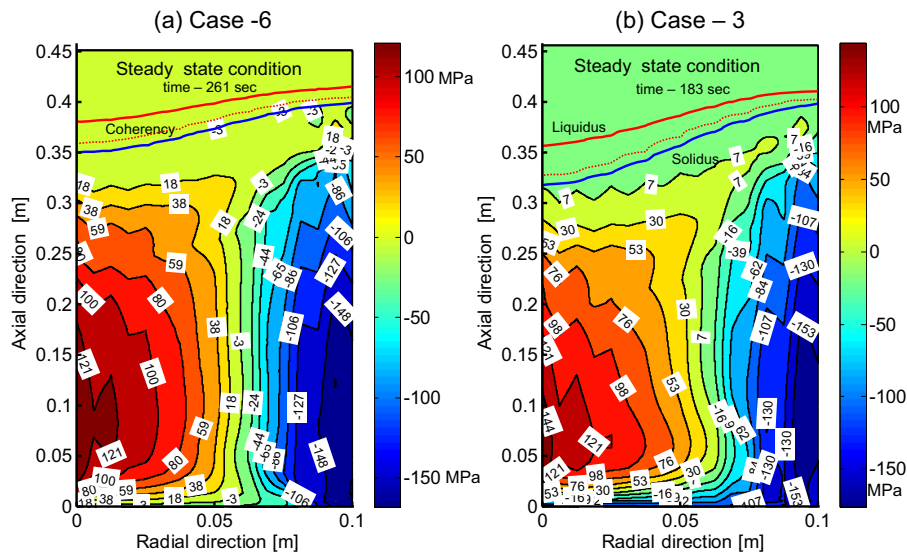


Figure 5.25: Influence of casting speed profile: steady state circumferential stress distribution for (a) case-6, and (b) case-3

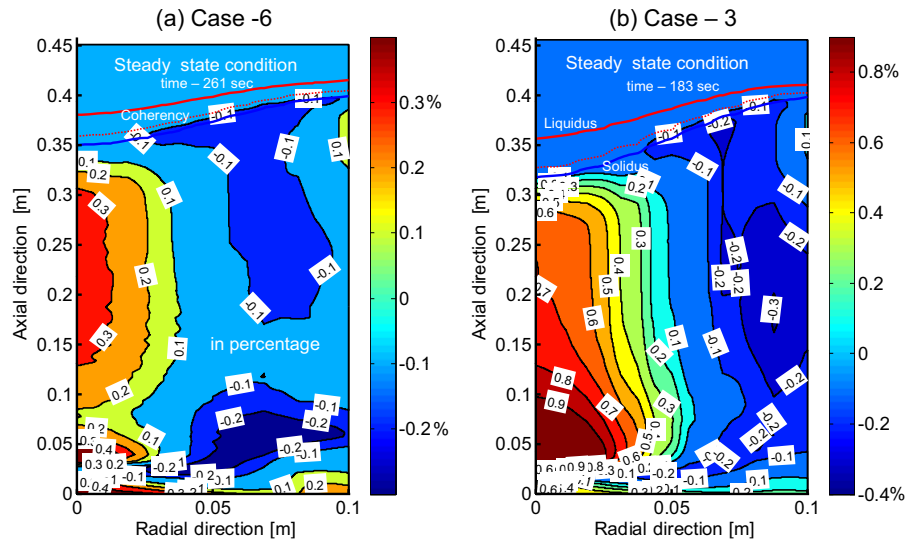
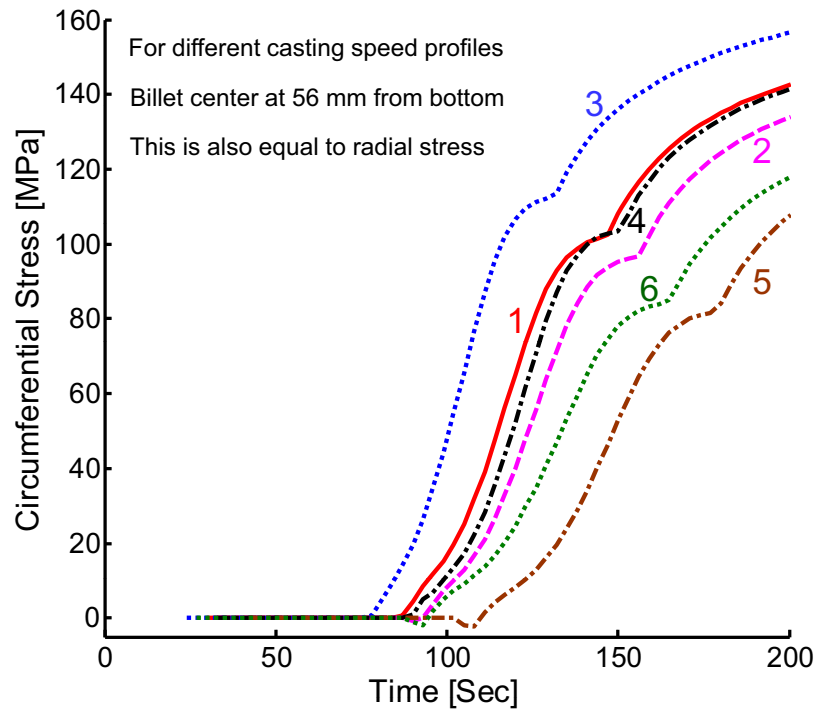


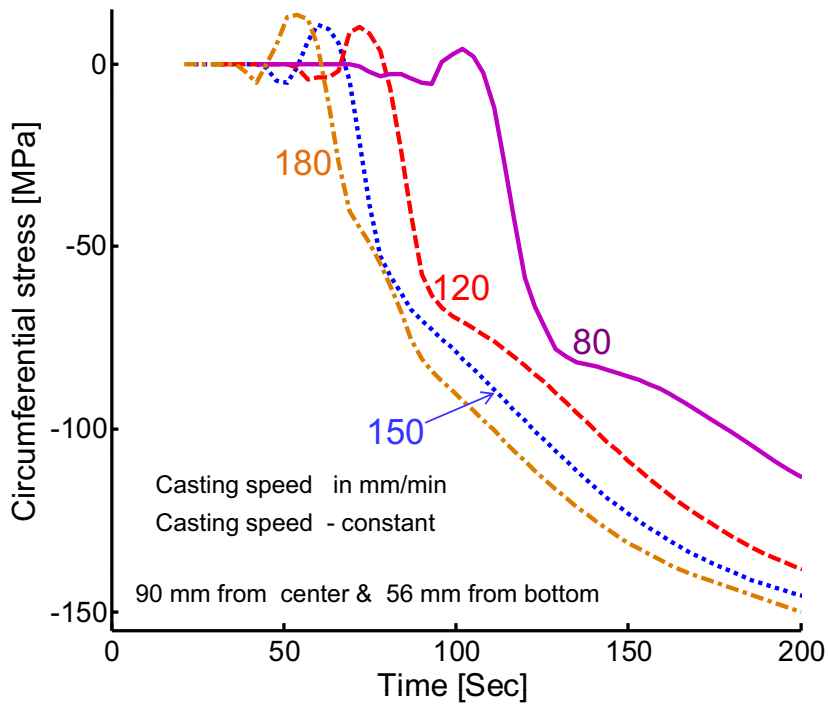
Figure 5.26: Influence of casting speed profile: steady state circumferential viscoplastic strain distribution for (a) case-6 and (b) case-3

To further ensure the influence of the casting speed, the previous conditions are repeated for different constant casting speeds, and the results are shown in Fig. 5.29. It is obvious that increase in casting speed results in an increase of stress and strain in the mushy. If the casting speed is sufficiently lower, the nature of the stress and strain in the mushy will become compressive. Even though, the constitutive equation changes at the end of the solidification, the strain pattern is uniform but the stress change is not smooth irrespective of the casting speed.

The circumferential component of stress and viscoplastic strain at the solidus temperature vs. billet height at the center are shown in Fig. 5.30 for the different casting

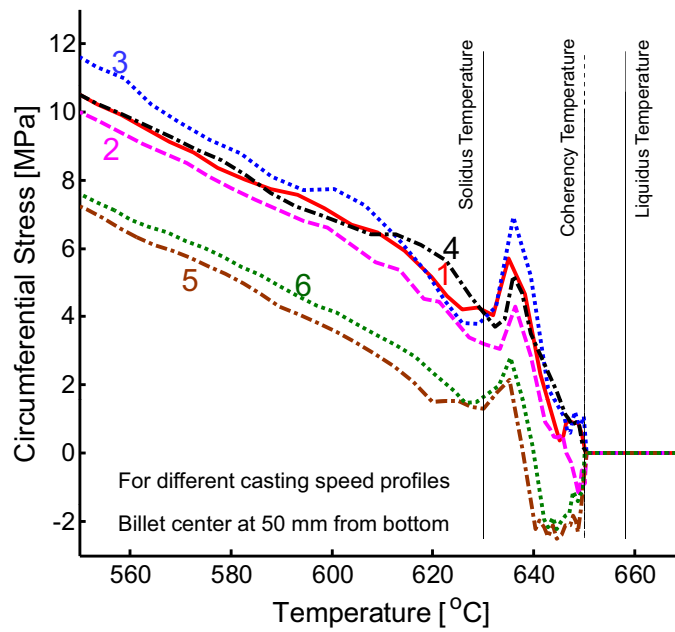


(a) center

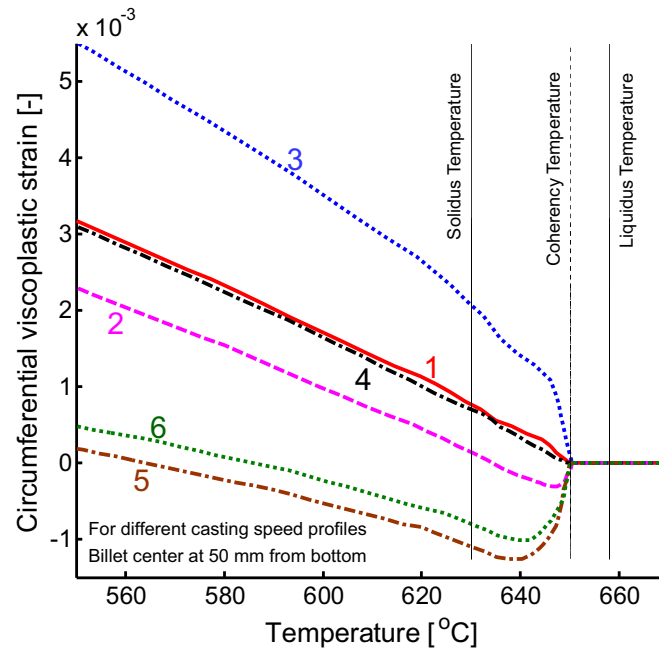


(b) subsurface

Figure 5.27: Influence of casting speed and profile: evolution of circumferential stresses at 56 mm from bottom (a) center and (b) subsurface of 90 mm from center



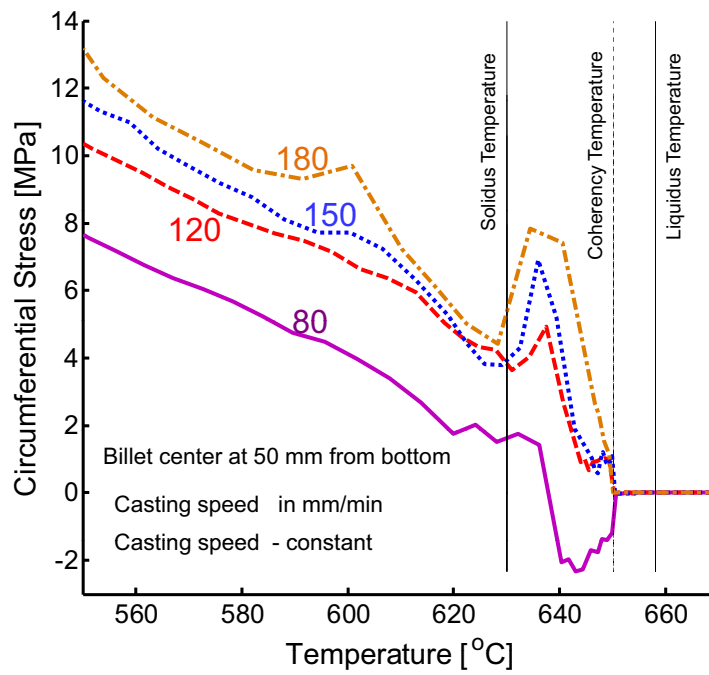
(a) Circumferential stress



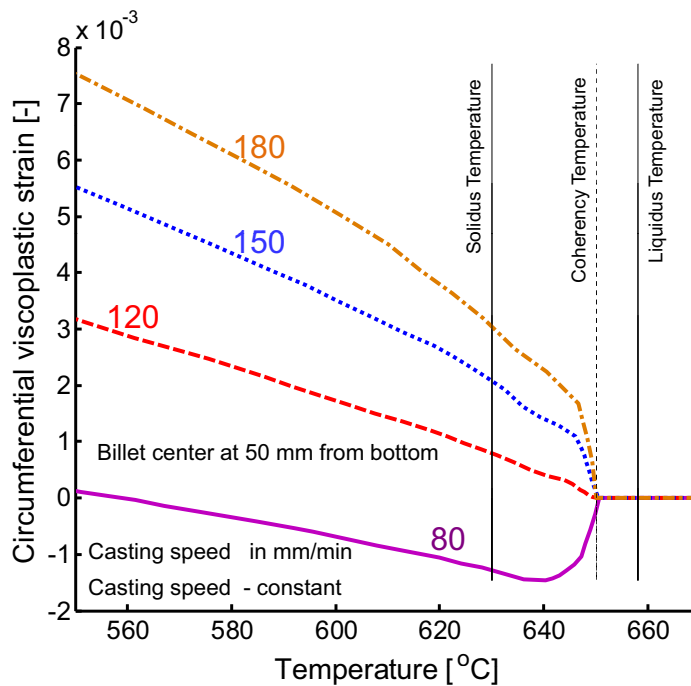
(b) Circumferential viscoplastic strain

Figure 5.28: Influence of casting speed profile: circumferential stress and viscoplastic strain as a function of temperature

profiles. In all cases, the maximum tensile stress occurs at a height of 48–54 mm which corresponds to the start-up phase. However, for the cases 5 and 6, the stress becomes compressive after the peak and remains compressive during the steady state. In contrast to case-5 and case-6, in all other cases, the nature of steady state stress is tensile which is favorable for the growth of existing crack or hot tear. For case-3, not only in the start-up



(a) Circumferential stress



(b) Circumferential viscoplastic strain

Figure 5.29: Influence of casting speed: circumferential stress and viscoplastic strain as a function of temperature

phase, during the steady state also hot crack may form due to relatively higher tensile stress. The strain concentration nearby the bottom block zone is very high. Therefore, for plotting of viscoplastic strain, 35 mm from bottom is omitted (Fig. 5.30(b)). For the

cases 1 to 4, the start-up phase strains are tensile and then remains tensile for the cases 3 and 4 during the steady state. The steady state strains are compressive for the cases 1, 2, 5, and 6. In contrast to the stress behavior near the mushy zone during the start-up phase, the viscoplastic strains are compressive for the cases 5 and 6. Finally, the rating is same as before.

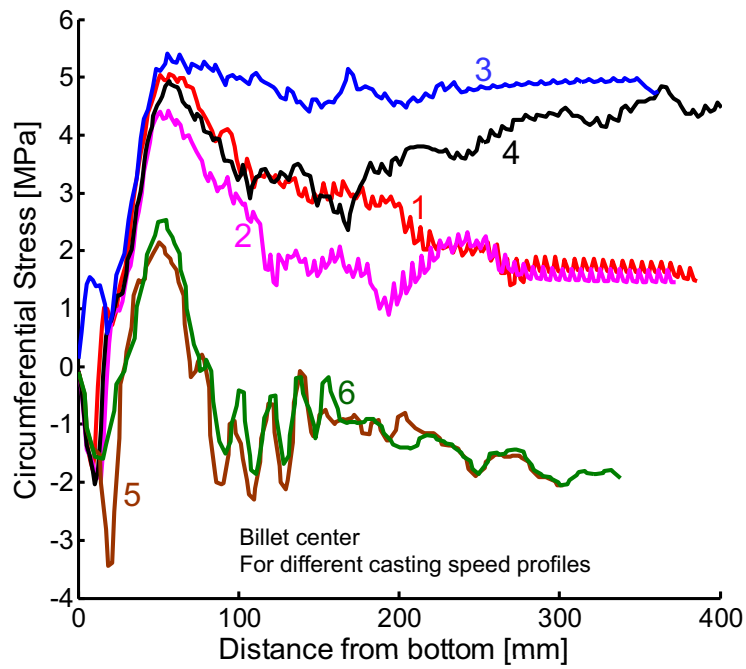
The axial stress and axial viscoplastic strain at the solidus temperature are shown in Fig. 5.31 at the billet center during the start-up phase and the steady state. Fig. 5.31(a) shows that during the start-up phase, the axial stresses are tensile for all the casting speeds and remains tensile for higher casting speeds such as 120, 150, and 180 mm/min during the steady state. For the lower casting speed (80 mm/min), the steady state stress becomes compressive. The axial viscoplastic strain is completely opposite to that of the axial stress. Fig. 5.31(b) shows that for the case of 80 mm/min, higher tensile viscoplastic strain is developed during the steady state phase. In other casting speeds, the axial viscoplastic strains are always compressive at the end of the solidification. Using axial stress as a criterion, the hot tear is most likely to occur for the higher casting speed. The situation is reverse if the axial viscoplastic strain is used as a criterion. Similar phenomena are reported in Suyitno *et al.* [56].

The behavior of the butt is presented in Fig. 5.32 for the different casting profiles and speeds. According to the maximum butt curl which occurs during the start-up phase, the rating is the same as previously discussed. However, based on the steady state butt curl, the rating is exactly opposite and the situation is complicated as shown in Fig. 5.32(a). Therefore, Fig. 5.32(b) is used to clarify this controversy. It shows that the higher the casting speed, the lower will be the steady state butt curl. This is due to higher reheating at the butt for the higher casting speed. Therefore, the thermal stresses relax faster.

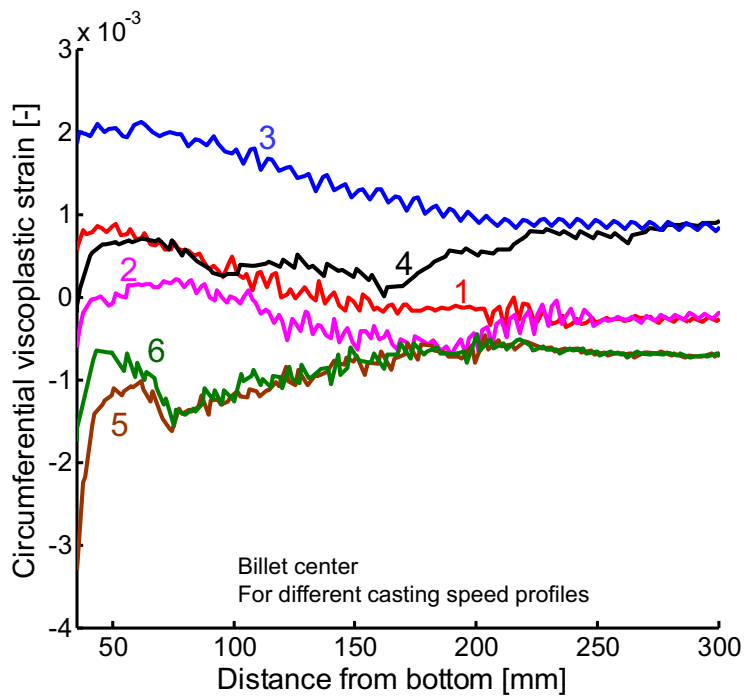
### 5.3.3 Hot tearing criterion

Clyne and Davies [87] criterion is applied to all the different casting speed profiles and the results are shown in Fig. 5.33(a) as a function of the distance from the bottom of the billet at center. It is observed that in all the cases, nearby the bottom block contact area, the hot tearing susceptibility (HTS) is very high and then decreases to a constant value within a short distance. There is not much difference between the various casting speed profiles. Therefore, the radial distribution of HTS at the steady state condition is plotted and shown in Fig. 5.33(b) for different casting speeds. Nearly similar curves are obtained for all the casting speeds. HTS is lower at the center and outer surface when compared to the intermediate sections. Further, HTS at the surface is higher than the center. Similar kind of results are reported by Suyitno *et al.* [84]. Even though this criterion is easy to implement, it does not provide any useful informations such as the influence of ramping,





(a) Circumferential stress



(b) Circumferential viscoplastic strain

Figure 5.30: Influence of casting speed profile: circumferential stress and viscoplastic strain at solidus temperature as a function of distance from bottom of the billet

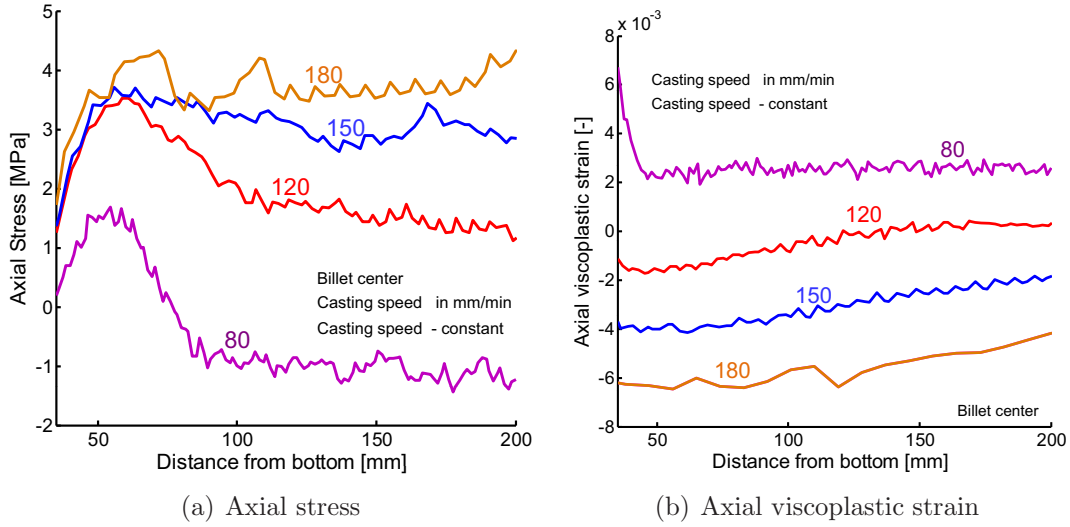


Figure 5.31: Influence of casting speed: axial stress and viscoplastic strain at solidus temperature as a function of distance from bottom of the billet

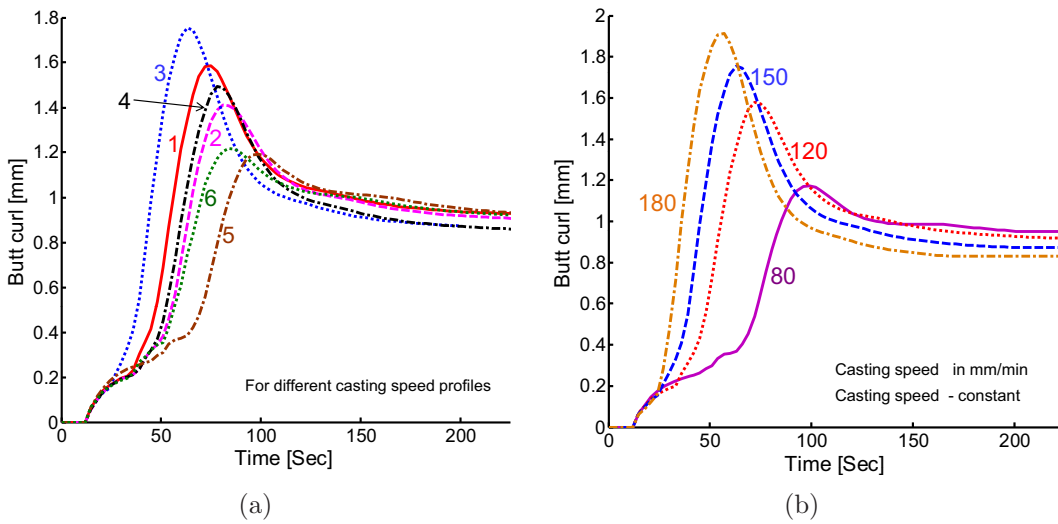


Figure 5.32: Influence of casting speed and profile: butt curl evolution for (a) different casting profiles and (b) different constant casting speeds

higher sensitivity at center, etc.

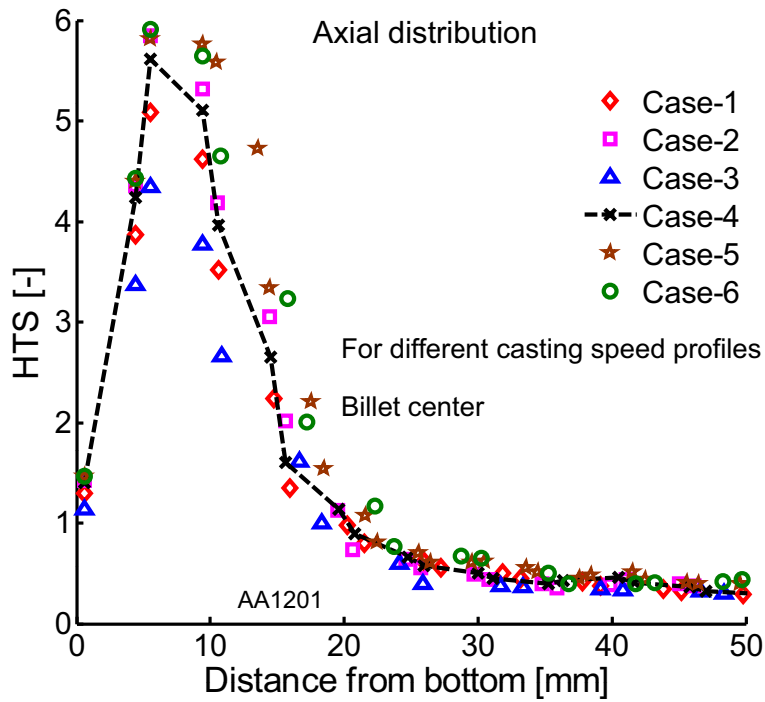
## 5.4 Influence of secondary cooling

At present, the influence of secondary cooling is not well understood in the DC casting research community. This is mainly due to the insufficient experimental techniques to describe the boiling curve. Apart from the experimentations, the inverse nature of this problem increases the computational difficulty. Therefore, the exact relation between the major controlling variables such as water flow rate, water quality, surface roughness, thermophysical properties of the casting materials is not yet well established. Even though, there are some empirical relations existing based on the convection correlations [64, 58, 63], further research is required to reveal the controlling parameters. Based on the quenching experiments (Chapter 3) conducted in our laboratory, the heat flux is not linearly varying with the change in water flow rate or the water velocity. Further, it is not possible to directly apply the quenching experiment results in the secondary cooling of DC casting. The major reason for this inconsistency is due to the following reasons: (a) film boiling phenomena is not well captured during the experiments, (b) the plate is maintained in static condition, and (c) during quenching, the plate is not exposed to constant heat source. Therefore, a theoretical study is conducted to establish the influence of secondary cooling.

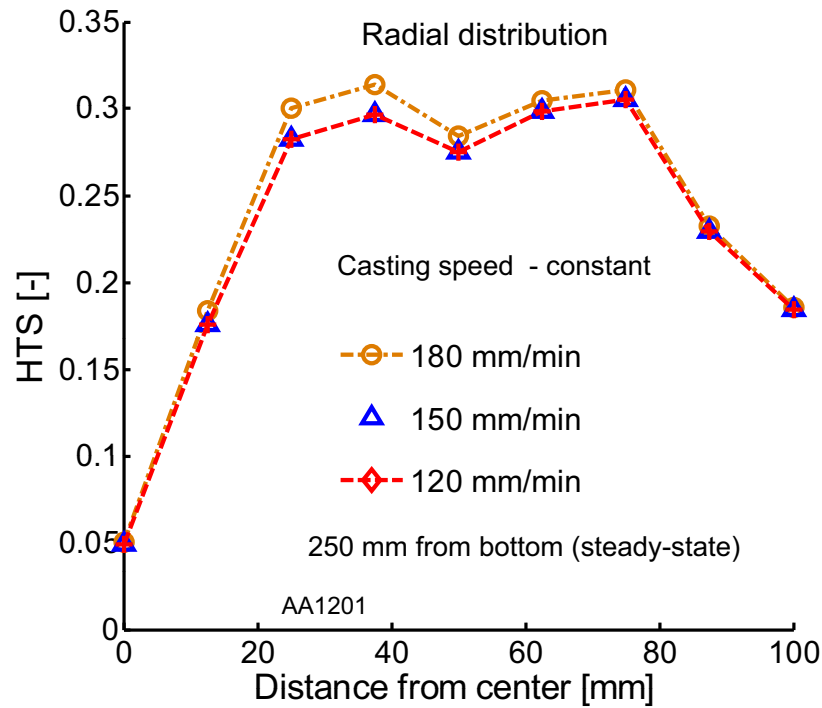
### 5.4.1 Influence of secondary cooling HTC profile

It is well known fact that any major change in the secondary cooling parameter will affect the HTC profile (boiling curve). Therefore, to illustrate the importance of secondary cooling, an attempt is made to theoretically understand the significance of secondary cooling HTC profile. To achieve this motive, the previously mentioned secondary HTC is multiplied by a factor which varies from 0.5–2 with an increment of 0.5. The resulting HTC profiles are shown in Fig. 5.34. Here, it should be noted that the Leidenfrost point, maximum HTC temperature intervals, and nucleate boiling start temperature are not changed. Only, the existing HTC profile is allowed to shrink or enlarge by a factor. A constant casting speed of 120 mm/min is employed. Other casting conditions are the same as before. The case-B corresponds to a factor of 1 which is the standard case because the results are already discussed in Section. 5.2.

The temperature contours during the steady state are plotted for case-A and case-D in Fig. 5.35. It is evident that the billet is hotter in case-A when compared to case-D. The position of the liquidus and solidus lines are relatively lower for case-A due to low HTC.



(a) Axial



(b) Radial

Figure 5.33: Influence of casting speed: (a) HTS for different casting speed profiles vs. distance from bottom and (b) radial distribution of HTS at steady state

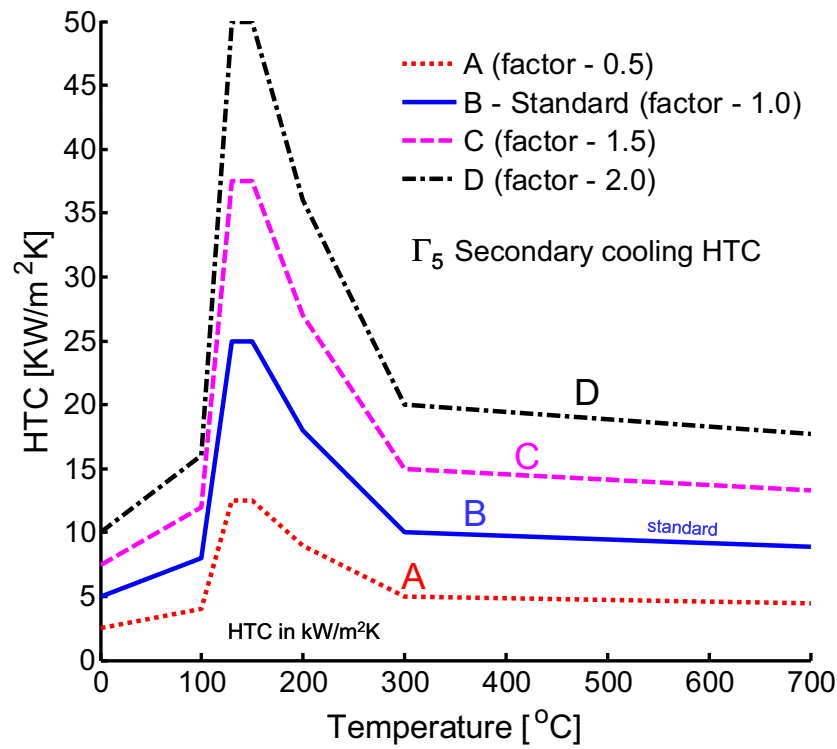


Figure 5.34: Influence of secondary cooling: different HTC profiles

In the water impingement zone, the distance between the solidus and the Leidenfrost point (LFP) is in the order of centimeters for case-A. However for case-D, the surface temperature nearby impingement zone drops to less than 200°C within few millimeters.

The temperature evolution at the extreme bottom corner of the billet known as butt is shown in Fig. 5.36(a). Before water striking, the temperature drop is same for all the cases. Once water touches the butt, due to rapid cooling in case-D, the temperature drops from 552°C to 130°C within 9 seconds. This increases the butt deformation due to the higher accumulation of irreversible viscoplastic strain. Fig. 5.36(b) shows the butt deformation for all the cases. In case-A, the temperature drop is not so rapid and the butt curl is only half of case-D. Hence, the decrease in secondary cooling reduces the butt curl.

Fig. 5.37 shows that the evolution of the sump depth and the mushy zone length. When compared to all other cases, the maximum sump depth, steady state sump depth, maximum MZL, and steady state MZL are always higher for case-A. The radial distribution of sump depth and MZL at the steady state condition are shown in Fig. 5.38. The difference in sump depth between the case-A and the standard case is higher at the center than at the surface. Similar behavior is observed for MZL but for all the cases, the MZL at the surface is almost same. It can be concluded that the increase in secondary cooling decreases the sump depth and MZL.

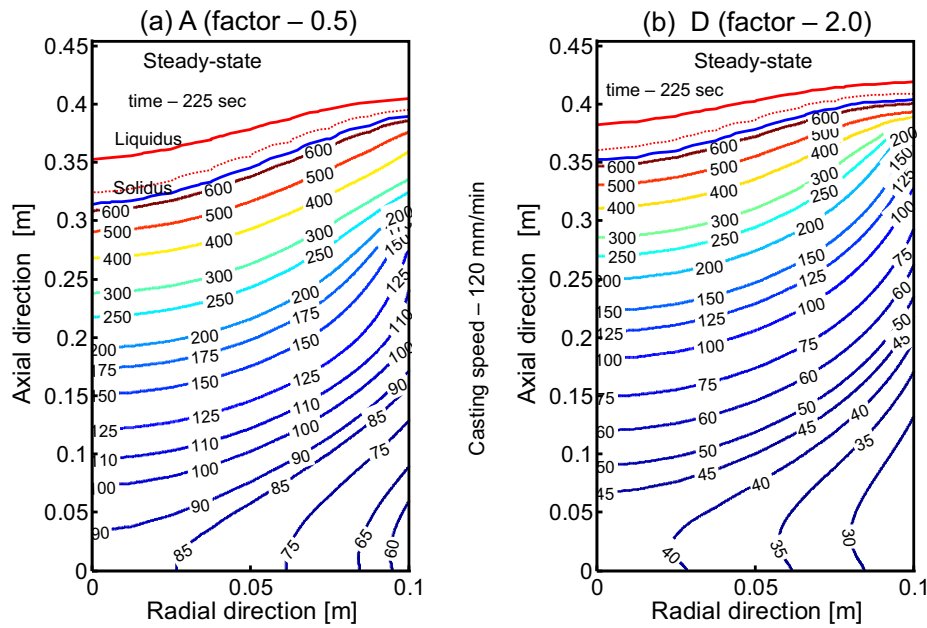
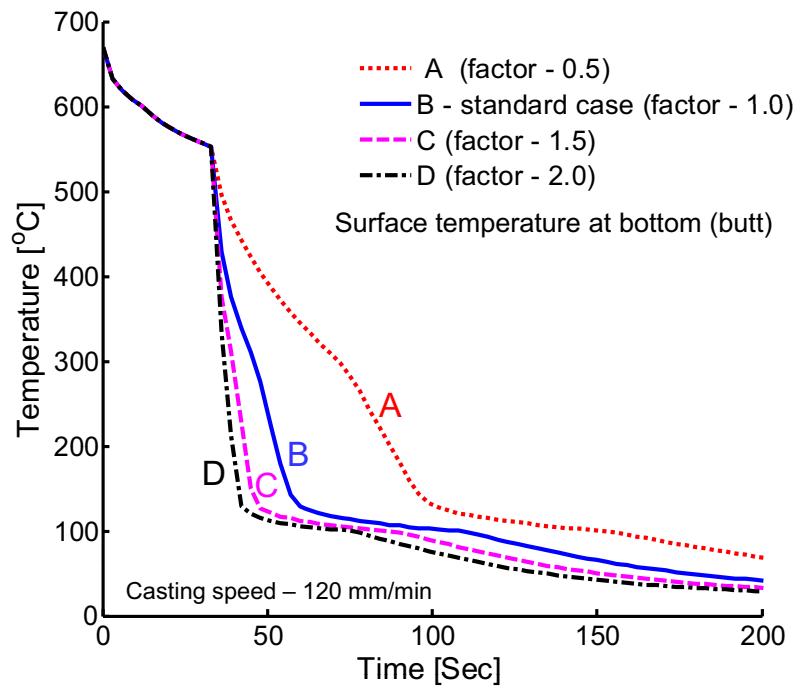


Figure 5.35: Influence of secondary cooling profile: steady state temperature distribution for (a) case-A and (b) case-D

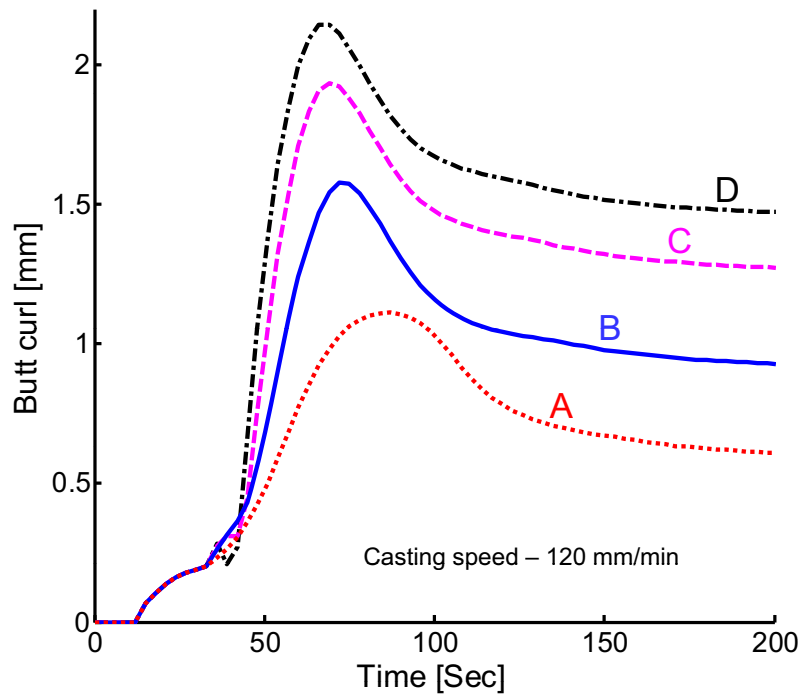
The characteristic time at the center of the billet is always higher for case-A in all the locations as shown in Fig. 5.39(a). The surface temperature of the billet at which water starts striking is lower for case-D. Fig. 5.39(b) shows that the temperature is around  $550^{\circ}\text{C}$  for case-A and  $240^{\circ}\text{C}$  for case-D. The temperature for case-D is lesser than LFP. Therefore, it is important to know the length of different boiling zones. Fig. 5.40 shows the film boiling and combined nucleate and transition boiling zone lengths for all the cases. The length of film boiling zone is extremely high for case-A (54 mm) and low for case-D (3 mm) during the steady state. The similar kind of behavior is observed in the case of nucleate and transition boiling. Therefore, in case-D, most of the billet surface area comes under the category of forced convection zone.

The distribution of circumferential stress for the cases A and D are shown in Fig. 5.41. In the entire billet, the stresses are relatively higher in magnitude for case-D than case-A. Further, near the water impingement zone, higher tensile stresses are induced in case-D which may lead to develop the surface cracks. In the case of circumferential viscoplastic strain (Fig. 5.42), the strain concentration near the bottom block is more for case-D. Higher compressive strain near the subsurface is observed in case-A. Very high tensile strains are induced during the start-up phase for case-D. Hence, increase in secondary cooling, increases the stress and strain.

The evolution of stresses during the start-up phase is compared for case-A and case-D as shown in Fig. 5.43. Two locations at the start-up phase are selected such as the center and subsurface at 90 mm from center. In both the locations, all components of stresses

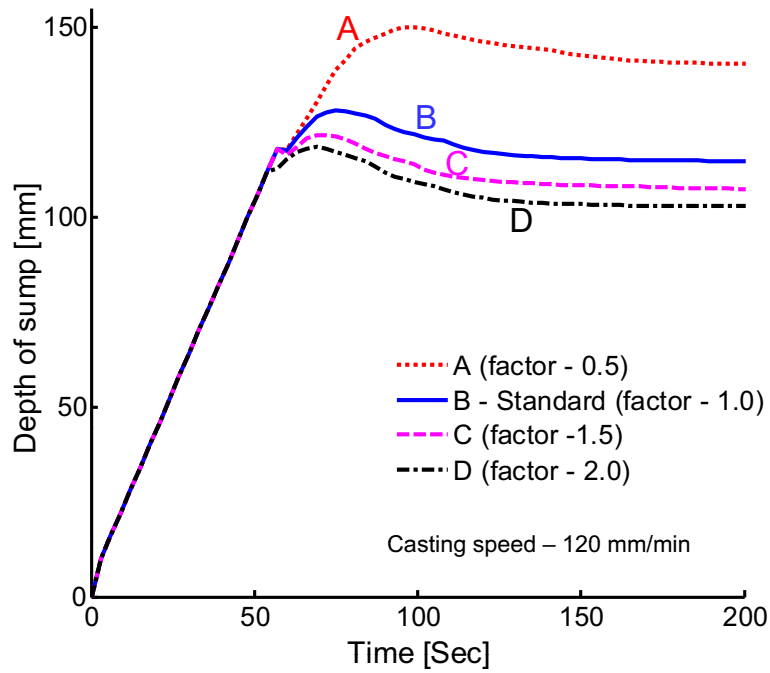


(a) Butt temperature

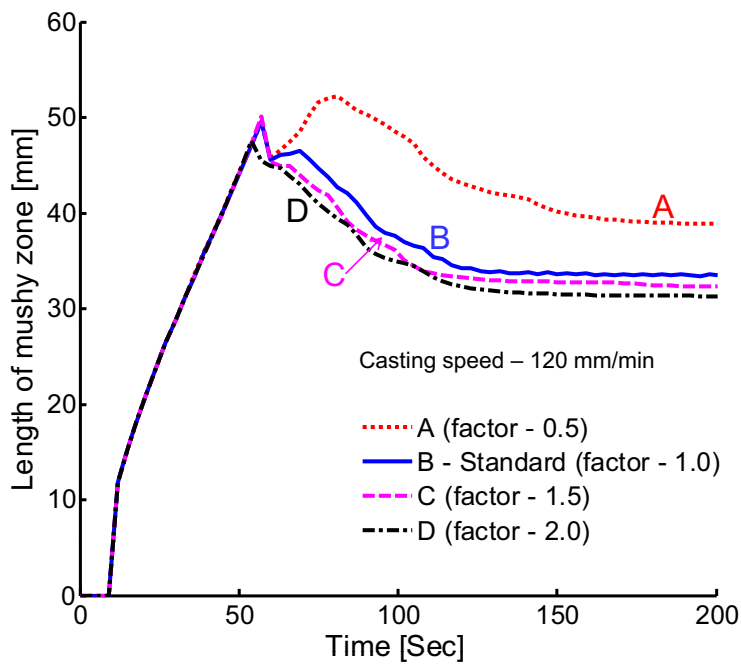


(b) Butt curl

Figure 5.36: Influence of secondary cooling profile: temperature evolution and butt curl



(a) Evolution of sump depth



(b) Evolution of mushy zone length

Figure 5.37: Influence of secondary cooling profile: evolution of sump depth and mushy zone at center



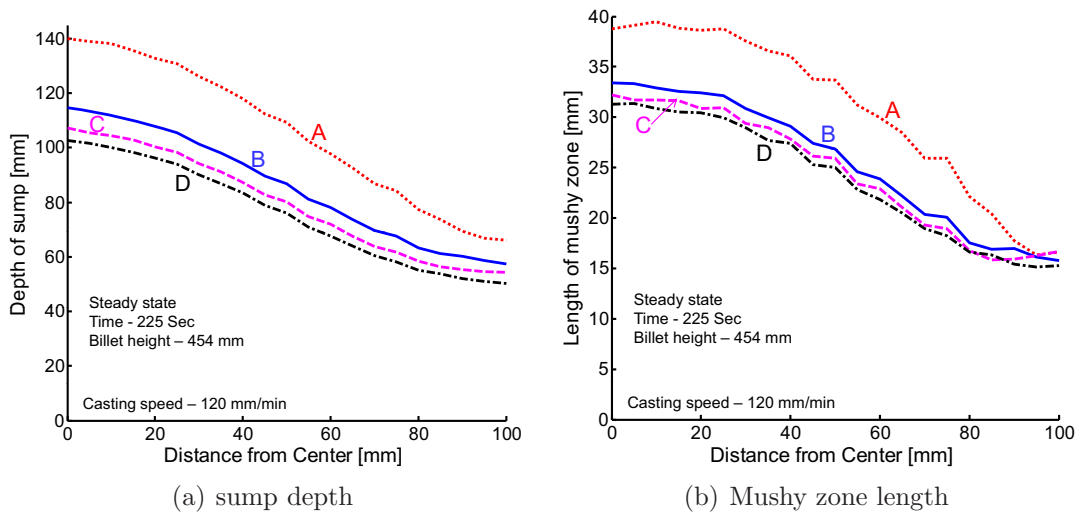


Figure 5.38: Influence of secondary cooling profile: radial distribution of sump depth and mushy zone at steady state

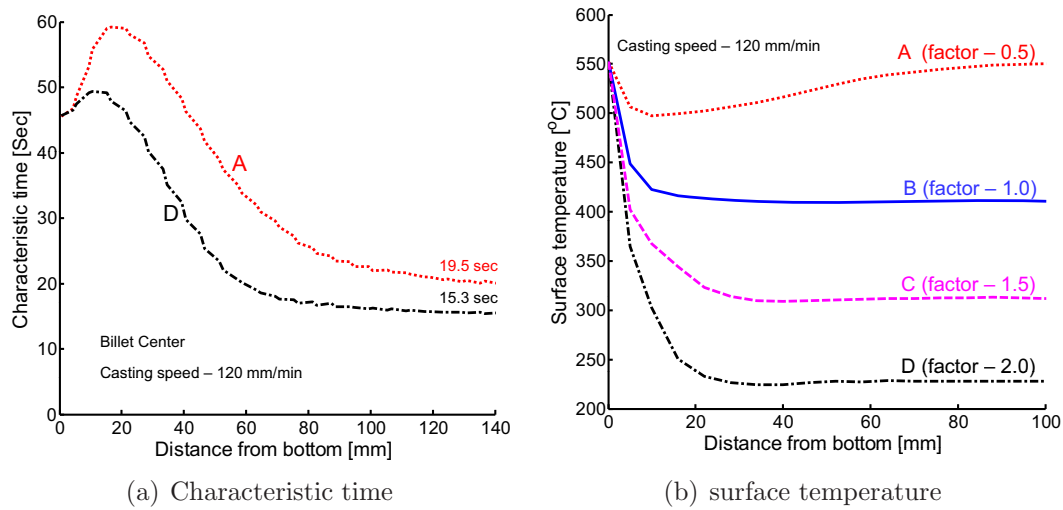


Figure 5.39: Influence of secondary cooling profile: Characteristic time and surface temperature of billet at which water strikes first vs. distance from bottom of the billet

are lower for case-A than case-D. The circumferential component of stress is considerably reduced in case-A when compared to axial and radial components. The axial stress at the subsurface changes its nature from tensile to compressive in case-D but surprisingly in case-A, the nature of stress is monotonically compressive. Generally, during the time of water start striking, the axial stress becomes tensile and in later stages it turns into compressive. This behavior is missing in case-A. Therefore, the chances of quench crack formation at the surface is lower for case-A.

The circumferential stress and viscoplastic strain as a function of temperature is shown in Fig. 5.44 for three different locations such as the center at 50 mm from bottom, center at steady state, and subsurface of 90 mm from center at steady state. For case-D, only

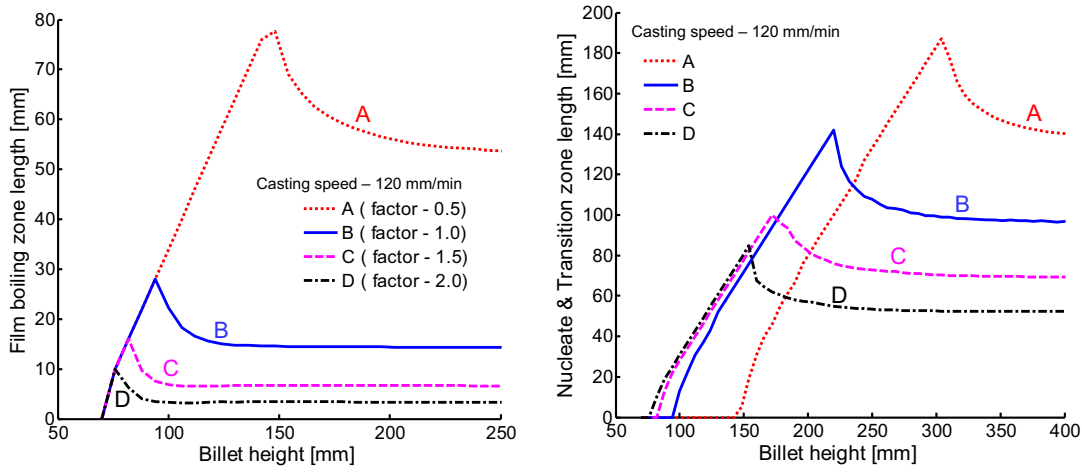


Figure 5.40: Influence of secondary cooling profile: different boiling zone length as a function of billet height

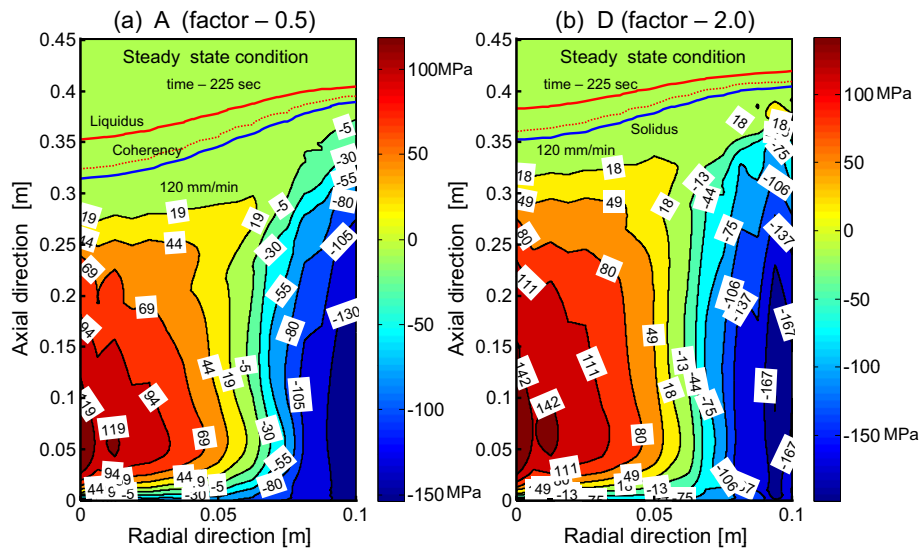


Figure 5.41: Influence of secondary cooling profile: steady state circumferential stress distribution for (a) case-A and (b) case-D

during the start-up phase, the stresses are higher, but during the steady state the stresses are lower than case-A. Further, in case-A, the subsurface stress during the steady state turn into tensile at  $570^{\circ}\text{C}$  but in case-D, it remains compressive. If the stress is a deciding factor, the chances of developing cold cracks are more for case-A than case-D. However, the probability of hot tear formation for case-D is higher than case-A. A similar behavior is observed for the viscoplastic strain except the subsurface at steady state where case-D dominates than case-A. The compressive nature of stress and strain are highly preferred than the tensile one at the vicinity of cracks. With this notion, case-D is better than case-A at the center during the steady state but in the subsurface situation is complicated due to the opposite nature of stress and strain.

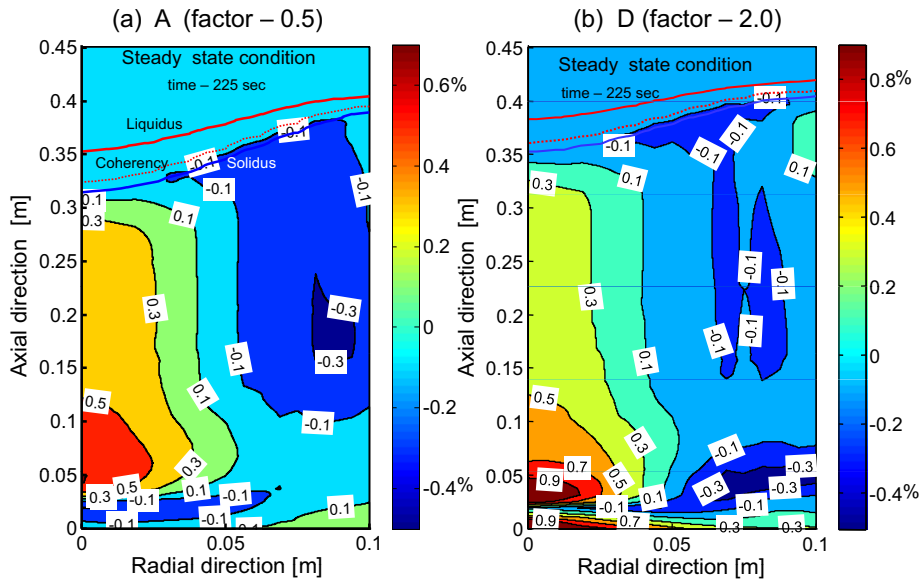


Figure 5.42: Influence of secondary cooling profile: steady state circumferential viscoplastic strain distribution for (a) case-A and (b) case-D

The axial and circumferential components of stress and viscoplastic strain at the solidus temperature are plotted along the distance from bottom of the billet as shown in Fig. 5.45. In the early stages of start-up phase, the stresses are compressive for case-A and then turn into tensile. However for case-D, the stresses are tensile from the beginning itself. The steady state stresses are higher for case-A than case-D. This fact indicates that for reducing the possibilities of hot tearing, the secondary cooling in the start-up phase has to be reduced. With respect to the cold crack formation, the secondary cooling has to be promoted during the steady state phase. The circumferential viscoplastic strain at the solidus temperature enhances this fact, however the axial viscoplastic strain contradicts it. The higher tensile axial viscoplastic strain is induced during the start-up phase for case-A and during the steady state phase it becomes zero as shown in Fig. 5.45(b). An exactly opposite behavior is observed for case-D, and the steady state values are higher than case-A. This kind of complex nature of stress and strain restricts any such generalized conclusions.

## 5.4.2 Time dependent HTC profiles

From the above-mentioned simulation results regarding the secondary cooling profile, it can be possible to theoretically optimize the cooling curve. Instead of maintaining a constant profile, it is also feasible to vary with respect to time. One such possibility is that the reduced cooling at the beginning and enhanced cooling at the steady state. Therefore, an attempt is made to vary the cooling curves in the time direction. At the

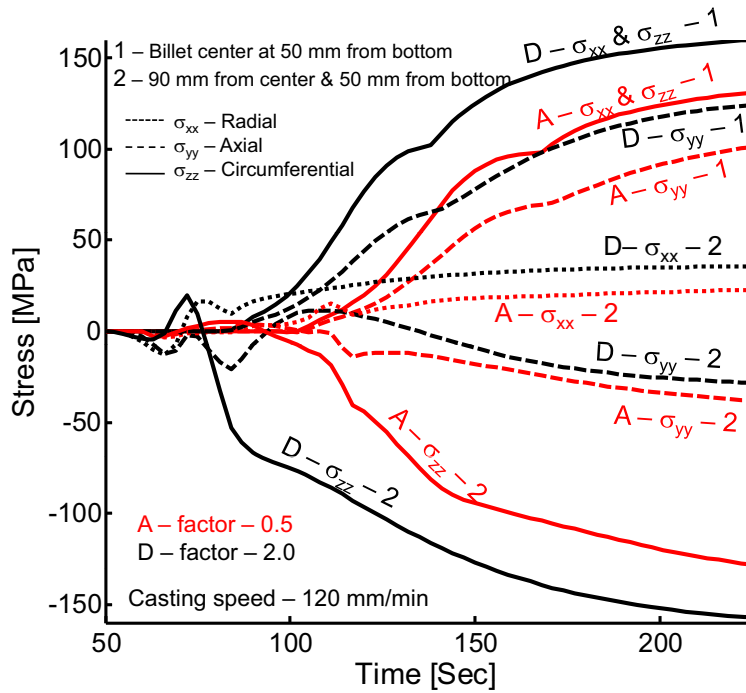


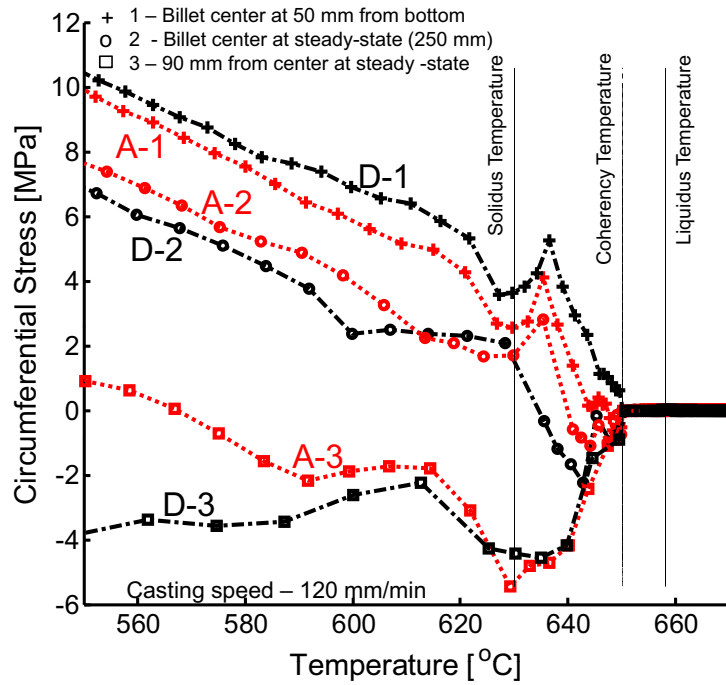
Figure 5.43: Influence of secondary cooling profile: evolution of stress at center and a radial distance of 90 mm (50 mm from bottom)

time of secondary cooling starts (billet height - 70 mm), the multiplying factor is taken as  $\lambda_1$ . Similarly, the final factor at a billet height of 300 mm is taken as  $\lambda_2$ . In between these two stages, the factor  $\lambda$  is obtained by a liner interpolation. For better illustration, four different combinations are considered which are given below.

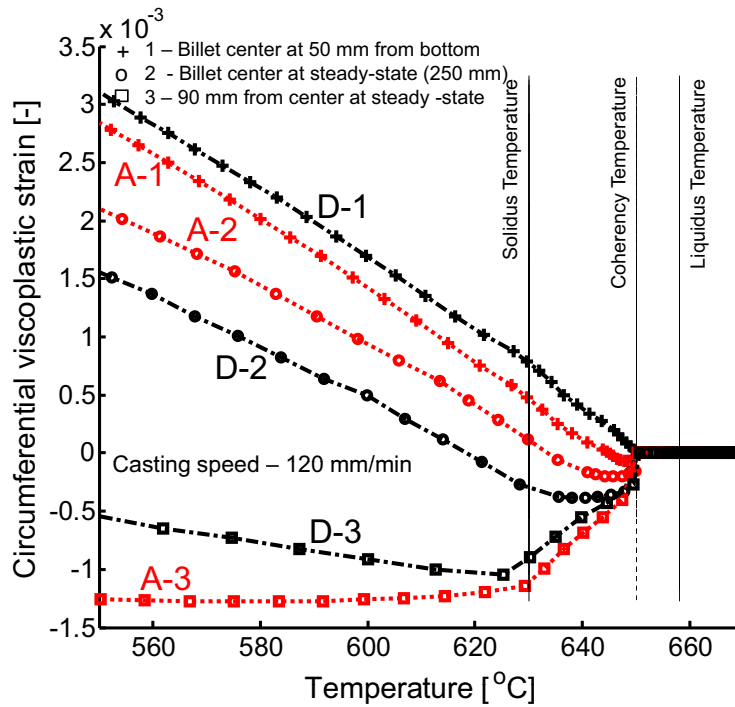
- Case-A:  $\lambda_1 = 0.5$ , and  $\lambda_2 = 0.5$  (reduced cooling)
- Case-E:  $\lambda_1 = 0.5$ , and  $\lambda_2 = 2.0$  (decreased-increased cooling)
- Case-F:  $\lambda_1 = 2.0$ , and  $\lambda_2 = 0.5$  (increased-decreased cooling)
- Case-D:  $\lambda_1 = 2.0$ , and  $\lambda_2 = 2.0$  (enhanced cooling)

In cases A and D, a constant factors are used which repeats the same cases A and D as discussed before. Only, the cases E and F are new in which HTC profiles are varied from  $\lambda_1$  to  $\lambda_2$ . In case-E, the HTC profile is increased from a factor of 0.5 to 2. Case-F is the exact opposite of case-E. In all the cases, a constant speed of 120 mm/min is used. Other casting parameters are kept constant and only the secondary cooling profile is supplied as a function of time.

The evolution of sump depth at the center is shown in Fig. 5.46(a). In case-F, the curve shifts from D and reaches A. Similarly, in case-E, the curve follows the path of case-A until certain time and then tends to reach case-D. Similar trends are observed in

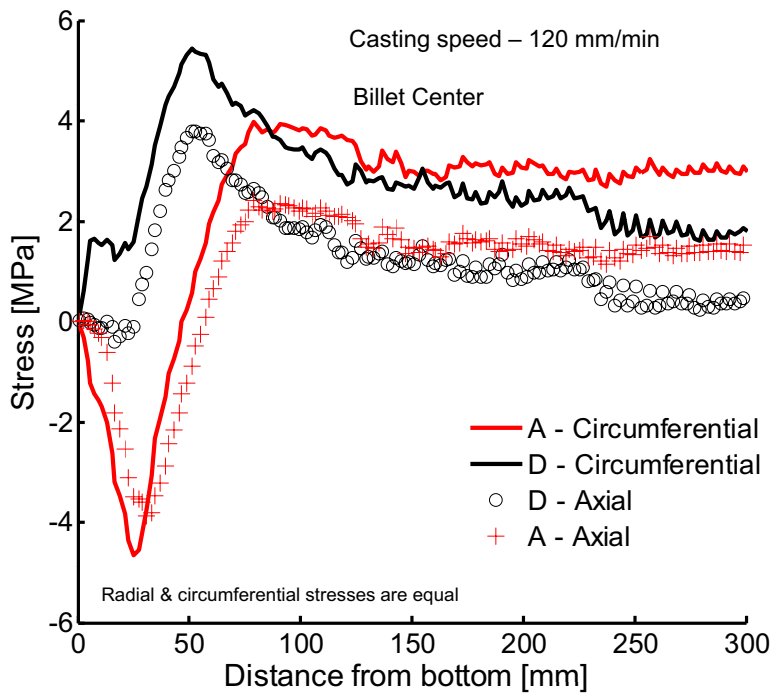


(a) Circumferential stress

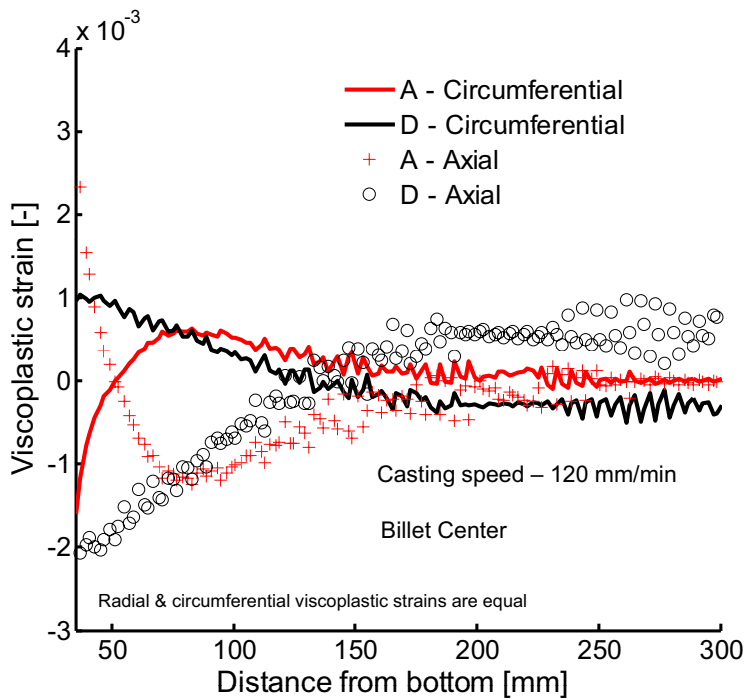


(b) Circumferential viscoplastic strain

Figure 5.44: Influence of secondary cooling profile: circumferential stress and viscoplastic strain as a function of temperature



(a) Stress



(b) Viscoplastic strain

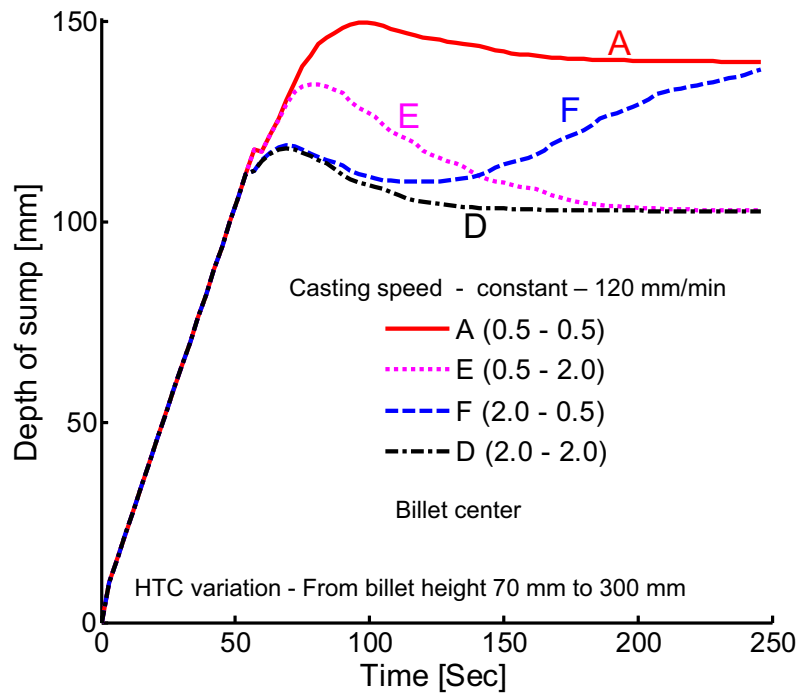
Figure 5.45: Influence of secondary cooling profile: stress and viscoplastic strain at solidus temperature as a function of distance from bottom of the billet at center

the evolution of mushy zone length as shown in Fig. 5.46(b). Only the evolution pattern changes from one case to another. This behavior is similar to the ramping which are discussed in Section 5.3. Increased cooling during the start-up phase and reduced cooling at the steady state (case-F) or reduced cooling during the start-up phase and increased cooling at the steady state (case-F) will not alter the steady state sump depth and MZL. However, the start-up phase sump depth can be reduced using a strategy F. The rating can be given based on the start-up phase as A-E-F-D and based on the steady state as A-F-E-D.

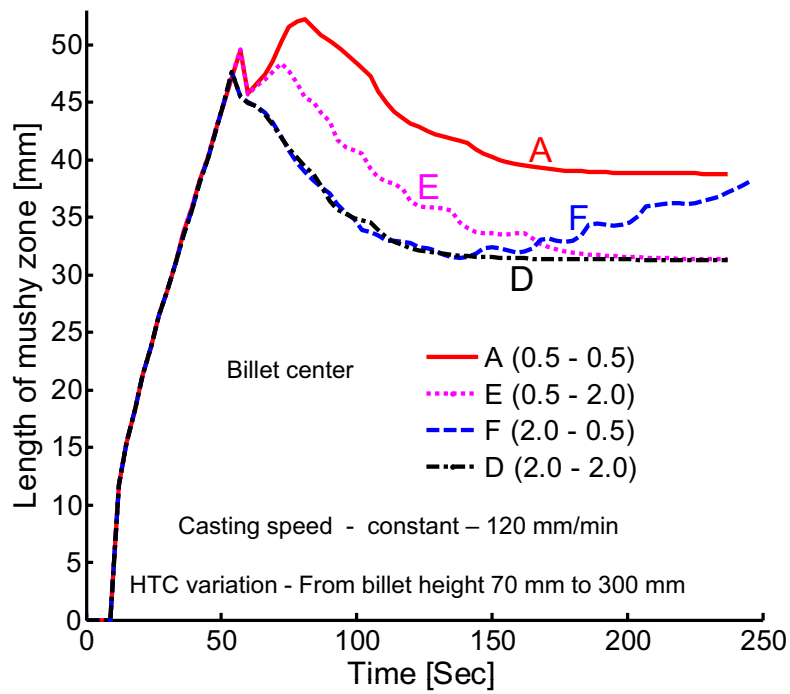
The circumferential stress and circumferential viscoplastic strain at the center of the billet during the start-up phase is plotted as a function of temperature as shown in Fig. 5.47. There is not much change in stress observed even at the very low temperature. Surprisingly, the stress and viscoplastic strain are always higher in Case-E when compared to case-F. The same plot is repeated for another center location which is taken at 300 mm from bottom where the HTC profile is started maintaining constant. Fig. 5.48(a) shows that the evolution of stress in the vicinity of the phase-change interval is minimum for case-E. However, after the solidification, case-E slowly reaches case-F. Similar behavior is observed in the viscoplastic strain (Fig. 5.48(b)). This creates an ambiguity to identify the best cooling strategy. According to the stress, the rating can be given based on the stress evolution within the mushy zone as A-D-F-E and based on the stress after solidification as D-A-F-E. The rating again changes based on the viscoplastic strain and given as A-F-E-D.

The circumferential stress and circumferential viscoplastic strain at the solidus temperature along the distance from the bottom of the billet at the center is shown in Fig. 5.49. In the stress plot, except case-A, all other cases show higher tensile stress during the start-up phase. After certain distance, the cases D, E, and F reaches a same steady state value which is lower than case-A. Nearly similar behavior is observed in the viscoplastic strain, except case-E which reaches a tensile maximum during the start-up phase. However, the steady state values of case-E is lower than case-A. At a certain region, case-F exhibits the minimum before reaching the steady state.

The complicated behavior of stress and strain restricts the possibilities to make any such conclusions. Further the complexity increases if the axial component of stress and strain are taken into account. This study reveals the fact that through the controlled cooling, the pattern of evolution of stress and strain can be changed. With a proper optimization, it may be possible to reduce the probability of hot or cold cracking. At this moment, it is not possible to conclude which cooling strategy is the better one.



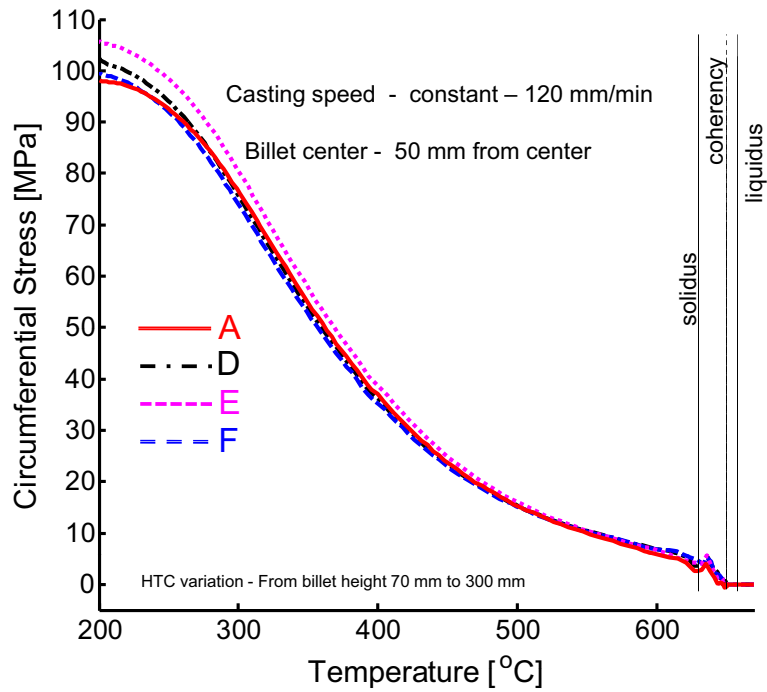
(a) Evolution of sump depth



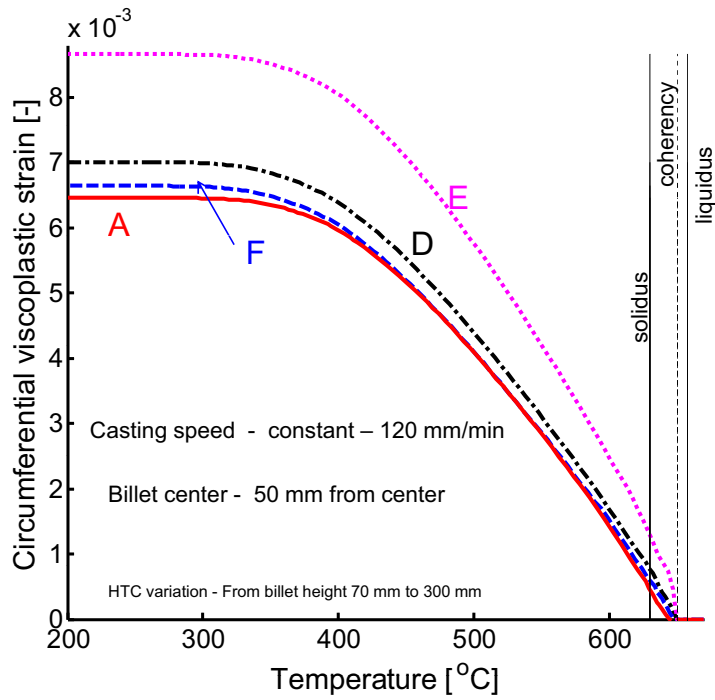
(b) Evolution of mushy zone length

Figure 5.46: Time varying HTC profile: evolution of sump depth and mushy zone at center



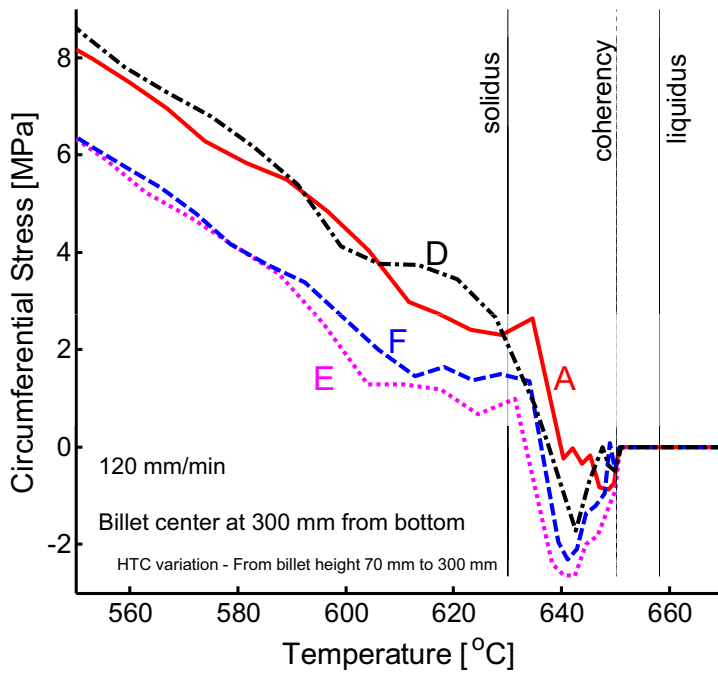


(a) Circumferential stress

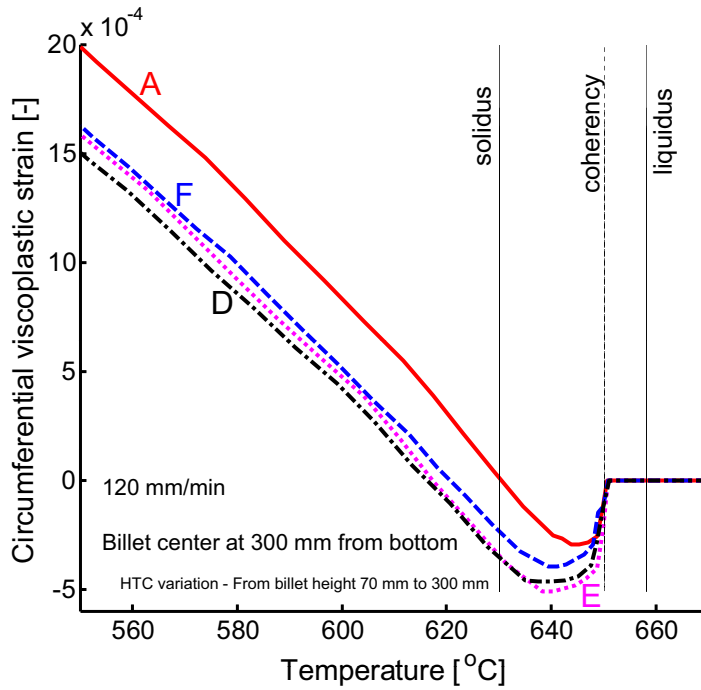


(b) Circumferential viscoplastic strain

Figure 5.47: Time varying HTC profile: circumferential stress and viscoplastic strain as a function of temperature at center (50 mm from bottom)

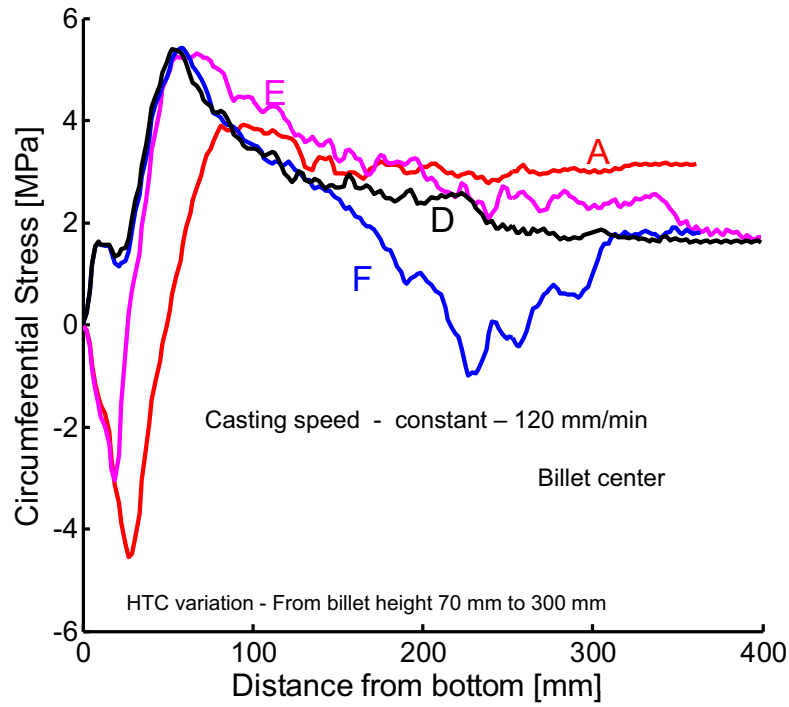


(a) Circumferential stress

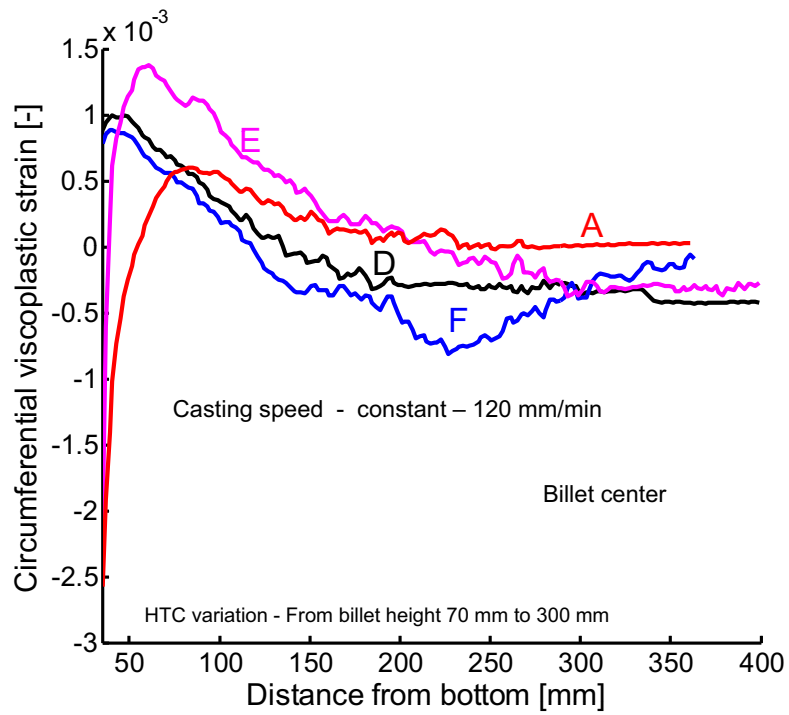


(b) Circumferential viscoplastic strain

Figure 5.48: Time varying HTC profile: circumferential stress and viscoplastic strain as a function of temperature at center (300 mm from bottom)



(a) Stress



(b) Viscoplastic strain

Figure 5.49: Time varying HTC profile: circumferential stress and circumferential viscoplastic strain at solidus temperature as a function of distance from bottom of the billet at center

### 5.4.3 Influence of other parameters

The influence of the maximum HTC at nucleate and transition boiling (represented as MHTC in Fig. 5.4), Leidenfront temperature (LFP), and film boiling HTC (represented as FHTC in Fig. 5.4) are investigated. The results are shown in Fig. 5.50 and Fig. 5.51(a). Generally, the sump parameters are described by the following four quantities: (a) maximum sump depth, (b) steady state sump depth, (c) maximum MZL, and (d) steady state MZL. MHTC is varied in the range -10% to 40% from its standard value (25 kW/m<sup>2</sup>K). The corresponding change in sump depth and MLZ are not so high. Even for the case of 40% increase, the above-mentioned four parameters vary less than 2%. Similarly, the LFP and FHTC are varied and no significant change is observed. However, the trend of the approximate curve shows that the influence of LFP is relatively higher than the MHTC and FHTC. In overall, MHTC, LFP, and FHTC do not influence the sump parameters at a greater extend. It is obvious that if there is no significant change in the sump parameters, the change in stress and strain behavior will be almost null. Therefore, the change in displacement field results are not shown here. However, from the stress point of view, it is observed that the increase in LFP promotes the chances of hot cracking at the billet center during the start-up phase.

## 5.5 Influence of melt superheat

The influence of melt superheat is studied by varying the melt temperature. Fig. 5.51(b) shows the variations in sump parameters. The change in melt temperature significantly changes the sump parameters. It is found that the sump depth and the mushy zone length behave oppositely. Increase in melt superheat increases the sump depth and decreases the mushy length. Further, the mushy length decrease rate is higher than the sump depth increase rate. This fact indicates that the liquidus line shifts faster than the solidus line when the melt temperature is increased. Nearly similar effect at the center of the billet is reported in Eskin *et al.* [106]. However, they mentioned that at the surface, the situation is reversed when compared to the center. In the present simulation, this effect is not observed.

Due to the strong influence of melt superheat on the sump parameters, it is quite interesting to analyze the displacement field results. Three different cases of melt temperature are considered:(a) 670°C (standard case), (b) 680°C, and (c) 690°C. The circumferential stress plot is shown in Fig.5.52. It indicates that there is not much change in stress. In the stress-temperature plot, at the phase-change interval, all the cases behave slightly different manner and after that all cases coincide. Even for the circumferential stress at the solidus temperature plot shows the similar behavior. However, during the start-up

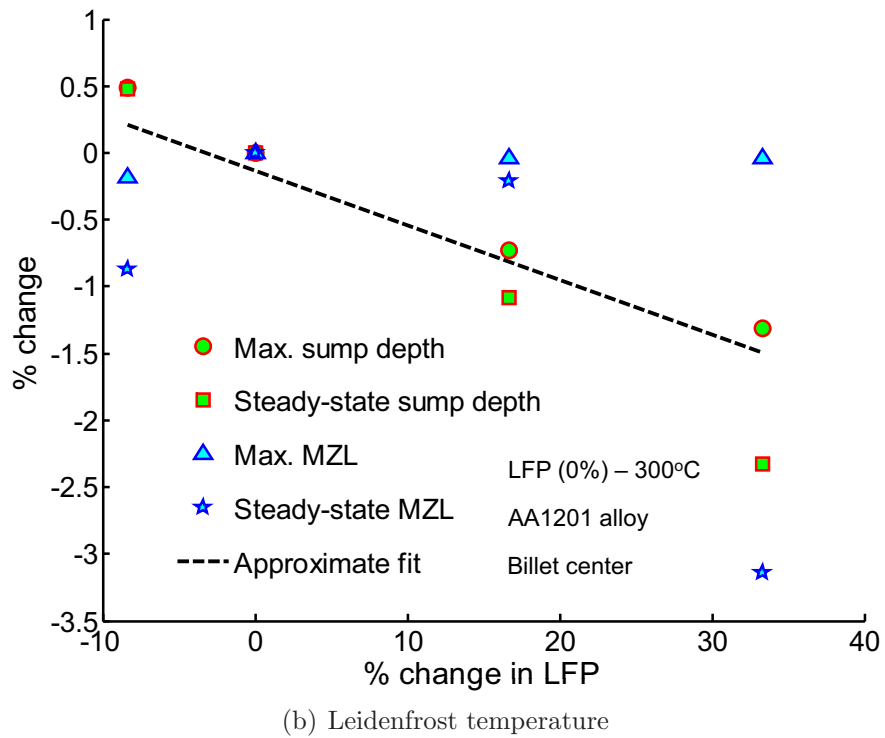
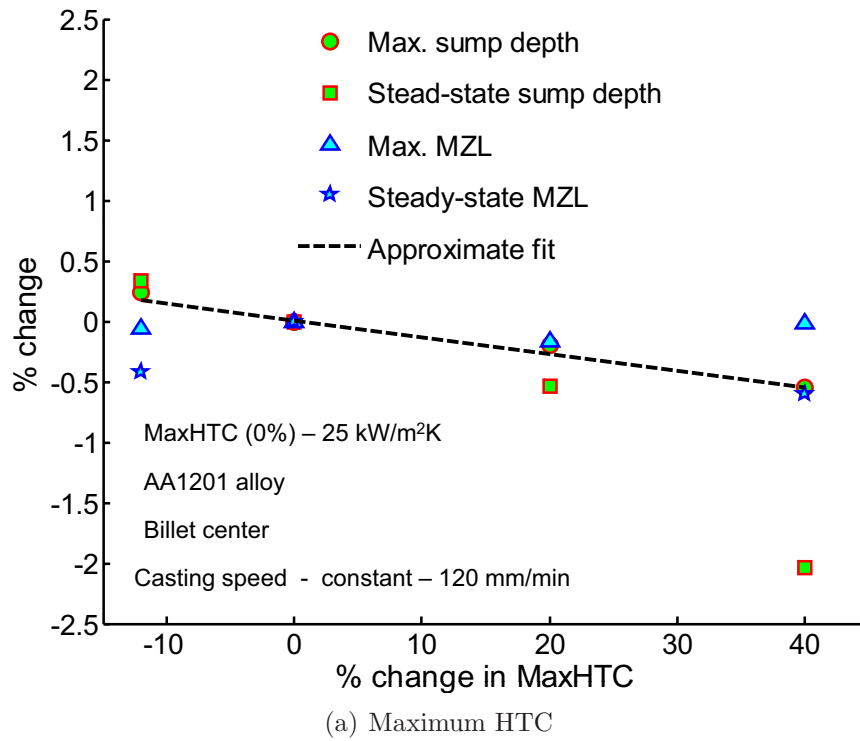


Figure 5.50: Influence of (a) maximum HTC and (b) LFP on sump parameters

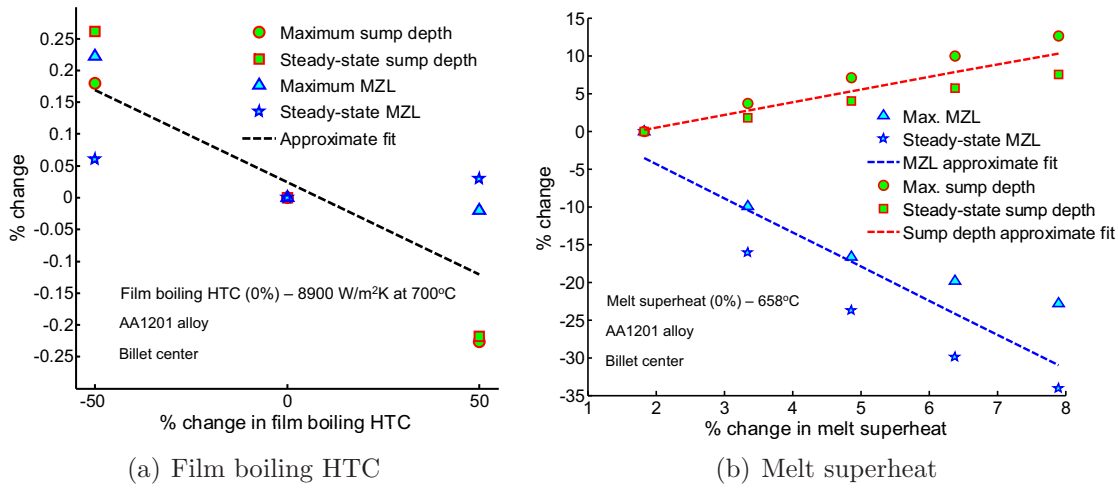


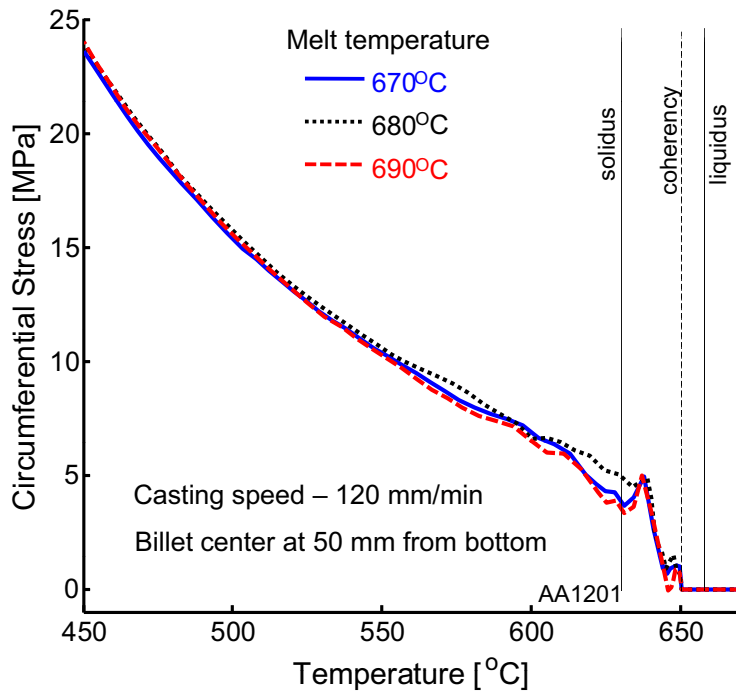
Figure 5.51: Influence of (a) film boiling HTC, and (b) melt superheat

phase, the stresses are higher in the case of higher melt temperature. Due to similar behavior, it is difficult to frame any such conclusions based on the stress plot.

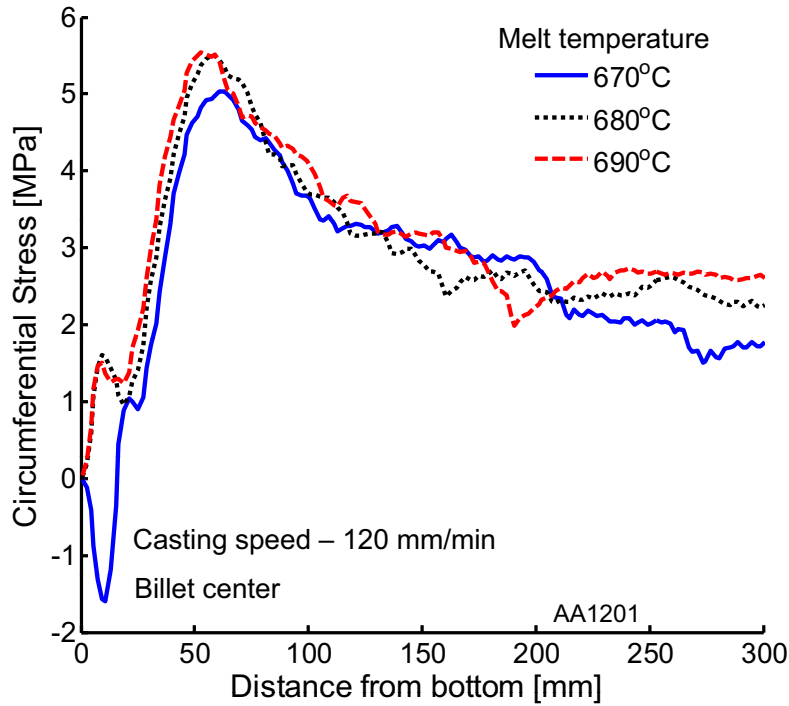
The circumferential viscoplastic strain as a function of temperature is shown in Fig. 5.53(a). The influence of the melt temperature is clearly visible. The increase in melt temperature increases the viscoplastic strain. Fig. 5.53(b) shows the viscoplastic strain at a solidus temperature. In all positions, the strains are higher for the case of 690°C. It can be concluded that the increase in melt superheat promotes the viscoplastic strain. According to Magnin *et al.* [91], increase in viscoplastic strain increases the HTS. Based on this, the increase in melt superheat increases the possibility hot tearing. This observation agrees with Spittle and Cushway [105] and contradicts with Eskin *et al.* [106]. However, Eskin *et al.* [106] mentioned that the decrease in HTS is substituted by other forms such as micro cracks, pores and healed cracks.

## 5.6 Mesh convergence study

In the numerical methods, the infinite degrees of freedom of the computational domain is forcefully reduced to finite degrees in space and time. This itself indicates that the accuracy of the numerical solution is lower than the analytical solution. Due to the limitations, it is practically impossible to obtain the analytical solution for highly complex problems like DC casting. However, for the reasonably accurate solution, the best choice is no other than the numerical one. The number of elements in the radial direction and the size of time step are the two important parameters which control the accuracy of the DC casting numerical solution. It is essential to understand the influence of these two parameters on the final solution. Here, the sump parameters are taken as a measure of

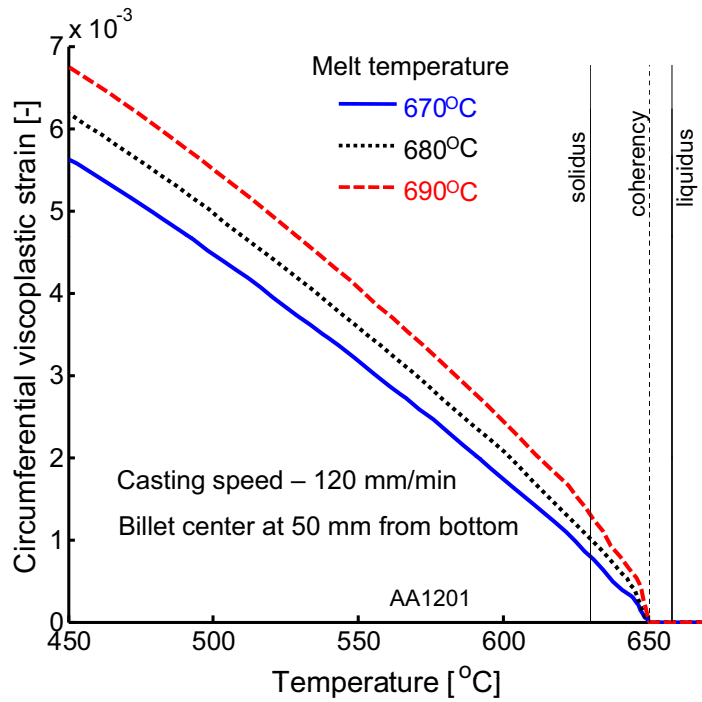


(a) Stress vs. Temperature

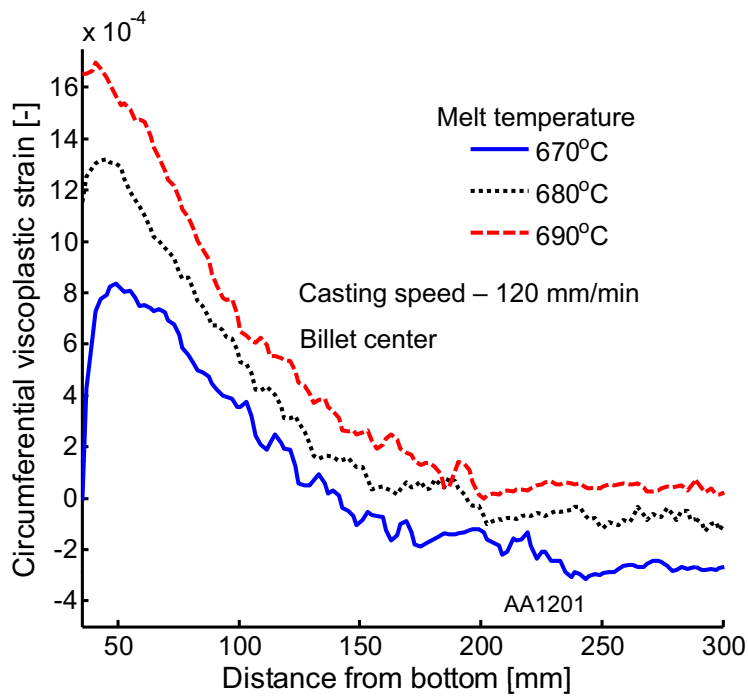


(b) Stress vs. distance

Figure 5.52: Melt superheat: circumferential stress as function of temperature and distance from bottom



(a) Stress vs. Temperature



(b) Stress vs. distance

Figure 5.53: Melt superheat: circumferential viscoplastic strain as function of temperature and distance from bottom



accuracy. Therefore, the thermal part of the problem is sufficient to perform the mesh convergence study. It is equally important to know the accuracy of the displacement field. However, if the thermal solution is accurate enough, definitely the mechanical part will be accurate due to the incorporation of higher order elements. It is already mentioned that the mechanical elements are 9-noded with 9 integration points and the thermal elements are 4-noded with 4 integration points. With this notion, the mesh convergence study is presented in this section based on the sump parameters taken at the billet center.

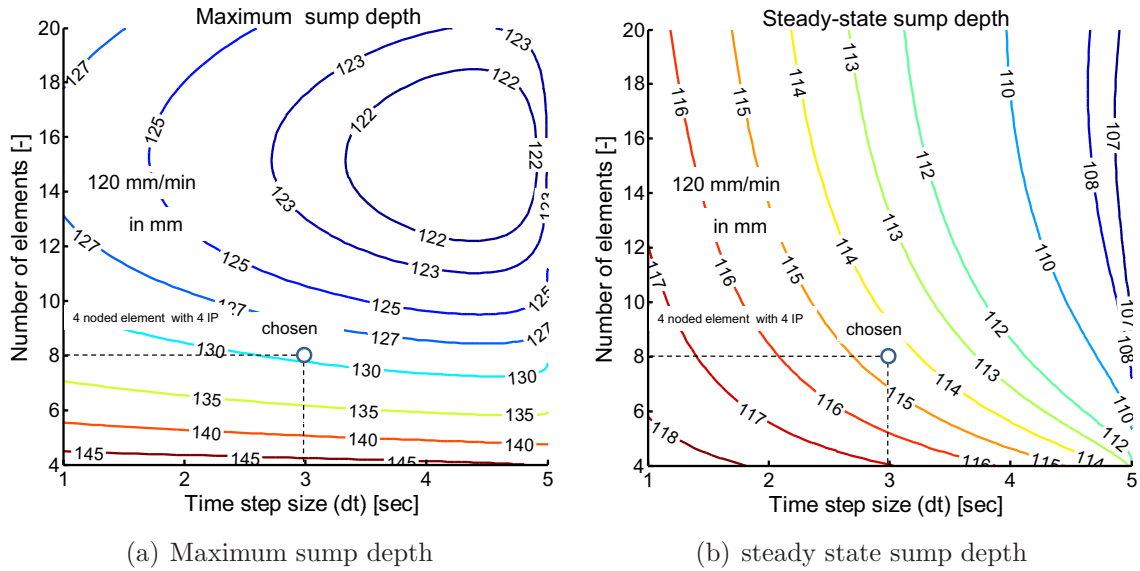


Figure 5.54: Mesh convergence: sump depth

The contour plots of the sump depth are shown in Fig. 5.55. The maximum sump depth plot indicates that if the number of elements are less than 10, the influence of the time step will be almost null. However, it may be overpredicted if the number of elements is further reduced. The steady state sump depth plot shows that the time step size is more important than the number of elements. From the sump depth observations, the maximum sump depth is strongly influenced by the number of elements, and the steady state sump depth is controlled by the size of the time step.

The mushy length is plotted as shown in Fig. 5.56. According to the maximum MZL, if the number of elements higher than 10 and time step size is less than 3, the solution will be more accurate. Further, the steady state MZL is independent of number of elements. These trends are almost similar to that of sump depth. The reason for the selection of 8 elements and 3 seconds is due to the restriction given by MATLAB. In the case of DC casting, the domain grows continuously. Even for the case of 8 elements, 34 mechanical nodes (8 thermal nodes) are additionally added at the beginning of every time step. Finally, for the case of the 100<sup>th</sup> time step, the number of nodes exceed more than 3000. MATLAB is not good enough to handle if the total nodes are more than 2000. Therefore,

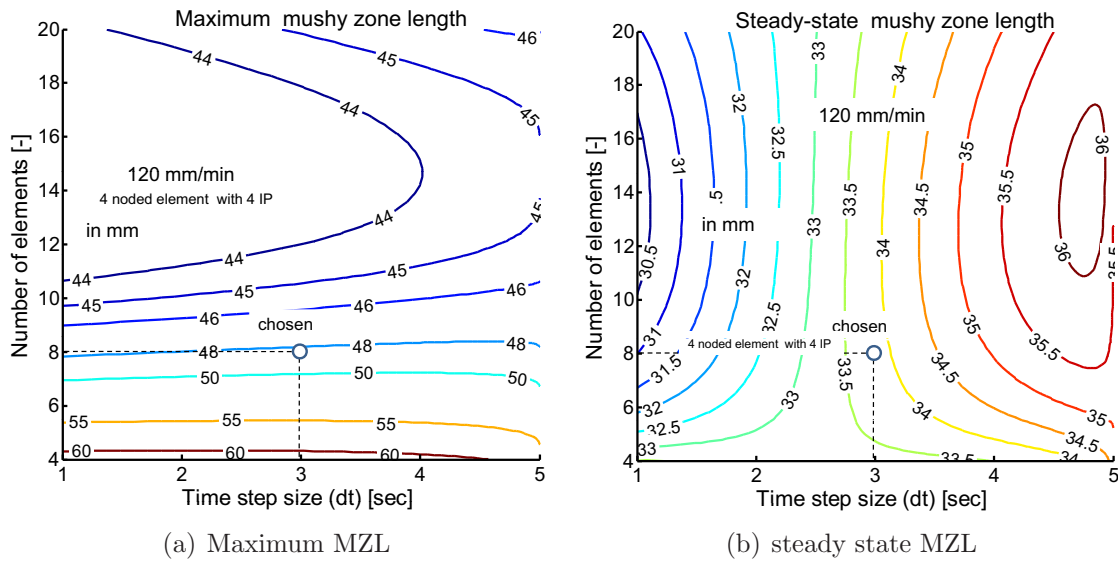


Figure 5.55: Mesh convergence: mushy zone length

8 elements are selected in the radial direction. The decrease in time step size increases the number of nodes. This obviously increases the total computational time.

The mean iterations per time step for the thermal problem is shown in Fig. 5.56(a). The variation is not so high. An average of 4–6 iterations are required for every time step. The total computational time for the thermal problem is shown in Fig. 5.56(b). If the number of elements is above 10 and the time step size is less than 3, the total computational time exceeds one hour.

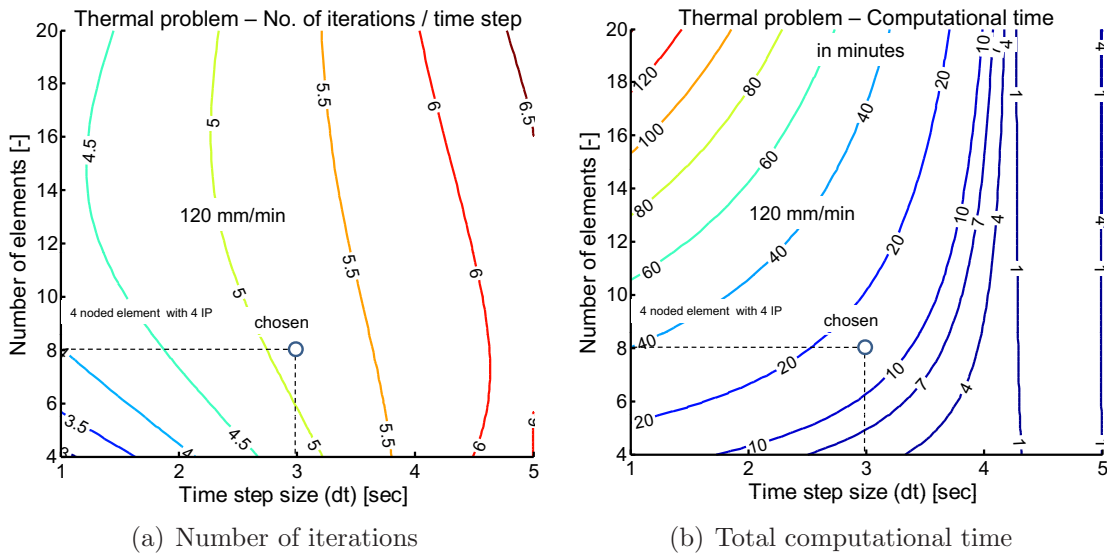


Figure 5.56: Computational details: thermal problem

The average number of iterations for the mechanical field is around 4–4.5. The number of local time steps used in the mechanical problem is 8. Fig. 5.57 shows the computational

time per time step. In both the problems, computational time per time step increases gradually due to the addition of elements. When compared to the thermal problem, the mechanical problem needs an 80 times higher computational time. Finally, for each simulation, a minimum of 8–10 hours is required to solve the complete DC casting problem with a casting speed of 120 mm/min up to a height of 500 mm.

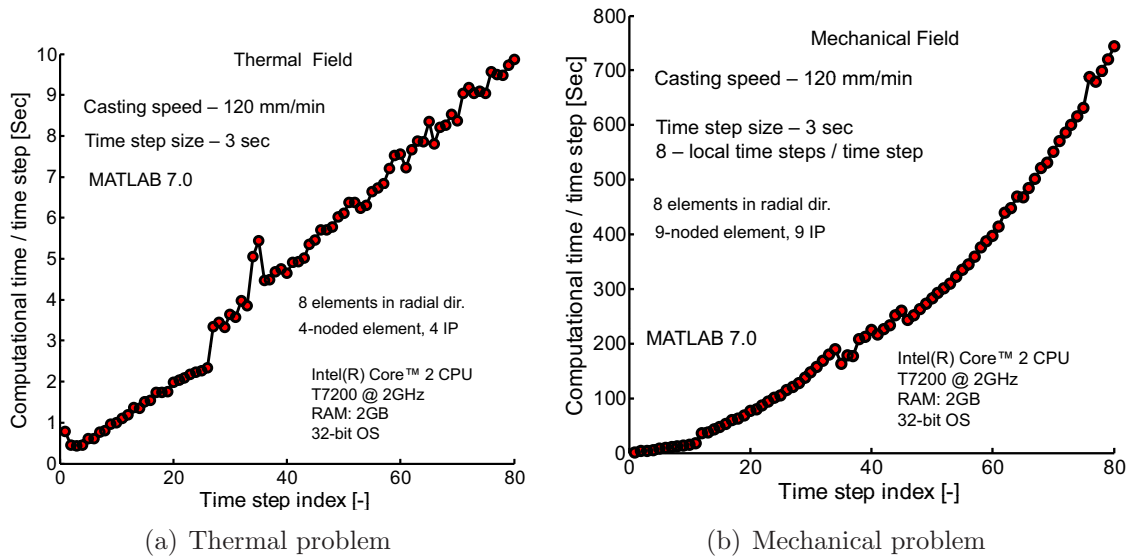


Figure 5.57: Computational time per time step

## 5.7 Summary and conclusions

The start-up and steady state phases of DC casting is modeled. An axisymmetric round billet with a radius of 100 mm is simulated. Thermal and metallurgical fields are solved in a strongly coupled manner. Within a time step, thermal and mechanical problems are decoupled using an isothermal staggered approach. 4-noded thermal element and 9-noded mechanical elements are employed. The bottom block and mold are not included in the computational domain. The interfacial heat transfer is incorporated through the temperature-dependent heat transfer coefficient. The contact between the bottom block–billet and mold–billet are neglected. Therefore, the bottom of the billet is fixed for the first 15 seconds and then released. 8 elements are taken in the radial direction, and the time increment is considered as 3 seconds. An aluminum alloy of AA1201 is considered for the study. The mushy behavior is represented by the Norton–Hoff viscoplastic law, and the solid is assumed to follow the Garafalo law.

A constant casting speed of 120 mm/min has been considered to illustrate the evolution of temperature and residual stresses during the start-up phase of DC casting. The sump depth, mushy zone length, and characteristic time are higher at the billet center

when compared to the surface. When the water starts contacting the surface of the billet, the surface temperature of the billet is above the Leidenfrost temperature. Therefore, film boiling is the dominant mode of heat transfer in the water impingement zone. The lengths of different boiling zones are computed. It is found that all components of stresses and viscoplastic strains are maximum at the billet center. Further, the nature of stresses and strains at the center are tensile and its maximum occur during the start-up phase except the axial viscoplastic strain. The attention is focused on the mushy zone and found that all the components of stresses and viscoplastic strains in the lower mushy are tensile except the axial viscoplastic strain. Tensile nature of stress and strain at the end of the solidification is a favorable situation for the development of hot tears. From the above observations, it can be concluded that the start-up phase is the most critical phase in DC casting. And also the hot tearing most likely occurs during the start-up phase than the steady phase.

The influence of different the start-up conditions are studied through different casting speed profiles. It is found that the vulnerability of start-up phase can be minimized through a proper ramping procedure. Further, ramping delays the time and increases the billet height to reach the steady state. Increase in the casting speed increases the steady state sump depth and mushy length. Stresses and strains in the mushy zone increase with increasing casting speed and they are maximum in the start-up phase. Ramping reduces the start-up phase stresses and strains. The probability of hot tearing increases with increase in casting speed. The Clyne and Davies hot tearing criterion is evaluated for different casting speed profiles. There is no significant change in hot tearing susceptibility observed. This criterion is insensitive to the ramping procedure.

The influence of secondary cooling is studied in detail. It is observed that reduced cooling increases the length of the film boiling zone. Increased secondary cooling reduces the sump parameters. Reduced secondary cooling reduces the start-up phase stresses and strains. However, during the steady state, increased cooling decreases the stresses and strains in the mushy. Therefore, the secondary cooling has to be decreased to reduce the chances of hot crack formation during the start-up phase. Similarly for the steady state, increase in secondary cooling reduces the hot crack development. Therefore, an attempt is made to vary the secondary cooling with respect to time. Even though the pattern of stress and strain evolution changes for different cooling strategies, due to the complex nature of residual stresses and strains, there is no specific conclusion made in this regarding. However, through the optimized cooling strategy, it is always possible to reduce the chances of hot crack initiation. It is also found that the following secondary cooling parameters have the least influences in the DC casting: film boiling and maximum heat transfer coefficient, and Leidenfrost temperature.

The melt temperature significantly changes the sump parameters. Increase in melt temperature decreases the mushy length and increases the sump depth. Further, increase in melt temperature increases the stress and viscoplastic strain and therefore promotes the hot cracking. A detailed study has been performed regarding the mesh convergence and time step size.

# Bibliography

- [1] D. Larouche, J. Langlais, W. U. Weili, and M. Bouchard, “A constitutive model for the tensile deformation of a binary aluminum alloy at high fractions of solid,” *Metallurgical and Materials Transactions B: Process Metallurgy and Materials Processing Science*, vol. 37, no. 3, pp. 431–443, 2006.
- [2] P. Barral and P. Quintela, “A numerical method for simulation of thermal stresses during casting of aluminium slabs,” *Computer Methods in Applied Mechanics and Engineering*, vol. 178, no. 1-2, pp. 69–88, 1999.
- [3] S. K. Das, “Modeling and optimization of direct chill casting to reduce ingot cracking,” tech. rep., University of Kentucky, 2006.
- [4] J. Zuidema, *Modelling of Flow Phenomena during DC Casting*. PhD thesis, Netherlands Institute for Metals Research, The Netherlands, 2005.
- [5] Suyitno, *Hot tearing and deformation in direct-chill casting of aluminum alloys*. PhD thesis, Netherlands Institute for Metals Research, The Netherlands, 2005.
- [6] D. Mortensen, “A mathematical model of the heat and fluid flows in direct-chill casting of aluminum sheet ingots and billets,” *Metallurgical and Materials Transactions B: Process Metallurgy and Materials Processing Science*, vol. 30, no. 1, pp. 119–132, 1999.
- [7] “International aluminium institute.” [www.world-aluminium.org](http://www.world-aluminium.org).
- [8] “Standard CIB global research.” [www.standardbank.co.za](http://www.standardbank.co.za).
- [9] “London metal exchange.” [www.lme.com](http://www.lme.com).
- [10] “Alumatter.” [www.aluminium.matter.org.uk](http://www.aluminium.matter.org.uk).
- [11] J. Randolph Kissell and R. L. Ferry, *Aluminum structures: A Guide to Their Specifications and Design*. New York: John Wiley & Sons, Inc., 2002.

- [12] J. Sengupta, B. G. Thomas, and M. A. Wells, "The use of water cooling during the continuous casting of steel and aluminum alloys," *Metallurgical and Materials Transactions A: Physical Metallurgy and Materials Science*, vol. 36 A, no. 1, pp. 187–204, 2005.
- [13] V. Venkateswaran, *Three dimensional heat flow in the direct chill casting of non-ferrous metals*. PhD thesis, The University of British Columbia, Canada, 1980.
- [14] H. Fjær and D. Mortensen, *Modeling for casting and solidification processing*, ch. Direct chill casting, pp. 541–564. Switzerland: Marcel Dekker, Inc., 2002.
- [15] J. M. Drezet and M. Rappaz, "Modeling of ingot distortions during direct chill casting of aluminum alloys," *Metallurgical and Materials Transactions A: Physical Metallurgy and Materials Science*, vol. 27, no. 10, pp. 3214–3225, 1996.
- [16] J. Sengupta, S. L. Cockcroft, D. M. Maijer, and A. Larouche, "Quantification of temperature, stress, and strain fields during the start-up phase of direct chill casting process by using a 3D fully coupled thermal and stress model for AA5182 ingots," *Materials Science and Engineering A*, vol. 397, no. 1-2, pp. 157–177, 2005.
- [17] W. van Haaften, *Constitutive behavior and hot tearing during aluminium DC casting*. PhD thesis, Delft University, The Netherlands, 2002.
- [18] M. M'hamdi, A. Mo, and H. G. Fjær, "TearSim: A two-phase model addressing hot tearing formation during aluminum direct chill casting," *Metallurgical and Materials Transactions A: Physical Metallurgy and Materials Science*, vol. 37, no. 10, pp. 3069–3083, 2006.
- [19] J. Mitchell, *Strain evolution during hot tearing in aluminum alloys*. PhD thesis, The University of British Columbia, Canada, 2009.
- [20] M. Lalpoor, D. G. Eskin, and L. Katgerman, "Cold-cracking assessment in AA7050 billets during direct-chill casting by thermomechanical simulation of residual thermal stresses and application of fracture mechanics," *Metallurgical and Materials Transactions A: Physical Metallurgy and Materials Science*, vol. 40, no. 13, pp. 3304–3313, 2009.
- [21] M. Založnik and B. Šarler, "Modeling of macrosegregation in direct-chill casting of aluminum alloys: Estimating the influence of casting parameters," *Materials Science and Engineering A*, vol. 413-414, pp. 85–91, 2005.

- [22] D. G. Eskin, *Physical metallurgy of direct chill casting of aluminum alloys*. CRC Press, Taylor & Francis Group Ltd, 2008.
- [23] H. J. Thevik, M. O. Asbjørn, and T. Rusten, “A mathematical model for surface segregation in aluminum direct chill casting,” *Metallurgical and Materials Transactions B: Process Metallurgy and Materials Processing Science*, vol. 30, no. 1, pp. 135–142, 1999.
- [24] D. Celentano, E. Onate, and S. Oller, “A temperature-based formulation for finite element analysis of generalized phase-change problems,” *International Journal for Numerical Methods in Engineering*, vol. 37, no. 20, pp. 3441–3465, 1994.
- [25] V. D. Fachinotti, A. Cardona, and A. E. Huespe, “A fast convergent and accurate temperature model for phase-change heat conduction,” *International Journal for Numerical Methods in Engineering*, vol. 44, no. 12, pp. 1863–1884, 1999.
- [26] M. A. Crisfield, *Non-linear Finite Element Analysis of Solids and Structures, Vol. 1: Essentials*. New York: John Wiley & Sons, 1991.
- [27] R. W. Lewis and K. Ravindran, “Finite element simulation of metal casting,” *International Journal for Numerical Methods in Engineering*, vol. 47, no. 1-3, pp. 29–59, 2000.
- [28] M. Cervera, C. A. De Saracibar, and M. Chiumenti, “Thermo-mechanical analysis of industrial solidification processes,” *International Journal for Numerical Methods in Engineering*, vol. 46, no. 9, pp. 1575–1591, 1991.
- [29] X. Ling, R. Keanini, and H. Cherukuri, “A non-iterative finite element method for inverse heat conduction problems,” *International Journal for Numerical Methods in Engineering*, vol. 56, no. 9, pp. 1315–1334, 2003.
- [30] A. F. Saleeb, T. E. Wilt, and W. Li, “An implicit integration scheme for generalized viscoplasticity with dynamic recovery,” *Computational Mechanics*, vol. 21, no. 6, pp. 429–440, 1998.
- [31] P. M. M. Vila Real, C. A. M. Oliveira, and J. T. Barbosa, “Thermo-elasto-viscoplastic numerical model for metal casting processes,” *International Journal of Mechanical Sciences*, vol. 46, no. 2, pp. 245–261, 2004.
- [32] F. Armero and J. Simo, “A new unconditionally stable fractional step method for nonlinear coupled thermo mechanical problems,” *International journal of numerical methods in engineering*, vol. 35, pp. 737–766, 1992.



- [33] C. Agelet De Saracibar, M. Cervera, and M. Chiumenti, “On the formulation of coupled thermoplastic problems with phase-change,” *International Journal of Plasticity*, vol. 15, no. 1, pp. 1–34, 1999.
- [34] D. A. Knoll, D. B. Kothe, and B. Lally, “New nonlinear solution method for phase-change problems,” *Numerical Heat Transfer, Part B: Fundamentals*, vol. 35, no. 4, pp. 439–459, 1999.
- [35] S. Koric and B. G. Thomas, “Efficient thermo-mechanical model for solidification processes,” *International Journal for Numerical Methods in Engineering*, vol. 66, no. 12, pp. 1955–1989, 2006.
- [36] N. Zabaras, Y. Ruan, and O. Richmond, “Front tracking thermomechanical model for hypoelastic-viscoplastic behavior in a solidifying body,” *Computer Methods in Applied Mechanics and Engineering*, vol. 81, no. 3, pp. 333–364, 1990.
- [37] M. Salcudean and Z. Abdullah, “On the numerical modelling of heat transfer during solidification processes,” *International Journal for Numerical Methods in Engineering*, vol. 25, no. 2, pp. 445–473, 1988.
- [38] A. K. Nallathambi, Y. Kaymak, E. Specht, and A. Bertram, “Optimum strategies to reduce residual stresses and distortion during the metal quenching process,” *Journal of ASTM International*, vol. 6, no. 4, p. JAI101806, 2009.
- [39] A. K. Nallathambi, Y. Kaymak, E. Specht, and A. Bertram, “Distortion and residual stresses during metal quenching process,” in *Micro-Macro-Interactions in Structured Media and Particle Systems* (A. Bertram and J. Thomas, eds.), pp. 145–157, Springer-Verlag, Berlin, 2008.
- [40] S. Bounds, K. Davey, and S. Hinduja, “A modified effective capacitance method for solidification modelling using linear tetrahedral finite elements,” *International Journal for Numerical Methods in Engineering*, vol. 39, no. 18, pp. 3195–3215, 1996.
- [41] V. R. Voller, C. R. Swaminathan, and B. G. Thomas, “Fixed grid techniques for phase change problems. A review,” *International Journal for Numerical Methods in Engineering*, vol. 30, no. 4, pp. 875–898, 1990.
- [42] K. K. Tamma and R. R. Namburu, “Recent advances, trends and new perspectives via enthalpy-based finite element formulations for applications to solidification problems,” *International Journal for Numerical Methods in Engineering*, vol. 30, no. 4, pp. 803–820, 1990.

- [43] A. A. Samarskii, P. N. Vabishchevich, O. P. Iliev, and A. G. Churbanov, “Numerical simulation of convection/diffusion phase change problems-A review,” *International Journal of Heat and Mass Transfer*, vol. 36, no. 17, pp. 4095–4106, 1993.
- [44] P. R. Cha, D. H. Yeon, and J. K. Yoon, “A phase field model for isothermal solidification of multicomponent alloys,” *Acta Materialia*, vol. 49, no. 16, pp. 3295–3307, 2001.
- [45] J. Chessa, P. Smolinski, and T. Belytschko, “The extended finite element method (XFEM) for solidification problems,” *International Journal for Numerical Methods in Engineering*, vol. 53, no. 8, pp. 1959–1977, 2002.
- [46] K. N. Shukla, “A short review of classical Stefan problem,” *Indian journal of engineering and materials sciences*, vol. 9, no. 1, pp. 25–34, 2002.
- [47] K. N. Seetharamu, R. Paragasam, G. A. Quadir, Z. A. Zainal, B. S. Prasad, and T. Sundararajan, “Finite element modelling of solidification phenomena,” *Sadhana*, vol. 26, no. 1-2, pp. 103–120, 2001.
- [48] C. Y. Li, S. V. Garimella, and J. E. Simpson, “Fixed-grid front-tracking algorithm for solidification problems, part I: Method and validation,” *Numerical Heat Transfer, Part B: Fundamentals*, vol. 43, no. 2, pp. 117–141, 2003.
- [49] D. J. Browne and J. D. Hunt, “A fixed grid front-tracking model of the growth of a columnar front and an equiaxed grain during solidification of an alloy,” *Numerical Heat Transfer, Part B: Fundamentals*, vol. 45, no. 5, pp. 395–419, 2004.
- [50] N. Nigro, A. Huespe, and V. Fachinotti, “Phasewise numerical integration of finite element method applied to solidification processes,” *International Journal of Heat and Mass Transfer*, vol. 43, no. 7, pp. 1053–1066, 2000.
- [51] D. Celentano, S. Oller, and E. Onate, “A coupled thermomechanical model for the solidification of cast metals,” *International Journal of Solids and Structures*, vol. 33, no. 5, pp. 647–673, 1996.
- [52] J. C. Simo and T. J. R. Hughes, *Computational Inelasticity*. New York: Springer Verlag, 1997.
- [53] H. Hao, D. M. Maijer, M. A. Wells, S. L. Cockcroft, D. Sediako, and S. Hibbins, “Development and validation of a thermal model of the direct chill casting of AZ31 magnesium billets,” *Metallurgical and Materials Transactions A: Physical Metallurgy and Materials Science*, vol. 35 A, no. 12, pp. 3843–3854, 2004.

- [54] L. Katgerman, S. C. Flood, and A. H. Langille, “Modelling of D.C. casting of aluminium alloys,” *Production, Refining, Fabrication and Recycling of Light Metals*, pp. 96–110, 1990.
- [55] J. Sengupta, S. L. Cockcroft, D. M. Maijer, M. A. Wells, and A. Larouche, “On the development of a three-dimensional transient thermal model to predict ingot cooling behavior during the start-up phase of the direct chill-casting process for an AA5182 aluminum alloy ingot,” *Metallurgical and Materials Transactions B: Process Metallurgy and Materials Processing Science*, vol. 35, no. 3, pp. 523–540, 2004.
- [56] Suyitno, W. H. Kool, and L. Katgerman, “Finite element method simulation of mushy zone behavior during direct-chill casting of an Al-4.5 pct Cu alloy,” *Metallurgical and Materials Transactions A: Physical Metallurgy and Materials Science*, vol. 35-A, no. 9, pp. 2917–2926, 2004.
- [57] A. Stangeland, A. Mo, O. Nielsen, D. Eskin, and M. M’Hamdi, “Development of thermal strain in the coherent mushy zone during solidification of aluminum alloys,” *Metallurgical and Materials Transactions A: Physical Metallurgy and Materials Science*, vol. 35 A, no. 9, pp. 2903–2915, 2004.
- [58] J. Wiskele, *Thermal analysis of the startup phase for D.C casting of an AA5182 aluminum ingot*. PhD thesis, The University of British Columbia, Canada, 1995.
- [59] J. M. Drezet, M. Rappaz, G. U. Grun, and M. Gremaud, “Determination of thermophysical properties and boundary conditions of direct chill-cast aluminum alloys using inverse methods,” *Metallurgical and Materials Transactions A: Physical Metallurgy and Materials Science*, vol. 31, no. 6, pp. 1627–1634, 2000.
- [60] A. J. Williams, T. N. Croft, and M. Cross, “Modeling of ingot development during the start-up phase of direct chill casting,” *Metallurgical and Materials Transactions B: Process Metallurgy and Materials Processing Science*, vol. 34, no. 5, pp. 727–734, 2003.
- [61] W. E. Droste, G. U. Grün, W. Schneider, and J. M. Drezet, “Thermo-mechanical modeling to predict shrinkage, shape and mold openings for DC-cast rolling ingots,” in *Light Metals: Proceedings of Sessions, TMS Annual Meeting (Warrendale, Pennsylvania)*, pp. 703–708, 2002.
- [62] J. Sengupta, *Mathematical modeling of the evolution of thermal field during start-up phase of the direct chill casting process for AA5182 sheet ingots*. PhD thesis, The University of British Columbia, Canada, 2002.

- [63] I. J. Opstelten and J. M. Rabenberg, "Determination of the thermal boundary conditions during aluminum DC casting from experimental data using inverse modeling," in *Light Metals: Proceedings of Sessions, TMS Annual Meeting (Warrendale, Pennsylvania)* (C. E. Eckert, ed.), pp. 729–735, 1999.
- [64] D. C. Weckman and P. Niessen, "A numerical simulation of the D.C. continuous casting process including nucleate boiling heat transfer," *Metallurgical Transactions B*, vol. 13, no. 4, pp. 593–602, 1982.
- [65] B. Šarler and J. Mencinger, "Solution of temperature field in DC cast aluminium alloy billet by the dual reciprocity boundary element method," *International Journal of Numerical Methods for Heat and Fluid Flow*, vol. 9, no. 3, pp. 269–295, 1999.
- [66] J. Sengupta, S. Cockcroft, D. Maijer, M. Wells, and A. Larouche, "The effect of water ejection and water incursion on the evolution of thermal field during the start-up phase of the direct chill casting process," *Journal of Light Metals*, vol. 2, no. 3, pp. 137–148, 2002.
- [67] E. J. F. R. Caron and M. A. Wells, "Effect of advanced cooling front (ACF) phenomena on film boiling and transition boiling regimes in the secondary cooling zone during the direct-chill casting of aluminum alloys," vol. 519-521, no. PART 2, pp. 1687–1692, 2006.
- [68] M. Rappaz, J. L. Desbiolles, J. M. Drezet, C. A. Gandin, A. Jacot, and P. Thevoz, "Application of inverse methods to the estimation of boundary conditions and properties," in *Modeling of Casting, Welding and Advanced Solidification Processes, TMS Annual Meeting (Warrendale, Pennsylvania)* (M. Cross and J. Campbell, eds.), pp. 449–457, 1995.
- [69] J. B. Wiskel and S. L. Cockcroft, "Heat-flow-based analysis of surface crack formation during the start-up of the direct chill casting process: Part I. Development of the inverse heat-transfer model," *Metallurgical and Materials Transactions B: Process Metallurgy and Materials Processing Science*, vol. 27, no. 1, pp. 119–127, 1996.
- [70] J. B. Wiskel and S. L. Cockcroft, "Heat-flow-based analysis of surface crack formation during the start-up of the direct chill casting process: Part II. Experimental study of an AA5182 rolling ingot," *Metallurgical and Materials Transactions B: Process Metallurgy and Materials Processing Science*, vol. 27, no. 1, pp. 129–137, 1996.

- [71] M. Tsunekawa, N. Hayashi, and T. Uno, “Effects of various cooling conditions on the characteristic properties of aluminum DC ingots,” *Keikinzoku/Journal of Japan Institute of Light Metals*, vol. 46, pp. 132–137, 1996.
- [72] J. Grandfield, A. Hoadley, and S. Instone, “Water cooling in direct chill casting: Part 1, boiling theory and control,” in *Light Metals: Proceedings of Sessions, TMS Annual Meeting (Warrendale, Pennsylvania)*, pp. 691–699, 1997.
- [73] L. Maenner, B. Magnin, and Y. Caratini, “Comprehensive approach to water cooling in DC casting,” in *Light Metals: Proceedings of Sessions, TMS Annual Meeting (Warrendale, Pennsylvania)*, pp. 701–707, 1999.
- [74] L. Kiss, T. Meenken, A. Charette, Y. Lefebvre, and R. Lévesque, “Effect of water quality and water type on the heat transfer in DC casting,” *TMS Light Metals*, pp. 829–834, 2003.
- [75] A. Sabau, K. Kuwana, S. Viswanathan, K. Saito, and L. Davis, “Heat transfer boundary conditions for the numerical simulation of the DC casting process,” *TMS Light Metals*, pp. 667–672, 2004.
- [76] P. Barral and P. Quintela, “Numerical algorithm for prediction of thermomechanical deformation during the casting of aluminum alloy ingots,” *Finite Elements in Analysis and Design*, vol. 34, no. 2, pp. 125–143, 2000.
- [77] H. G. Fjær and A. Mo, “ALSPEN-A mathematical model for thermal stresses in direct chill casting of aluminum billets,” *Metallurgical Transactions B*, vol. 21, no. 6, pp. 1049–1061, 1990.
- [78] Y. Kaymak, *Modeling of Metal Quenching Process and Strategies to Minimize Distortion and Stresses*. PhD thesis, Otto von Guericke University, Magdeburg, Germany, 2007.
- [79] R. Pietzsch, M. Brzoza, Y. Kaymak, E. Specht, and A. Bertram, “Simulation of the distortion of long steel profiles during cooling,” *Journal of Applied Mechanics*, vol. 74, pp. 427–437, 2007.
- [80] B. Magnin, L. Maenner, L. Katgerman, and S. Engler, *Ductility and rheology of an Al-4.5% Cu alloy from room temperature to coherency temperature*, vol. 217-222. 1996.
- [81] M. M’Hamdi, S. Benum, D. Mortensen, H. G. Fjær, and J. M. Drezet, “The importance of viscoplastic strain rate in the formation of center cracks during the

- start-up phase of direct-chill cast aluminum extrusion ingots,” *Metallurgical and Materials Transactions A: Physical Metallurgy and Materials Science*, vol. 34 A, no. 9, pp. 1941–1952, 2003.
- [82] T. G. Nguyen, D. Favier, and M. Suery, “Theoretical and experimental study of the isothermal mechanical behaviour of alloys in the semi-solid state,” *International Journal of Plasticity*, vol. 10, no. 6, pp. 663–693, 1994.
- [83] S. Benke and G. Laschet, *On a class of thermo-visco-plastic constitutive equations for semi-solid alloys*, vol. 141-143. 2008.
- [84] Suyitno, W. H. Kool, and L. Katgerman, “Hot tearing criteria evaluation for direct-chill casting of an Al-4.5 pct Cu alloy,” *Metallurgical and Materials Transactions A: Physical Metallurgy and Materials Science*, vol. 36, no. 6, pp. 1537–1546, 2005.
- [85] D. G. Eskin, Suyitno, and L. Katgerman, “Mechanical properties in the semi-solid state and hot tearing of aluminium alloys,” *Progress in Materials Science*, vol. 49, no. 5, pp. 629–711, 2004.
- [86] U. Feurer *Quality Control of Engineering Alloys and the Role of Metals Science*, pp. 131–145, 1977.
- [87] T. W. Clyne and G. J. Davies, “Comparison between experimental data and theoretical predictions relating to dependence of solidification cracking on composition,” *Proc.Conf. 'Solidification and Casting of Metals'*, pp. 275–278, 1979.
- [88] L. Katgerman, “Mathematical model for hot cracking of aluminum alloys during D.C casting,” *Journal of Metals*, vol. 34, no. 2, pp. 46–49, 1982.
- [89] N. N. Prokhorov, “Resistance to hot tearing of cast metals during solidification,” *Russian Castings Production*, vol. 2, no. 2, pp. 172–175, 1962.
- [90] I. I. Novikov *Goryachelomkost Tsvetnykh Metallov I Splavov (Hot Shortness of Non-ferrous Metals and Alloys)*, 1966.
- [91] B. Magnin, L. Katgerman, and B. Hannart, “Physical and numerical modelling of thermal stress generation during DC casting of aluminum alloys,” pp. 303–310, 1995.
- [92] M. Rappaz, J. M. Drezet, and M. Gremaud, “A new hot-tearing criterion,” *Metallurgical and Materials Transactions A: Physical Metallurgy and Materials Science*, vol. 30, no. 2, pp. 449–455, 1999.

- [93] M. Braccini, C. L. Martin, M. Suéry, and Y. Bréchet, “Relation between mushy zone rheology and hot tearing phenomena in al–cu alloys,” *Modelling of Casting, Welding and Advanced Solidification Processes - IX*, pp. 18–24, 2000.
- [94] D. G. Eskin and L. Katgerman, “A quest for a new hot tearing criterion,” *Metallurgical and Materials Transactions A: Physical Metallurgy and Materials Science*, vol. 38 A, no. 7, pp. 1511–1519, 2007.
- [95] I. Farup and A. Mo, “Two-phase modeling of mushy zone parameters associated with hot tearing,” *Metallurgical and Materials Transactions A: Physical Metallurgy and Materials Science*, vol. 31, no. 5, pp. 1461–1472, 2000.
- [96] R. K. Paramatmuni, K. M. Chang, B. S. Kang, and X. Liu, “Evaluation of cracking resistance of DC casting high strength aluminum ingots,” *Materials Science and Engineering A*, vol. 379, no. 1-2, pp. 293–301, 2004.
- [97] M. Lalpoor, D. G. Eskin, G. ten Brink, and L. Katgerman, “Microstructural features of intergranular brittle fracture and cold cracking in high strength aluminum alloys,” *Materials Science and Engineering A*, vol. 527, no. 7-8, pp. 1828–1834, 2010.
- [98] A. B. Phillion, S. L. Cockcroft, and P. D. Lee, “A new methodology for measurement of semi-solid constitutive behavior and its application to examination of as-cast porosity and hot tearing in aluminum alloys,” *Materials Science and Engineering A*, vol. 491, no. 1-2, pp. 237–247, 2008.
- [99] M. M’Hamdi, A. Mo, and C. L. Martin, “Two-phase modeling directed toward hot tearing formation in aluminum direct chill casting,” *Metallurgical and Materials Transactions A: Physical Metallurgy and Materials Science*, vol. 33, no. 7, pp. 2081–2093, 2002.
- [100] C. S. Wu, “Causes of the formation of longitudinal surface cracks on the DC–cast 7039 aluminium alloy,” *Journal of Materials Science*, vol. 23, no. 2, pp. 606–610, 1988.
- [101] J. Mao, V. L. Keefer, K. M. Chang, and D. Furrer, “An investigation on quench cracking behavior of superalloy udimet 720LI using a fracture mechanics approach,” *Journal of Materials Engineering and Performance*, vol. 9, no. 2, pp. 204–214, 2000.
- [102] C. L. Martin, D. Favier, and M. Suéry, “Fracture behaviour in tension of viscoplastic porous metallic materials saturated with liquid,” *International Journal of Plasticity*, vol. 15, no. 10, pp. 981–1008, 1999.

- [103] C. L. Martin, M. Braccini, and M. Suéry, “Rheological behavior of the mushy zone at small strains,” *Materials Science and Engineering A*, vol. 325, no. 1-2, pp. 292–301, 2002.
- [104] D. J. Lahaie and M. Bouchard, “Physical modeling of the deformation mechanisms of semisolid bodies and a mechanical criterion for hot tearing,” *Metallurgical and Materials Transactions B: Process Metallurgy and Materials Processing Science*, vol. 32, no. 4, pp. 697–705, 2001.
- [105] J. A. Spittle and A. A. Cushway, “Influences of superheat and grain structure on hot-tearing susceptibilities of Al-Cu alloy castings,” *Metals Technology*, vol. 10, no. pt 1, pp. 6–13, 1983.
- [106] D. G. Eskin, V. I. Savran, and L. Katgerman, “Effects of melt temperature and casting speed on the structure and defect formation during direct-chill casting of an Al-Cu alloy,” *Metallurgical and Materials Transactions A: Physical Metallurgy and Materials Science*, vol. 36, no. 7, pp. 1965–1976, 2005.
- [107] A. K. Nallathambi, E. Specht, and A. Bertram, “Computational aspects of temperature-based finite element technique for the phase-change heat conduction problem,” *Computational Materials Science*, vol. 47, no. 2, pp. 332–341, 2009.
- [108] O. C. Zienkiewicz and R. L. Taylor, *Finite Element Method*, vol. 1. New York: McGraw-Hill, 4<sup>th</sup> ed., 1989.
- [109] H. Budhia and F. Kreith, “Heat transfer with melting or freezing in a wedge,” *International Journal of Heat and Mass Transfer*, vol. 16, no. 1, pp. 195–211, 1973.
- [110] Y. Nishida, W. Droste, and S. Engler, “The air-gap formation process at the casting-mold interface and the heat transfer mechanism through the gap,” *Metallurgical Transactions B*, vol. 17, no. 4, pp. 833–844, 1986.
- [111] A. K. Nallathambi and E. Specht, “Estimation of heat flux in array of jets quenching using experimental and inverse finite element method,” *Journal of Materials Processing Technology*, vol. 209, no. 12-13, pp. 5325–5332, 2009.
- [112] A. Mozumder, P. Woodfield, M. Islam, and M. Monde, “Maximum heat flux propagation velocity during quenching by water jet impingement,” *International Journal of Heat and Mass Transfer*, vol. 50, pp. 1559–1568, 2007.
- [113] E. Elias and G. Yadigaroglu, “A general one-dimensional model for conduction-controlled rewetting of a surface,” *Nuclear Engineering and Design*, vol. 42, no. 2, pp. 185–194, 1977.



- [114] W. Peyayopanakul and J. W. Westwater, "Evaluation of the unsteady-state quenching method for determining boiling curves," *International Journal of Heat and Mass Transfer*, vol. 21, no. 11, pp. 1437–1445, 1978.
- [115] J. J. Carbajo, "A study on the rewetting temperature," *Nuclear Engineering and Design*, vol. 84, no. 1, pp. 21–52, 1985.
- [116] S. K. Roy Chowdhury and R. H. S. Winterton, "Surface effects in pool boiling," *International Journal of Heat and Mass Transfer*, vol. 28, no. 10, pp. 1881–1889, 1985.
- [117] M. Shoji, L. C. Witte, and S. Sankaran, "The influence of surface conditions and subcooling on film-transition boiling," *Experimental Thermal and Fluid Science*, vol. 3, no. 3, pp. 280–290, 1990.
- [118] J. W. Westwater, J. J. Hwalek, and M. E. Irving, "Suggested standard method for obtaining boiling curves by quenching," *Industrial and Engineering Chemistry Fundamentals*, vol. 25, no. 4, pp. 685–692, 1986.
- [119] Z. Guo and M. S. El-Genk, "An experimental study of saturated pool boiling from downward facing and inclined surfaces," *International Journal of Heat and Mass Transfer*, vol. 35, no. 9, pp. 2109–2117, 1992.
- [120] M. S. El-Genk and Z. Guo, "Transient boiling from inclined and downward-facing surfaces in a saturated pool," *International Journal of Refrigeration*, vol. 16, no. 6, pp. 414–422, 1993.
- [121] M. S. El-Genk and A. G. Glebov, "Transient pool boiling from downward-facing curved surfaces," *International Journal of Heat and Mass Transfer*, vol. 38, no. 12, pp. 2209–2224, 1995.
- [122] W. P. Klinzing, J. C. Rozzi, and I. Mudawar, "Film and transition boiling correlations for quenching of hot surfaces with water sprays," *Journal of Heat Treating*, vol. 9, no. 2, pp. 91–103, 1992.
- [123] M. S. El-Genk and C. Gao, "Transient heat conduction during quenching of downward facing copper and stainless steel convex surfaces," *Numerical Heat Transfer; Part A: Applications*, vol. 29, no. 6, pp. 543–573, 1996.
- [124] R. Jeschar, H. Kraushaar, and H. Griebel, "Influence of gases dissolved in cooling water on heat transfer during stable film boiling," *Steel Research*, vol. 67, no. 6, pp. 227–234, 1996.

- [125] D. E. Hall, F. P. Incropera, and R. Viskanta, “Jet impingement boiling from circular free-surface jets during quenching experiments,” *American Society of Mechanical Engineers, Heat Transfer Division, (Publication) HTD*, vol. 333, pp. 131–141, 1996.
- [126] D. E. Hall, F. P. Incropera, and R. Viskanta, “Jet impingement boiling from a circular free-surface jet during quenching: Part 1-single-phase jet,” *Journal of Heat Transfer*, vol. 123, no. 5, pp. 901–910, 2001.
- [127] A. K. Mozumder, P. L. Woodfield, M. A. Islam, and M. Monde, “Maximum heat flux propagation velocity during quenching by water jet impingement,” *International Journal of Heat and Mass Transfer*, vol. 50, no. 7-8, pp. 1559–1568, 2007.
- [128] F. Puschmann, E. Specht, and J. Schmidt, “Measurement of spray cooling heat transfer using an infrared-technique in combination with the phase-doppler technique and a patternator,” *International Journal of Heat and Technology*, vol. 19, no. 2, 2001.
- [129] J. Zuidema, L. Katgerman, I. Opstelten, and J. Rabenberg, “Secondary cooling in DC casting: Modeling and experimental results,” in *Light Metals: Proceedings of Sessions, TMS Annual Meeting (Warrendale, Pennsylvania)*, pp. 873–878, 2001.
- [130] M. Wells, D. Li, and S. Cockcroft, “Influence of surface morphology, water flow rate, and sample thermal history on the boiling-water heat transfer during direct-chill casting of commercial aluminum alloys,” *Metallurgical and Materials Transactions B: Process Metallurgy and Materials Processing Science*, vol. 32, no. 5, pp. 929–939, 2001.
- [131] A. Mozumder, M. Monde, and P. Woodfield, “Delay of wetting propagation during jet impingement quenching for a high temperature surface,” *International Journal of Heat and Mass Transfer*, vol. 48, no. 25-26, pp. 5395–5407, 2005.
- [132] M. Akmal, A. Omar, and M. Hamed, “Experimental investigation of propagation of wetting front on curved surfaces exposed to an impinging water jet,” *International Journal of Microstructure and Materials Properties*, vol. 3, no. 4-5, pp. 645–681, 2008.
- [133] J. V. Beck and B. Blackwell, *Inverse Heat Conduction: Ill-Posed Problems*. New York: Wiley Inter science, 1985.
- [134] M. Monde, “Analytical method in inverse heat transfer problem using laplace transform technique,” *International Journal of Heat and Mass Transfer*, vol. 43, pp. 3965–3975, 2000.

- [135] U. Ijaz, A. Khambampati, M. Kim, S. Kim, and K.-Y. Kim, “Estimation of time-dependent heat flux and measurement bias in two-dimensional inverse heat conduction problems,” *International Journal of Heat and Mass Transfer*, vol. 50, pp. 4117–4130, 2007.
- [136] S. Deng and Y. Hwang, “Applying neural networks to the solution of forward and inverse heat conduction problems,” *International Journal of Heat and Mass Transfer*, vol. 49, pp. 4732–4750, 2006.
- [137] C. Huang and H. Wu, “An inverse hyperbolic heat conduction problem in estimating surface heat flux by the conjugate gradient method,” *Journal of Physics D: Applied Physics*, vol. 39, no. 18, pp. 4087–4096, 2006.
- [138] Q. Xue and H. Yang, “Conjugate gradient method for the hyperbolic inverse heat conduction problem with multi-variables,” *Jisuan Wuli / Chinese Journal of Computational Physics*, vol. 22, no. 5, pp. 417–424, 2005.
- [139] K. Bathe, *Finite Element Procedures in Engineering Analysis*. New Jersey: Prentice-Hall, 1982.
- [140] X. Ling, H. Cherukuri, and M. Horstemeyer, “A hybrid regularization method for inverse heat conduction problems,” *International Journal for Numerical Methods in Engineering*, vol. 65, no. 13, pp. 2246–2264, 2006.
- [141] B. Hernandez-Morales, J. K. Brimacombe, and E. B. Hawbolt, “Characterization of the boundary condition in heat treatment operations using an inverse heat conduction algorithm,” in *American Society of Mechanical Engineers, Heat Transfer Division, (Publication) HTD*, vol. 317-2, pp. 559–566, 1995.
- [142] D. Li and M. A. Wells, “Effect of subsurface thermocouple installation on the discrepancy of the measured thermal history and predicted surface heat flux during a quench operation,” *Metallurgical and Materials Transactions B: Process Metallurgy and Materials Processing Science*, vol. 36, no. 3, pp. 343–354, 2005.
- [143] W. F. Chen, *Constitutive Equations for Engineering Materials, Vol:2 Plasticity and Modelling*. New York: Elsevier, 1994.
- [144] E. A. de Souza Neto, D. Peric, and D. R. J. Owen, *Computational methods for plasticity: Theory and applications*. West Sussex: John Wiley & Sons Ltd, 2008.

# List of Publications

## International Journals

1. **Ashok Kumar Nallathambi**, Y. Kaymak, E. Specht, and A. Bertram, “Distortion and residual stresses during metal quenching process”, in *Micro-Macro-Interactions in Structured Media and Particle Systems* (A. Bertram and J. Thomas, eds.), pp. 145–157, Springer-Verlag, Berlin, 2008.
2. **Ashok Kumar Nallathambi**, Y. Kaymak, E. Specht, and A. Bertram, “Optimum strategies to reduce residual stresses and distortion during the metal quenching process”, *Journal of ASTM International*, vol. 6, no. 4, JAI101806, 2009.
3. **Ashok Kumar Nallathambi** and E. Specht, “Estimation of heat flux in array of jets quenching using experimental and inverse finite element method”, *Journal of Materials Processing Technology*, vol. 209, no. 12–13, pp. 5325–332, 2009.
4. **Ashok Kumar Nallathambi**, E. Specht, and A. Bertram, “Computational aspects of temperature-based finite element technique for the phase-change heat conduction problem”, *Computational Materials Science*, vol. 47, no. 2, pp. 332–341, 2009.
5. **Ashok Kumar Nallathambi**, Y. Kaymak, E. Specht, and A. Bertram, “Sensitivity of material properties on distortion and residual stresses during metal quenching processes”, *Journal of Materials Processing Technology*, vol. 210, no. 2, pp. 204–211, 2010.

## International Conferences

1. **Ashok Kumar Nallathambi**, U. Alam, Eckehard Specht, “Heat flux estimation in direct chill casting using experimental and inverse finite element method”, *ASME 2008 Summer Heat Transfer Conference*, August 10–14, Jacksonville, Florida, USA, 2008.

2. **Ashok Kumar Nallathambi**, E. Specht, and A. Bertram, “Finite element technique for phase-change heat conduction problem”, *ASME 2009 Summer Heat Transfer Conference*, July 19–23, San Francisco, California, USA, 2009.
3. **Ashok Kumar Nallathambi**, Y. Kaymak, E. Specht, and A. Bertram, “Influence of material properties on distortion and residual stresses during metal quenching process”, *Coupled Problems 2009*, June 8–10, Ischia Island, Italy, 2009.
4. **Ashok Kumar Nallathambi**, Y. Kaymak, E. Specht, and A. Bertram, “Distortion prediction during atomized spray and array of jets quenching”, *18<sup>th</sup> International conference on Computer Methods in Mechanics*, May 18–21, Zielona Gora, Poland, 2009.

# Curriculum Vitae

First name **Ashok Kumar**  
Family name **Nallathambi**  
Nationality Indian  
Date of birth 19-02-1980  
Place of birth Dindigul, Tamil nadu, India.  
Parents V. Nallathambi and N. Rukmani  
Marital status Single  
Email ashokkumar1980n@gmail.com



1985 – 1997 Study in St.Mary’s Higher Secondary School, Dindigul, TN, India.

1997 – 2001 Bachelor of Engineering in Mechanical Engineering,  
PSNA CET, Madurai Kamaraj University, TN, India.

2001 – 2004 Lecturer in PSY Engineering College, Anna University, TN, India.  
subjects handled are *Engineering Mechanics, Solid Mechanics, Fluid Mechanics, Thermodynamics, and Operations Research.*

2004 – 2006 Master of Technology in Engineering Mechanics (Solid),  
Indian Institute of Technology Madras, Chennai, TN, India.

2006 – 2007 Project Officer in Indian Institute of Technology Madras,  
under the guidance of Prof. Srinivasan M Sivakumar.

**2007 – 2010** **Ph.D study**, GKMM 828, ISUT,  
Otto von Guericke University, Magdeburg, Germany.  
under the guidance of Prof. E. Specht and Prof. A. Bertram.

2010 – Till date Post Doctoral Research Fellowship, GRK 1554, ISUT,  
Otto von Guericke University, Magdeburg, Germany.

# Contact Information

## **Ashok Kumar Nallathambi,**

G10-132, ISUT,

Otto von Guericke University Magdeburg,

Universitätsplatz 2, 39106 Magdeburg.

Ph: 0049 391 67 12737

Fax: 0049 391 67 12762

Email: ashokkumar1980n@gmail.com

Webpage: <http://sites.google.com/site/ashok1980nalla/>

## **Prof. Eckehard Specht,**

Professor, Institute of Fluid Dynamics and Thermodynamics,

G10-135, Otto von Guericke University Magdeburg,

Universitätsplatz 2,

39106 Magdeburg.

Ph: 0049 391 67 18765

Fax: 0049 391 67 12762

Email: eckehard.specht@ovgu.de

## **Prof. Albrecht Bertram,**

Professor, Institute of Mechanics,

G10-057, Otto von Guericke University Magdeburg,

Universitätsplatz 2,

39106 Magdeburg.

Ph: 0049 391 67 12607

Email: albrecht.bertram@ovgu.de